UNIVERSITY OF CALIFORNIA, SAN DIEGO

Development and Validation of Compressible Mixture Viscous Fluid Algorithm Applied to Predict the Evolution of Inertial Fusion Energy Chamber Gas and the Impact of Gas on Direct-Drive Target Survival

A dissertation submitted in partial satisfaction of the
requirements for the degree Doctor of Philosophy

in

Engineering Sciences with Specialization in Computational Sciences

by

Robert Scott Martin

Committee in charge:

Professor Farrokh Najmabadi, Chair
Professor Thomas Bewley
Professor Michael Holst
Professor Kevin Quest
Professor George Tynan

2011

.

The Dissertation of Robert Scott Martin is approved, and it is acceptable in quality and form for publication on microfilm and electronically:

_____

_____

_____

_____

_____

Chair

University of California, San Diego

2011

DEDICATION

This work is dedicated to my parents, grandmother, Natasha, and all of the friends I have made along the way throughout my graduate career;

To my parents and grandmother for instilling in me the importance of education at all levels from an early age and, in the case of my parents, finding ways of incentivizing it when necessary;

To Natasha for sticking with me and providing her continuous support, patience, and faith in my abilities even as schedules slipped and time-lines changed. Her love and trust has been a singular motivation driving me to push harder and succeed. She has also helped me maintain my perspective and sanity throughout the final push to finish;

And finally, to all the friends I've made along the way whether room-mates, colleagues, neighbors or otherwise. Whether on adventure trips, in random discussions during coffee-breaks, or during GSA work, these friends are what have made this the best time of my life thus far. In particular, I acknowledge the key role that Doug, Brian, and Ashton have made to this end.

TABLE OF CONTENTS

LIST OF FIGURES

LIST OF TABLES

ACKNOWLEDGMENTS

I would like to acknowledge and thank Professor Najmabadi for his support as chair of my committee. Through introducing me to the field of fusion technology, he provided me with a rich field of unsolved problems with the potential to make a dramatic impact on society and has also supported me with the flexibility to discover how best I can contribute even in the face of shifting program priorities.

I thank Dr. Dragojlovic for his work in the initial construction of the SPARTAN code and for helping me understand the details of its construction and function. I also thank Dr. Day for his feedback on the gas mixture algorithm modifications introduced into SPARTAN. His encouragement to more thoroughly explore convergence and stability properties of the algorithm led to a better understanding of its limits and greater confidence in its results.

I also thank the members of my committee for their interest and patience throughout my doctoral studies. In particular, I would like to acknowledge the formative role my early coursework under Professors Bewley and Holst played in my interest in numerical methods. Similarly, I thank Professors Williams and Bahadori for introducing me to physical gas dynamics and kinetic theory, the physics on which this work is founded. I also thank Professor Bahadori for providing me with a teaching assistant opportunity in the gas dynamics course to further my understanding of the field.

I thank Professor Miller, Nora Burnett, and Dr. Rothe, for helping me identify, track down, and understand Dr. Rothe's early experimental work that plays a key role in the validation of my algorithm.

Finally, I would like to thank the ARCS foundation and the Marshall H. and Nellie Alworth Memorial Fund for providing additional financial assistance during portions of my graduate career. I would particularly like to thank Sharon and Carlos Arbelaez for sponsorship of my ARCS award.

Chapter 1, in part, contains material in preparation for submission for

publication. Martin, R.; Najmabadi, F., Journal of Computational Physics, 2011. The dissertation author was the primary investigator and author of this material.

Chapter 2, in part, is a reprint of material as it appears in Proceedings of the 27th International Symposium on Rarefied Gas Dynamics, July 2010. Martin, R.; Najmabadi, F., 2010. The dissertation author was the primary investigator and author of this paper.

Chapter 2, in part, contains material in preparation for submission for publication. Martin, R.; Najmabadi, F., Journal of Computational Physics, 2011. The dissertation author was the primary investigator and author of this material.

Chapter 2, in part, contains material in preparation for submission for publication. Martin, R.; Najmabadi, F., Physics of Fluids, 2011. The dissertation author was the primary investigator and author of this material.

Chapter 3, in part, is a reprint of material submitted to Fusion Science and Technology, November 2010. Martin, R.; Najmabadi, F., 2010. The dissertation author was the primary investigator and author of this paper.

Chapter 4, in part, is a reprint of material submitted to Fusion Science and Technology, November 2010. Martin, R.; Najmabadi, F., 2010. The dissertation author was the primary investigator and author of this paper.

Chapter 5, in part, contains material in preparation for submission for publication. Martin, R.; Najmabadi, F., Journal of Computational Physics, 2011. The dissertation author was the primary investigator and author of this material.

VITA

2004	Bachelor of Science, Iowa State University
2004-2010	Research Assistant, University of California, San Diego
2007	Master of Science, University of California, San Diego
2007	Teaching Assistant, Department of Mechanical and Aerospace Engineering, University of California San Diego
2011	Doctor of Philosophy, University of California, San Diego

PUBLICATIONS

"Simulation of Diffusive Separation in Helium-Argon Free Jet Mixture", R. Martin and F. Najmabadi, (To be Submitted - Physics of Fluids)

"Diffusion Flux Limited Multi-Component Compressible Flow with Thermal Mass Diffusion", R. Martin and F. Najmabadi, (To be Submitted - Journal of Computational Physics)

"Improved Inertial Fusion Energy Direst-Drive Target Survival In Chamber Gas through Validated Simulation", R. Martin, F. Najmabadi, Submitted to Fusion Science and Technology (Proceedings of 19th ANS Topical Meeting on the Technology of Fusion Engineering), November 2010

"Breakdown and Limit of Continuum Diffusion Velocity for Binary Gas Mixtures from Direct Simulation", R. Martin and F. Najmabadi, To Appear Proceedings of the 27th International Symposium on Rarefied Gas Dynamics, July 2010

"Prediction of Inertial Confinement Fusion Chamber Gas Evolution using Multi-species Computational Fluid Dynamics", R. Martin, University of California Masters Thesis, UMI ProQuest, Committee: F. Najmabadi, Z. Dragojlovic, F. Williams, 2007

"High Average Power Laser Program Optics and Chamber Studies: 2005 Progress Report", M. S. Tillack, F. Najmabadi, A. R. Raffray, K. Cockrell, Z. Dragojlovic, R. Harrison, A. Iroezi, R. Martin, J. E. Pulsifer, K. Sequoia and X. Wang, UCSD report UCSD-CER-06-01, February 2006

TALKS AND PRESENTATIONS

"Improved Inertial Fusion Energy Chamber Inter-Shot Relaxation through Validated Simulation", R. Martin, Oral Presentation, 19th ANS Topical Meeting on the Technology of Fusion Engineering, November 2010

"Breakdown and Limit of Continuum Diffusion Velocity for Binary Gas Mixtures from Direct Simulation", R. Martin, Oral Presentation, 27th International Symposium on Rarefied Gas Dynamics, July 2010

"Multi-Species Computational Fluid Dynamics For Inertial Fusion Energy Chamber Gas", R. Martin, Z. Dragojlovic, F. Najmabadi, Poster, Jacobs Research Expo, March 2008

"Multi-Species Computational Fluid Dynamics For Inertial Fusion Energy Chamber Gas", R. Martin, Oral Presentation, UCSD All-Grad Research Symposium, February 2008

"Simulation of Gas Mixtures For Inertial Confinement Fusion, R. Martin, Z. Dragojlovic, F. Najmabadi, UCSD All-Grad Research Symposium Poster Session, January 2007

SERVICE

Student Representative, "Coordinating Committee on Graduate Affairs - University of California Academic Senate", (2009-2010)

Coffeehouse Commissioner, "Graduate Student Association - University of California, San Diego", (2009-2010)

Legislative Liaison, "Graduate Student Association - University of California, San Diego", (2008-2009)

External Vice President, "Graduate Student Association - University of California, San Diego", (2006-2008)

MAE Department Representative, "Graduate Student Association - University of California, San Diego", (2005-2007)

AWARDS

Achievement Rewards for College Scientists (ARCS), Scholar, 2008-2010

Graduate Student Association of the Year, University of California Student Association, 2007-2008

Marshall H. and Nellie Alworth Scholarship Recipient, 2000-2008

Alumni Development Scholarship Recipient, Department of Aerospace Engineering, Iowa State University, 2002-2004

FIELDS OF STUDY

Major Field: Engineering

Studies in Physical Gas Dynamics

Fluids

Computational Sciences

Radiation Transport

ABSTRACT OF THE DISSERTATION

Development and Validation of Compressible Mixture Viscous Fluid Algorithm Applied to Predict the Evolution of Inertial Fusion Energy Chamber Gas and the Impact of Gas on Direct-Drive Target Survival

by

Robert Scott Martin

Doctor of Philosophy in Engineering Sciences with Specialization in Computational Sciences

University of California, San Diego, 2011

Professor Farrokh Najmabadi, Chair

Inertial confinement fusion is one of two primary approaches to the production of fusion energy for power generation. Due to the high cost of experimentation for large scale systems such as Laser Inertial Fusion Energy (Laser IFE), the ability to accurately simulate the expected performance using properly validated models is of critical importance. The evolution of the chamber environment from target injection through the generation of fusion energy is a key issue for the success of Laser IFE. Because burn emissions have the potential to damage IFE chamber walls, chamber gas is investigated to protect the wall. In the research presented, a new fluid algorithm for gas mixtures is created through the extension and correction of a prior single gas algorithm for IFE chamber gases. Once validated, this algorithm is applied to an array of chamber gases, densities, and geometric configurations. Resulting chamber states are used to estimate direct-drive target survival within the gas. This defines a new safe design window for chamber gas. This work also highlights key areas of future research to minimize uncertainty in the system design window.

Chapter I

Introduction

I.A Motivation

I.A.1 Controlled Nuclear Fusion

Fusion energy from the sun is the source of energy driving the existence of life. Safely harnessing the power of fusion on earth would provide mankind with a clean and abundant power supply into the future. This is why the National Academy of Engineering has identified fusion energy as one of its grand challenges. Though the physical process of fusion is well understood, the conditions required for sustained net energy production push the limits of technical understanding across a broad spectrum of engineering disciplines.

The field of fusion science and engineering can be broadly separated between the approaches of inertial and magnetic confinement which have been identified as the two primary means with the potential to result in an economical path to fusion energy. This work focuses on inertial fusion energy (IFE), and in particular on the direct drive (DD) approach which uses an array of intense lasers to symmetrically illuminate a cryogenic target of hydrogen isotopes within a vacuum chamber. As the outer layers of the target are heated and propelled off the surface, the remainder of the target is compressed and heated to undergo thermonuclear burn. The energy released by the target is then recovered within the chamber

walls and converted into electricity. For economic viability, this process must be repeated 5-10 times per second necessitating targets to be continuously launched into the chamber and compressed by the lasers.

Though the most recent direct drive IFE designs include very little gas within the chamber to improve survival of the cryogenic target, some mass is introduced to the chamber from each target injected. Though this gas may be removed through vacuum pumping, the parasitic power required to evacuate the chamber to arbitrarily low densities places a floor on the realizable chamber density. The most efficient power-plant design must balance the cost of this parasitic power with constraints on the survivability of chamber conditions.

Furthermore, small amounts of gas within the chamber can act as a buffer for the intense ion and x-ray energy burst resulting from the fusion burn and reduce damage to the armor on the walls of the chamber. Designing a powerplant that efficiently operates near the boundary of target survival requires detailed understanding of the evolution of the chamber environment between subsequent target injections as well as the impact of that environment on a target.

I.A.2 Target Damage from Chamber Gas

A thorough analysis of the risk posed to direct drive IFE targets can be found in the Center for Energy Research (CER) report 06-02, References [13] as well as the subsequent paper, [15]. In this work, Boehm modeled the time dependent thermodynamics and mechanics of direct drive targets including an analysis of phase change and bubble nucleation within the deuterium-tritium (DT) ice layer. The primary modes of target heating during injection result from interaction with the chamber gas and radiation from the chamber walls. He paid particular attention to the decay of tritium into ^{3}He between target fabrication and use. This helium remains gaseous at the DT ice temperature and diffuses through the lattice until falling into a trap such as a vacancy.

These helium atoms become relevant when the target heat-loading causes

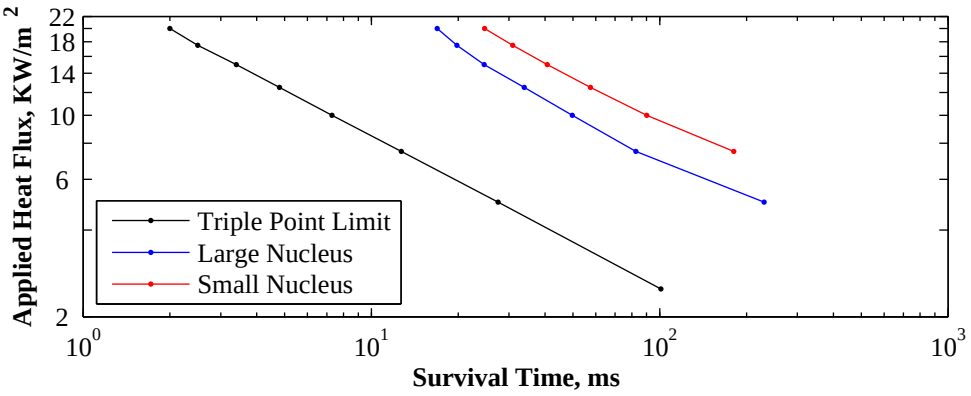

Figure I.1: Allowable heat flux versus survival time by target failure mode for $18K$ IFE target injection temperature with $4mm$ diameter

the DT-ice to reach its triple point temperature. The helium in the lattice is then free to nucleate into bubbles in the melt layer. It is believed that the formation of these helium bubbles is much more detrimental to target symmetry and impedes target implosion much more than the melt layer alone.

Figure I.1 shows the survival times for a target initially at $18K$ relative the imposed heat flux from Reference [15]. Though several initial temperatures were considered in that work, this work focuses only on the $18K$ cases for simplicity with the understanding that some flexibility may remain in this choice. The three survival criteria were the time to reach triple point (Triple Point Limit), time before onset of bubble growth with initial $1.8\mu m$ ^{3}He nucleus (Large Nucleus), and time before onset of bubble growth with initial $0.4\mu m$ ^{3}He nucleus (Small Nucleus). These bubble nucleus sizes depend on the delay between fabrication of the target and injection and are the upper and lower bounds on the expected nucleus size based on matching the bubble growth models with observed growth rates in data from Los Alamos National Laboratory [15].

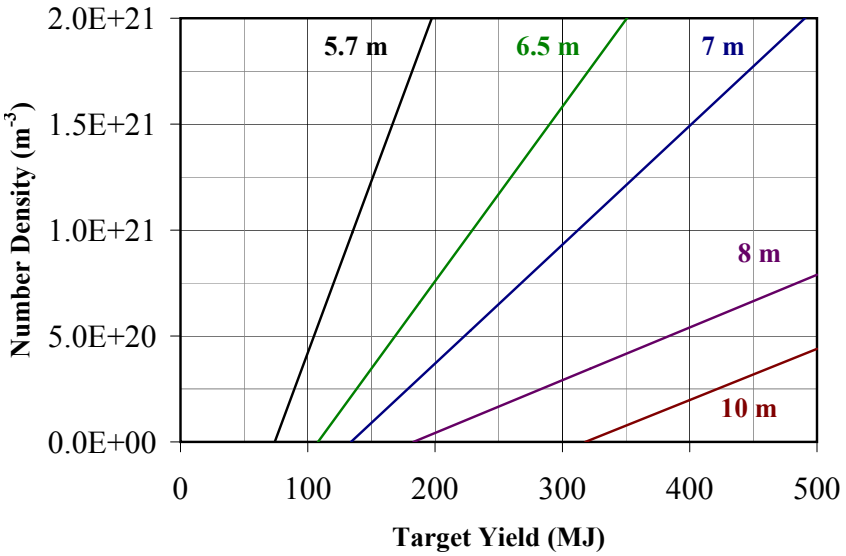

Figure I.2: Survivable target yields by chamber radius and chamber gas density for direct drive IFE chamber walls

I.A.3 Benefit of Chamber Gas to Wall Damage

Emissions from fusion target burn pose several different hazards to the first wall of the target chamber. The threats consist of x-rays, fast burn ions, and slower thermal ions. Reference [67] provides a thorough analysis of these hazards for dry wall direct drive IFE chambers.

In general, more gas and larger radius chambers decrease the average heat flux on the wall and improve survivability. Based on the criteria that the surface of the tungsten wall armor must remain below its melting point, Reference [67] provides survivability contours by gas density and chamber radius for target yields up to approximately 400 MJ. The calculation uses the x-ray and ion spectra from a LASNEX simulation of a 154 MJ Navy Research Laboratory (NRL) target design[66]. The other yield spectra were simple linear scaling of the 154 MJ target's spectra. Figure I.2 shows the resulting survival curves from the data of Reference [67]. Using this information and the highest density that allows target survival enables design of the lowest power vacuum system necessary to sustained powerplant operations.

It is important to note that this constraint simply ensures that the tungsten armor stays below its melt temperature. Another failure mode of the armor results from fast helium ions implanting in the armor. If this helium implants further into the tungsten than it can diffuse out, the accumulation can cause blistering and loss of wall material. This problem has been studied extensively and several options are being considered to address the problem including nano-engineered armor and magnetic intervention. Reference [75] provides an overview of these efforts as well as other key components of direct drive IFE technology.

I.A.4 Vacuum System Scale and Cost

As a potential solution to the risk posed by chamber gas, an effectively complete elimination of the gas has been proposed[65]. In that work, it was recognized that even without the intentional inclusion of chamber gas, some remnant gas from target byproducts would remain. In that study, the effect of remnant deuterium was considered at densities from approximately 0 to $3.2e20/m^3$. These cases were found to provide greatly improved target survival over the original concepts with chambers filled at up to an order of magnitude higher density to enhance wall survival.

Obviously, zero density is impossible to achieve and is only intended as the level at which the target hazard is negligible. The absolute minimum realizable chamber density in steady operation results from a vacuum system that consumes the entire electrical output of the powerplant. The higher the allowable density, the lower this recirculation power becomes. Relatively little work has been done on optimizing IFE chamber vacuum system design though it is generally considered tractable. Reference [28] provides an example design point for an $11m$ radius chamber with 60 beamlines and 120 Varian-V 6000 turbo pumps. The result of the analysis is that this chamber can operate in steady state at $1.8mtorr$ pressure assuming a $5Hz$ target injection rate. This pressure assumes a gas temperature of $1000K$ which implies a chamber density of only $1.7e19/m^3$. The dominant source

of additional particles in this analysis is the 1e21 particles per target at 5 Hz from Reference [66]. Based on the manufacturer's data[83], each of these pumps consumes 1500 W at peak load resulting in only $180KW$ of vacuum power necessary to operate the powerplant. This low operating cost means that the approximately $6 million replacement cost of the turbo-pumps amortized over the 120,000+ hour mean time to failure[83] is the dominant cost of the vacuum system.

High vacuum system costs at the density levels required to ensure target survival only occur when attempting to operate a chamber that is of a composition significantly different than the makeup of the target. Assuming approximately equal pumping speeds for all gas constituents [83], maintaining 90% or 99% pure xenon chamber gas requires additional xenon injection proportional to the target particle addition which would increase the total particle load on the vacuum system by 10× or 100× the number of particles in each target. To maintain these mixtures without increasing the total combined density of all chamber particles requires scaling the vacuum system in proportion to this increased particle load. This would drive the cost based on the design of Reference [28] from approximately $12 million up to prohibitively large $120 million or $1.2 billion if it is even physically possible to fit 12,000 turbo-pumps around the chamber for the 99% pure xenon case. This clearly shows that the the vacuum level must be relaxed from the very low $1.7e19/m^3$ if high xenon purity is expected. However, the original vacuum system design is sufficient for 90% pure xenon at $1.7e20/m^3$ or 99% pure xenon at $1.7e21/m^3$. The difference between 75% pure xenon and 99% pure xenon at $1.7e20/m^3$ is the difference between 8× two-foot diameter, 550 lbs turbo pumps per beamline and 200 pumps per beamline. Clearly it is impractical to operate with highly pure xenon at low densities. Whether even attempting highly pure xenon is necessary or beneficial is addressed in this work. This is also the primary motivation for development of the tools required to study mixture chamber gases.

Furthermore, the benefit of even low levels of chamber gas can be seen from Figure I.2. Consider a 350 MJ target such as that of Reference [61] which

requires an $11m$ radius chamber with no xenon in a gas composed of only $1.7e19/m^3$ target burn products. Running the chamber instead at $1.7e20/m^3$ with 90% pure xenon can potentially reduce the diameter by approximately $1m$. This reduction translates into a 30% decrease in the volume and required vacuum system scale and power to maintain the design chamber density. However, this assumes that target is a the survival limit for both chamber configurations. Evaluating this tradeoff requires detailed knowledge of the expected chamber states and their impact on target survival.

I.A.5 Purpose of Research

In this research, expected chamber states at injection time for an array of chamber gas compositions are calculated. This information is used to estimate target survival characteristics to determine the bounds of a design window for dry wall direct drive IFE chamber gas. Due to the high cost of experimentation for large scale systems such as Laser IFE, the ability to accurately simulate the expected performance using properly validated models is vital. Through development and extension of these models, this work aims to identify areas of uncertainty that have significant impact on target survival. Identification of these important uncertainties enables the design of future small scale experiments targeted specifically at improving and validating the component models in relevant regimes. Because the models used for design must assume 'worst case scenarios' whenever uncertainty exists, reducing the uncertainty allows for more aggressive designs enhancing efficiency prior to the construction of a costly and time consuming prototype powerplant. The algorithmic development also provides useful new research tools for analysis of other compressible gas mixtures in the future.

Table I.1: Gas mean free path for a selection of relevant chamber gases

Gas	Density ($\times 10^{20}/m^3$)	Temperature (K)	Mean Free Path (mm)
He	1	4000	70.2
	16.5	1000	3.43
D	1	4000	74.4
	16.5	1000	4.51
Xe	1	4000	17.8
	16.5	1000	0.84

I.B Physical Models

I.B.1 Continuum Approximation

Before developing the fluid equations in the subsequent sections, it is important to investigate the validity of the continuum approximation in the proposed application of Laser IFE. To achieve this goal, the Knudsen number seen in Equation I.1 must first be defined. In this equation, λ_{mfp} is the mean free path as defined in Equation I.2 from Reference [84] and L is a characteristic length scale of the boundaries. A flow is called "free-molecular flow" if $\mathcal{K} \geqq 1$. If this is the case, statistical mechanics rather than continuum mechanics should be used to describe the fluid dynamics of the system.

$$\mathcal{K} = \frac{\lambda_{mfp}}{L} \tag{I.1}$$

$$\lambda_{mfp} = \frac{\mu}{\rho}\sqrt{\frac{\pi m}{2kT}} \tag{I.2}$$

Table I.1 shows the mean free path for several IFE relevant chamber gases. This table shows that even a small IFE chamber with a diameter of only $10m$ has a Knudsen number of less that 0.01 making continuum simulations a reasonable choice. Even $1m$ radius beamline is more than 25 mean free paths wide in the largest mean free path gas.

In contrast to the chamber, the mean free path of he flow around a $4mm$ diameter IFE target much more comparable. This implies that, though the con-

tinuum treatment for the full chamber and even beam lines is reasonable, it should not be applied to the target. That is Monte Carlo simulations and free molecular flow analysis are employed in Chapter IV.

I.B.2 Multi-Component Conservation Laws

The behavior of a gas may be described by the convective fluxes, accelerations, and collisions between individual particles. The Boltzmann equation for the probability distribution function, $f(v_i)$, in velocity space results from a summation of all such processes for a given particle in a differential volume of velocity space around v_i subject to the dilute gas and molecular chaos assumptions. When more than a single gas species is involved, each species, s, obeys an individual probability conservation equation as seen in the multi-component Boltzmann equation, Equation I.3. Though more tractable than the set of equations of motion for all particles, as with the single component Boltzmann equation, the collision integral term on the right side of Equation I.3 remains prohibitively computationally expensive for most fluid flows of engineering interest.

$$\frac{\partial f_s}{\partial t} + \left(\vec{v}_s \cdot \frac{\partial f_s}{\partial \vec{x}}\right) + \left(\frac{\vec{F}_s}{m_s} \cdot \frac{\partial f_s}{\partial \vec{v}_s}\right) = 2\pi \sum_r \iint (f'_s f'_r - f_s f_r) g_{sr}\, b\, db\, d\vec{v}_r \qquad \text{(I.3)}$$

In the absence of chemical reactions, collisions of particles of like or different species class, r or s, conserve individual species mass, overall momentum and overall energy. Equation I.4 shows these summational invariants for the multi-component Boltzmann equation in the post- (primed) and pre-collision (unprimed) variables. Because these quantities are preserved for any collision, they are also conserved in the sum of all possible collisions within a gas. The fluid approximation results from integrating these conserved quantities as the moments m_s, $m_s v_s$, and $\frac{1}{2} m_s v_s^2$ in generic form as ψ_s against the Boltzmann equation as shown in Equation I.5 where the over-line represents integration against the velocity probability distribution function as shown in Equation I.6. Equations I.10 through I.12 show the

result of taking these moments for ψ_s equal to m_s, $m_s\vec{v}_s$, and $\frac{1}{2}m_s v_s^2$ respectively as in Hirschfelder, Curtiss, and Bird [38] subject to the definitions of Equations I.13-I.18.

The resulting equations per unit volume for each of the conserved quantities respectively yields Equations I.7 - I.9 as outlined in Chapter IX of Vincenti, [84]. In all of these equations, the overbar notation refers to an average over the distribution function as shown in Equation I.6. Indices i, j, k refer summation notation over spacial dimensions and indices q, r, s refer to gas species numbered from $1 - S$.

$$\begin{aligned} &m_r = m_r' \qquad m_s = m_s' \\ &m_r\vec{v}_r + m_s\vec{v}_s = m_r\vec{v}_r' + m_s\vec{v}_s' \\ &\frac{1}{2}m_r v_r^2 + \frac{1}{2}m_s v_s^2 = \frac{1}{2}m_r {v_r'}^2 + \frac{1}{2}m_s {v_s'}^2 \end{aligned} \tag{I.4}$$

$$\frac{\partial n_s\overline{\psi}_s}{\partial t} + \left(\frac{\partial}{\partial\vec{x}}\cdot n_s\overline{\psi_s\vec{v}_s}\right) - n_s\left(\overline{\frac{\partial\psi_s}{\partial t}} + \left(\overline{\vec{v}_s\cdot\frac{\partial\psi}{\partial\vec{x}}}\right) + \left(\frac{\vec{F}_s}{m_s}\cdot\overline{\frac{\partial\psi_s}{\partial\vec{v}_s}}\right)\right) = 0 \tag{I.5}$$

$$\overline{Q_s} \equiv \int_{-\infty}^{\infty}\int_{-\infty}^{\infty}\int_{-\infty}^{\infty} Q_s f_s dv_1 dv_2 dv_3 \tag{I.6}$$

$$\frac{\partial\rho}{\partial t} + \frac{\partial}{\partial x_j}[\rho\overline{v}_j] = 0 \tag{I.7}$$

$$\frac{\partial}{\partial t}[\rho\overline{v}_i] + \frac{\partial}{\partial x_j}[\rho\overline{v_i v_j}] = \rho\overline{F_i} \tag{I.8}$$

$$\frac{1}{2}\frac{\partial}{\partial t}[\rho\overline{v^2}] + \frac{1}{2}\frac{\partial}{\partial x_j}[\rho\overline{v_j v^2}] = \rho\overline{F_j v_j} \tag{I.9}$$

$$\frac{\partial n_s}{\partial t} + \left(\frac{\partial}{\partial\vec{x}}\cdot n_s\overline{\vec{v}_s}\right) = \left(\frac{\partial}{\partial\vec{x}}\cdot n_s(\vec{v}_0 + \overline{\vec{V}}_s)\right) = 0 \tag{I.10}$$

$$\frac{\partial\vec{v}_0}{\partial t} + \left(\vec{v}_0\cdot\frac{\partial}{\partial\vec{x}}\vec{v}_0\right) = -\frac{1}{\rho}\left(\frac{\partial}{\partial\vec{x}}\cdot\overline{\overline{P}}\right) + \frac{1}{\rho}\sum_s n_s\vec{F}_s \tag{I.11}$$

$$\frac{\partial}{\partial t}(\rho\hat{U}^{(tr)}) + \left(\frac{\partial}{\partial \vec{x}} \cdot \rho\hat{U}^{(tr)}\vec{v}_0\right) = -\left(\frac{\partial}{\partial \vec{x}} \cdot \vec{q}\right) - \left(\overline{\overline{P}} : \frac{\partial}{\partial \vec{x}}\vec{v}_0\right) + \sum_s n_s(\vec{F}_s \cdot \overline{V}_s) \quad \text{(I.12)}$$

$$\vec{v}_0 = \frac{1}{\rho}\sum_s n_s m_s \overline{\vec{v}}_s \quad \text{(I.13)}$$

$$\overline{\vec{V}_s} = \frac{1}{n_s}\int (\vec{v}_s - \vec{v}_0) f_s d\vec{v}_s \quad \text{(I.14)}$$

$$\rho_s = \sum_s n_s m_s \quad \text{(I.15)}$$

$$\overline{\overline{P}} = \sum_s n_s m_s \overline{\vec{V}_s \vec{V}_s} \quad \text{(I.16)}$$

$$\hat{U}^{(tr)} = \frac{1}{\rho}\sum_s \frac{1}{2} n_s m_s \overline{V_s^2} \quad \text{(I.17)}$$

$$\vec{q} = \sum_s \frac{1}{2} n_s m_s \overline{V_s^2 \vec{V}_s} \quad \text{(I.18)}$$

I.B.3 Moment Closure and Constitutive Relations

Closure of the moment equations requires constitutive relations such as Fick's law of diffusion, Newton's law of viscosity, and Fourier's law of heat conduction for higher order moments. Using these constitutive relations for the diffusion, pressure, stress tensor, and heat flux vector along with the usual definitions of temperature, and total specific energy, the moment equations reduce to the familiar form of the Navier-Stokes equations with an additional set of s species mass conservation equations which sum to the overall mass conservation equation of Navier-Stokes as shown in Equations I.19-I.21. Sufficiently close to equilibrium, expressions for these closure relations may be derived from the linear perturbation of the Boltzmann equation in terms of Sonine polynomials in a procedure known as the Chapman-Enskog expansion. The following subsections show the results of this procedure for the heat flux, shear, and diffusion which allows the formation of a complete set of fluid equations for the multi-component flow.

$$\frac{\partial}{\partial t}[\rho_s] + \frac{\partial}{\partial x_j}[\rho_s v_{0j} + \rho_s(\overline{V}_j)_s] = 0 \tag{I.19}$$

$$\frac{\partial}{\partial t}[\rho v_{0i}] + \frac{\partial}{\partial x_j}[P\delta_{ij} + \rho v_{0i} v_{0j}] = \frac{\partial \tau_{ij}}{\partial x_j} + \sum_{s=1}^{S} \rho_s(\overline{F_i})_s \tag{I.20}$$

$$\frac{\partial}{\partial t}[\rho e_t] + \frac{\partial}{\partial x_j}[v_{0j}(P + \rho e_t)] = \frac{\partial}{\partial x_j}[v_{0k}\tau_{kj} - q_j] + \sum_{s=1}^{S} \rho_s(\overline{F_{sj} v_j})_s \tag{I.21}$$

Heat Flux

The heat flux vector can also be evaluated using the techniques of Reference [38]. The resulting equation is shown in Equation I.22. In the equation, the diffusion velocities, V_{is}, coefficient of thermal diffusion, D_s^T, and generalized concentration gradient, d_{is}, defined earlier are again used. In addition, the coefficient of thermal conductivity, λ_0 is used as defined in Equation I.23. In this equation, a_{s1} is yet another of the Sonine expansion coefficients.

Equations I.22 and I.23 show heat fluxes in terms of λ_0, but λ_0 is not the normal definition of thermal conductivity. Equation I.24 from Reference [38], shows the heat flux in terms of the normal λ. Equation I.25, show the relationship between λ and λ_0. Though this looks like a complication, using the heat flux vector in this form allows for direct comparison between analytical and experimentally reported values for λ.

This form of the heat flux vector does not include radiation contributions already present in the code. The heat flux vector was also derived for a monatomic gas. Hirschfelder, Curtis, and Bird do derive the equations for polyatomic gas mixtures, but these corrections have not yet been included in the formulation.

$$q_i = \frac{5}{2} kT \sum_s n_s V_{is} - \lambda_0 \frac{\partial T}{\partial x_i} - nkT \sum_{s=1}^{S} \frac{1}{n_s m_s} D_s^T d_{is} \tag{I.22}$$

$$\lambda_0(\xi) = -\frac{5}{4} k \sum_s n_s \sqrt{\frac{2kT}{m_s}} a_{s1}(\xi) \tag{I.23}$$

$$q_i = \frac{5}{2}kT\sum_s n_s V_{is} - \lambda\frac{\partial T}{\partial x_i} - \frac{kT}{n}\sum_{r,s=1}^{S}\frac{n_s D_r^T}{m_r \mathcal{D}_{rs}}\left(V_{ir} - V_{is}\right) \tag{I.24}$$

$$\lambda = \lambda_0 - \frac{k}{2n}\sum_{r,s=1}^{S}\frac{n_r n_s}{\mathcal{D}_{rs}}\left[\frac{D_r^T}{n_r m_r} - \frac{D_s^T}{n_s m_s}\right] \tag{I.25}$$

Shear

The viscous forces on the gas come into the momentum and energy equations through the shear tensor, τ_{ij}. For a multi-species gas, the shear tensor has the form shown in Equation I.26. In the equation, μ is the coefficient of viscosity, S is the stress tensor, and κ is the coefficient of bulk viscosity.

The bulk viscosity is zero for all monatomic gases as it has to do with the rate of transfer of kinetic energy to the internal energy states. For polyatomic gasses, the equation for the bulk viscosity requires relaxation times for the energy transfer to the internal degrees of freedom.

Reference [38] provide a means of calculating the coefficient of viscosity similar to that of calculating the diffusion coefficients from the Enskog expansion. The resulting expression for the coefficient is shown in Equation I.27.In this equation, b_{s0} is another Sonine expansion coefficient. Like the multi-species diffusion coefficient, $\xi = 1$ is sufficient to calculate the viscosity coefficient to a reasonable accuracy.

$$\tau_{ij} = -2\mu S_{ij} + \left(\frac{2}{3}\mu - \kappa\right)\frac{\partial v_{0k}}{\partial x_k}\delta_{ij} \tag{I.26}$$

$$\mu(\xi) = \frac{1}{2}kT\sum_{s=1}^{S} n_s b_{s0}(\xi) \tag{I.27}$$

Diffusion

The concept of diffusion velocity is the result of considering the mass average bulk velocity separate from the random noise. This random noise is in fact

closely tied to the concept of temperature as shown in the preceeding definitions. For multi-species fluid dynamics, the species average diffusion velocity, $(\overline{V}_i)_s$, is defined in Equation I.28 by summing over N_s molecules of class s. For this reason, though the density weighted sum of species average diffusion velocities, $\sum_s^S \rho_s V_{is}$, is zero by definition, the individual species average diffusion velocities are not necessarily. In fact, resulting from imbalances in the random velocities for different classes of molecules, these diffusion velocities result in the classical concept of Fickian diffusion due to concentration gradients as well as higher order phenomena such as thermal diffusion resulting from different sound speeds in molecules of different mass.

$$V_{is} = (\overline{V}_i)_s = \frac{1}{N_s} \sum_{n=1}^{N_s} m_n V_{ni} \tag{I.28}$$

An equation for the diffusion velocity, V_{is}, can be written in terms of a generalized concentration gradient vector, d_{is}, and temperature gradient as shown in Equation II.85. The form of the generalized concentration gradient is shown in Equation II.26. The diffusion velocities depend on multi-species diffusion coefficients, D_{sr}, and coefficients of thermal diffusion, D_s^T. These coefficients can be derived using a Chapman-Enskog expansion of the Boltzmann equation in Sonine polynomials as shown in Reference [38]. Equations I.31 and I.32 give the multi-species diffusion coefficient and coefficient of thermal diffusion respectively.

Because of the orthogonality of the Sonine polynomials, the resulting expressions for the diffusion coefficients depend only upon one Sonine expansion coefficient each, $c_{s0}^{(r,s)}(\xi)$ and $a_{s0}(\xi)$. However, the value of the expansion coefficients is dependant on the number of terms taken in the expansion, ξ. For multi-species diffusion, taking $\xi = 1$ is sufficient, but for thermal diffusion, ξ must be greater than or equal to 2 for the coefficient to be nonzero.

The Sonine polynomial expansion depends on the true distribution function being reasonably represented by perturbations from equilibrium in the Sonine polynomials. This requires that averages be taken over a sufficient number of col-

lisions as to ensure the validity through the central limit theorem. This results in a strengthening of the continuum constraint on the Knudsen number. However, as long as the fluid properties only vary slightly over $10s$ of mean free paths, the results are likely to be reasonably valid.

The Sonine expansion coefficients may be evaluated by solving sets of linear equations that use tabulated collision integral data, $\Omega_{sr}^{(m,n)}$ for specified potential representations of the molecules such as the Jones (6-12) potential. This approach has some limitations such as the Jones potential being spherical and therefore unable to fully represent polyatomic gases. Hirschfelder, Curtiss, and Bird, Reference [38], also show a method of converting binary diffusion coefficients to multi-species diffusion coefficients as shown in Equations I.34 and I.36 where F^{sr} is the cofactor of F_{sr} in the determinant of $|F|$ as shown in Equation I.35. In Equation I.34, $\mathcal{D}_{sr}$ is the diffusion coefficient for a binary mixture. Using this approach, experimental data based on binary diffusion can be used when available and the system can be completed if necessary using the estimated coefficients.

Rather than reporting the thermal diffusion coefficient directly, most experimental data available uses the thermal diffusion ratio, k_T, as defined in Equation I.33 for binary mixture AB. This is because classical examples of thermal diffusion are typically performed in binary, incompressible, steady state settings where k_T is more natural. However, because the IFE system has strong thermal gradients, an investigation into the relative contribution of the effect needs to be done. As explained later in the implementation section, the concept of the thermal diffusion ratio is used in the case of a light gas diffusing through a heavier gas mixture as a first approximation to thermal diffusion.

$$V_{is} = \left(\frac{n^2}{n_s \rho}\right) \sum_{r=1}^{S} m_r D_{sr} d_{ir} - \frac{1}{n_s m_s} D_s^T \frac{\partial \ln T}{\partial x_i} \tag{I.29}$$

$$d_{is} = \frac{\partial}{\partial x_i}\left(\frac{n_s}{n}\right) + \left(\frac{n_s}{n} - \frac{n_s m_s}{\rho}\right) \frac{\partial \ln p}{\partial x_i} - \left(\frac{n_s m_s}{P\rho}\right) \left[\frac{\rho}{m_s} F_{is} - \sum_{r=1}^{S} n_r F_{ir}\right] \tag{I.30}$$

$$D_{rs}(\xi) = \frac{\rho n_s}{2nm_r}\sqrt{\frac{2kT}{m_s}}c_{s0}^{(r,s)}(\xi) \tag{I.31}$$

$$D_s^T(\xi) = \frac{n_s m_s}{2}\sqrt{\frac{2kT}{m_s}}a_{s0}(\xi) \tag{I.32}$$

$$k_T = \frac{\rho}{n^2 m_A m_B}\frac{D_A^T}{\mathcal{D}_{AB}} \tag{I.33}$$

$$F_{sr} = \left\{\frac{n_s}{\rho\mathcal{D}_{sr}(1)} + \sum_{q=1,q\neq r}^{S}\frac{n_q m_q}{\rho m_i \mathcal{D}_{sq}(1)}\right\}(1-\delta_{sr}) \tag{I.34}$$

$$F^{sr} = (-1)^{s+r}\begin{vmatrix} F_{11} & \cdots & F_{1,r-1} & F_{1,r+1} & \cdots & F_{1\nu} \\ \cdot & & \cdot & \cdot & & \cdot \\ \cdot & & \cdot & \cdot & & \cdot \\ \cdot & & \cdot & \cdot & & \cdot \\ F_{s-1,1} & \cdots & F_{s-1,r-1} & F_{s-1,r+1} & \cdots & F_{s-1,\nu} \\ F_{s+1,1} & \cdots & F_{s+1,r-1} & F_{s+1,r+1} & \cdots & F_{s+1,\nu} \\ \cdot & & \cdot & \cdot & & \cdot \\ \cdot & & \cdot & \cdot & & \cdot \\ \cdot & & \cdot & \cdot & & \cdot \\ F_{\nu,1} & \cdots & F_{\nu,r-1} & F_{\nu,r+1} & \cdots & F_{\nu,\nu} \end{vmatrix} \tag{I.35}$$

$$D_{sr}(1) = \frac{F^{sr} - F^{ss}}{m_r|F|} \tag{I.36}$$

I.B.4 Radiation Model

Optically Thin Assumption

Radiative cooling plays an important role in the relaxation of IFE chamber gas. In this work we assume the gas can be approximated as optically thin for the states of interest. To verify this assumption, we consider the Rosseland mean

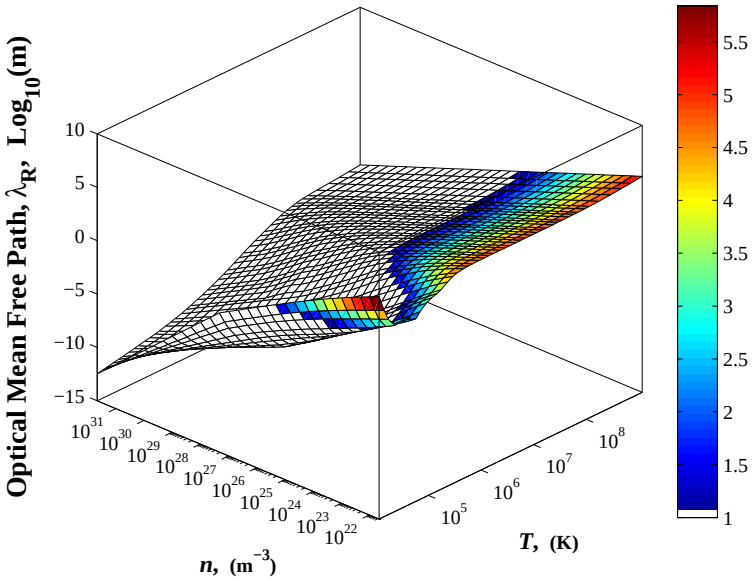

Figure I.3: Helium Rosseland optical mean free path from SESAME database.

free path for radiation from Reference [84]. Equation I.37 shows the relationship of the Rosseland mean free path, λ_R, to the frequency dependent opacity, σ_ν.

$$\lambda_R = \frac{15}{4\pi^4} \int_0^\infty \frac{1}{\rho\sigma_\nu} \frac{e^{h\nu/kT}}{\left(e^{h\nu/kT}-1\right)^2} \left(\frac{h\nu}{kT}\right)^4 d\left(\frac{h\nu}{kT}\right) \tag{I.37}$$

Los Alamos National Laboratory maintains equation of state and opacity databases for many of the elements of interest for IFE chamber gasses. In particular, the database provides the Rosseland mean opacity, κ_r, which is equivalent to $(\rho\lambda_R)^{-1}$. This allows the behavior of the optical mean free path to calculated directly from experimentally verified data. Figures I.3 and I.4 show these optical mean free paths for helium and xenon gas respectively.

For direct drive target chambers, the density range available in SESAME tables is generally several orders of magnitude too high to be used directly. The behavior of the mean free paths shown in Figures I.3 and I.4 indicates that, for both gasses, mean free paths in excess of $10m$ can be expected across a broad temperature range for densities below approximately $10^{23}/m^3$.

It is important to note that these mean free paths are the gray average

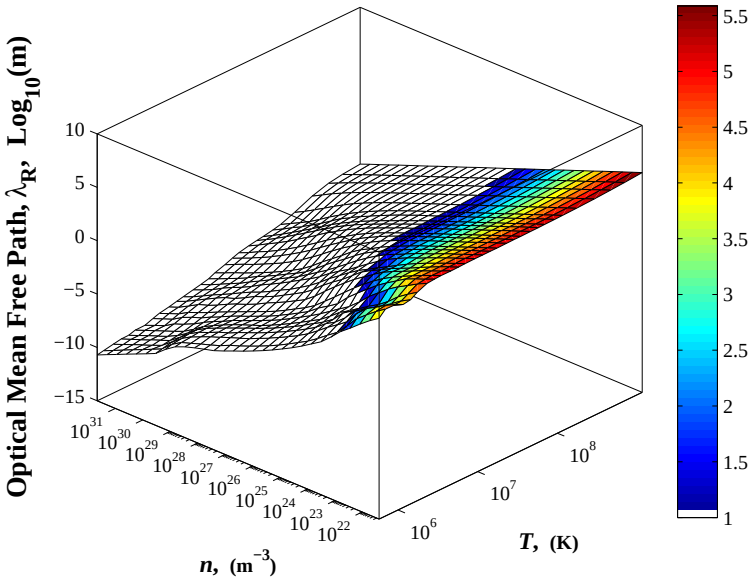

Figure I.4: Xenon Rosseland optical mean free path from SESAME database.

for blackbody emitting gas. The opacities for hard x-rays up to the $1Mev$ range during the fusion burn are handled separately within the fusion burn codes used to generate initial conditions. The optically thin assumption does not apply to these hard x-rays. For further details on this topic, the reader is referred to the description in the BUCKY reference manual[47].

Plasma Cooling Rate

Because SESAME data is unavailable at the densities of interest for direct-drive IFE chambers, opacities and plasma cooling rates are generated and tabulated using the IONMIX code[48]. IONMIX was created to investigate the radiative effects of plasmas ranging from relatively high densities down to low density regimes as found in inertial confinement fusion target implosions and chambers. IONMIX produces the multi-group opacities needed to describe the absorption, emission, and transport of radiation in the local thermodynamic equilibrium (LTE) and non-LTE limits. It first calculates steady-state ionization populations using detailed balance accounting for collisional, radiative, and dielectric ionization

and excitation processes. The contributions of bremsstrahlung, photoionization, bound-bound transitions, Thomson scattering, and plasma waves are then used to calculate absorption, emission, and scattering coefficients at hundreds of photon energies. The plank mean opacity of emission, $\sigma^E_{p,tot}$, is then used to calculate the plasma cooling rate as shown in Equation I.38. In this equation, n_e and n_{tot} are the electron and total combined neutral and ion number densities.

$$\Lambda(T) = \frac{4\sigma_{SB}\rho T^4}{n_e n_{tot}}\sigma^E_{p,tot} \tag{I.38}$$

To generate the tables for SPARTAN, this cooling rate is multiplied by $(\bar{Z}n_{tot})n_{tot}$ to produce cooling rates in W/m^3. This causes some difficulty as the plasma transitions to neutral gas and $\bar{Z} \rightarrow 0$. To avoid division by zero, as $\bar{Z}$ approaches the double precision machine limit, the cooling rate is set to zero. Physically, as the number of free electrons approaches zero, neutral-neutral collisions will become the dominate collisional processes. This will likely allow for continued collisional de-excitation, but the authors know of no such model calibrated for relevant conditions for IFE chamber gas. For this reason, the IONMIX cooling rates are used as an initial approximation to the qualitative behavior of the chamber gas radiative cooling until a more complete model may be obtained.

Chapter 1, in part, contains material in preparation for submission for publication. Martin, R.; Najmabadi, F., Journal of Computational Physics, 2011. The dissertation author was the primary investigator and author of this material.

Chapter II

Numerical Models

II.A Background

The SPARTAN code was created by Zoran Dragojlovic, Farrokh Najmabadi, and Marcus Day specifically to study the evolution of IFE chamber gas. Reference [23] provides specific details on the original construction of the code. SPARTAN is a 2D-axisymmetric shock capturing Navier-Stokes code. It was built on the BoxLib AmrLib libraries of the Lawrence Berkeley Lab's Center for Computational Sciences and Engineering. These libraries handle data structures and memory management for block structured grids with adaptive mesh refinement and facilitates parallelization through this infrastructure. The code employs a second-order Godunov-based advection scheme with a second order Runge-Kutta stepping of diffusive terms. Significant development effort was placed on incorporating the embedded boundary method of Reference [60] to allow sub-grid modeling of boundary conditions within a structured cartesian mesh.

II.A.1 Review of 2nd Order Godunov Method

The algorithm for solving the inviscid fluxes on which the IFE chamber code used in Reference [23] was built is a second order Godunov method. The technique used for the multi-species code follows that of Reference [23] closely.

A basic explanation of the Godunov method for Euler equations can be found in Reference [46]. The Riemann solver implemented in the IFE chamber code is based the work of Colella in References [22] and [21].

To achieve higher order spatial accuracy, the algorithm uses slopes as developed in Reference [22]. The face states are calculated using a single step of the hybrid Glimm-Godunov approximate Riemann solver developed in the Appendix of Reference [21]. In particular, Equations II.36 and II.37 are used to determine the pressure and velocity between the $u \pm c$ sonic characteristics.

$$p^{*,0} = \frac{C_L p_R + C_R p_L + C_L C_R (u_L - u_R)}{C_L + C_R} \tag{II.1}$$

$$u^* = \frac{W_L u_L + W_R u_R + (p_L - p_R)}{W_L + W_R} \tag{II.2}$$

$$W_{L,R}(p^*) = C_{L,R}\sqrt{1 + \frac{\gamma + 1}{2\gamma}\frac{p^* - p_{L,R}}{p_{L,R}}} \tag{II.3}$$

$$C_{L,R} = \rho_{L,R} c_{L,R} = \sqrt{\gamma p_{L,R} \rho_{L,R}} \tag{II.4}$$

Unlike Roe's scheme, this approach correctly handles the case in which a the cell face lies within a rarefaction wave. Figure II.9 shows a view of the Riemann problem in such a configuration. In Roe's scheme, the rarefaction wave is just treated as another shock with an average velocity and sound speed.

II.A.2 Review of Embedded Boundary Method

Though the complete development of the embedded boundary method is found in Reference [60], it is useful to review some of the key concepts of the method to understand the limits of its applicability. The following section follows directly from Reference [60] The goal of the method is to represent a surface cutting through a rectangular mesh in a stable and consistent manner without a significant drop in the order of the algorithm or maximum time step.

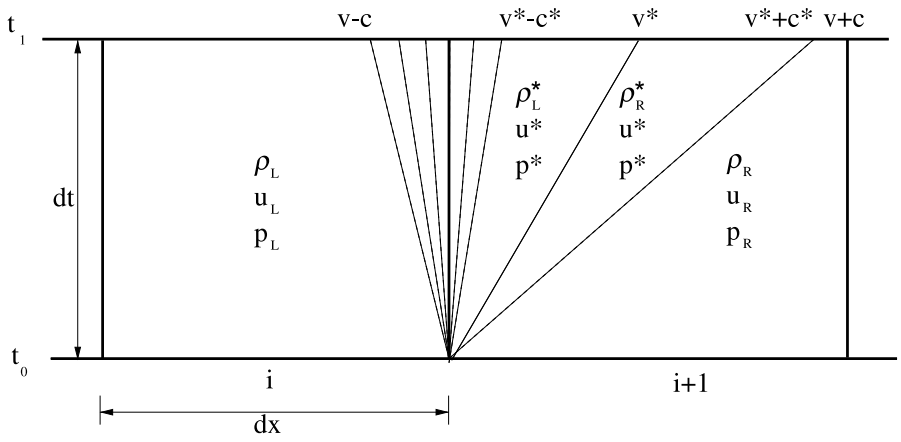

Figure II.1: Riemann problem with rarefaction wave

Though it is simple enough to define an algorithm that calculates the fluxes across fractional cell faces in a conservative manner, applying these fluxes to update the state of a fluid within a control volume may result in division by an arbitrarily small volume. To avoid this situation, the embedded boundary method first calculates a 'reference state' which uses fluxes across full cell faces to 'extended states' of the cells near the boundary defined by Equation II.5. In this equation, U is some state variable, Λ is the fraction of the cell volume within the fluid, and $nbh(i,j,k)$ are the cells within ± 1 of the cell of interest in each direction. Though shown for 2D, these extended states are defined identically in 3D with the addition of the third index. In the cells that are partially fluid, a correction $\delta M_{i,j}$ is then calculated which represents correction needed to go from the reference state to the the state defined by the true conservative fractional cell face fluxes and fractional cell volumes which is not necessarily stable if Λ is small. The formula for δM is seen in Equation II.6 where V is the cell volume. These δM values are then used to calculate a preliminary stable nonconservative update with Equation II.7. To restore conservation, the remaining $(1-\Lambda_{i,j})\delta M$ mass is then redistributed to the neighboring cells in a mass averaged manner.

$$U^{ext}_{i,j} = \frac{\sum_{(l,m)\in nbh(i,j)} \Lambda_{l,m} U^n_{l,m}}{\sum_{(l,m)\in nbh(i,j)} \Lambda_{l,m}} \tag{II.5}$$

$$U_{i,j}^{n+1} = U_{i,j}^{ref} + \frac{\delta M_{i,j}}{\Lambda_{i,j} V} \tag{II.6}$$

$$U_{i,j}^{p} = U_{i,j}^{n+1,ref} + \frac{\delta M}{V} \tag{II.7}$$

The choice of reference state through the use of extended states is of critical importance in the accuracy of the algorithm. As long as the reference state is close to the state in the conservative update, δM is small and the error introduced through redistribution is small. This is why, for example, the choice of $U_{i,j}^{ref} = U_{i,j}^{n}$ from earlier work in Reference [17] is an inappropriate choice of reference state. This choice actually causes the boundary to "appear to exert drag on the flow"[60].

Reference [60] also covers several scenarios of possible geometries in which the embedded boundary method fails. They difficulties generally result from thin fluid or solid regions and can be broken down as resulting from the extended state formula, the redistribution algorithm, or the inability of the method to represent two wall intersections within one cell face. If a body is too thin relative to the grid (¡1 cell), the redistribution algorithm can actually transfer mass between discontiguous fluid regions. If the fluid region is too narrow, the redistribution of δM can cause large changes in neighboring cells simply because there exists little mass in the neighborhood of each cell.

II.B Improvements to SPARTAN Code

II.B.1 Viscous Effects on Axis of Symmetry

One of the major deficiencies in older versions of SPARTAN was how it handled viscous terms on the axis of symmetry in cylindrical coordinates. The Godunov scheme's Euler solver relies heavily on Colella's development in Reference [22]. In this work, the influence of the coordinate system in applied by formulating the Euler equations in a conservative finite volume manner as shown in Equation

II.8. Rather than the typical derivatives along the coordinate directions, in this form the spatial derivatives are calculated by premultiplying the flux dyadic, F, by the cell face area, A, and taking the derivative with respect to a differential volume element. This has the effect of producing all of the extra terms for compressible fluxes due to the coordinate system in cylindrical and spherical coordinates while maintaining a formulation that resembles conservative cartesian coordinates. This can be confirmed by carrying out the prescribed differentiation and comparing it to inviscid terms of the of the conservative form of the compressible Navier-Stokes equations for cylindrical coordinates found in Bertin [8]. It is important to note that this formulation only applies to fluxes of conserved quantities which is why the pressure gradient term must be treated separately. The implications of this can be seen again in Reference [60], where the pressure gradient term requires particular care in the embedded boundary algorithm for cylindrical coordinates.

$$\frac{\partial U}{\partial t} + \frac{\partial AF}{\partial V} + \frac{\partial H}{\partial r} = 0 \tag{II.8}$$

In the inclusion of viscous effects in SPARTAN, it was assumed that this style of volumetric differentiation would be sufficient to populate the coordinate system induced viscous terms. This assumption ignores the tensorial nature of shear stress in that momentum perpendicular to a face can be transported across a face. When compared to the fully viscous conservative form of the Navier-Stokes equations in Bertin, it becomes clear that additional v_θ term and $\tau_{\theta\theta}$ term are missing from the spatial term of the r-momentum equation as seen in Equation II.9.

$$\begin{aligned}
\frac{\partial A(F_i - F_v)}{\partial V} &= \frac{\partial \left[r d\theta dz (\rho v_r^2 - \tau_{rr}) \right]}{\partial \left[r dr d\theta dz \right]} \\
&= \frac{1}{r}\frac{\partial r}{\partial r}(\rho v_r^2 - \tau_{rr}) + \frac{r}{r}\frac{\partial (\rho v_r^2 - \tau_{rr})}{\partial r} \\
&\neq \frac{\partial (\rho v_r^2 - \tau_{rr})}{\partial r} + \frac{1}{r}\left(\rho v_r^2 - \rho v_\theta^2 - \tau_{rr} + \tau_{\theta\theta} \right)
\end{aligned} \tag{II.9}$$

Both Reference [22] and Reference [60] are constrained to Euler equations and at most address axii-symmetric cylindrical coordinates which allows the v_θ term to be set to zero. Though the velocity term is zero, the viscous term, $\tau_{\theta\theta}$ is not. The fully compressible expression for $\tau_{\theta\theta}$ from Bertin[8] may be seen in Equation II.10. It is important to note also that the cylindrical divergence of velocity as seen in Reference [59] is also complicated by the change in geometry as seen in Equation II.11. Combining these equations for axii-symmetric flow in which both $v_\theta = 0$ and $\frac{\partial}{\partial\theta} = 0$, results in Equation II.12.

$$\tau_{\theta\theta} = 2\mu\left(\frac{1}{r}\frac{\partial v_\theta}{\partial\theta} + \frac{v_r}{r}\right) - \frac{2}{3}\mu\nabla\cdot\vec{V} \tag{II.10}$$

$$\nabla\cdot\vec{V} = \frac{1}{r}\frac{\partial r v_r}{\partial r} + \frac{1}{r}\frac{\partial v_\theta}{\partial\theta} + \frac{\partial v_z}{\partial z} \tag{II.11}$$

$$\tau_{\theta\theta}^{axii} = 2\mu\left(\frac{v_r}{r}\right) - \frac{2}{3}\mu\left(\frac{1}{r}\frac{\partial r v_r}{\partial r} + \frac{\partial v_z}{\partial z}\right) \tag{II.12}$$

This error does not effect the solution in axial incompressible flows because $v_r = 0$ and $\nabla\cdot\vec{V} = 0$ in this case. This error resulted in curvature of the spherically propagating shocks formed as the pressure wave from the IFE target burn propagated outward.

Figure II.2 shows a comparison of the effect of the change in viscosity formulation from the older and new versions of SPARTAN. The plots are the log of density on the same color scale with contours every half order of magnitude. The old version has a larger solid angle because the solution would fail at smaller angles. The majority of the defect can be seen in the blue region of the old plot where the contours are no longer arcs. This is where momentum has decreased from the initial conditions so that the effect of viscosity plays a more significant role. Where the momentum is still large, the flow primarily behaves as it would in an inviscid simulation in short time scales.

The -6 and -5.5 contours converge on the axis and there are actually a few cells at nearly -7 at this point which are absent with the new formulation.

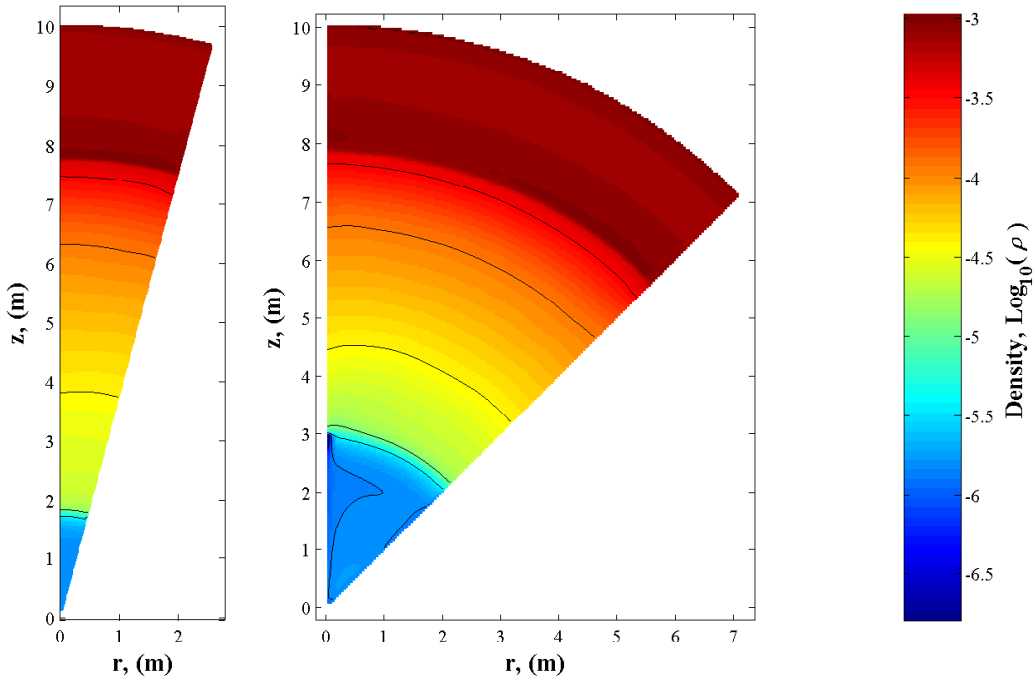

(a) New Formulas (b) Old Formulas

Figure II.2: Comparison density for old and new version of viscosity formulas showing defect on axis of symmetry from old formulas

This point caused the majority of the problems running the older version because it drove the time step several orders of magnitude lower. This essentially froze the simulation at higher grid resolutions and led to the discovery of the error in the viscosity formulation because when plotted with a linear instead of log scale, the imperfection is not apparent unless focused on the very low density region.

II.B.2 Improved Boundary Conditions

The original version of SPARTAN handled boundary conditions as shown in Figure II.3. In this scheme, the near and far points were quadratically interpolated between point along cell centers. Depending on the wall normal angle, θ, relative to $\pi/4$ these cell center interpolations are either vertical or horizontal. The wall normal derivative is then calculated with a finite difference equation of the form shown in Equation II.13 as shown in Reference [23]. In this equation, l_{near} is the distance to the near point on the normal, l_{far} is the distance to the far point on the normal, and s is the state variable of interest. This finite difference approach was first developed in Reference [43]. However, the finite difference algorithm is only 2^{nd} order accurate when $l_{far} = 2l_{near}$ and not in general when $\Delta_{near} \neq \Delta_{far}$. Because the wall can cut the cells at an variable distance from the next normal line of centers, this boundary condition produced erroneous results.

$$\left(\frac{\partial s}{\partial n}\right)_{i,j}^{EB} = \frac{1}{l_{far} - l_{near}} \left[\frac{l_{far}}{l_{near}}(s_{near} - s_{wall}) - \frac{l_{near}}{l_{far}}(s_{far} - s_w)\right] \tag{II.13}$$

To modify this approach for a uniform second order consistent boundary condition, instead of quadratically interpolating on the nearest two lines of centers, the near and far points are set at uniform distances from the face center. The value at these points is then calculated with bilinear interpolation. The interpolation error is zero at cell centers and can be shown to scales with Oh^2 with grid refinement similar to the proof for bilinear interpolation on triangular elements in the appendix of Reference [78]. The derivative at the wall is then calculated with a standard one

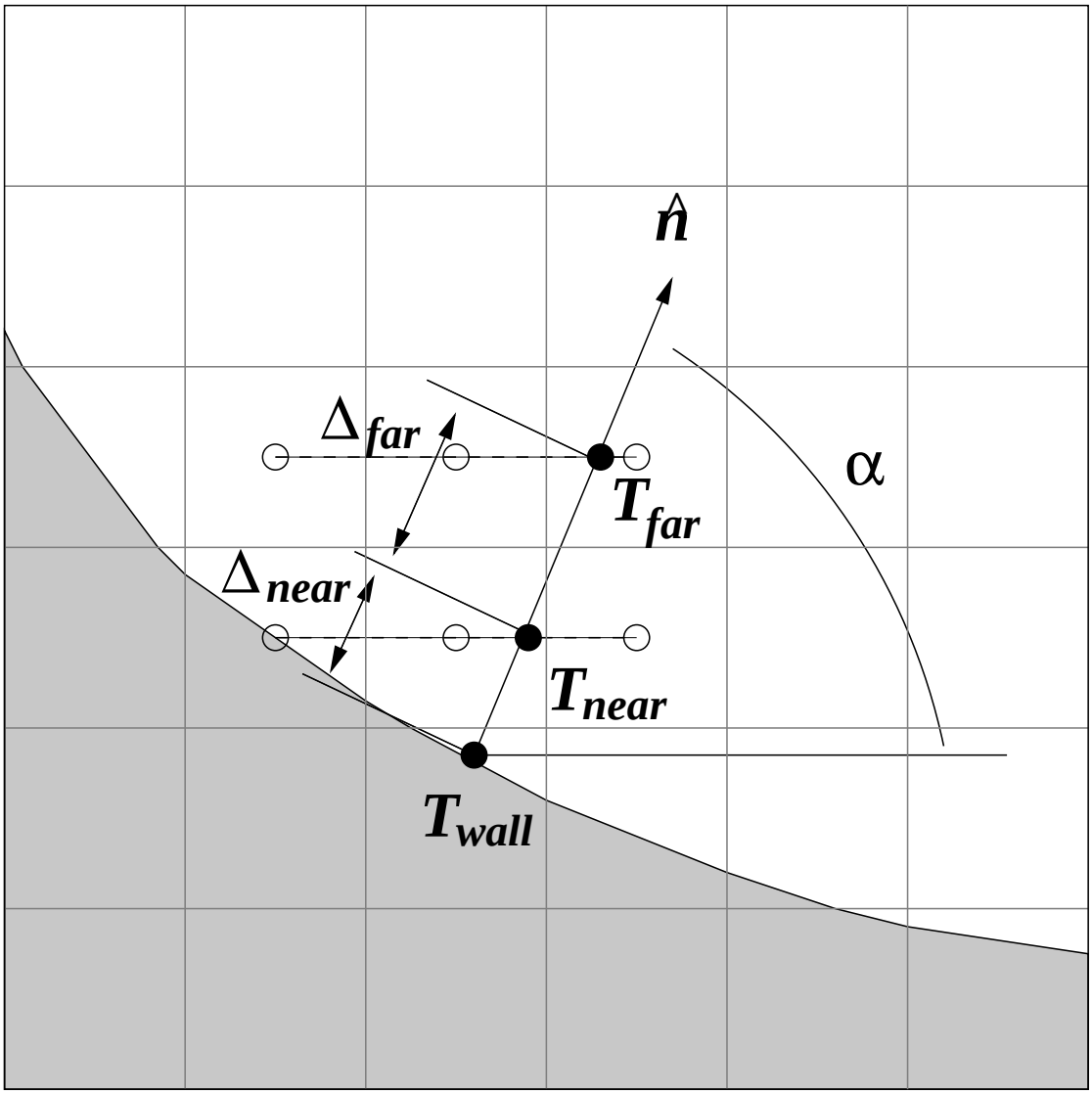

Figure II.3: Interpolation stencils for original SPARTAN wall boundary conditions

sided $2nd$ order finite difference as shown in Equation II.14 as shown in Reference [80]. To ensure that the cell centers surrounding the point are for full fluid cells, the wall normal delta is chosen based on the on the ellipse that circumscribes the four cells surrounding a cell corner. Though this results in a large stencil, the 2^{nd} order accuracy dominates the stencil size with grid refinement.

$$\left(\frac{\partial s}{\partial n}\right)_{i,j}^{EB} = \frac{-3s_w + 4s_{near} - s_{far}}{2\Delta} + O(h^2) \tag{II.14}$$

Finally, additional care is taken in applying boundary conditions on slip-wall domains that is ignored in the original version of SPARTAN. For the no-slip walls, the wall state is fully defined such that wall tangent derivatives are fully specified and generally zero. Though derivatives in the normal direction of the slip-wall are defined as zero, the tangential derivatives are not. This manifests in a requirement to calculate τ_{tt}^{EB} along the slip-wall. To do this we extend the wall stencil in perpendicular directions to the wall normal as shown in Figure II.5.

The values of the point on the tangent segments of the stencil are again calculated with bilinear interpolation. The wall tangential velocity gradient is then calculated with a simple space centered finite difference using the near tangential points. Finally, care must be taken when calculating τ_{tt}^{EB} in cylindrical coordinates on the wall because of the additional contribution related to the u/r term described in Section II.B.1. To derive the correct shear stress terms in the wall centric cylindrical coordinates, the tensorial description of the shear stress tensor in cylindrical coordinates from Reference [4] is followed. The wall centric coordinate system is defined in Equation II.15. In this system, (n, t, θ), are the coordinates and (R, α) are local constants for the given wall point at which the coordinate system is centered.

From these equations, the metric, g^{ij} can be calculated and used to evaluate the stress tensor equation shown in Equation II.16. Equation II.17 shows the resulting wall tangent shear stress of wall direction momentum. Looking at the limits of $\alpha = 0$ and $\alpha = \pi/2$ angled walls, it is clear that this equation recovers the

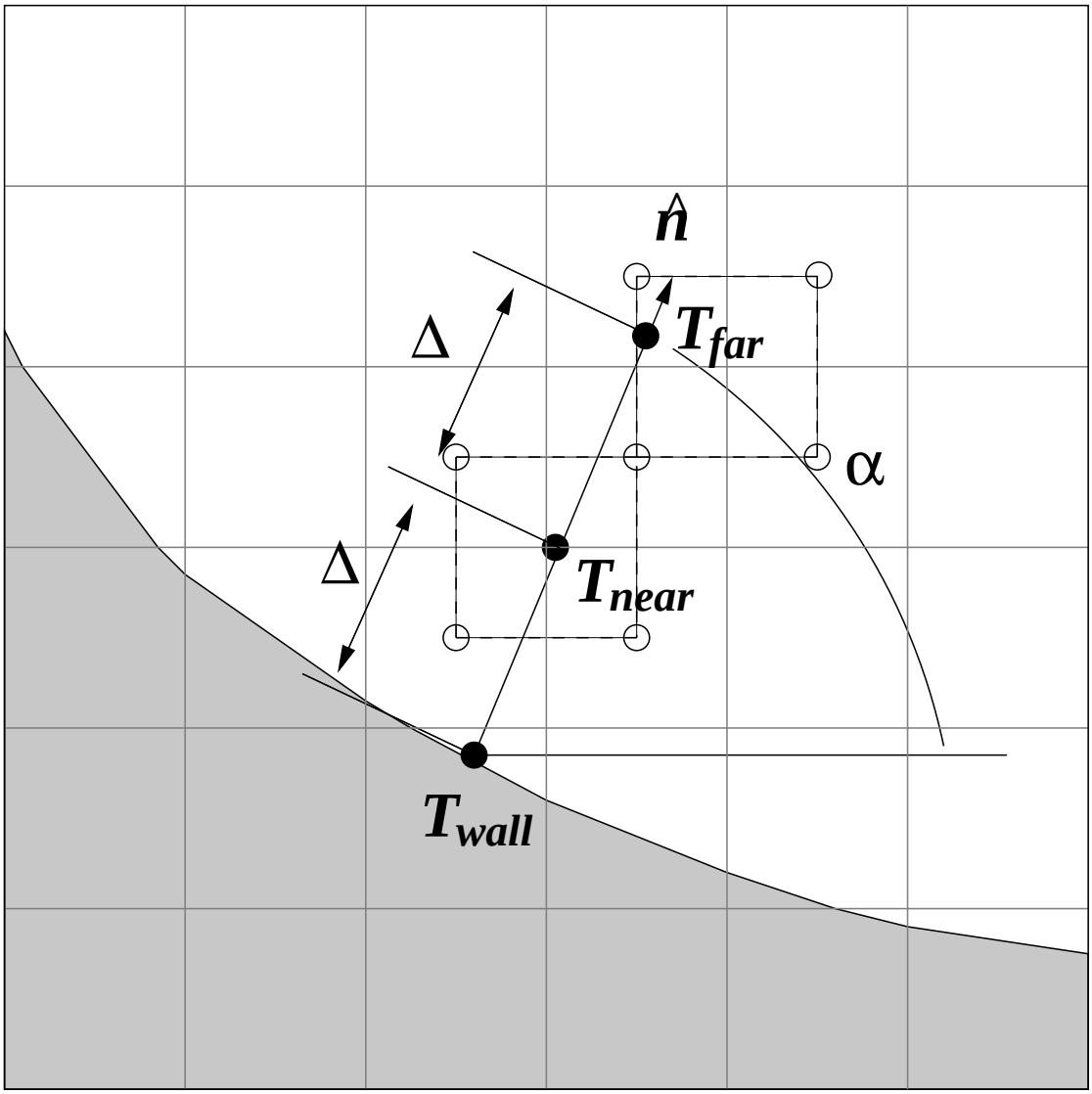

Figure II.4: Interpolation stencils for new SPARTAN wall boundary conditions

normal cylindrical equations for τ_{rr} and τ_{zz} if the proper substitutions are made between (V^t, V^n) and (V^r, V^z). For the slip wall, the wall normal velocity is zero, but the wall normal derivative of the wall normal velocity can be nonzero. This simplifies Equation II.17 by dropping the V^n term.

$$\begin{pmatrix} x^1 \\ x^2 \\ x^3 \end{pmatrix} = \begin{pmatrix} (R + t\cos\alpha - n\sin\alpha)\cos\theta \\ (R + t\cos\alpha - n\sin\alpha)\sin\theta \\ t\sin\alpha + n\cos\alpha \end{pmatrix} \tag{II.15}$$

$$T^{ij} = -\left(P + \frac{2}{3}\mu e^m_m\right) g^{ii} + 2\mu e^{ij} \tag{II.16}$$

$$e_{ij} = \frac{1}{2}\left(g_{jk}\left(\frac{\partial V^k}{\partial x^i} + \Gamma^k_{in}V^n\right) + g_{ik}\left(\frac{\partial V^k}{\partial x^j} + \Gamma^k_{jn}V^n\right)\right)$$

$$\tau^{EB}_{tt} = 2\mu\left(\frac{\partial V^t}{\partial t} - \frac{1}{3}\left(\frac{\partial V^t}{\partial t} + \frac{\partial V^n}{\partial n} + \frac{V^t\cos\alpha + V^n\sin\alpha}{R}\right)\right) \tag{II.17}$$

II.B.3 Transport Coefficient Model

. The new version of Spartan calculates viscosity and thermal conductivity based on collision integrals and Lennard-Jones potentials. This modification is incorporated to facilitate gas mixture simulations which is discussed and validated in great detail in Chapter III.B. The collision integrals are calculated inline using a version of O'Hara and Smith's transport integrals code [57] that was modernized to compile on new compiler versions. Given the Lennard-Jones radius and well depth, transport properties for gases can be calculated across a wide range of temperatures.

The expressions for mixture viscosity and conductivity use the pure gases. Equations for pure species s viscosity and conductivity in terms of reduced collision integrals, $\Omega^{(m,n)}$, are given in Reference [45] and shown in Equations II.18 and II.19. SPARTAN now includes all the terms in the conductivity equation,

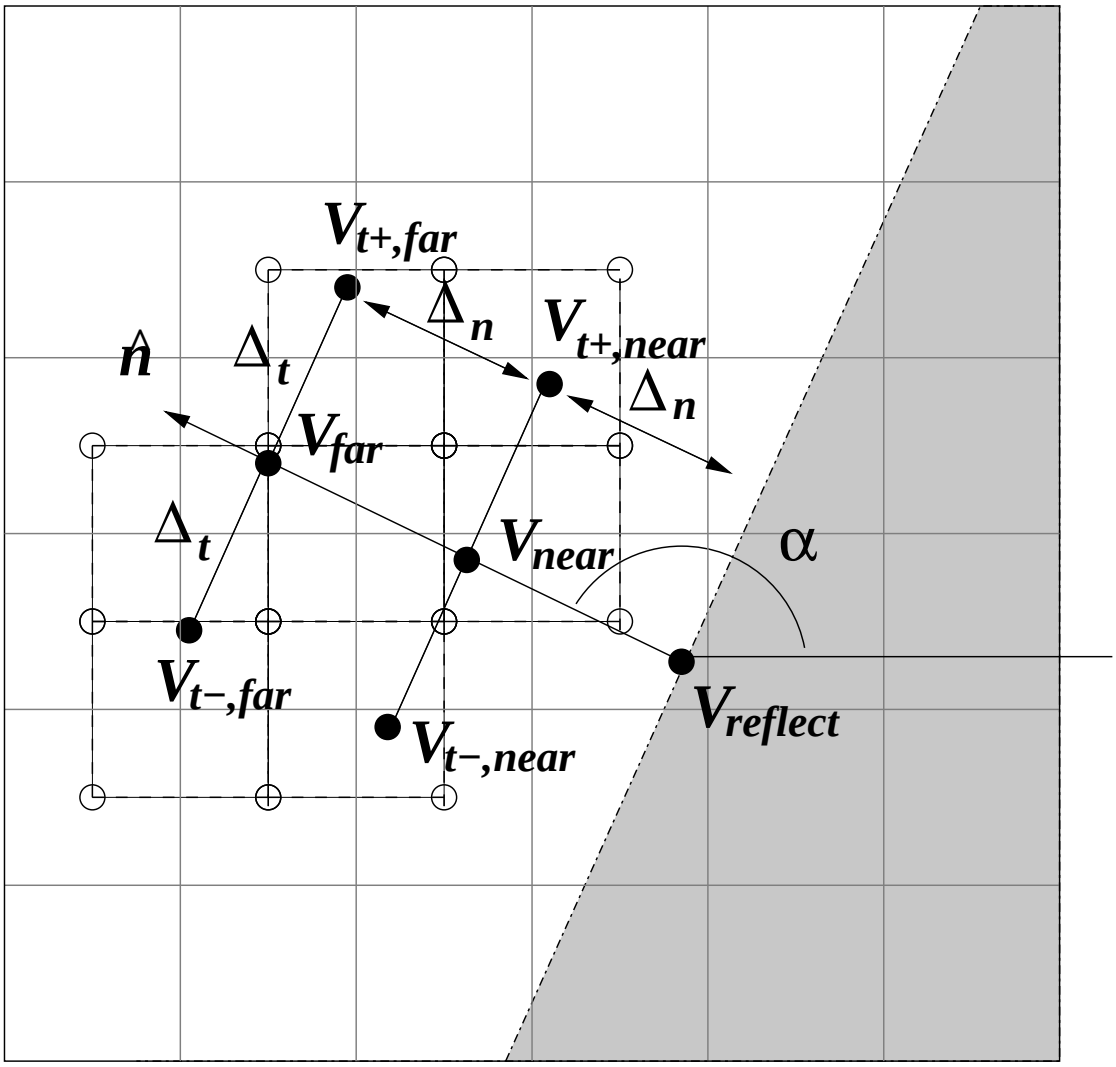

Figure II.5: Interpolation stencils for new SPARTAN reflecting wall boundary conditions

but the gases included in this work are all monatomic noble gases or dissociated. For these gases, only the translational component contributes to the equation for conductivity which simplifies to Equation II.20.

$$\mu_s = \frac{5}{16}\frac{\sqrt{\pi m_s kT}}{\pi\sigma_k^2\Omega^{(2,2)\star}} \tag{II.18}$$

$$K_s = \frac{\mu_s}{m_s}\left(f_{trans.}C_{v,trans} + f_{rot.}C_{v,rot.} + f_{vib.}C_{v,vib.}\right) \tag{II.19}$$

$$K_s^{mono} = \frac{15}{4}\frac{\mu_s}{m_s} \tag{II.20}$$

II.B.4 Radiation Source Improvements

SPARTAN was originally provided radiative cooling rates in tabular form from researchers at the University of Wisconsin, Madison's Fusion Technology Institute (UWFTI). These tables were generated using the IONMIX code written by members of that research unit. However, it was later discovered that a complete version of IONMIX source was published in Computer Physics Communications[48]. Using this code to produce the tables enabled a broader range of chamber gases and states to rapidly be considered without the turnaround time required requesting new tables from UWFTI. Learning to operate IONMIX also provided insight into its assumptions and limitations.

Figures II.6 shows the plasma cooling rate for Xenon gas calculated using IONMIX. For these results, the full set of ionization potentials are inputed from Reference [74]. Figure II.7 shows the original plasma cooling rate table for Xenon gas provided by the UWFTI. Though the exact input parameters such as the photon group boundaries and number of points per group is unknown for the data provided, the figures show reasonable agreement providing confidence that IONMIX is compiled and operating correctly.

Slight modification to IONMIX was required to enable compilation in double precision on a modern compiler. Though attempts were made to minimize

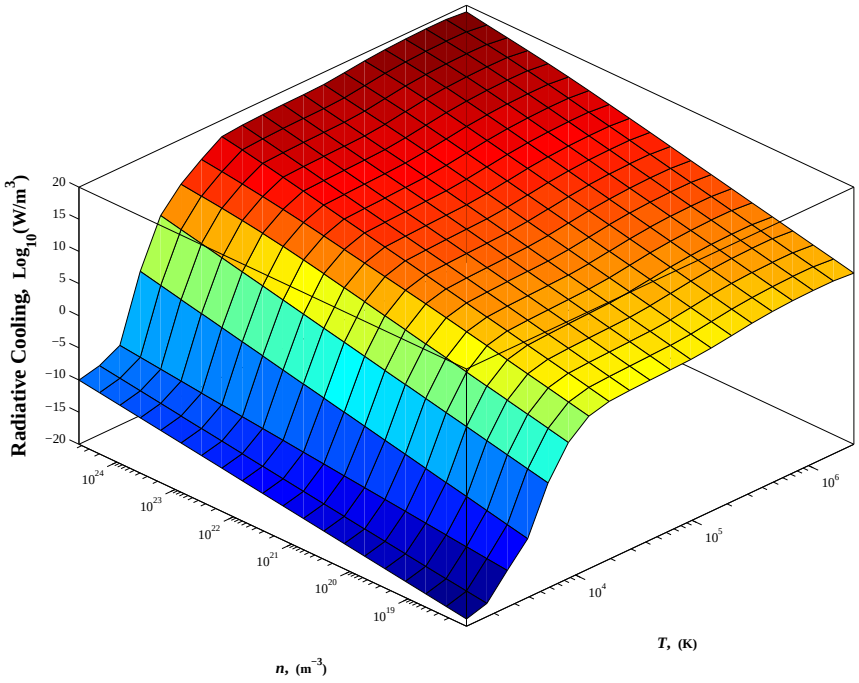

Figure II.6: Tabulated plasma cooling rates for xenon gas from IONMIX code

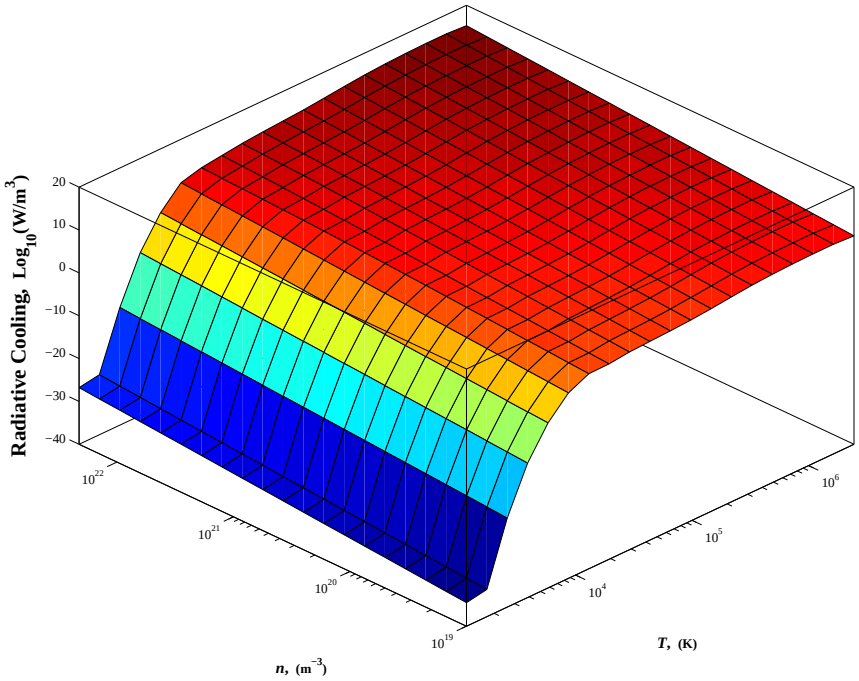

Figure II.7: Tabulated plasma cooling rates for xenon gas provided by UWFTI

these changes, errors may have been introduced through these modifications or through the compilers interpretation of the older style code. Though results compare favorably with xenon cooling rate tables provided, further validation for the other gases would be provide more confidence in the accuracy of these results. Because of the large impact radiative cooling plays on the chamber gas, the accuracy of the simulations depends heavily on the radiation source calculation. The results demonstrate the capability of the code, but future work is required to ensure the cooling rates are quantitatively correct.

An important difference between Figures II.6 and II.7 is the choice of density grid. The new table covers a wider range of densities because it was found that the lower density xenon solution had regions of the flow drop below the minimum table density. The original version of SPARTAN simply set the radiative cooling to zero whenever the a numerical cells state was not within the table boundaries. Though this prevented extrapolation error, the code also provided no output warning that this had been done. Though this choice is reasonable at the low temperature boundary assuming that the cooling rate tables are generated such that the cooling rate is negligible or zero on this boundary, the cooling rates are in general very large on the other boundaries. This resulted in erroneous results where slightly higher density gas would continue to cool while lower density gas adjacent to it remained hot. A strong fictitious pressure gradient between the regions resulted and produced further expansion of the low density region.

Extrapolation off the table is a poor choice because the relative importance of 3-body and 2-body radiative decay mechanisms can result in significant changes in cooling rate behavior cross certain density regimes. Instead, the new version of SPARTAN simply provides a warning whenever the low density boundary or the high density and temperature boundaries are crossed by a request for a cooling rate. The the boundaries are then adjusted and a new cooling rate table is generated. This process is repeated until the flow remains within the table of states for the duration of the simulation.

Finally, the original version of SPARTAN employed a standard quadratic Lagrangian interpolation of points on the $\rho - T$ tables for the plasma cooling rate, Λ. Because these values cross many orders of magnitude as do the table coordinates, this interpolation was switched to be performed for $\log(\Lambda)$ on a $(\log(\rho), \log(T))$ grid. The cooling rate can be locally approximated well by power laws. This change is believed to reduce the interpolation error and is consistent with BUCKY's choice of bilinear interpolation of opacities on a $(\log(\rho), \log(T))$ grid[47]. The new interpolation is functionally the same as a quadratic interpolating on the surface depicted in Figure II.6.

II.C Extension to Compressible Gas Mixtures

Before analysis of gas mixtures in IFE chambers, it is important to review the implementation and validation of the gas mixture models. This work represents a significant advancement of the physical processes that can be represented within SPARTAN and require special care in determining the range of applicability and validity of the solutions through comparison with experimental data as well as Monte Carlo simulations in the rarefied limit.

II.C.1 Numerical Methods

Conservation Form

In deriving classic shock capturing methods, it is common to cast Navier-Stokes into conservation-law form as in References [80, 49, 44], as Equation II.21 shows in dyadic form. In this equation, U is the state vector, $\bar{\bar{F}}_I$ is the inviscid flux dyadic, $\bar{\bar{F}}_V$ is the viscous flux dyadic, and S is the source term from effects such as body forces. These states and fluxes are defined for the multicomponent system in Equation II.22, but for the purposes of this work, the source terms set to be zero. It is also important to note that from this point on, the vector notation is replaced by index subscripts where i and j represent spatial directions and r and

s continue to represent species molecular classes.

The multi-component equations developed here extend this conservation form of the equations by adding $s-1$ species conservation equations to the set where s is the number of unique gas species in the fluid. In this work, the species number density conservation equations derived in Hirschfelder are multiplied by species mass, m_s. The resulting species mass conservation equations are in terms of the species partial density, ρ_s, bulk velocity, v_{i0}, and species diffusion velocity V_{is}. Because the s species conservation equations sum to the continuity equation, the s^{th} species conservation equation is dropped so that the system is not over-determined. The species conservation equations only interact with the original Navier-Stokes equations through transport coefficients and additional heat fluxes due to the energy transported via thermal mass diffusion, $q_i^{(d)}$, and the Dufour effect, $q_i^{(x)}$, as seen in Equations II.23 and II.24 respectively.

$$\frac{\partial U}{\partial t} + \frac{\partial}{\partial x_i}\left[\bar{\bar{F}}_I - \bar{\bar{F}}_V\right]_i = S \tag{II.21}$$

$$U = \begin{Bmatrix} \rho \\ \rho v_{j0} \\ \rho e_t \\ \rho_1 \\ . \\ . \\ . \\ \rho_{s-1} \end{Bmatrix} \quad \bar{\bar{F}}_{Ii} = \begin{Bmatrix} \rho v_{i0} \\ P\delta_{ij} + \rho v_{i0} v_{j0} \\ (P + \rho e_t) v_{i0} \\ \rho_1 \left(v_{i0} + V_{i1}\right) \\ . \\ . \\ . \\ \rho_{s-1}\left(v_{i0} + V_{i(s-1)}\right) \end{Bmatrix} \quad \bar{\bar{F}}_{Vi} = \begin{Bmatrix} \vec{0} \\ \bar{\bar{\tau}}_{ij} \\ v_{i0} \cdot \bar{\bar{\tau}}_{ij} + \kappa \frac{\partial T}{\partial x_i} + q_i^{(d)} + q_i^{(x)} \\ \vec{0} \\ . \\ . \\ . \\ \vec{0} \end{Bmatrix} \tag{II.22}$$

$$q_i^{(d)} = \frac{\gamma}{\gamma - 1} kT \sum_s n_s V_{is} \tag{II.23}$$

$$q_i^{(x)} = \frac{kT}{n} \sum_s \sum_r \frac{n_r D_s^T}{m_s \mathcal{D}_{sr}} (V_{is} - V_{ir}) \tag{II.24}$$

Diffusion Velocity

The concept of a diffusion velocity results from the decomposition of bulk mass averaged velocity into average velocities for each different class of molecules representing only one gas species as mentioned earlier. The complete details of the process can be seen in Hirschfelder [38]. In Hirschfelder, an expression for the diffusion velocity is derived via the Chapman-Enskog solution and is shown in Equation II.25. In this equation, the diffusion velocity depends on diffusion coefficient D_{sr}, thermal diffusion coefficient D_s^T and the generalized concentration gradient. The form of the generalized concentration gradient, d_{is}, can be seen in Equation II.26. From these equations, it can be seen that the diffusion velocity depends not only on the concentration gradient as in Fickian diffusion but also upon temperature and pressure gradients within the gas.

$$V_{is} = \left(\frac{n^2}{n_s \rho}\right) \sum_{r=1}^{S} m_r D_{sr} d_{ir} - \frac{1}{n_s m_s} D_s^T \frac{\partial \ln T}{\partial x_i} \tag{II.25}$$

$$d_{is} = \frac{\partial}{\partial x_i}\left(\frac{n_s}{n}\right) + \left(\frac{n_s}{n} - \frac{\rho_s}{\rho}\right)\frac{\partial \ln p}{\partial x_i} - \left(\frac{\rho_s}{P\rho}\right)\left[\frac{\rho}{m_s}F_{is} - \sum_{r=1}^{S} n_r F_{ir}\right] \tag{II.26}$$

Equation II.25 requires the ordinary multicomponent species diffusion coefficients. Rather than solving expensive equations for these coefficients, a mixture average diffusion coefficient shown in Equation II.27 is defined as in Reference [45] such that the diffusion velocity can be calculated using Equation II.28 instead of Equation II.25.

$$D_{sm} = \frac{1 - (\rho_s/\rho)}{\sum_{r,\, r \neq s} n_s/(n\mathcal{D}_{rs})} \tag{II.27}$$

$$V_{is} = -\frac{n}{n_s} D_{sm} d_{is} - \frac{D_s^T}{\rho_s}\frac{\partial ln T}{\partial x_i} \tag{II.28}$$

Equation II.28 remains equivalent to the full multi-component formulation. However, direct calculation of the thermal diffusion coefficient requires

solution of a complicated and numerically intensive set of linear equations via Cramer's rule. This requires determinants of $2sX2s$ matrices whose components involve sums of products of s collision integrals. Though not prohibitive for small numbers of gas species, this approach would have involved a considerably more extensive modification of the existing code. Instead, this work incorporates a simplified method based on Equation II.66 for the thermal diffusion term of the diffusion velocity as outlined in Reference [45]. Though the formulation is only valid for binary gases and in the trace light component limit, it provides a first approximation to the thermal mass diffusion effects. The method uses the thermal diffusion ratio, Θ_s, in the form shown in Equation II.30. The form of thermal diffusion factor, $k_{sr}(T)$, as well as a more complete explanation of the other transport coefficients used can be found in Section II.C.3.

$$V_{is} = -\frac{n}{n_s} D_{sm} d_{is} - \frac{n D_{sm} \Theta_s}{n_s} \frac{\partial ln T}{\partial x_i} \tag{II.29}$$

$$\Theta_s = \sum_{r,\, r \neq s} k_{sr}(T) \frac{n_r n_s}{n^2} \tag{II.30}$$

With this final approximation, the form of the diffusion velocity equation can be simplified further to that of Equation II.31.

$$V_{is} = -\frac{n}{n_s} D_{sm} \left(d_{is} + \ \Theta_s \frac{\partial ln T}{\partial x_i} \right) \tag{II.31}$$

Discretization

These differential equations are actually solved in their weak finite volume form as shown in Equation II.32. Because the equations are in conservative form, only information about the fluxes on the cell boundaries as well as any volumetric source terms are needed to calculate the cell averaged state variables.

$$\int_\Omega \frac{\partial U}{\partial t} d\Omega + \int_{\partial\Omega} [\bar{\bar{F}}_I - \bar{\bar{F}}_V] \cdot \vec{n} \, dA = \int_\Omega S d\Omega \tag{II.32}$$

Solution proceeds in a manner common across flux-splitting solutions of the Riemann problem for single-component gas such as those used to develop the Roe and Godunov methods in References [46, 80].The inviscid portion is solved first by decomposing the flux Jacobian as shown in Equation II.33. In Equation II.33, L and R are the left and right eigenvectors and Λ is the diagonal matrix of eigenvalues such that $L\Lambda R$ is equal to the flux Jacobian $\frac{\partial \bar{\bar{F}}_I}{\partial U}$.

$$\frac{\partial U}{\partial t} + \frac{\partial \bar{\bar{F}}_I}{\partial x} = \frac{\partial U}{\partial t} + \frac{\partial \bar{\bar{F}}_I}{\partial U}\frac{\partial U}{\partial x} = \frac{\partial U}{\partial t} + [L\Lambda R]\frac{\partial U}{\partial x} = 0 \tag{II.33}$$

In the classic first order solution of the Riemann problem, the gas state is assumed constant within control volume numerical cells at the beginning of each time step. However, these jump discontinuities at the cell interfaces are not appropriate for calculating the diffusion velocities. The diffusion velocities are dependent on gradients in concentration, pressure, and temperature. Because the diffusion velocities are driven by these gradients, the code instead uses gradients between cell centers and volume average states spanning the boundary between neighboring cells when calculating the diffusion velocities. Because the explicit time step limit is selected such that the flow characteristics cross no more than half of a cell, both the volume average of conserved quantities and face spanning gradients are constant for the time step. This approximation results in diffusion velocities that are constant across the time step. This approach is consistent with assumptions of constant average state of conserved variables and face spanning gradients due to explicit time-stepping. This gradient also minimizes the steepest local gradient connecting the two cell states resulting in an under-prediction of the diffusion that approaches the physical value with numerical grid refinement for a stable solution in under-resolved flows. This representation also yields a relatively simple flux Jacobian shown in Equation II.34 and corresponding eigenvalues for the gas characteristics as shown in Equation II.35.

This representation is intuitively attractive due to the analogy between the mass and species conservation characteristics. For mass conservation, the mass

average velocity v_0 corresponds to the characteristic velocity, while for species conservation, the characteristic velocity is $v_0 + V_s$ which is equivalent to species average velocity $\bar{v}_s$ for the s^{th} species. Figure II.8 shows a graphical representation of this hyperbolic portion of the problem for a sample representative configuration solved forward in time in one dimension.

$$\frac{\partial F}{\partial U} = \begin{bmatrix} 0 & 1 & 0 & 0 & 0 & 0 \\ \frac{(\gamma-3)}{2}v_0^2 & -(\gamma-3)v_0 & (\gamma-1) & 0 & 0 & 0 \\ (\gamma-1)v_0^3 - \gamma e_t v_0 & \gamma e_t - \frac{3}{2}(\gamma-1)v_0^2 & \gamma v_0 & 0 & 0 & 0 \\ -\frac{\rho_1 v_0}{\rho} & \frac{\rho_1}{\rho} & 0 & v_0+V_1 & 0 & 0 \\ -\frac{\rho_{...} v_0}{\rho} & \frac{\rho_{...}}{\rho} & 0 & 0 & v_0+V_{...} & 0 \\ -\frac{\rho_{s-1} v_0}{\rho} & \frac{\rho_{s-1}}{\rho} & 0 & 0 & 0 & v_0+V_{s-1} \end{bmatrix} \tag{II.34}$$

$$\lambda = \begin{bmatrix} v_0, & v_0 + c, & v_0 - c, & v_0 + V_1, & v_0 + V_{...}, & v_0 + V_{s-1} \end{bmatrix} \tag{II.35}$$

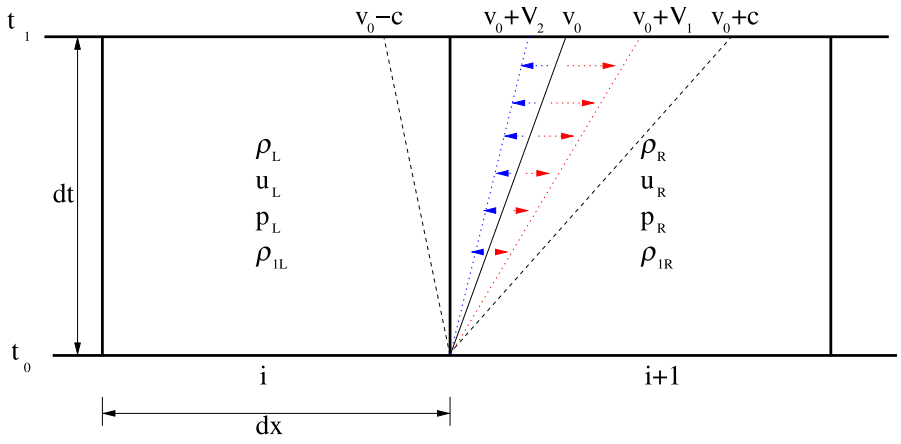

Figure II.8: Multi-species Riemann problem

Higher Order Godunov Method

The algorithm for solving the inviscid fluxes on which the IFE chamber code used in Reference [23] was built is a second order Godunov method. The

technique used for the multi-species code follows that of Reference [23] closely. A basic explanation of the Godunov method for Euler equations can be found in Reference [46]. The Riemann solver implemented in the IFE chamber code is based the work of Colella in References [22] and [21].

To achieve higher order spatial accuracy, the algorithm uses slopes as developed in Reference [22]. The face states are calculated using a single step of the hybrid Glimm-Godunov approximate Riemann solver developed in the Appendix of Reference [21]. In particular, Equations II.36 and II.37 are used to determine the pressure and velocity between the $u \pm c$ sonic characteristics.

$$p^{*,0} = \frac{C_L p_R + C_R p_L + C_L C_R (u_L - u_R)}{C_L + C_R} \tag{II.36}$$

$$u^* = \frac{W_L u_L + W_R u_R + (p_L - p_R)}{W_L + W_R} \tag{II.37}$$

$$W_{L,R}(p^*) = C_{L,R}\sqrt{1 + \frac{\gamma + 1}{2\gamma}\frac{p^* - p_{L,R}}{p_{L,R}}} \tag{II.38}$$

$$C_{L,R} = \rho_{L,R} c_{L,R} = \sqrt{\gamma p_{L,R} \rho_{L,R}} \tag{II.39}$$

Unlike Roe's scheme, this approach correctly handles the case in which a the cell face lies within a rarefaction wave. Figure II.9 shows a view of the Riemann problem in such a configuration. In Roe's scheme, the rarefaction wave is just treated as another shock with an average velocity and sound speed.

Diffusion terms

The diffusion terms were handled by a Crank-Nicholson implicit solve in conjunction with each Runge-Kutta sub-step. First the continuity equation updates, and the new and old densities are used to calculate explicit momentum and energy terms on both sides of the timestep update. Because the calculations presented in this paper are one-dimensional, the diffusive and conductive terms are

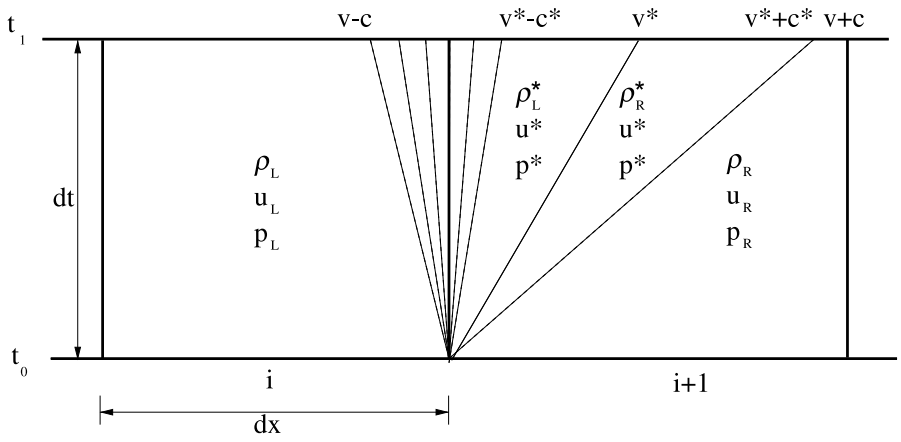

Figure II.9: Riemann problem with rarefaction wave

linear. The numerical stencil for these terms was cell centered using the neighboring cell values as shown in Equation II.40. These stencils provide second order accuracy for these terms as well though the domain of influence is wider than for the hyperbolic terms.

$$\nabla u|_i = \frac{u_{i+1} - u_{i-1}}{2dx} + O(h^2) \qquad \text{(II.40)}$$
$$\nabla^2 u|_i = \frac{u_{i+1} - 2u_i + u_{i-1}}{2dx} + O(h^2)$$

II.C.2 Incorporation in Godunov Method

The continuity and momentum equations appear identical to the original equations for the IFE chamber code. The continuity equation is uninfluenced by the multi-species formulation, and the momentum equation is only influenced through the effect of composition on the transport coefficients. The energy equation has an added term due to the heat flux carried by the diffusion velocity. This extra heat flux is included with the advective heat flux.

The flux for the species conservation equations were calculated in an analogous manner to the continuity equation. As with the continuity equation, a predictor step is first used to estimate the state variables at time $t^n + \frac{1}{2}\Delta t$ at the cell centers. The multi-species algorithm includes the individual species densities

in these estimates. The corrector step then uses the state at $t^n + \frac{1}{2}\Delta t$ to calculate the advective fluxes on the cell faces from time t^n to time t^{n+1} used to update the flow-field. However for the species conservation, the face state is determined by the sign of the bulk velocity plus the corresponding diffusion velocity rather than just the bulk velocity. This is the appropriate choice because the Riemann characteristic for the species conservation from the Jacobian of the flux is $v_0 + V_s$.

Once the state at the face has been determined, the fluxes are calculated as described in Equation II.22. The mass and bulk momentum flux terms are calculated as they were with the original IFE chamber code. The energy flux is first calculated exactly as in the original method, and then diffusion energy flux is added. Finally, the conservative species flux, $\rho_s(v_0 + V_s)$, is calculated using the cell face values as well as the cell centered left and right states when derivatives are needed.

II.C.3 Transport Coefficients

The transport coefficients used in this application closely follow the formulation found in Reference [45] using the ACQN package of Reference [57] for the calculation of collision integrals and ratios thereof. This Appendix reviews this formulation and provides sample calculations to compare the combined performance relative to experimentally measured data.

Pure species viscosity and thermal conductivity as well as binary diffusion coefficients and thermal diffusion coefficients were calculated from collision integrals using Lennard-Jones 6-12 potentials as developed in Hirschfelder [38]. Equations II.41 through II.42 result from equations found in Monchick and Mason [54] neglecting the higher order f_η, f_κ, f_D terms and assuming monatomic atoms.

The first approximation to the binary diffusion coefficient, $\mathcal{D}_{rs}$, is also calculated via the formula in Hirschfelder [38] shown in Equation II.65. In Equation II.65, the cross section is determined using Equation II.44 and $\Omega_{rs}^{(1,1)*}$ based on an averaged potential-well depth shown in Equation II.45 as in Reference [45].

$$\mu_s = \frac{5}{16}\frac{\sqrt{\pi m_s kT}}{\pi\sigma_{0s}^2\Omega^{(2,2)*}} \tag{II.41}$$

$$\kappa_s = \frac{15k}{4m_s}\mu_s \tag{II.42}$$

$$\mathcal{D}_{rs} = \frac{3(m_r + m_s)kT}{16nm_r m_s\sigma_{0rs}^2\Omega_{rs}^{(1,1)*}} \tag{II.43}$$

$$\sigma_{0rs} = \frac{1}{2}(\sigma_{0r} + \sigma_{0s}) \tag{II.44}$$

$$\frac{\epsilon_{rs}}{k} = \sqrt{\frac{\epsilon_r}{k}\frac{\epsilon_s}{k}} \tag{II.45}$$

The mixture average viscosity and thermal conductivity are produced using the pure species viscosity and thermal conductivity and the semi-empirical Equations II.46 and II.48 from Reference [9, 45].This is a tradeoff of accuracy for reduced computational complexity compared to the necessary collision integral matrix inversions necessary for the full-multicomponent formulation. In the validation section, comparison is made between these values and experimental data.

$$\mu = \sum_s \frac{n_s\mu_s}{\sum_r n_r\Phi_{sr}} \tag{II.46}$$

$$\Phi_{sr} = \frac{1}{\sqrt{8}}\left(1 + \frac{m_s}{m_r}\right)^{-\frac{1}{2}}\left[1 + \left(\frac{\mu_s}{\mu_r}\right)^{\frac{1}{2}}\left(\frac{m_r}{m_s}\right)^{\frac{1}{4}}\right]^2 \tag{II.47}$$

$$\kappa = \frac{1}{2}\left(\sum_s \frac{n_s}{n}\kappa_s + \frac{n}{\sum_s n_s\kappa_s}\right) \tag{II.48}$$

The thermal diffusion factor, $k_{sr}(T)$, is calculated via ratios of the mixture collision integrals as shown in Equation II.87. These ratios, A_{sr}^*, B_{sr}^*, and C_{sr}^*, are defined within the ACQN subsystem from Reference [57] with details therein. However, ACQN only considers binary mixtures. The formula given in Equation

II.30 is an extension of the concept of the binary thermal diffusion ratio to multi-species applications. In the case of binary mixtures, it can be shown that Θ_s reduces to common binary diffusion coefficient, k_T. In this case, Equation II.66 is also equivalent to Equation II.25. When more species are considered, this method becomes an estimate for the thermal diffusion of a light species within a heavier mixture.

$$k_{sr}(T) = \frac{15}{2} \frac{(2A^*_{sr} + 5)(6C^*_{sr} - 5)}{A^*_{sr}(16A^*_{sr} - 12B^*_{sr} + 55)} \frac{m_s - m_r}{m_s + m_r} \frac{n_s n_r}{n^2} \tag{II.49}$$

The values for xenon's Lennard-Jones potential used in this work were taken from Appendix Table I-A of Hirschfelder, Curtiss, and Bird [38]. Other potentials used values tabulated in Reaction Design's ChemKin database[68]. For hydrogen isotopes, the potentials were assumed the same as hydrogen. This does not mean that the isotopes remain uniformly mixed however, because the mass also plays a role along with the effective cross section in the collision scattering.

II.C.4 Stability

For the multi-species versions of the explicit Riemann solvers presented, the equation for the maximum time step, Equation II.50, remains the same as in the original single species version. This constraint is commonly referred to as the CFL condition. In the equation, λ refers to the eigenvalues of the fluid equations. The maximum eigenvalue corresponds to the maximum rate at which information can propagate across a numerical cell. By limiting the time step as shown, disturbances at the interface cannot propagate across more than one cell per time step. Because of the additional species governing equations, $s - 1$ more eigenvalues are included when compared to the single species versions. In practice, values for all s species diffusion velocities are included in the time step limitation to ensure a consistent stable treatment.

$$dt \leq \frac{dx}{|\lambda|_{max}} \tag{II.50}$$

However, writing the eigenvalues in terms of the diffusion velocity hides the effect of the diffusion on stability. To examine this closer we will assuming constant pressure and temperature to focus on only the species convection and Fickian diffusion. Under these assumptions, the maximum eigenvalue on the $(i + \frac{1}{2})^{th}$ face, $|\lambda_s|_{max}$, appears as shown in Equation II.51.

$$|\lambda_s|_{max} = \left| |v_0| - \frac{D_{sm}}{\rho_{s(i+1/2)}} \frac{\partial \rho_s}{\partial x_i} \right|_{max} \tag{II.51}$$

The resulting stability analysis requires that eigenvalue be calculated for the highest frequency wave representable on the grid rather than the maximum value on the solution because of the possibility for exponential growth in the mode. The face state is then calculated using some unspecified up-winding fraction, $\mathcal{F}$, satisfying Equation II.52.

$$\mathcal{F} = \begin{cases} 0 \leq \mathcal{F} \leq 1/2, & \text{if } v_0 \leq 0 \\ 1/2 \leq \mathcal{F} \leq 1, & \text{if } v_0 > 0 \end{cases} \tag{II.52}$$

An approximate discretized form of Equation II.51 can then be written as seen in Equation II.53. Substituting spectral modes, $\rho_{si} = A^n e^{(i\theta \mathbf{j})}$, Equation II.53 becomes equation II.54 and is maximized when $\theta = \pi$.

$$|\lambda_s|_{max} \approxeq \left| \left| v_0 - \frac{D_{sm}}{\mathcal{F}\rho_{si} + (1-\mathcal{F})\rho_{s(i+1)}} \frac{\rho_{s(i+1)} - \rho_{si}}{\Delta x} \right| \right|_{max} \tag{II.53}$$

$$|\lambda_s|_{max} \approxeq \left| \left| |v_0| + \frac{D_{sm}}{\mathcal{F} + (1-\mathcal{F})e^{\theta \mathbf{j}}} \frac{1 - e^{\theta \mathbf{j}}}{\Delta x} \right| \right|_{max} = |v_0| + \frac{D_{sm}/\Delta x}{|\mathcal{F} - 1/2|} \tag{II.54}$$

For full up-winding, Equation II.54 simply recovers the stability limit for explicitly stepped up-winded Convection-Diffusion such that $|c| + 2\alpha < 1$ where $c = Udt/dx$ and $\alpha = Ddt/dx^2$ as shown in introductory numerical methods texts such as Reference [64].

At this point, the remaining terms of the diffusion velocity are reintroduced to provide an estimate of the stability of the system including the Soret effect. In this form, the diffusion effects driven by the temperature and pressure gradients are treated simply as additions to the bulk velocity for the species. This neglects the possibility of exponential mode growth in these terms through the Soret effect to the energy equation and back through the Dufour effect. However, considering the relatively small contribution of the Dufour effect, this possibility is likely small.

$$\begin{aligned} |\lambda_s|_{max} &= ||v_0 + V_{is}||_{max} \\ &\cong \left| v_0 - \frac{D_{sm}}{X_s}\left(\frac{\partial X_s}{\partial x_i} + \frac{X_s - Y_s}{P}\frac{\partial P}{\partial x_i} + \frac{\Theta_s}{T}\frac{\partial T}{\partial x_i}\right)\right|_{max} \\ &\cong \left| v_o + \frac{D_{sm}}{X_s}\left(\frac{X_s - Y_s}{P}\frac{\partial P}{\partial x_i} + \frac{\Theta_s}{T}\frac{\partial T}{\partial x_i}\right)\right| + \frac{D_{sm}/\Delta x}{|\mathcal{F} - 1/2|} \end{aligned} \tag{II.55}$$

Though from a numerical standpoint this time-step limit appears to be a reasonable choice, diffusion velocities of the order of the sound speed are physically unreasonable in the fluid limit. The Chapman-Enskog expansion uses a series solution based on a high collision frequency to expand the distribution function around equilibrium. For a diffusion velocity large compared to the thermal velocity, this approximation is no longer applicable. The velocity distribution for the mixture deviates significantly from a Gaussian indicating low collisionality and results in a breakdown of the expansion.

II.D Diffusion Flux Limits

II.D.1 Simple Diffusion Flux Limit Model

The information propagation speed line of thought of the stability analysis leads directly to the concept of flux limiters. As mentioned in Reference [58], the multi-species equations can produce erroneously large fluxes for plasma and strong shock-waves due to the near-equilibrium assumptions in the derivation. However

as mentioned in Reference [84], though the flow structures of sizes on the order of mean free paths may be incorrect using Navier-Stokes on non-equilibrium flows, this does not mean that the macro scale conservation is violated.

This implies that a breakdown in the continuum approximation locally such as in the interior of shocks does not necessarily invalidate results further from such discontinuities. Diffusion velocities large relative to thermal velocities not only likely produce erroneous results, but also inhibit the flow evolution through restrictive time-step limits. For these reasons, flux limiters for the multi-species mass and energy fluxes in the code were also investigated with respect to experimentally indicated limitations on the continuum formulation.

The flux limiters were of the form suggested in Reference [58] and shown in Equations II.56 and II.57 where v_{th} corresponds to the thermal velocity. The thermal velocity is proportional to the sound speed with a constant of $\sqrt{3/\gamma}$ as shown in Reference [84].

To ensure a smooth transition between normal and flux limited regions, an ad-hoc tan^{-1} transformation was applied as shown in Equation II.58. Figure II.10 shows a comparison between the original flux, F_0, and the limited flux, F_s for the tan^{-1} flux limiter. Though the limited flux necessarily deviates from the original flux, the important features are that the original and limited flux are tangent near zero flux and the limited flux asymptotically approaches the maximum flux at $\pm\infty$. The requirement on the slope of the flux limiter being tangent to the original flux near zero results in the the maximum flux being the only free parameter.

In the case of the energy flux limiter, the limit was only applied to the heat flux resulting from diffusion velocities and Dufour effect seen in Equations II.23 and II.24. The sound speed was also used as the thermal speed. Despite being smaller than the actual thermal speed, this limit was quite unrestrictive and much larger than the few percent of the maximum limit suggested in [58]. In order to assure consistency in the fluxes, after application of the energy limit, the diffusion velocities were scaled down by a factor of F/F_0 as well. This is reasonable

because the factor is constant with respect to species and can therefore be linearly distributed inside the summations to multiply the diffusion velocities in Equations II.23 and II.24.

The species flux limit is applied only to the diffusion velocity relative to the thermal velocity leaving the species partial density constant at the flux surface. For this velocity flux limiter, various thermal velocities were investigated including individual species thermal and sound speeds as well as various average bulk speeds. All of these restrictions appeared to be quite severe and easily overwhelmed any effect from an energy flux limiter. This is particularly true using the individual species sound or thermal speed when the number fraction of the heavy species was small. In the results presented, the number averaged thermal speed shown in Equation II.59 was used for the limit of all the gas species.

The sum of species density and diffusion velocity for all species must be zero by the definition of the bulk velocity, v_{i0}. To ensure this is true, Equation II.60 from Reference [45] is applied to the diffusion velocities. When the velocity flux limiter is applied, all of the velocities are scaled down by the most restrictive limit to maintain this balance as well.

$$F_{s,max} = \rho_s \bar{v}_{th} \tag{II.56}$$

$$F_{\rho e,max} = \frac{P}{(\gamma - 1)} v_{th} \tag{II.57}$$

$$F = \frac{F_{max}}{\pi/2} tan^{-1}\left(\frac{\pi/2}{F_{max}} F_0\right) \tag{II.58}$$

$$\bar{v}_{th} = \sqrt{\sum_s \frac{n_s}{n} \frac{3kT}{m_s}} \tag{II.59}$$

$$V_{is} = V_{is} - \sum_s \frac{\rho_s}{\rho} V_{is} \tag{II.60}$$

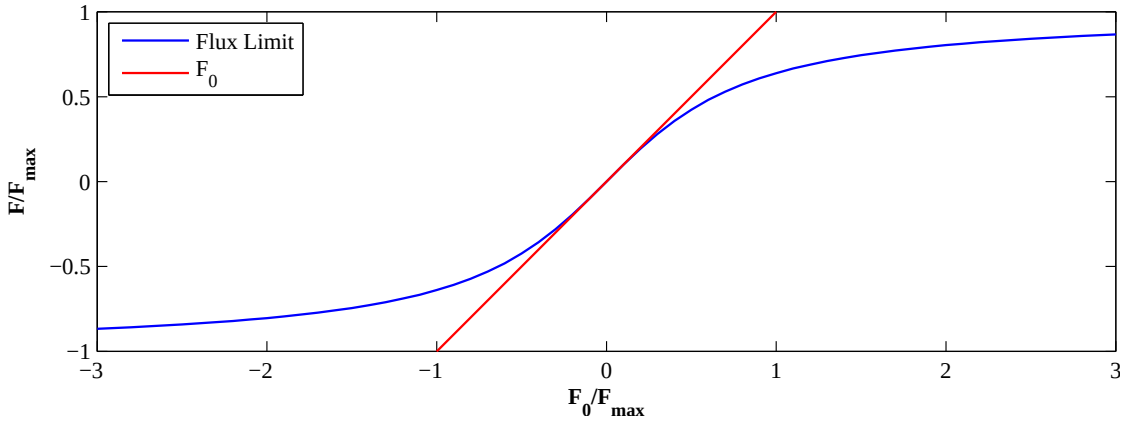

Figure II.10: Comparison between original and limited fluxes

II.D.2 Binary Diffusion Flux Limits from Direct Simulation

With only a few experimental results available, in early work, we could not determine an optimal fraction of the thermal velocity for the diffusion velocity limit or even whether it should include a dependence on local composition.

In this section, we attempt to answer these question using Bird's DS2V Monte Carlo code to perform computational experiments across a wide range of flow conditions. We use mixtures of noble gasses in under-expanded jets based on Rothe's experimental setup[73, 71] to probe these conditions. The continuum diffusion velocities are calculated using the average pressure, density, composition and temperature fields from the DS2V solution to avoid confounding influences from other continuum breakdowns expected in a full continuum solution.

Posteriori Calculation of Diffusion Velocity

The diffusion velocity, V_{is}, is defined in Equation II.61 as the difference between the average velocity of particles in one gas species relative to the mixture mass average velocity, v_{i0}, of the bulk fluid defined in Equation II.62. Equation II.85 shows the constitutive relation for the diffusion velocity of the s^{th} species in a mixture resulting from Chapman-Enskog theory. The formulation follows that of Reference [45] using a mixture diffusion coefficient, D_{sm}, defined in terms of the

normal binary diffusion coefficients, $\mathcal{D}_{rs}$, in Equation II.64. The binary diffusion coefficient is calculated in terms of the average molecular diameter, d_{rs}, reduced mass, m_{rs}, and collision integral, $\Omega_{rs}^{1,1\star}$ as shown in Equation II.65. The thermal diffusion ration, Θ_s, to first approximation is shown in Equation II.66 in terms of k_{rs} as seen in Equation II.87. The ratios of collision integrals, $A^\star, B^\star$, and $C^\star$, are all equal to unity for the hard sphere model and are generally weak functions of temperature for other inter-molecular force models.

$$V_{is} \equiv \overline{v_i}_s - v_{i0} \tag{II.61}$$

$$\rho v_{i0} \equiv \frac{1}{\rho} \sum_{s=1}^{N_s} \rho_s \overline{v_i}_s \tag{II.62}$$

$$\vec{V}_s = -D_{sm} \left[\frac{\nabla X_s}{X_s} + \left(1 - \frac{m_s}{\overline{m}}\right) \frac{\nabla P}{P} + \frac{\Theta_s}{X_s} \frac{\nabla T}{T} \right] \tag{II.63}$$

$$D_{sm} = \frac{1 - Y_s}{\sum_{r \neq s} X_s \mathcal{D}_{rs}} \tag{II.64}$$

$$\mathcal{D}_{rs} = \frac{3}{16} \frac{(2\pi kT/m_{rs})^{1/2}}{n\pi d_{rs}^2 \Omega_{rs}^{1,1\star}} \tag{II.65}$$

$$\Theta_s = \sum_{r \neq s} k_{rs} X_r X_s \frac{m_s - m_r}{m_r + m_s} \tag{II.66}$$

$$k_{rs} = \frac{15}{2} \frac{(2A_{rs}^\star + 5)(6C_{rs}^\star - 5)}{A_{rs}^\star (16A_{rs}^\star - 12B_{rs}^\star + 55)} \tag{II.67}$$

To ensure the Monte Carlo and continuum diffusion velocities differences result from a breakdown in the continuum approach rather than the molecular model, collision integrals using the variable soft sphere (VSS) molecular model are needed. Equation II.68 shows these integrals as derived from Bird's description of the VSS model using Chapman-Enskog theory[10]. In the collision integrals, $\nu + 1/2$ is the temperature viscosity power law, α is the VSS parameter adjusted

to match both the viscosity and diffusion coefficient, and E_{ref} is a constant defined to match the gas viscosity at a reference temperature. For collisions between unlike species, the mixture values of these parameters were calculated using the averages found in source of Bird's DSMC0 code[10] to ensure an equivalent treatment with DS2V.

$$\begin{aligned}
{\Omega^{1,1}_{VSS}}^{\star} &= \frac{\Gamma(3-\nu)}{2}\left(\frac{E_{ref}}{2kT}\right)^{\nu}\frac{2}{\alpha+1} \\
{\Omega^{1,2}_{VSS}}^{\star} &= \frac{\Gamma(4-\nu)}{6}\left(\frac{E_{ref}}{2kT}\right)^{\nu}\frac{2}{\alpha+1} \\
{\Omega^{1,3}_{VSS}}^{\star} &= \frac{\Gamma(5-\nu)}{24}\left(\frac{E_{ref}}{2kT}\right)^{\nu}\frac{2}{\alpha+1} \\
{\Omega^{2,2}_{VSS}}^{\star} &= \frac{\Gamma(4-\nu)}{6}\left(\frac{E_{ref}}{2kT}\right)^{\nu}\frac{6\alpha}{(\alpha+1)(\alpha+2)}
\end{aligned} \tag{II.68}$$

Comparison of Concentrations and Diffusion Velocities for Experimental Conditions

Rothe's experimental setup[73, 71] for electron beam studies of He:Ar mixture under-expanded free jets was used for boundary conditions in DS2V. In the experiment, a 12% argon mixture at $2.56 mmHg$ expands through a $15mm$ diameter sonic orifice into a chamber at a pressure of $17 \mu mHg$. This orifice was in a flat plate affixed to a $47.5mm$ diameter converging nozzle. In the simulations, a uniform choked flow is used to approximate the plate orifice. Figure II.31 shows the numerical domain used in DS2V as well as its reflection over the axis of symmetry. The flow from the nozzle is shown broken down into regions consisting of the expansion, Mach disc, barrel shock, and streamline jet boundary. Flow within the expansion closely resembles a 1D spherical expansion centered slightly downstream of the orifice. The diffusion velocities within this region remain relatively small, consistent with Bird's result for 1D free expansions[10]. However, in the Mach disc and barrel shock large diffusion velocities produce significant composition variation.

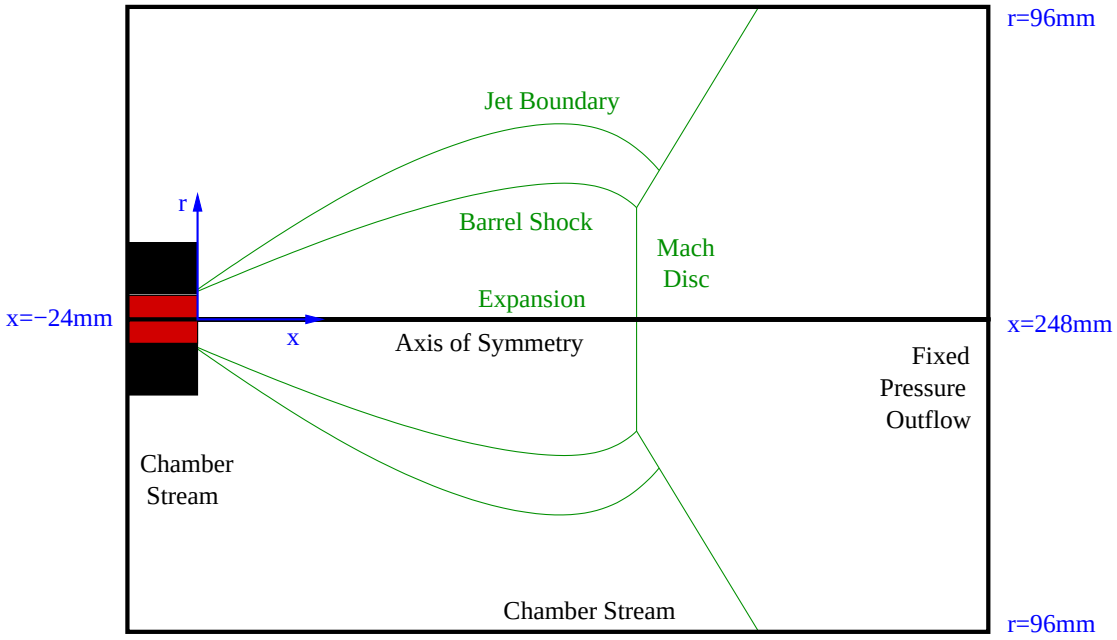

Figure II.11: Monte Carlo geometry (blue) and boundary conditions (black) relative to flow regions (green). The inside of the nozzle is marked in red to denote fixed choked sonic conditions within the region.

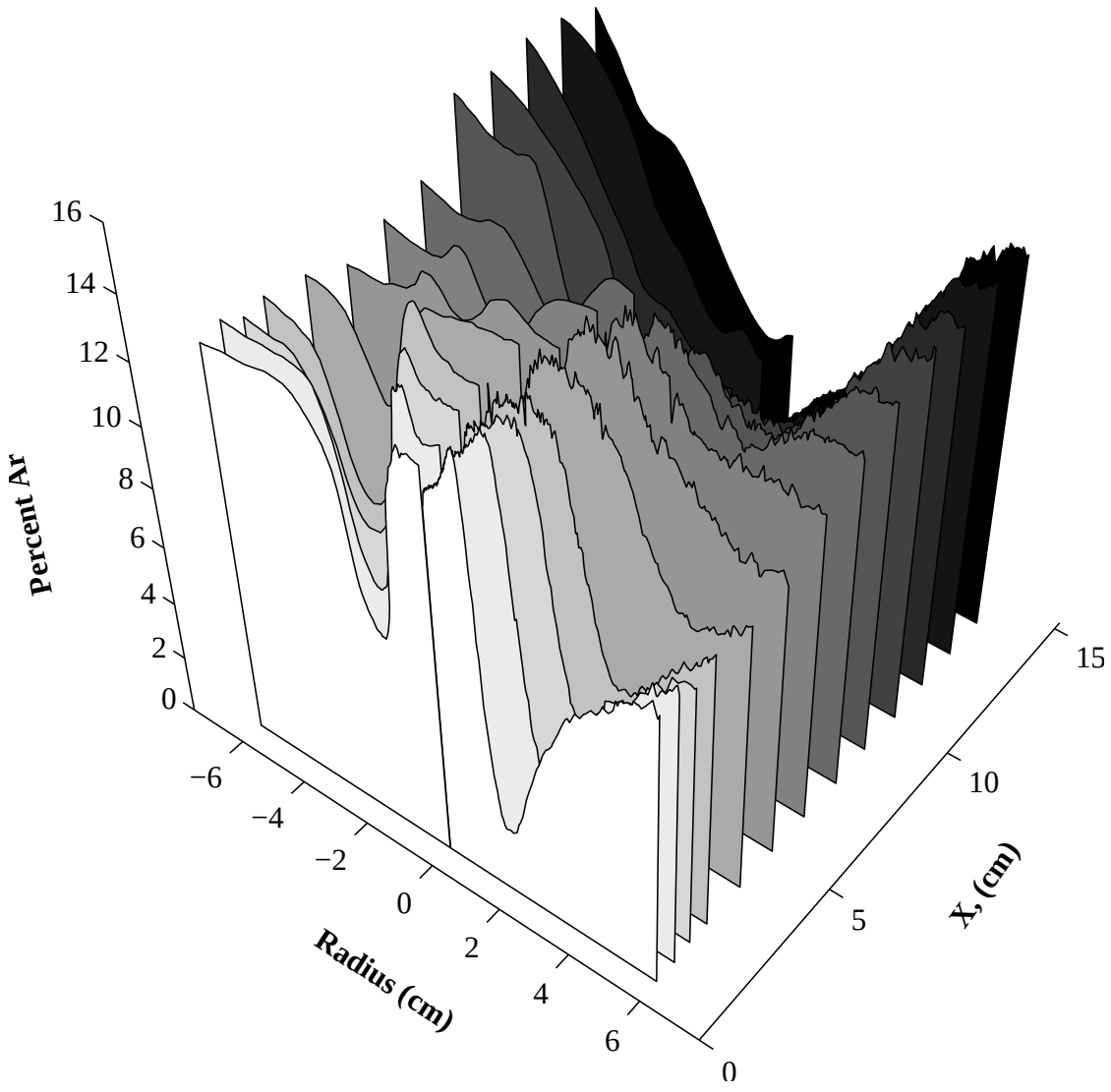

Figure II.12: Argon molar percentage throughout the flow. Front side shows Monte Carlo solution and back side shows experimental results from Rothe's electron beam study.

Rothe's setup was selected because experimentally measured argon concentrations throughout the flow are provided. Figure II.12 shows both the DS2V and experimental concentrations adjacent to each other. This figure shows that DS2V reproduces the concentration variations within the jet providing confidence in DS2V's diffusion velocities.

The only significant difference between the experiment and DS2V's results occur in the region outside the edge of the jet extending to the boundary. This difference is likely due to differential vacuum pumping fluxes between the gasses[72] which would result in argon enrichment within the chamber in the experiment. Because this value was not experimentally measured beyond the apparent composition at the edge, in this work the chamber boundary conditions were set to equal the jet composition. Regardless of the true chamber composition, because the continuum diffusion velocity calculation depends only on the DS2V fields, the continuum calculation remains consistent with DS2V's results for the remainder of this work.

Figure II.13 shows the radial and axial components of the diffusion Velocity for the experimental configuration as calculated by DS2V as well as the associated velocities based on the continuum formulas resulting from DS2V's average pressure, density, and temperature fields. Note that the continuum results appear noisier than the Monte Carlo side because the derivative of the average fields needed to calculate the diffusion velocity amplify the fluctuations inherent in the Monte Carlo result. Other than this noise, the largest discrepancy appears between the axial diffusion velocities in the highly rarefied region adjacent to the nozzle.

Diffusion Velocity Limit

The diffusion velocity and transport coefficients result from Chapman-Enskog theory and therefore assume a small perturbation from equilibrium for the velocity distribution. Within shocks and rarefied flows, both of these assumptions

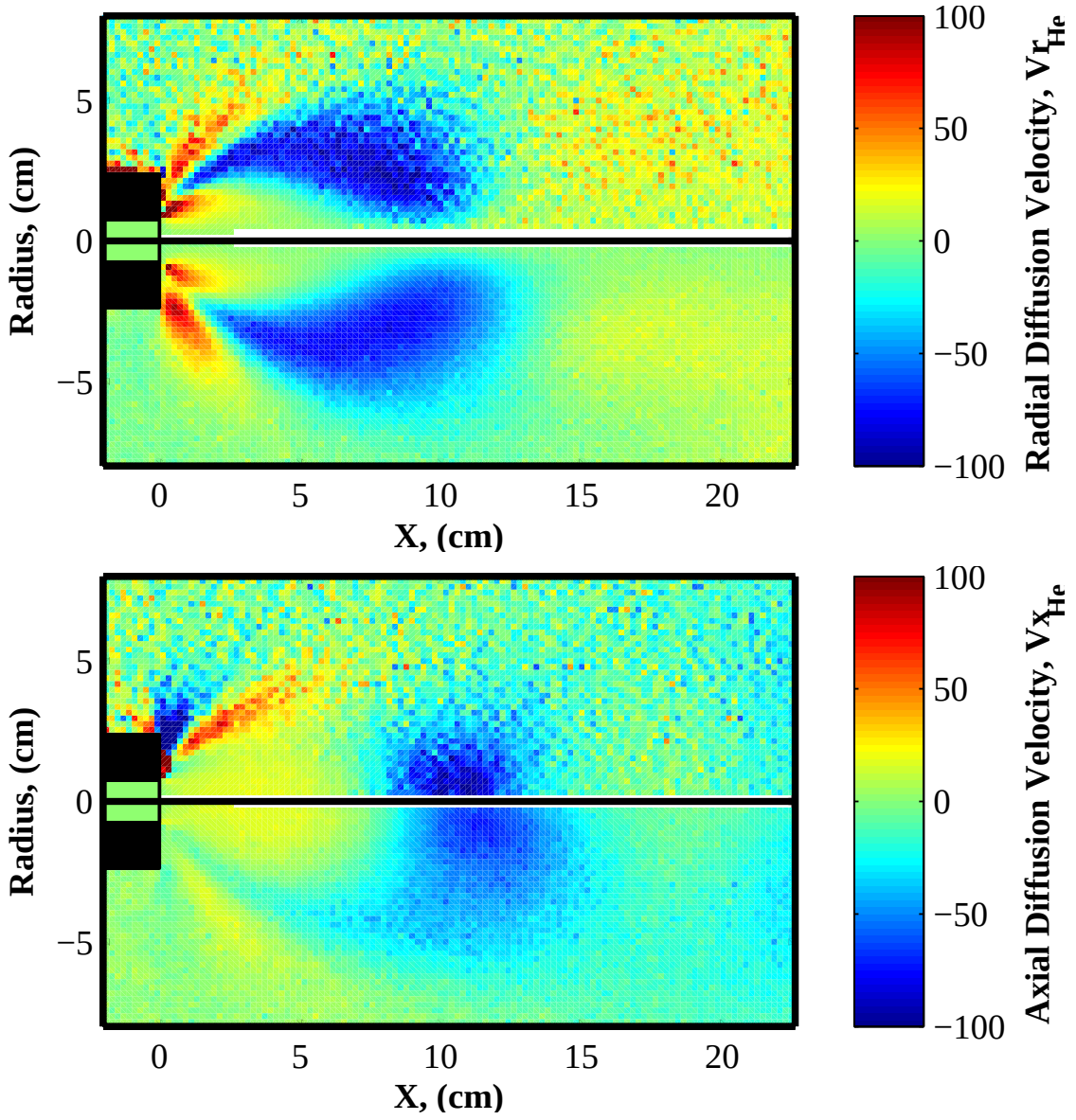

Figure II.13: Comparison of radial (left) and axial (right) diffusion velocities in (m/s) between the DS2V results(bottom) and equivalent continuum values(top).

can break down. For mixtures, the perturbation assumption clearly fails whenever the diffusion velocities are large relative to the thermal velocity. The theory also assumes sufficient collisionality to ensure equal and isotropic temperatures for all gas components. To derive an absolute upper limit on the diffusion velocity for a given mixture kinetic temperature, we consider Bird's definitions of the kinetic temperature and species kinetic temperature[10] as seen in Equations II.69 and II.70. This species kinetic temperature can be shown to be proportional to the sum of squares about the species mean velocity plus the square of the species diffusion velocity. Equation II.71 combines these equations defining an individual species thermal velocity $c_{is}^2 \equiv \overline{(v_{is} - \overline{v_{is}})^2}$ for the sake of readability.

$$\frac{3}{2}kT_{tr} = \frac{1}{2}\sum_{s=1}^{N_s} X_s m_s \overline{(v_{is} - v_{i0})^2} \tag{II.69}$$

$$\frac{3}{2}kT_{trs} = \frac{m_s}{2}\overline{(v_{is} - v_{i0})^2} = \frac{m_s}{2}\left(\overline{(v_{is} - \overline{v_{is}})^2} + V_{is}^2\right) \tag{II.70}$$

$$3kT_{tr} = \sum_{s=1}^{N_s} X_s m_s \left(c_{is}^2 + V_{is}^2\right) \tag{II.71}$$

We define a Cartesian velocity coordinate system such that the diffusion velocity is aligned to the v_x-coordinate. The expansion of Equation II.71 for these coordinates is shown in Equation II.72. Consistent with the single isotropic temperature assumption of Chapman-Enskog theory, we assume the contributions of each direction's kinetic energy is equal to the overall kinetic temperature therefore the continuum temperature. Using this assumption, Equation II.73 shows the remaining v_x direction contribution. This equation can then be simplified to relate the quantities back to the bulk sound speed, a, as seen in Equation II.74.

$$T_{tr} = \frac{1}{3}\left(T_{trx} + T_{try} + T_{trz}\right) = \frac{1}{3k}\sum_{s=1}^{N_s} X_s m_s \left((c_{x_s}^2 + V_{x_s}^2) + c_{y_s}^2 + c_{z_s}^2\right) \tag{II.72}$$

$$T_{tr} = T_{trx} = \frac{1}{k}\sum_{s=1}^{N_s} X_s m_s \left(c_{x_s}^2 + V_{x_s}^2\right) \tag{II.73}$$

$$a^2/\gamma = \frac{kT_{tr}}{\overline{m}} = \sum_{s=1}^{N_s} Y_s \left({c_{x_s}}^2 + {V_{x_s}}^2 \right) \tag{II.74}$$

For binary mixtures, this can be taken further to provide a bound on the diffusion velocity. The maximum diffusion velocity occurs when $c_{i_s}^2 = 0$ for one of the gas species. This does not necessarily occur simultaneously for both gasses, yet the limits are connected through the definition of the diffusion velocity. Combining the definitions of the diffusion velocity and mass average velocity, it can be shown that the species densities multiplied by diffusion velocities sum to zero as seen in Equation II.75. This means that for a binary mixture, $\rho_1 V_{i1} = -\rho_2 V_{i2}$. Using this relationship, we define a mean diffusion velocity, $\hat{V}_i = \sqrt{\rho_1/\rho_2} V_{i1} = -\sqrt{\rho_2/\rho_1} V_{i2}$ such that both components of diffusion velocity can be scaled to be equal in magnitude in opposite directions. Next we assume that $({c_{x_r}}^2 + {V_{x_r}}^2)$ is equal to the thermal velocity squared of the species,kT_{tr}/m_r, in the species that is not limited while $c_{x_s}^2 = 0$ in the limited direction. Using the $\hat{V}$ definition in Equation II.74 results in Equation II.76 after simple algebraic manipulation.

$$\sum_s \rho_s V_{is} = 0 \tag{II.75}$$

$$\left| {\hat{V}_x}^2 \right|_{max} = \frac{a^2}{\gamma} \min \left(\frac{X_1}{Y_2}, \frac{X_2}{Y_1} \right) \tag{II.76}$$

We can now define the species maximum as $V_{max_s} = \frac{1}{2}\sqrt{\rho_r/\rho_s} \left| \hat{V}_x \right|_{max}$. Scaling both velocity components by their corresponding V_{max_s} allows the components to be plotted symmetrically together because $V_s/V_{max_s} = -V_r/V_{max_r}$. Figure II.14, shows an example case for a He:Ar jet with a 50:50 composition. Figure II.15 contains plots for He:Ar, He:Xe, and Ar:Xe systems. Each figure is the sum of 9 initial jet mixtures such as the one depicted in Figure II.14. Each set of 9 ranges between 10:90 and 90:10 in 10% increments. The plots use a log scale with the color representing the number of points, N, contained by each cell on a grid with a resolution of 100-cells per 1 normalized velocity unit. In Figures II.14 and II.15,

we scale both the Monte Carlo (DSMC) and continuum (Cont.) diffusion velocity calculations by these V_{max} limits.

A *tanh* curve is included based on a best fit for the data points across a wide range of gasses and mixtures against several test curves including $tanh$, erf, and a scaled tan^{-1}. The test curves were selected with the constraints that the curve's slope must be 1:1 near the origin where the perturbations from equilibrium are small and that the curve must asymptote to ± 1 at infinity. The factor of 1/2 in the limit resulted from this fitting procedure as well though cases with more significant breakdown are needed to confirm this result because the fitting procedure breaks down for cases when the points do not deviate significantly beyond the noise relative to the 1:1 line.

Though the bulk of the points lay on or near the 1:1 line near the origin, the plots all exhibit a bulge around the origin. This is due in large part to the noise in the low density region exterior to the jet. This can be seen in the noise on the top half of the plots in Figure II.13. The flow-field output of DS2V lacks sampling cell grid information providing only unstructured point values. Significant noise is introduced from resampling these unstructured data points onto a uniform mesh to calculate the diffusion velocities. Coarse uniform meshes under-predict the maximum diffusion velocities because the gradients are reduced. Fine meshes capture the maximum velocities but produce noise because of erroneous gradient calculations from sub-sampling the coarse sampling cells in highly rarefied regions of the flow.

II.D.3 Effect of Limited Diffusion on Stability

In order for the original time-step limit to be exceeded after application of the flux limiter, a new effective mixture average diffusion coefficient, $D_{sm}^{\text{Eff.}}$, is needed. This coefficient is simply the effective coefficient that produces the limited diffusion velocities. As seen in Equation II.31, the terms of the diffusion velocity are all multiplied by the mixture average diffusion coefficient in this application. The

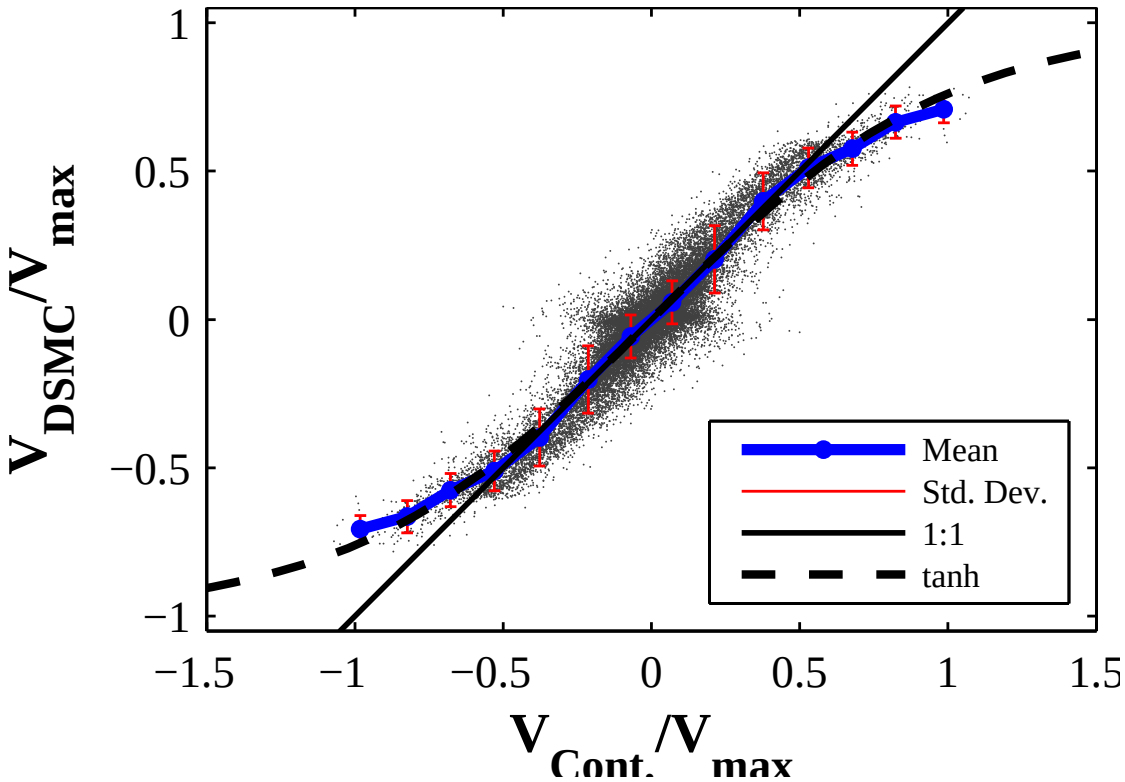

Figure II.14: Scaled DSMC versus Continuum diffusion velocities from a 50:50 He:Ar expansion jet simulation.

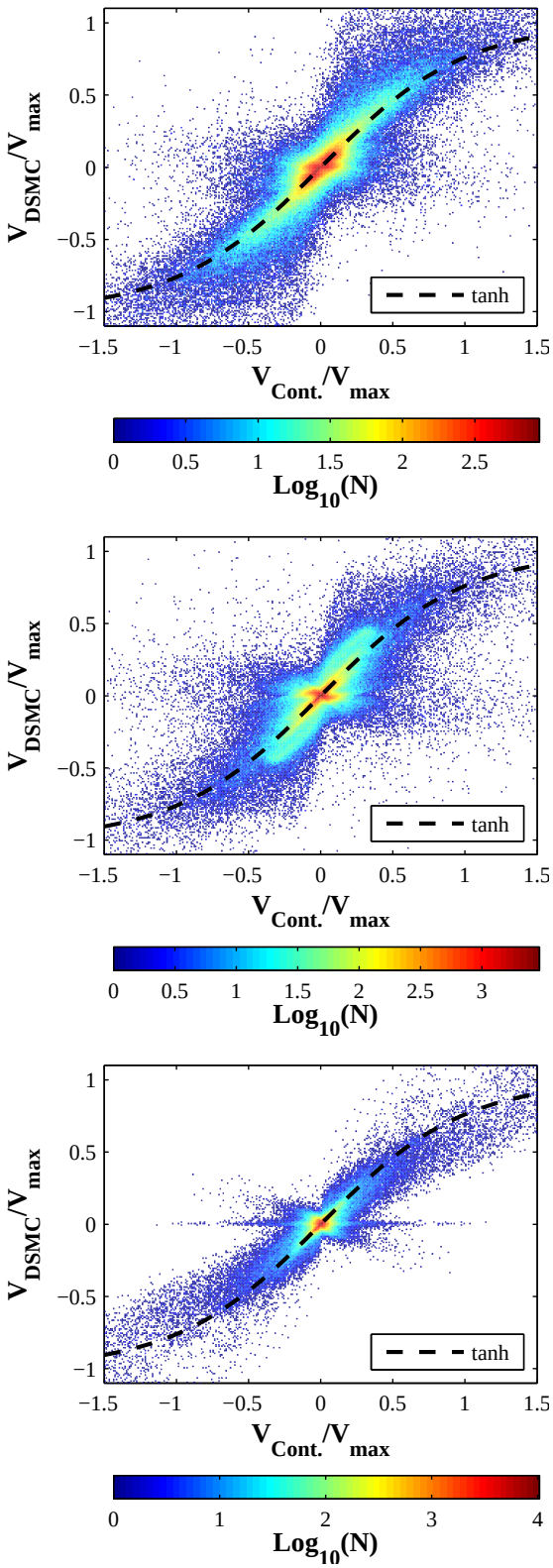

Figure II.15: Log plot of accumulated point counts for jet simulations from 10% - 90% of each component. Left is the He:Ar system, middle is the He:Xe system, and right is the Ar:Xe system.

effective mixture average diffusion coefficient is thus determined using Equation II.77. Finally, the flux limited time-step is calculated using Equation II.78.

$$D_{sm}^{\text{Eff.}} = D_{sm} \left[\frac{F}{F_o} \right]_{s,\rho e} \tag{II.77}$$

$$|\lambda_s|_{max} \approxeq \left| v_o + \frac{D_{sm}^{\text{Eff.}}}{X_s} \left(\frac{X_s - Y_s}{P} \frac{\partial P}{\partial x_i} + \frac{\Theta_s}{T} \frac{\partial T}{\partial x_i} \right) \right| + \frac{D_{sm}^{\text{Eff.}} / \Delta x}{|\mathcal{F} - 1/2|} \tag{II.78}$$

II.E Validation of Compressible Mixture Models

The validation of the multicomponent algorithm consists of five sections. In the first, comparison is made between experimental values and numerical estimates for the composition dependence of the transport coefficients. The second section shows the effect of the diffusion velocities on the shape of shock waves. The third examines the limit at which the shock solutions become non-physical. The fourth section shows some numerical convergence properties for two of the shock wave cases. Finally, the fifth section compares the mixture separation in a 2D-axisymmetric free expansion jet to experimental and Monte Carlo results.

II.E.1 Transport Coefficients

In Figures II.16 through II.19, comparison is made between tabulated experimental data and numerical estimates for viscosity and thermal conductivity across the range of compositions for Helium-Xenon and Argon-Xenon gas mixtures. Experimental values for viscosity and thermal conductivity are tabulated in Reference [81]. Thermal diffusion ratios are also compared to values from Reference [1]. Finally in Table II.1, the binary diffusion coefficients for the gas mixtures used in the shock validation cases are compared to analytical and experimental values.

The largest discrepancy appears in the thermal diffusion ratios. Because $k_{sr}(T)$ is independent of composition, the equation necessarily produces parabolic

Table II.1: Reference and Application Binary Diffusion Coefficients at 1 Atm

Gas Pair	T(K)	Analytical $\mathcal{D}, (cm^2/s)$	Experimental $\mathcal{D}$	Application $\mathcal{D}$
He:He	300	1.700 [42]		1.649
He:Ar	273.2	0.653 [38]	0.641 [38]	0.644
Ar:Ar	273.2	0.154 [38]	0.156 ± 0.002 [38]	0.157
He:Xe	303	0.604 [79]	0.600 [79]	0.561
Xe:Xe	300.5	0.0571 [38]	0.0576 ± 0.0009 [38]	0.0573

thermal diffusion ratios when plotted against number fraction. This discrepancy results in an almost 50coefficient for the 2.2%X_{xe} shock profiles shown later.

The Sandia Report of Reference [45] mentions that this method of calculating thermal diffusion is considerably less accurate than the full multicomponent method now used in subsequent applications, but due to the complexity and expense of the full multi-component method, this approximation is used to provide initial investigation of several compressible flows to determine whether further refinement is warranted.

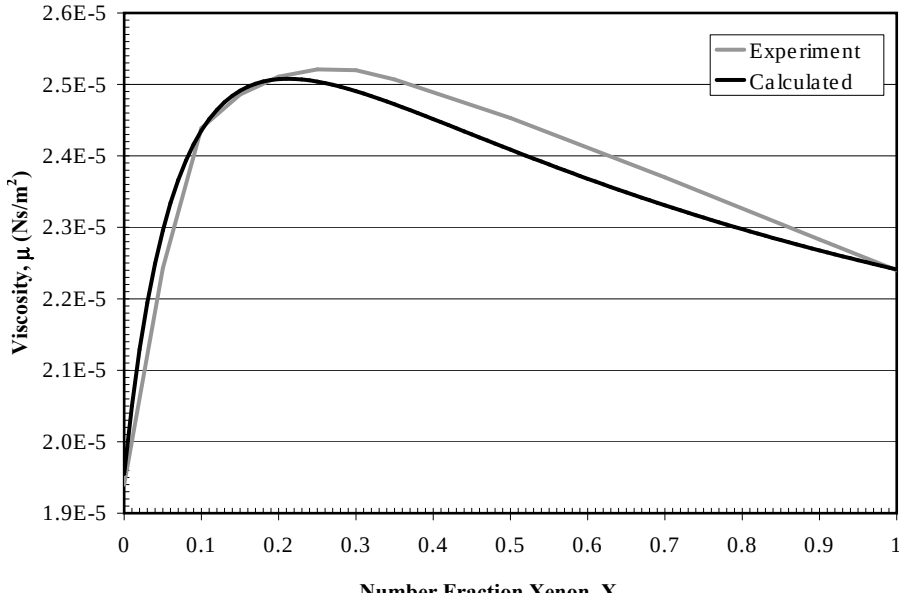

Figure II.16: Viscosity by Composition for He:Xe Mixture

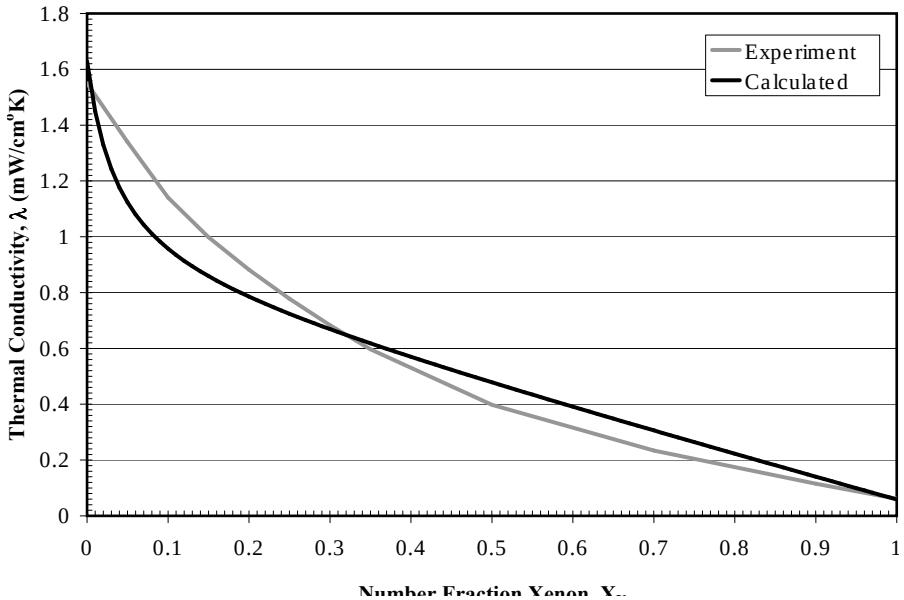

Figure II.17: Thermal Conductivity by Composition for He:Xe Mixture

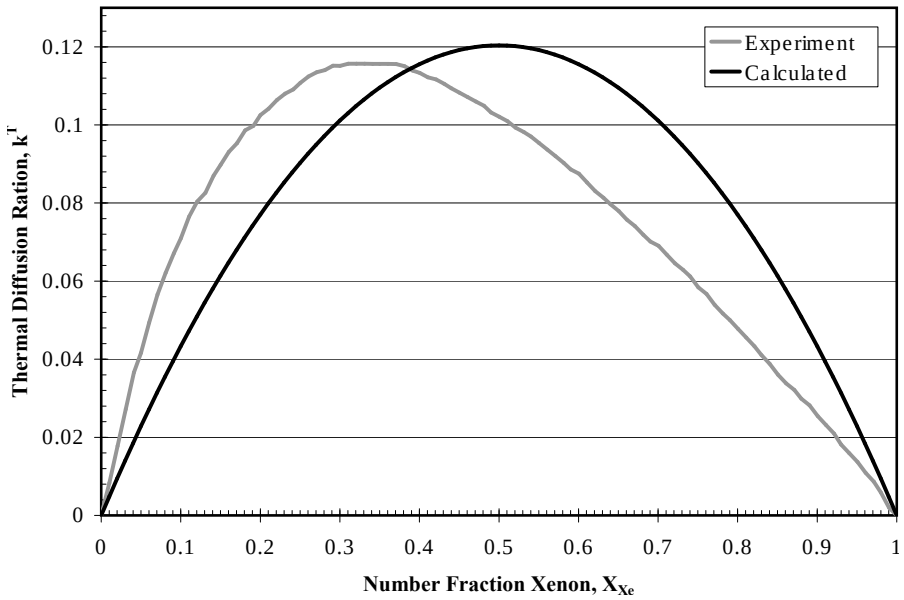

Figure II.18: Thermal Diffusion Ratio by Composition for He:Xe Mixture

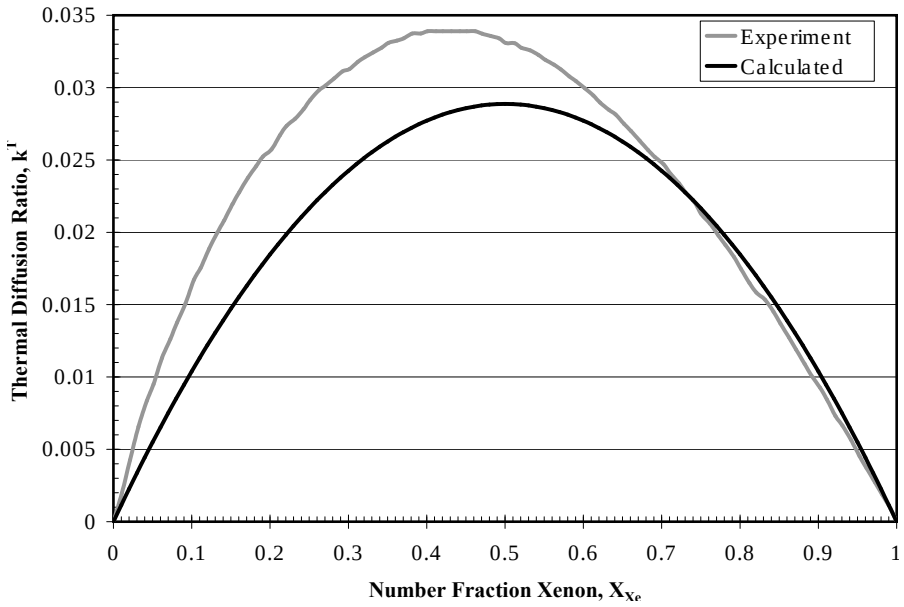

Figure II.19: Thermal Diffusion Ratio by Composition for Ar:Xe Mixture

II.E.2 Shock Broadening

In this section, comparison is made between experimental and simulation data for the composition dependence across a shock-wave for mixtures of noble gasses. The experimental data available shows the shock broadening and mixture separation for mixtures of Helium and Xenon gas at two different Mach numbers and two different Helium-Argon mixtures. The reason that the composition varies across the shock-wave is inherently due to the baro-diffusion and somewhat counteracted by the Soret effect. The strong pressure gradients within the shock drive these this pressure diffusion to work against the Fickian diffusion term and cause the gas to become less uniformly mixed. Because the energy is assumed to be partitioned equally between the Helium and Xenon atoms, the Helium atoms move on average $\sqrt{m_{Xe}/m_{He}}$ or approximately 5.7 times faster. This results in Helium atoms crossing the discontinuity from further upstream. The Xenon atoms also have more momentum and therefore take longer for their directional pre-shock velocity to randomize into thermal noise through collisions. The multi-species formulation is capable of capturing the continuum representation of some of these

effects as long as the gasses do not deviate far from equilibrium distribution functions.

The experimental curves for the Helium-Xenon mixtures were obtained from the work of Herczynski, Tarczynski, and Walenta[35]. These experiments were performed in a shock tube using an electron gun and laser differential interferometer to measure the composition across the shock. The experiments were performed with Helium-Xenon gas mixtures with percent composition by number fraction rather than by mass fraction. At 3% Xenon number fraction, the mass fraction is approximately 50% Xenon and 50% Helium.

One and two-dimensional multi-component Navier Stokes codes based on the development in the previous sections as well as a Roe's scheme variation were created to simulate the shock structure for the conditions in Reference [35]. The simulation results are shown in Figures II.20 and II.21 for Mach 1.54 and Mach 4.38 respectively. In the figures, the flow is from left to right across the shock.

In these figures, the simulation length scale results were nondimensionalized using the mean free paths listed in Reference [35]. The densities were normalized according to Equation II.79 as was the data in Reference [35]. In the equation, L and R subscripts refer to the state at the left and right edge of the numerical domain respectively. It is important to note that, due to this normalization, negative values on the plots do not correspond to negative species densities. Negative values simply correspond to the fraction of the shock jump that the species density decreases prior to jumping up to the shocked value. The discrepancy between the numerical and experimental value near the start and end of Figure II.20 might be an artifact due to this normalization. The experiment likely used left and right states based on the apparent start and end of the shock as measured by the experimental apparatus rather than the states further up and downstream. The curves plotted from the 2D codes were extracted from the centerline of the computational domain parallel to the flow.

As seen in Figures II.20 and II.21, the resulting shock composition agree

well between all the one and two-dimensional version. Both the one and two-dimensional codes showed better agreement to experimental data for the Mach 1.54 case than for the Mach 4.38 case.

$$\hat{\rho} = \frac{\rho - \rho_L}{\rho_R - \rho_L} \tag{II.79}$$

The experimental data for the Helium-Argon mixtures comes from the work of R.E. Center [16]. Figure II.22 shows the shock structure for a mixture of 2.2% Argon at Mach 2.07, and Figure II.23 show the structure for a mixture of 48% Argon at Mach 2.24. Center's work was designed to address the behavior of the Argon velocity predicted in Sherman's work [77]. For this reason, the curves labeled 'Sherman Analytical' on Figures II.22 and II.23 are included for comparison. These curves were generated by taking the inverse of the velocity plots in Sherman and scaling as with the normalized density of Equation II.79. These curves bear significant resemblance to those of the numerical simulations despite being generated for slightly different 2.0% and 50.0% number fractions at Mach 2.05. In particular, the difference in Mach numbers likely causes the different width between the Sherman and Godunov solutions in Figure II.23.

Figures II.24 through II.27 show the helium mass fraction variation for the prior cases. These plots demonstrate considerably better agreement with the experimental data than the density profiles for these shocks. In the weak He:Xe shock case shown in Figure II.24 the effect of both flux limiters is negligible. In the strong shock He:Xe profile of Figure II.25, the energy limiter produces a significant change while the velocity limiter results in underestimation of the peak mixture separation. In Figures II.26 and II.27 for the moderate He:Ar shocks, the effect of the energy flux limiter is negligible while the velocity flux limiter results in significant improvement in the profile.

The flux limiters only apply to flows far from equilibrium in which the mass and energy diffusion approaches physical theoretical limits. It is not unexpected the Navier-Stokes equations would begin to break down for flows in which

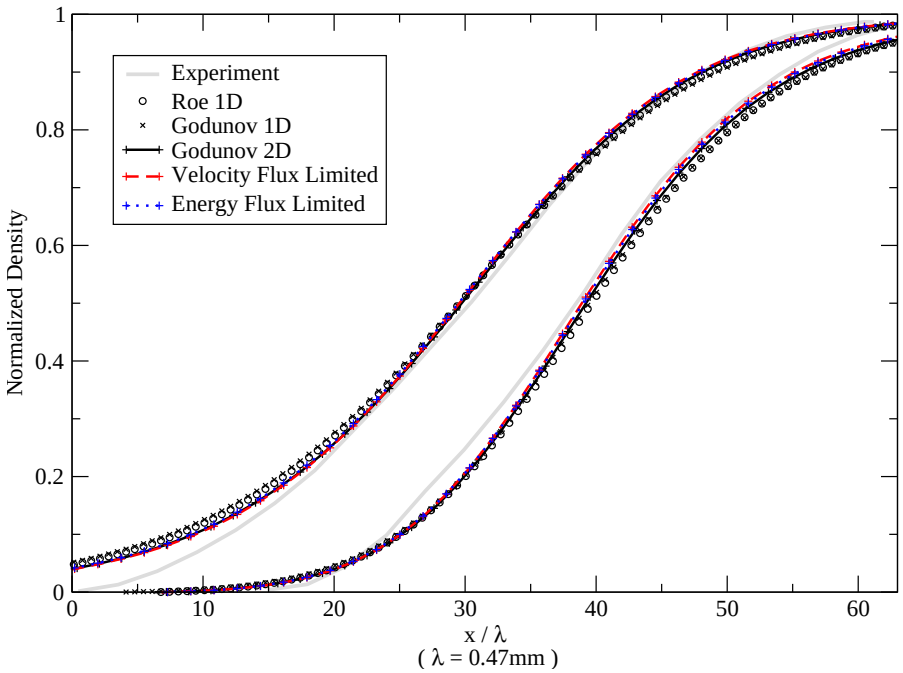

Figure II.20: He:Xe Shock broadening simulation results and experimental data, 3% Xenon at Mach 1.54.

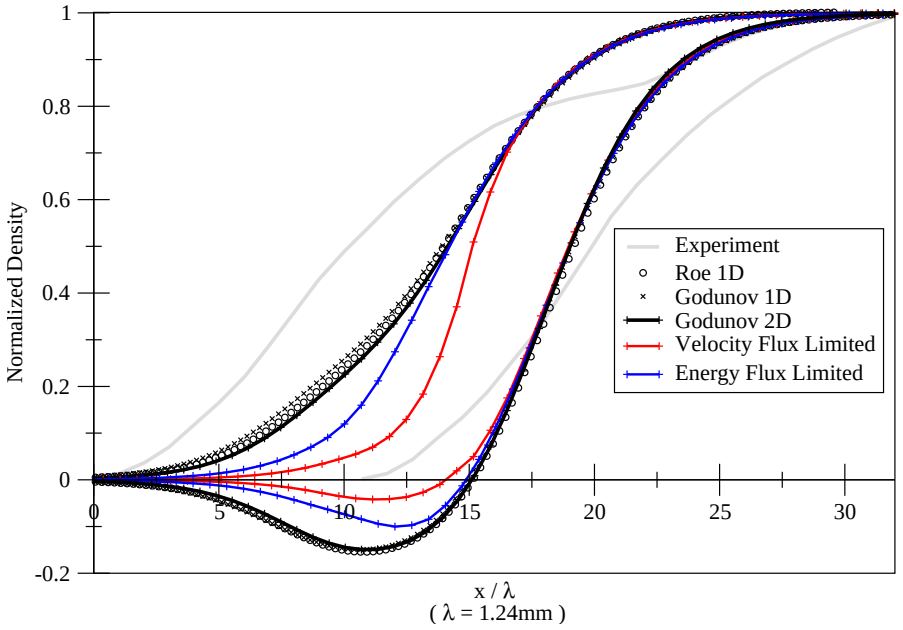

Figure II.21: He:Xe Shock broadening simulation results and experimental data, 3% Xenon at Mach 4.38.

this is the case. The assumption that all individual gas species temperatures are equal seems unrealistic when gradients drive the diffusion velocities to be of the order of thermal velocities. The fact that the mixture composition performs reasonably well even under these conditions indicates that the multi-species formulation is sufficient for flows in which Navier-Stokes is valid. This would include the majority of supersonic and hypersonic flows except within the interior of strong shocks.

As seen in Figure II.20 and II.23, the simulations match the experimental data and each other at for weak and moderate shocks. Figures II.22 and II.21 both exhibit the fictitious heavy component density drop at the beginning of the shock. Because the two He:Xe cases share a mixture fraction while the two He:Ar approximately share a Mach number, this indicates that the development of the density undershoot only occurs in moderate to strong shocks with low fractions of the heavy component. This is likely because the diffusion velocity in the heavy

component needed to balance a large diffusion velocity in the lighter component becomes large compared to the heavy component's thermal speed in these cases.

Figures II.21 and II.25 show that the simulations capture some of broadening of shock width and composition separation for the strong shock despite failing on the more complicated internal features of the flow. In particular, the simulations fail to capture the "hump" in the strong shock-wave which in particular indicates the a transition away from local equilibrium flow.

Along with the experimental data, a theoretical model was included in Herczynski, Tarczynski,and Walenta[35]. Their approach used a variational model to approximate the Boltzmann equation directly. They captured the "hump" in the shock-wave, but their model resulted in no separation at the beginning of the shock-wave along with a significantly quantitatively inaccurate shock composition and width. Their theoretical model did show a large temperature overshoot in the heavy component of the mixture near the "hump". Unfortunately, Herczynski, Tarczynski, and Walenta were unable to generated a temperature profile experimentally to confirm the overshoot. Monte Carlo simulations performed earlier by Bird in Reference [11] showed significant temperature separation between gas components as well.

The Navier-Stokes type derivation used in the simulations of this paper depend on instantaneous energy relaxation between the components because the distribution functions are assumed to be perturbations to the Maxwellian distribution when the Chapman-Enskog expansion is performed. The simulations therefore necessarily cannot capture a temperature overshoot in one component because the instantaneous energy relaxation corresponds to equal temperatures for all the components. This most likely explains the lack of a "hump" in the simulations.

Another variation of the strong shock solutions from the experiments is seen in the density undershoot effect. The effect was initially discovered by Sherman [77] using a more direct analytical approach for solving the multi-species Navier-Stokes equations. The similarity between the solutions from this code and

those of Sherman shown in Figures II.22 and II.23 indicates that the code is producing the same solution to the set of equations as Sherman. What remains is determining physical validity of this solution.

II.E.3 Continuum Limit

Sherman's density undershoot was investigated extensively in References [11, 16, 25, 31, 56] using experiments and various kinetic solutions to the Boltzmann equation. The density undershoot was found to be an artifact of the Champan-Enskog expansion and identified as the result of a missing eigenvalue in phase space in Reference [25].

In Reference [56], Oberai extends the method of Mott-Smith to binary mixtures and eliminates the density undershoot effect. Both the Mott-Smith and BGK models were developed in an attempt to calculate the shape of single species strong shock-waves more accurately. As seen in Reference [84], the BGK model predicts a velocity drop that begins much further upstream from the shock-wave than the Navier-Stokes shock solution. The better agreement found in the mass fraction plots indicate that, if the BGK profile was the underlying shock profile instead of the Navier-Stokes solution, the early deceleration of the profile could possibly compensate for the density undershoot discrepancy between the simulation and experimental curves. Unfortunately, the BGK model employs an iterative solution to a set of integro-differential equations and would be much more difficult and expensive to extend to multiple dimensions for complex flows.

The combined work of Goldman and Sirovich in References [31, 29, 30] provide the clearest explanation for why methods based on the Chapman-Enskog expansion fail for these strong shocks with trace heavy gas. The Chapman-Enskog expansion depends on the small parameter, ϵ, that relates the microscopic and macroscopic length scales as seen in Equation II.80. In the equation, Δ refers to some macroscopic length scale. For the shock solution, Goldman uses the velocity-gradient thickness in Equation II.81 as seen in Reference [84] in dimensional units.

In Reference [31], Goldman and Sirovich also consider relaxation rates present in gas mixtures that are absent for pure gasses that effect the validity of the Chapman-Enskog expansion. They are related to the difference in collision frequencies for all the combinations of similar and dissimilar collisions. Reference [31] includes an extension based on earlier work in Reference [29] for gas mixtures as seen in Equation II.82. In this equation, C is a modified Schmidt number that relates the thermal relaxation frequency, Θ_T, to the corresponding relaxation frequency Θ_μ derived from the definition of the bulk viscosity mean free path. The quantity is related to the Schmidt number as seen in Equation II.83 and approximately constant across composition for binary gas mixtures. The resulting λ/C, is effectively the microscopic thermal relaxation scale that indicates the relative importance of two temperature effects.

Values of C were calculated using the upstream conditions based on the applications calculations of transport coefficients. The values for C were found to be in good agreement with Goldman and Sirovich's work in References [31, 29, 30].The results of applying Equations II.80 and II.82 using the maximum slope $|du/dx|_{max}$ and mean free path from the simulations are shown in Table II.2. We note that the mean free paths for the He:Xe cases are slightly different than the values listed in Reference [35] that were used for the normalization in the plots of the previous section. The simulation values were used here for a consistent comparison to the He:Ar values while the mean free paths listed in Reference [35] were used for consistent comparison to the experimental values on the plots.

In Reference [10], Bird suggests a limit on the Knudsen number defined similarly to ϵ at 0.1 to ensure the validity of of the Navier-Stokes equations. While ϵ for the 48% Argon He:Ar case nearly matches that of the strong Mach 4.38 He:Xe case and both are near the 0.1 limit, the results of the strong shock case are considerably worse. However, the more restrictive ϵ_1 provides a clear distinction between cases containing the fictitious undershoot and those without. Table II.2 also provides the more intuitive ϵ_1^{-1} which provides a measure of the number of

Table II.2: Chapman-Enskog Expansion Small Parameters for Shock Simulation Results

Mach	Mixture	% X_{He}	$\|du/dx\|_{max}(s^{-1})$	λ (mm)	ϵ	ϵ_1	ϵ_1^{-1}
1.54	He:Xe	3.0 %	3.05e4	0.53	0.03	0.22	4.5
4.38	He:Xe	3.0 %	1.88e5	1.37	0.11	0.76	1.3
2.07	He:Ar	2.2 %	2.89e5	0.53	0.21	0.65	1.5
2.24	He:Ar	48 %	1.24e5	0.31	0.10	0.32	3.1

collisions per thermal relaxation scale. While more than three collisions appears sufficient, $\approx$1.5 collisions is not. This suggests that replacing the ill-defined $\epsilon_1 \ll 1$ with $\epsilon_1 < 1/3$ may provide a reasonable additional bound on applicability for the for the single temperature multi-component continuum formulation. However, comparisions of more experiments and simulations near this boundary are needed to confirm this.

$$\epsilon = \lambda/\Delta \tag{II.80}$$

$$\Delta_u = \frac{|u_\alpha - u_\beta|}{|\frac{\partial u}{\partial x}|_{max}} \tag{II.81}$$

$$\epsilon_1 = \lambda/C\Delta \tag{II.82}$$

$$C = \frac{\Theta_T}{\Theta_\mu} = \frac{2\rho Sc}{n(m_r + m_s)} \tag{II.83}$$

II.E.4 Convergence

Results for both the Mach 1.54 and Mach 4.38 Helium Xenon mixtures were calculated with a wide range of cell widths relative to the mean free path of the flow. Figures II.28 and II.29 are plots of the root mean square percent error of the solution on a given grid coarseness relative to the finest level simulation performed. The finest solution calculated corresponds to a cell width of 0.53 mean

free paths for the Mach 1.54 case and 0.20 mean free paths for the Mach 4.38 case. Percent RMS error was used instead of absolute RMS error to ensure equal weight given to the pre and post-shock density error. Though the final solution is steady in time for all of the cases, transients resulting from a step initial shock solutions result in slight up and downstream displacements of the position of the steady shock in the simulations. For this reason, when calculating the error, the shock position of the finest grid is translated with respect to the coarser grid until the error is minimized between the coarse grid and the finest solution linearly interpolated to the coarse mesh. This linear interpolation does introduce more error which would be most significant with respect to the simulation error for the finest grids, but was not immediately apparent relative to the other fluctuations between cases.

Both Figures II.28 and II.29 demonstrate a similar behavior of converging to the finest solution rapidly as the cell width decreases. However, the RMS error also decreases for very large cell widths in both figures. This is the result of the conservative shock capturing method converging to the weak form shock discontinuity solution when insufficient resolution exists to resolve the shock interior and associated mixture separation. It is also important to note that the peak error also occurs at different cell widths when compared to mean free paths.

Figure II.30 shows the two convergence cases replotted on one Log-Log scale. Instead of cell width in mean free paths, the figure compares cell width to shock widths calculated in the previous section. This indicates that the peak error occurs near a cell width of the order of the shock width in both cases. Though the weak shock has a smoother peak, in both cases the rapid convergence begins when the cell width is such that 2 or more cells are within the shock width. Table II.3 lists the slopes and fit quality for the trend-lines on the fully resolved shock side of the plot. The slope listed in the table is equivalent to an average convergence rate p_* of Equation II.84 defined in Reference [23] in which Dragojlovic examined the convergence rates of density, momentum, and energy for the single component

Table II.3: Shock Fine Grid Convergence Parameters

Convergence Case	Slope	R-square
Mach 1.54	1.8881	0.9887
Mach 4.38	1.8758	0.9932

version of the code on which the work in this paper was built. Though flow and error were defined differently, the RMS percent error used is approximately an L_2 norm with weighting for the low-density pre-shocked values and a very low-order quadrature. For the single-component code of Reference [23], the convergence rate for the L_2 norm in density ranged from $1.475 - 2.032$ for the grid resolutions tested. For the Mach 1.54 and Mach 4.38 cases, the convergence rate ranged from $1.25 - 2.46$ and $1.43 - 2.57$ yielding the average convergence rates of 1.89 and 1.88 that are comparable to the L_2 density convergence rate demonstrated in Reference [23].

$$p_* = log_2 \left(\frac{||E^n_{i,j}(2h)||_*}{||E^n_{i,j}(h)||_*} \right) \tag{II.84}$$

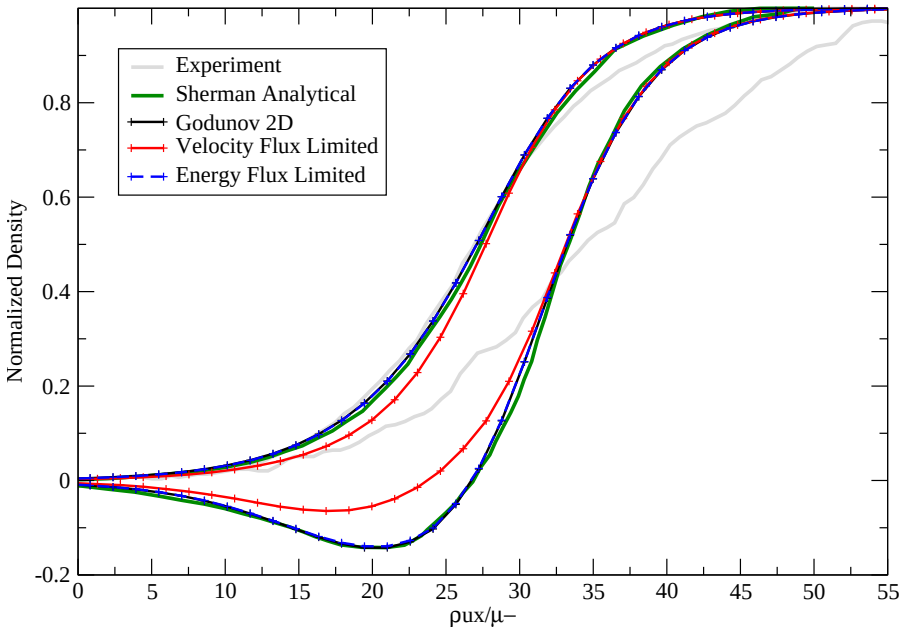

Figure II.22: He:Ar Shock broadening simulation results, analytical data, and experimental data, 2.2% Ar at Mach 2.07.

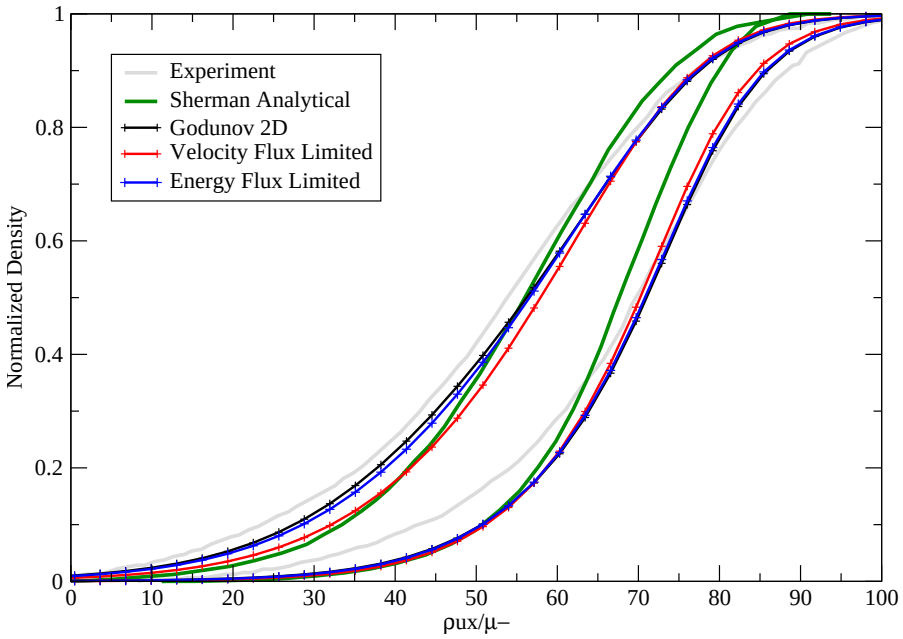

Figure II.23: He:Ar Shock broadening simulation results, analytical data, and experimental data, 48% Ar at Mach 2.24.

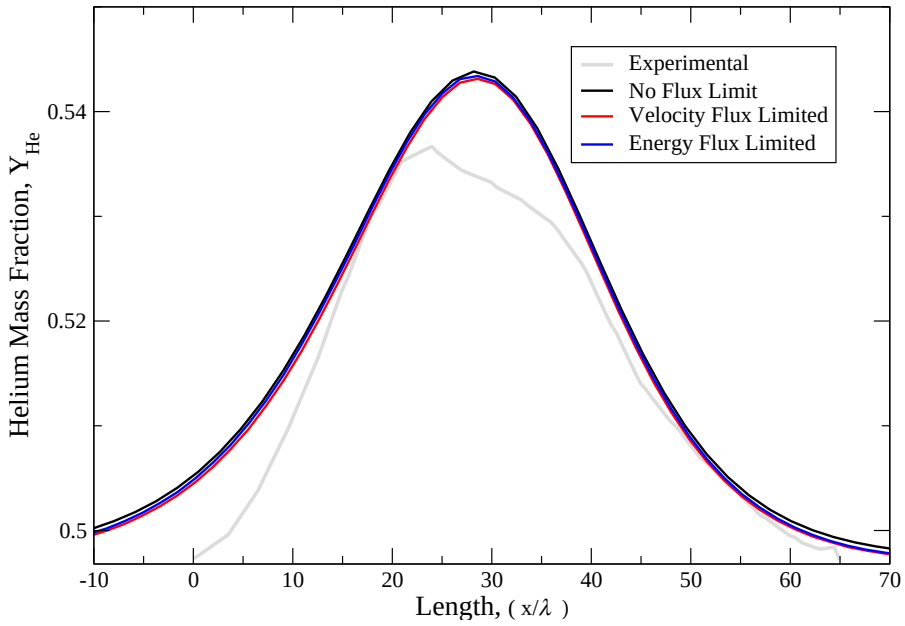

Figure II.24: Mass Fraction Helium experimental data as well as unlimited and flux limited simulations in Mach 1.54 He:Xe shock.

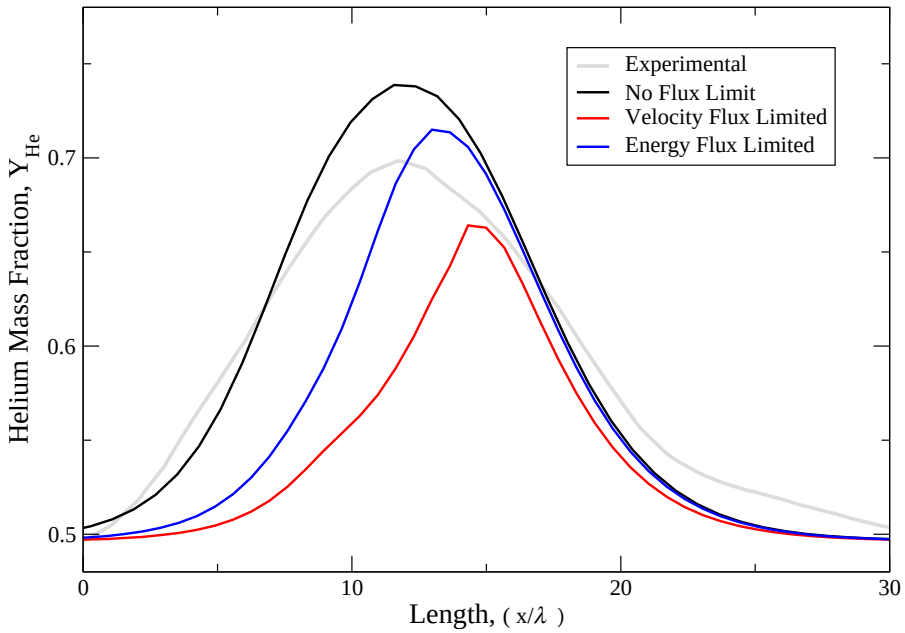

Figure II.25: Mass Fraction Helium experimental data with unlimited and flux limited simulations for Mach 4.38 He:Xe shock.

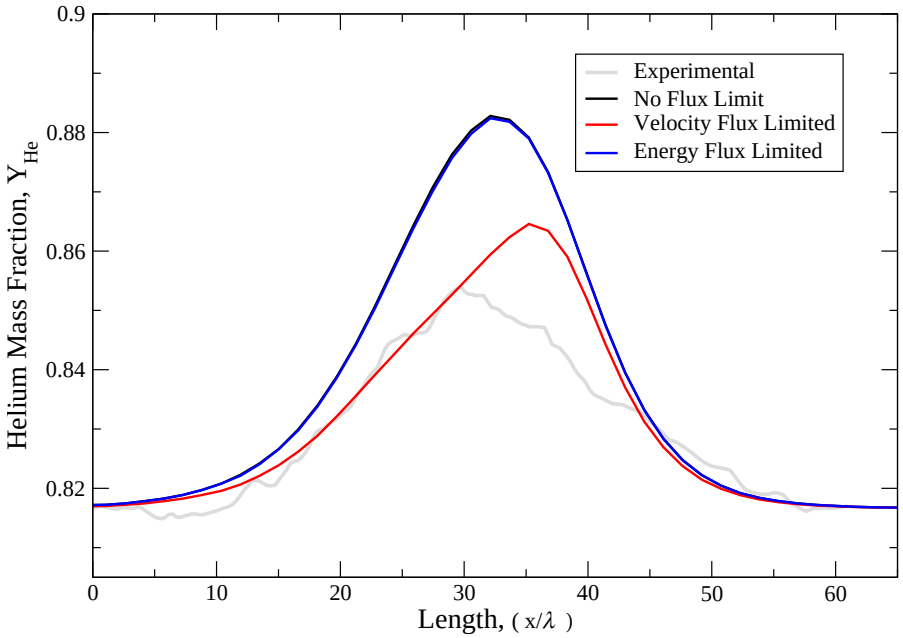

Figure II.26: Mass Fraction Helium experimental data with unlimited and flux limited simulations for Mach 2.07 He:Ar shock.

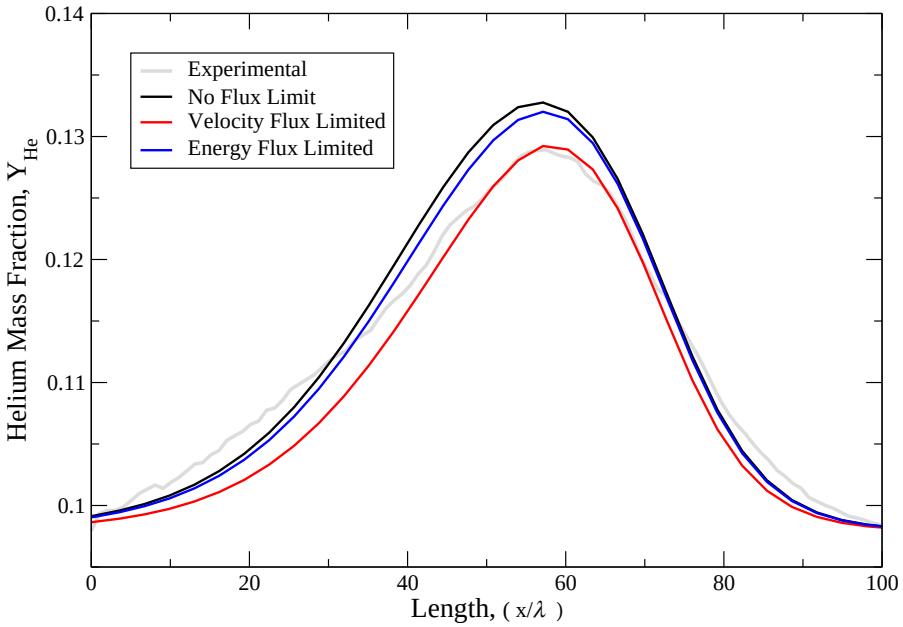

Figure II.27: Mass Fraction Helium experimental data with unlimited and flux limited simulations for Mach 2.24 He:Ar shock.

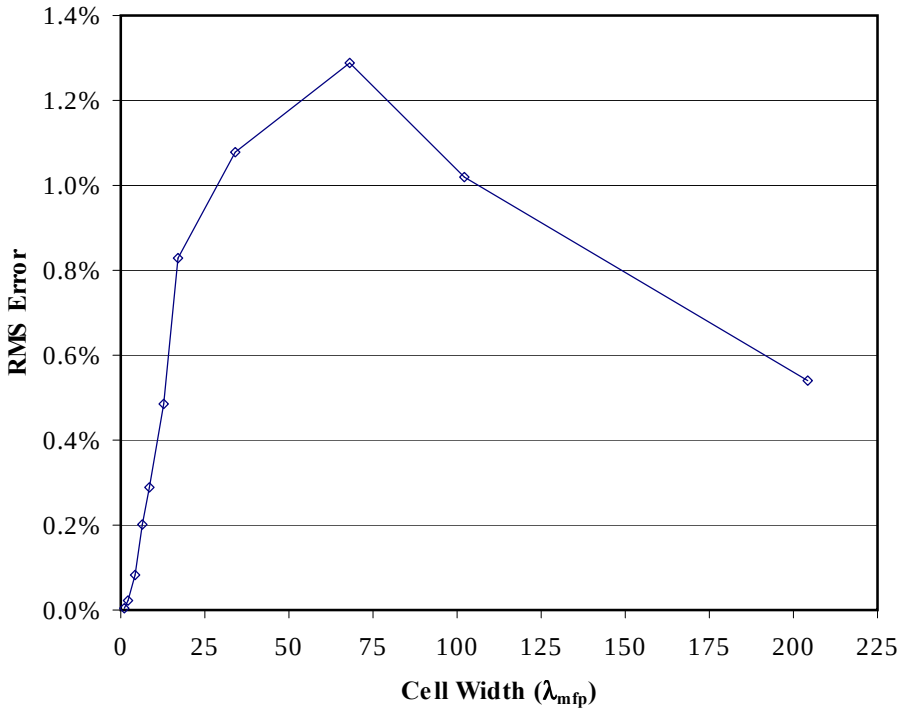

Figure II.28: Mach 1.54 shock simulation convergence results.

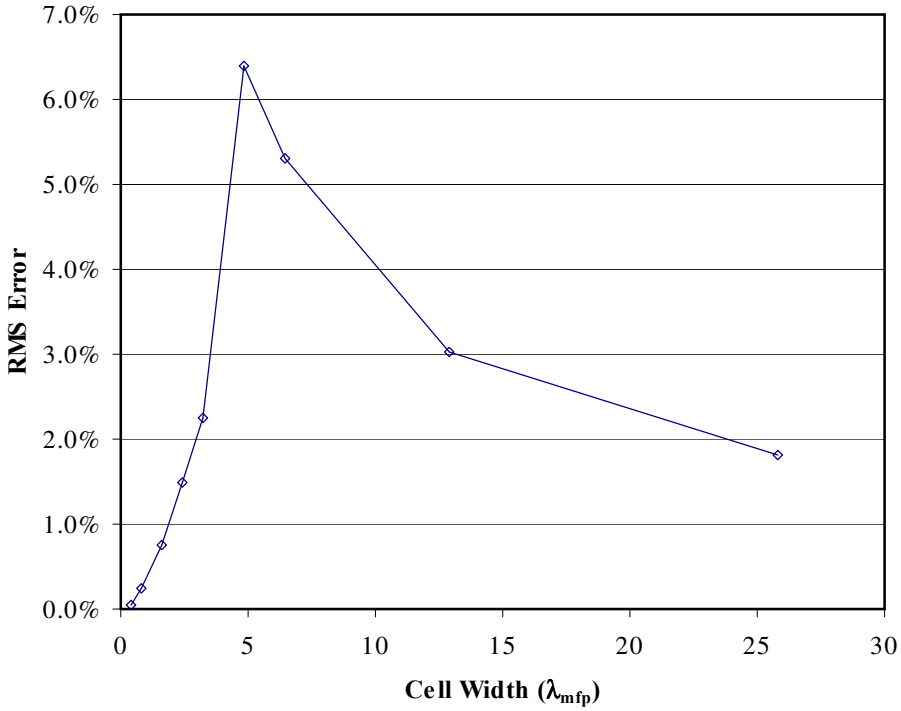

Figure II.29: Mach 4.38 shock simulation convergence results.

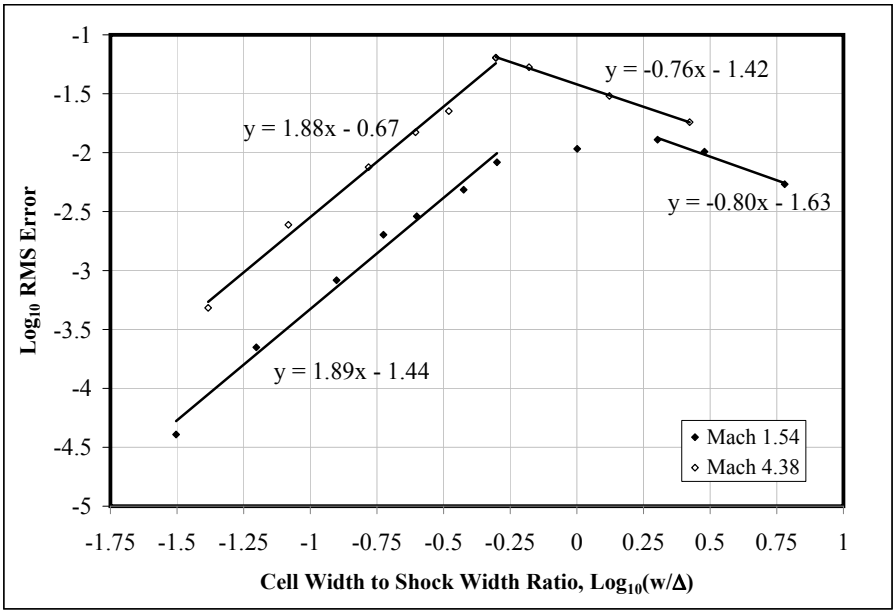

Figure II.30: Log-Log RMS Error versus Cell Width to Shock Width Ratio.

II.E.5 Mixture Expansion Jet

The free expansion jet has long served as an important testbed for theories of supersonic gas dynamics. Though analysis is considerably simplified for a single gas species, the strong gradients within the expansion as well as associated barrel shock and Mach disc result in complex flow phenomena in binary mixtures that provide a valuable resource for the validation of models for diffusive phenomena. These diffusion phenomena were first investigated in free jets in the mid 20th century both experimentally [86, 69, 73, 71, 16, 12] as well as analytically [90, 76]. The freejet experiments were originally used to produce normal shocks for the evaluation analytical and numerical predictions of mixture shock profiles. They were also considered as a means to either separate isotope mixtures or to produce high velocity molecular beams of heavy molecules by accelerating trace quantities of the heavy gas within a jet of predominately light gas. For the current work, particular attention is paid to Rothe's experimental work[73, 71] for jet mixtures of Helium and Argon due to the rich two-dimensional composition profiles provided therein as opposed to the axial or limited quantity of cross sections or influence of skimmer probes found the others [86, 69, 12].

In recent years, significant work has been done to couple stochastic and continuum flow solvers to optimize computational efficiency while maintaining physical validity. One major contributer in this arena is Garcia and Bell's adaptive mesh and algorithm refinement (AMAR) approach[27]. Using this AMAR algorithm, Wijesinghe et. al[87] extended the application to a binary mixture but coupled the flow to a continuum Euler solver that had no viscous terms let alone thermo- or baro-diffusion. Most recently, this model was again extended to couple the Landau-Lifshitz Navier-Stokes equations[7] demonstrating good agreement with theoretical results and molecular simulations including the thermo-diffusive Soret effect using the hard sphere transport model.

Bird's detailed description of these Monte Carlo methods in Reference [10] provided sufficient information to allow direct comparison of the combined

results from Bird's publicly available DS2V code along with the multi-component fluids code and Rothe's experimental data. The only modification to the prior multi-component code[51] required to implement the new transport model was replacing the Lennard Jones non-dimensional collision integrals with the values shown in Equation II.68 from Section .

This change ensures that the transport properties calculated by SPARTAN and DS2V are identical for all temperatures in the limit of perturbed-equilibrium flow. This eliminates the transport properties as a potential cause for discrepancies between the solutions focusing results on the flows deviation from equilibrium. In the future, the ability to operate SPARTAN with both collision models may be used to compare the effect of temperature variation on thermal diffusion because the VSS model is incapable of representing the temperature dependent variation. This could be particularly important at low temperatures where the Soret effect can actually change sign such that light gases diffuse away from heat.[38].

For the results presented, the variable hard sphere molecular model equivalent to $\alpha = 1$ was used for both the Monte Carlo and continuum transport coefficients. Though variable soft sphere cases were also run, the overall flow-field as well as differences between Monte Carlo and continuum solutions remained similar. This similarity may be because the steady state mixture composition is dominated by the balance of Fickian and baro-diffusion which are multiplied by the same mixture average diffusion coefficient. This is shown in Equation II.85 for the species diffusion velocity[45]. The dominance of the baro-diffusive term though mentioned in Bird[10], can be shown simply for a binary mixture by simplifying Equation II.85 to equation II.86 where k_{sr} is defined by Equation II.87. The factor k_{sr} is a constant weakly dependant on the temperature viscosity power law and VSS parameter which is equal to 105/118 for the hard sphere model when $A^{\star}_{sr}$, $B^{\star}_{sr}$, and $C^{\star}_{sr}$ all equal unity. It can be clearly seen that the coefficient on the pressure term is larger and in the opposite direction by a factor of $(m_1 + m_2)/(k_{12}\overline{m})$. To the extent to which the flow is approximately isentropic $P \tilde{\propto} T^{\gamma/(\gamma-1)}$ and therefore

$\nabla T/T = \frac{\gamma-1}{\gamma}\nabla P/P$ yielding Equation II.88 for the difference between the thermo- and baro- diffusive contributions under these conditions. Note that Equation II.88 is broken into 3 non-dimensional terms each greater than unity.

$$\vec{V}_s = -\frac{D_{sm}}{X_s}\left[\nabla X_s + (X_s - Y_s)\frac{\nabla P}{P} + \Theta_s\frac{\nabla T}{T}\right] \tag{II.85}$$

$$\vec{V}_1 = -\frac{D_{1m}}{X_1}\left[\begin{array}{r}\nabla X_s + X_1X_2\frac{m_r-m_s}{\overline{m}}\frac{\nabla P}{P} \\ +k_{12}X_1X_2\frac{m_s-m_r}{m_s+m_r}\frac{\nabla T}{T}\end{array}\right] \tag{II.86}$$

$$k_{sr} = \frac{15}{2}\frac{(2A^\star_{sr}+5)(6C^\star_{sr}-5)}{A^\star_{sr}(16A^\star_{sr}-12B^\star_{sr}+55)} \tag{II.87}$$

$$\frac{[\vec{V}_1]_P}{[\vec{V}_1]_T} = -\frac{(m_1+m_2)}{\overline{m}}\frac{\gamma}{\gamma-1}[k_{12}]^{-1} \tag{II.88}$$

The numerical simulations are based on the experimental setup in Rothe's electron beam studies of Helium-Argon free jets [73, 71]. In these experiments, Rothe used the University of Toronto Institute for Aerospace Studies (UTIAS) low pressure wind tunnel. Though a range mixture fractions, pressures, and nozzle diameters were investigated, the most extensive data was provided for the 12% Helium case with $p_0 = 2.56$ Torr and a $15mm$ nozzle diameter. This case had a corresponding chamber pressure of $p_\infty = 17\mu mHg$. For the experiment, a flat plate with the orifice was affixed to a $47.5mm$ converging nozzle. The plate's thickness was 3% of the orifice diameter.

Figure II.31 shows the layout of the the numerical domains and boundary conditions relative to the jet for the continuum and Monte Carlo numerical simulations. The domain for the Monte Carlo solution was set to range from $-24mm$ to $248mm$ relative to the orifice in the axial direction and from the axis of symmetry to $96mm$ in the radial direction. The continuum solution used the same radial and downstream domain but extended back to $-112mm$ in the axial direction. This was done to ease the influence of the rear boundary conditions as the external to the jet accelerates from rest as external gas in entrained in the jet. The continuum

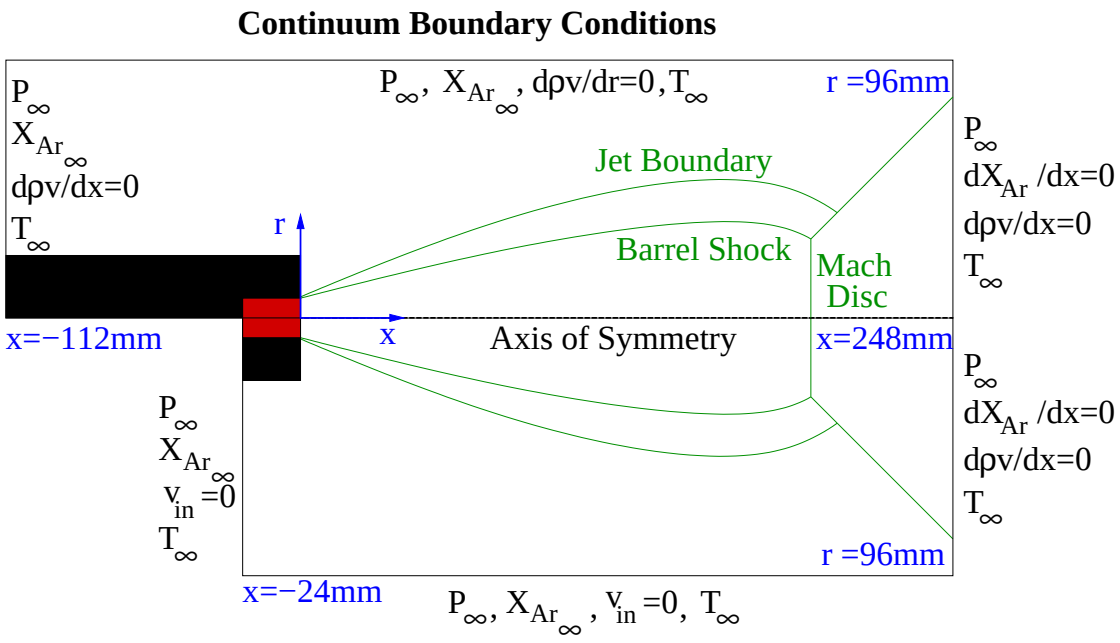

Figure II.31: Continuum (top) and Monte Carlo (bottom) boundary conditions relative to the jet. Boundary conditions and domain edges are shown in black. Filled black regions represent the jet nozzle. Jet flow features are shown in green. Fixed sonic jet inlet is shown in red. Geometric information is shown in blue.

solution used a $48x36$ radial by axial grid as the coarsest AMR level with two levels of refinement along the axis and around the nozzle. The Monte Carlo code used Bird's default combination of collision and sampling cells.

The jet boundary conditions were set as a $15mm$ sonic orifice using the isentropic relations. This orifice was surrounded by a $47.5mm$ solid cylinder that extended to the upstream edge of the domain. For the Monte Carlo simulation, both the remainder of the upstream boundary and the outer boundary parallel to the axis were set to stream conditions corresponding to chamber properties. For the continuum code, the pressure and flow composition were fixed on the remainder of the upstream and external boundary parallel to the axis. For both codes, the downstream boundary was set as an outflow fixed to the chamber pressure, but the velocity and composition were allowed to vary based on the mass flux. Both

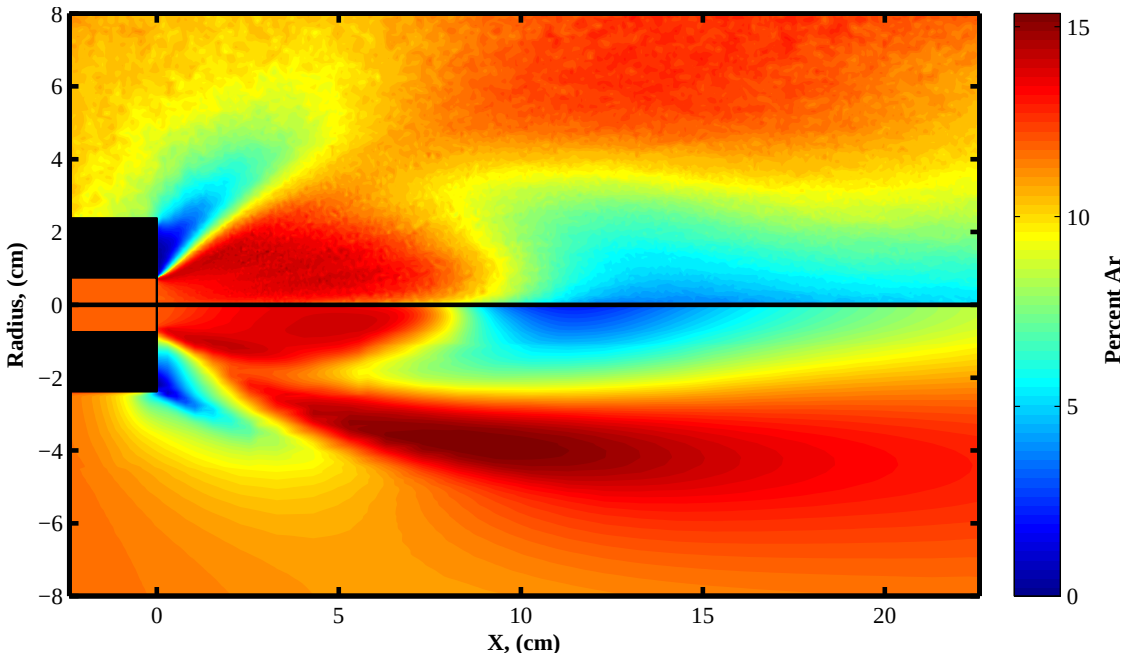

Figure II.32: Monte Carlo (top) and Continuum (bottom) number fractions as a function of axial and radial position. Jet nozzle is shown in black.

codes were initialized with the domain filled with the chamber gas and the jet was allowed to develop to steady state from the sonic orifice conditions.

Figure II.32 shows a comparison of the jet composition for the Monte Carlo and Continuum codes. The qualitative shape of the flow composition is similar between the two solutions, though quantitatively they diverge noticeably in that the continuum solution predicts a significantly higher fraction Argon along the edge of the jet as well as an earlier lower value along the jet axis.

The higher value along the jet edge is particularly prominent in the three-dimensional slice plots of Figures II.34-II.36. These plots were designed to parallel the composition plot for the jet experiments shown by Rothe[73, 71]. It appears that that the experimental data supports the Monte Carlo results for both the features noted as different in the continuum solution. This is not a particularly surprising result due to the low pressures and correspondingly high Knudsen numbers involved in the flow.

Figure II.33 shows a variation of a local Knudsen number defined by Equation II.89. Equation II.89 uses a multi-component mean free path as defined by Bird[10] and shown in Equation II.90 and a number density gradient length scale defined in Equation II.91. In Equation II.90, the total cross sections, σ_{Tpq}, relative velocities, c_{rpq}, and peculiar velocity, c'_p are defined in terms of local equilibrium temperature, number densities, and VHS model parameters for application to the continuum solution as described by Bird[10]. The number density length scale is equivalent to the density gradient length scale defined by Bird[10] when the number fraction and subsequent average molecular weight is constant. With most of the jet in flow Knudsen number in the range of 1e-2 to 1e-1 in the region of interest, Figure II.33 shows that this flow is certainly at the edge of what could be reasonably expected to be modeled with a continuum solution. In fact, the Monte Carlo solutions show significant non-equilibrium with an almost 20% higher axial temperature than overall temperature along the axis of the expansion at approximately 7cm downstream from the nozzle. Despite this effect and Knudsen numbers ranging between 1e0 and 1e1 throughout the rarefaction adjacent to the nozzle, the overall agreement of jet composition is quite good.

$$Kn = \lambda / D_n \tag{II.89}$$

$$\lambda = \sum_{p=1}^{s} X_p \lambda_p = \sum_{p=1}^{s} X_p \left(\sum_{q=1}^{s} (n_q \overline{\sigma_{Tpq} c_{rpq}} / \overline{c'_p} \right)^{-1} \tag{II.90}$$

$$D_n = \left|\left| \frac{1}{n} \frac{\partial n}{\partial x_i} \right|\right|^{-1} \tag{II.91}$$

The overshoot in Argon concentration in the continuum solution is believed to be related to fictitiously large diffusion velocities resulting from the deviation of the gas from local equilibrium. Work is underway to understand this phenomena and determine reasonable limits on the diffusion velocity[50], but application to the mixture free jet is left to future work.

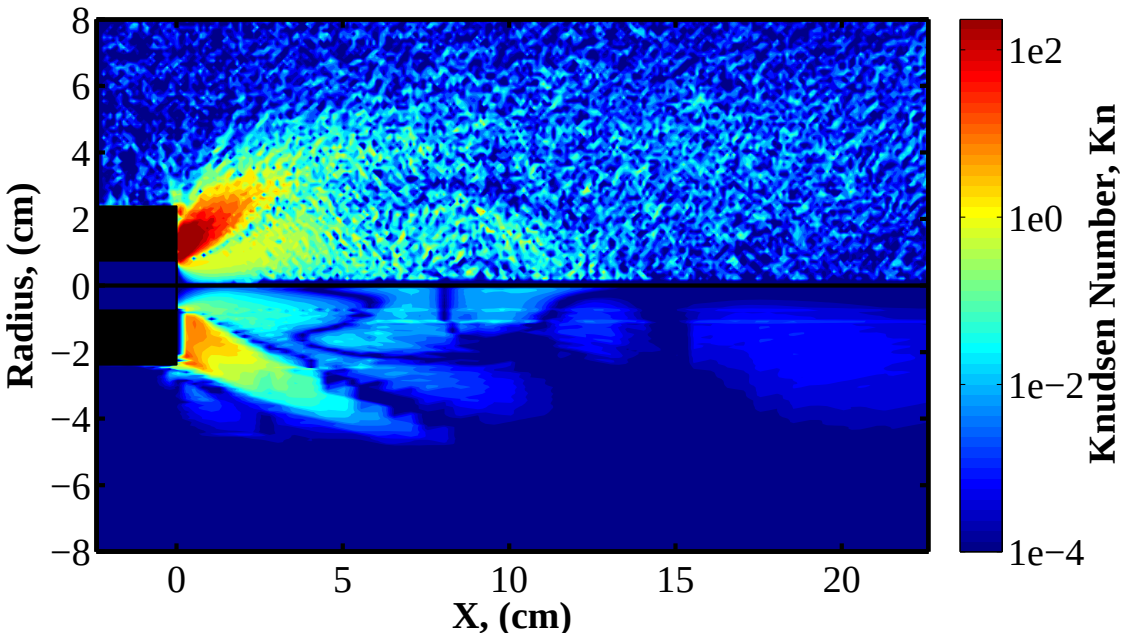

Figure II.33: Local Knudsen number based on number density gradient length scale for the Monte Carlo(top) and Continuum(bottom) solution.

Despite these differences, the Monte Carlo and continuum solutions agree with each other and differ with the experimental values in a few regions. First, neither simulation recovers to the original nozzle number fraction at the radial edge of the plots whereas the experimental values are found to recover to above the nozzle fraction at that radius. The difference in the Argon fraction along the radial edge of the plots from the experimental data is due to the boundary condition parallel to the axis being set to the stagnation fraction of 12% as opposed to the slightly Argon enriched value found in the experiment. This experimental Argon enrichment was due to different mass fluxes in the diffusion pumps for Helium and Argon.

However, the actual magnitude of this Argon enrichment was left unspecified. Though the fraction could be matched to the outer edge of the electron beam measurements, there is no guarantee that the value measured at the edge is equivalent to the actual chamber average. Investigation of the Argon enrichment required to produce optimal agreement with the experimental data is therfore left

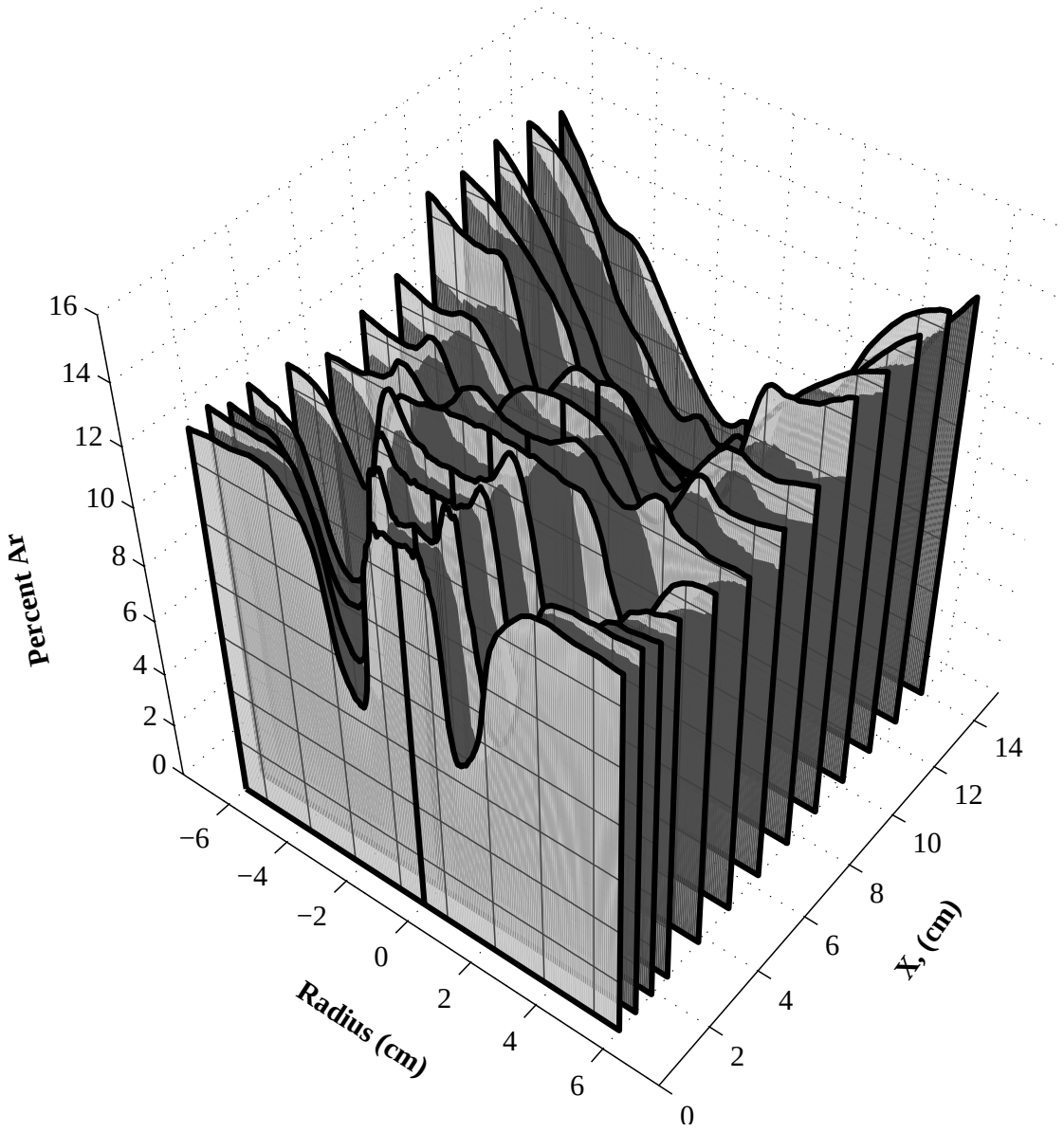

Figure II.34: Experimental number fraction profile for selected axial cross sections. Radial grid-lines represent the nozzle orifice edge and subsequent nozzle diameter multiples.

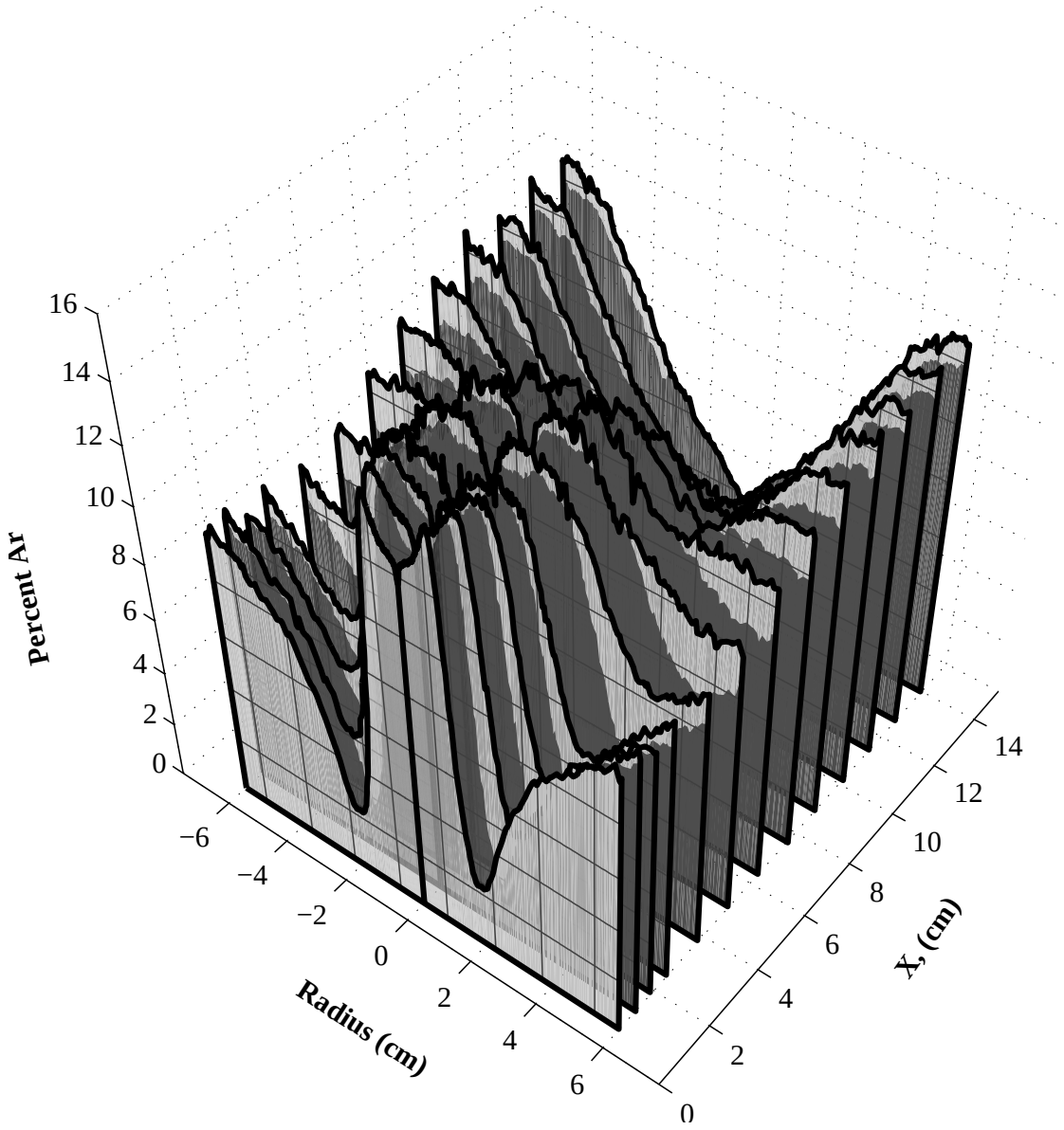

Figure II.35: Monte Carlo number fraction profile with the same selection of axial cross sections and radial grid-lines as the experimental data.

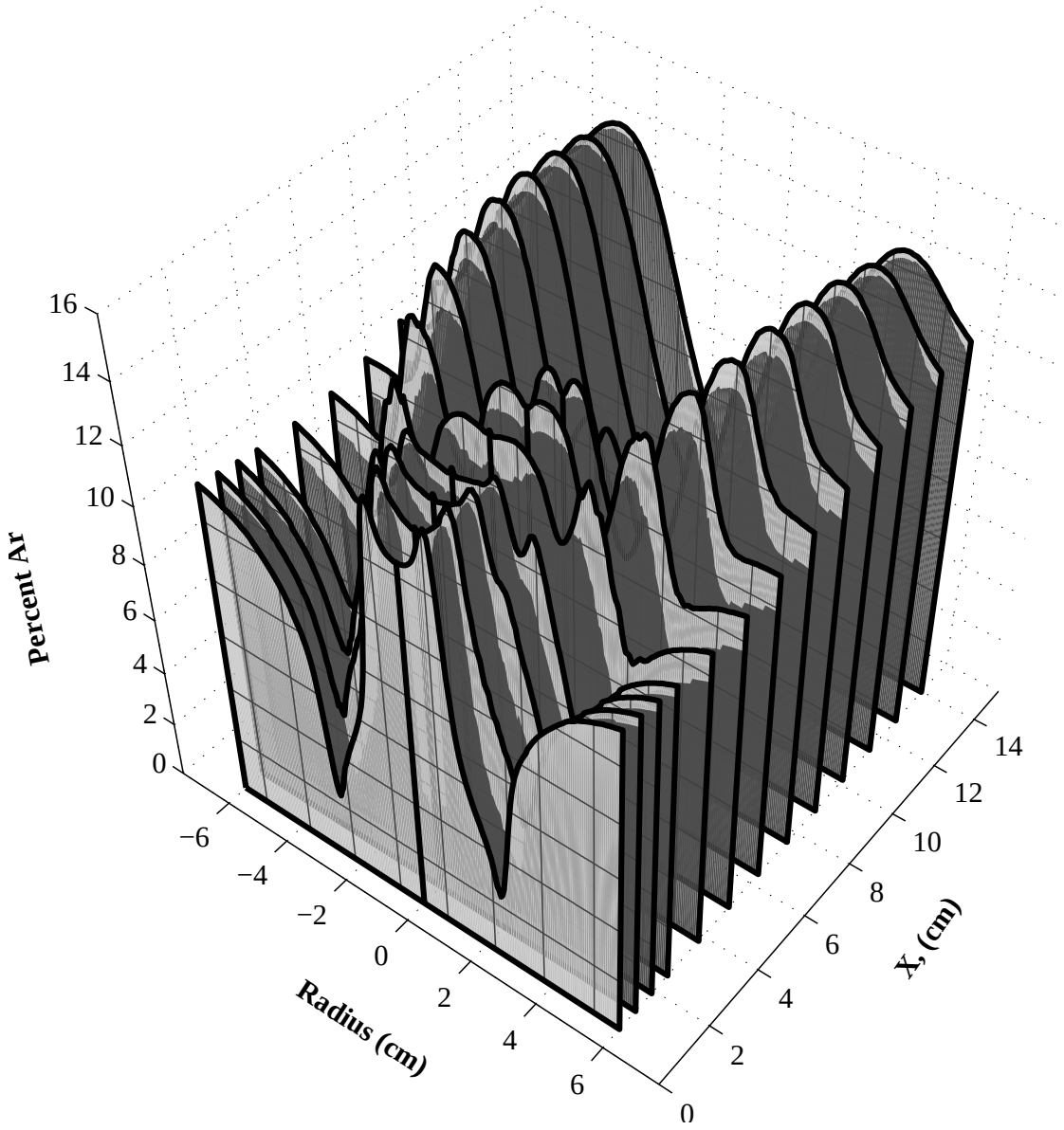

Figure II.36: Continuum number fraction profilewith the same selection of axial cross sections and radial grid-lines as the experimental data.

to future work.

Both simulations also show an Argon enrichment that peaks near the orifice radius that is absent in the original experimental plot. This disagreement was originally thought to be the result of the uniform sonic orifice boundary conditions applied to both simulations. However, upon reproducing the plot from the individual experimental number density profiles as seem in Figure II.34, the absence of this feature appears to be an artifact of processing the data. In the reprocessed data, the feature was only missing in the slice closest to the nozzle.

These peaks on the closest slice may also be a result of the numerical boundary conditions not accounting for the flow variations across the orifice. This is particularly true because the plate used to form the jet orifice is significantly thinner than the orifice diameter. Though the details of this nozzle geometry were only found in the full UTIAS report[71], the potential importance was not fully recognized until performing this first round of simulation.

The potential influence of nozzle geometry was then recognized in the work of Murphy and Miller that showed that the nozzle shape can significantly influence flow properties near the orifice[55] of a free-jet. In this work, Murphy and Miller both probed the a free-jet flow experimentally as well as performed numerical calculations along the jet axis. These effects were further investigated by Matsuo[52] with 2D-axisymmetric for air in several nozzle geometries. In particular, the sonic line actually moves from a bowed outward position into the inside of the nozzle as the geometry is changed from a sharp edge to capillary tube nozzle because of boundary layer effects. The uniform sonic conditions represent something between these extremes. Simulations with a more accurate nozzle configuration and particularly high resolution near the orifice exit will be necessary to determine if this difference is caused by the boundary conditions.

Finally, both simulations drop to approximately 2% Argon at approximately 1.5 jet diameters on the slice closest to the nozzle. This is significantly lower than Rothe's experimental measurements which reached a minimum Argon

fraction of only approximately 6%. The significantly stronger depletion of Argon adjacent to the jet may have a variety of causes.

Assuming the numerical predictions are accurate, the extremely low Argon number densities in this region would have resulted in photomultiplier currents of approximately 2e-9 Amps according to the calibration curves. That current is approximately equal to the dark current subtracted from the measurements in the EMI-9558A tube used to analyze the Argon densities. Though accounted for in the calibrations, the Argon error signal due to the helium at the density found in this region would also be nearly 1e-9 Amps according to the free jet error curves. All of these difficulties are further confounded by the the presence of a fluorescent halo that become more severe at low densities as well as reflections from the nozzle which required further unspecified calibrations. As noted in communication with Rothe[72], at the higher density near the nozzle the argon detector's resolution was approximately 3mm due to electron scattering. This would have the effect of smearing the solution near the nozzle which could potentially account for at approximately half of the disagreement. Finally, the numerical nozzle boundary conditions would also contribute to this difference. If the small argon enrichment at the jet edge was actually within the depression adjacent to the jet due to nozzle geometry, the same amount of argon would make a much larger difference as a percentage of the overall gas in the low density region adjacent to the jet.

The next obvious step is re-running the simulations with a more realistic nozzle geometry to determine the relative effect on the Argon depletion resulting from the uniform jet boundary condition. Should the differences persist beyond what may be accounted for due to the beam scattering, the complications as well as the agreement between the Monte Carlo and continuum solutions despite coming from significantly different physical models would suggest that the stronger Argon depletion may in fact be correct. This result would likely only be confirmed through revisiting the experiment with modern spectroscopic equipment and avoiding spectral lines that result in a fluorescent halo as suggested in the

conclusion Rothe's UTIAS report[71].

Though the continuum code has some significant differences unsupported by both the Monte Carlo and experimental data, it does capture many of the features of the flow that would be completely absent in a code that included only Fickian diffusion. It is not unexpected that the Monte Carlo code appears to outperforms the continuum code in this jet regime as significant non-equilibrium suggests limited applicability of the continuum approach. However, the similarity between the simulation results suggests that a handoff from statistical to continuum approaches is reasonable in regimes only moderately closer to equilibrium. This is important in particular when increasing spatial scales by a factor of 20-40 at similar number densities as is necessary for the fusion chamber design studies. At these scales, the Monte Carlo approach is not currently tenable for rapidly investigating the power-plant design space. However, working in this transition regime provides insights into the range of applicability for the continuum formulation due to the availability of both experimental data and Monte Carlo solutions.

Chapter 2, in part, is a reprint of material as it appears in Proceedings of the 27th International Symposium on Rarefied Gas Dynamics, July 2010. Martin, R.; Najmabadi, F., 2010. The dissertation author was the primary investigator and author of this paper.

Chapter 2, in part, contains material in preparation for submission for publication. Martin, R.; Najmabadi, F., Journal of Computational Physics, 2011. The dissertation author was the primary investigator and author of this material.

Chapter 2, in part, contains material in preparation for submission for publication. Martin, R.; Najmabadi, F., Physics of Fluids, 2011. The dissertation author was the primary investigator and author of this material.

Chapter III

SPARTAN IFE Chamber Gas Simulations

III.A Xenon Chamber Gas Evolution

III.A.1 BUCKY Solutions and Initial Conditions

The initial conditions used in the Spartan runs presented are the result of BUCKY simulations for the 154 MJ NRL reference target design [NRL target]. The chamber gas is xenon at number densities of $1.65e21/m^3$ (high density) and $1e20/m^3$ (low density). These correspond to initial pressures of 50 and 3 $mtorr$ at standard temperature respectively. The wall temperature is fixed at 973.16 K throughout the simulations. Figures III.1 and III.2 show the SPARTAN initial conditions from BUCKY burn simulations. Included are the density, velocity, and pressure profiles for the high and low density xenon cases. Because the shock from the burn reaches the wall later in the higher density case, the starting time for that case is $0.5ms$ instead of $0.1ms$ for the low density case. When BUCKY is run longer before switching to SPARTAN, the radiation intensity and degree of ionization decrease making the models employed by SPARTAN more applicable. However, once the spherical shock reaches the chamber wall, the BUCKY solution is no longer valid.

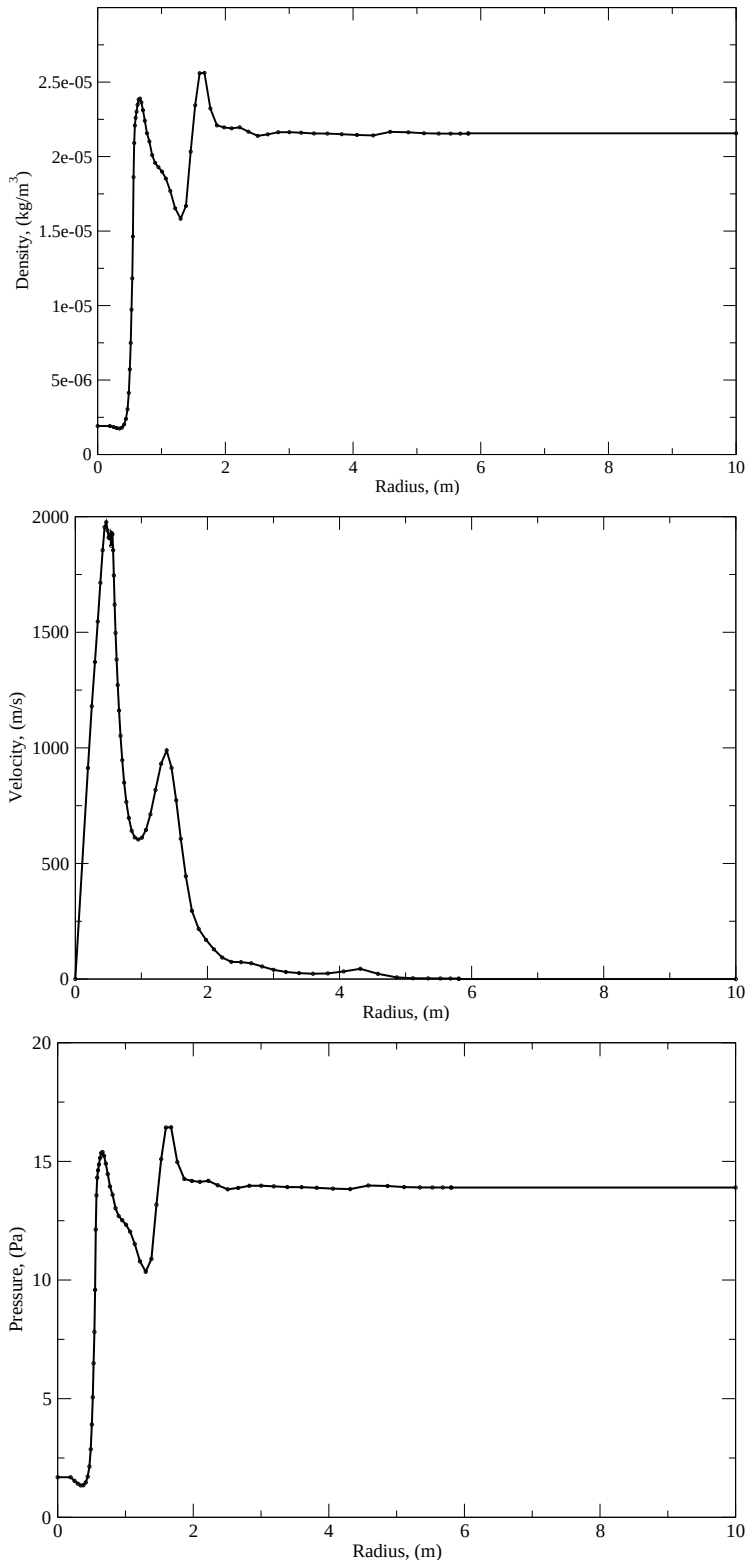

Figure III.1: BUCKY 154 MJ NRL target burn solution for SPARTAN xenon initial conditions at low density ($n = 1e20/m^3$) and $t = 0.1ms$.

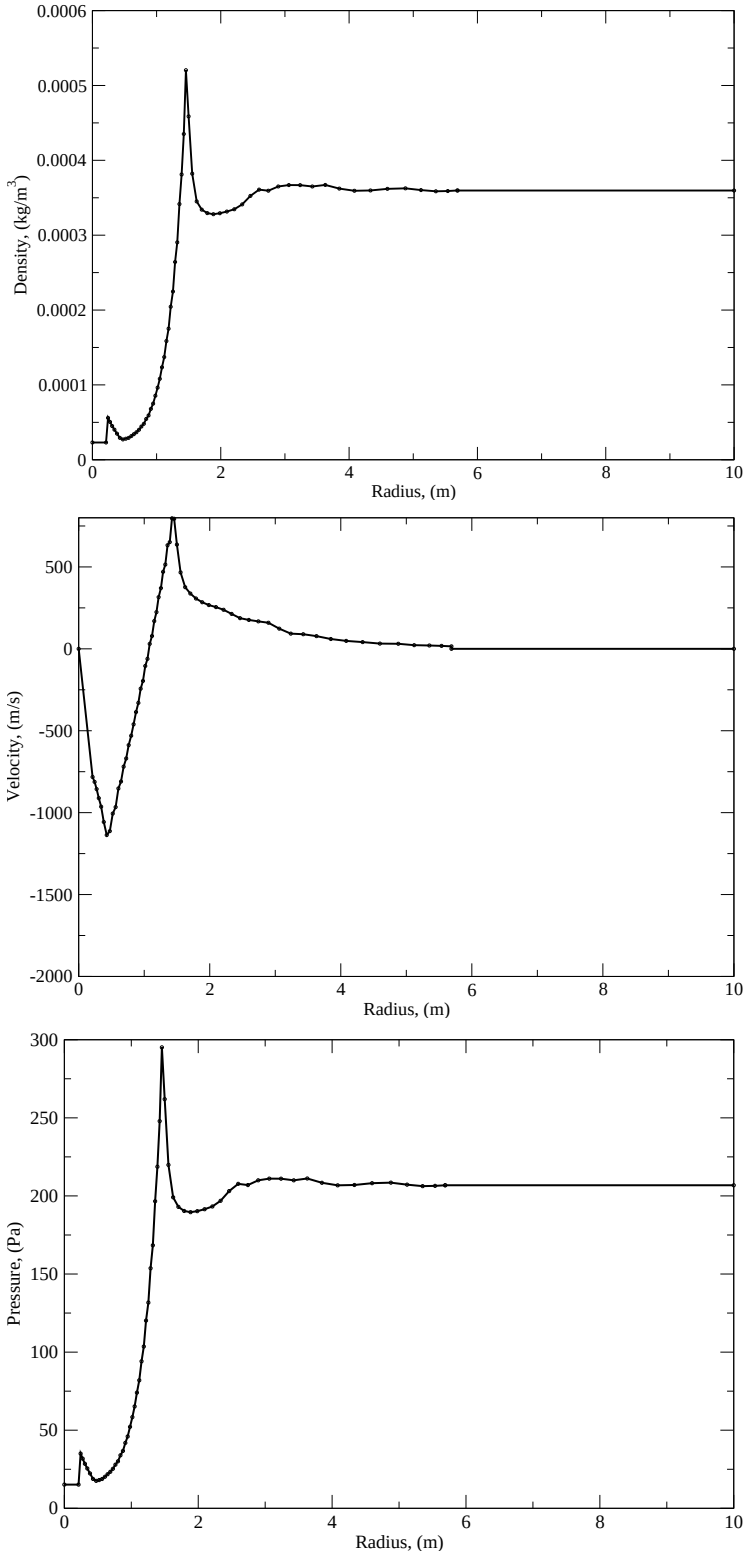

Figure III.2: BUCKY 154 MJ NRL target burn solution for SPARTAN xenon initial conditions at high density of ($n = 1.65e21/m^3$) and $t = 0.5ms$.

III.A.2 Chamber Geometry and Boundary Conditions

In this work, Spartan is run only in axii-symmetric mode. The initial conditions from BUCKY assume 1D spherical symmetry. Projecting the intrinsically spherical BUCKY solution onto a flat 2D cartesian grid misrepresent the expansion as from an infinite line instead of a point . This generates incorrect radial fluxes from the spherical velocities.

Four 2D-axiisymetric chamber geometries were considered. They include a spherical case, a 1/60th spherical wedge, the 1/60th spherical wedge with an additional spherical segment beam-line with a 1m radius at the chamber wall, and a cylindrical chamber. These geometries are depicted in Figure III.3.

The spherical design provides uniform wall damage load for a minimal volume. The wedge with beam-line case is selected to investigate the effect of the addition of 60 beams to the spherical chamber. This configuration has the correct beam-line shape as opposed to discs and cones resulting from beam-lines that do not include the axis. The configuration also has correct volume to surface area ratios. However, the configuration imposes an approximation at the edge where domains from neighboring beam-lines would either overlap or leave gaps in a real configuration. This approximation is likely no worse than the original axii-symmetric approximation. Figure III.4 shows the region of over- and under-represented surface for the 1/60 solid angle if beamlines were centered at the 60 vertices of a truncated icosahedron.

The wedge configuration suppresses low order modes in the ϕ direction. This is why the wedge configuration without beam-line is included to ensure that the sphere and wedge produce nearly identical results when the symmetry is not broken by a beam-line.

Finally, the cylinder case is included because simpler physical construction makes it an attractive choice. However, the cylinder radius must equal the sphere radius to prevent wall damage for the same target and gas backfill which results in a 50% larger volume and vacuum pumping load should the recirculating

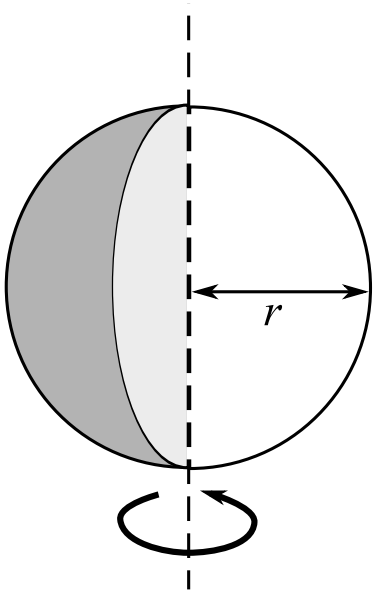

(a) Spherical

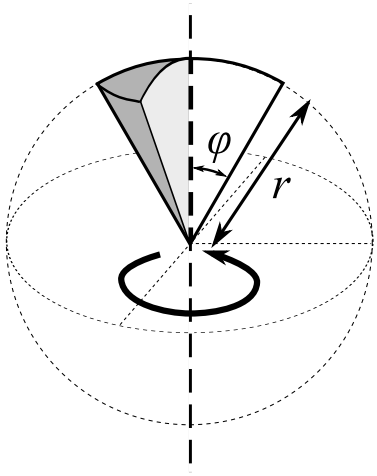

(b) Wedge

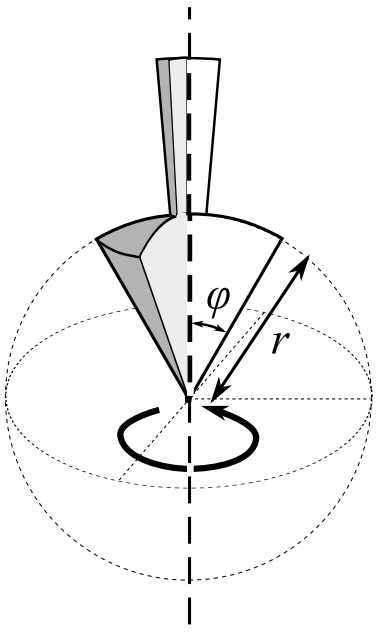

(c) Wedge+Beamline

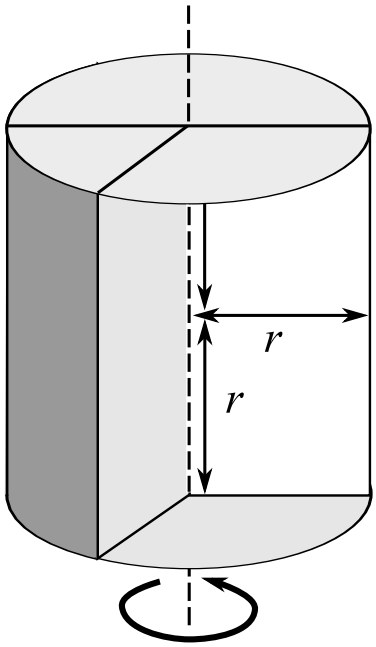

(d) Cylindrical

Figure III.3: Chamber simulation numerical domains. All domains are the 2D axii-symmetric cross sections of the volumes represented in gray. Domain boundaries are embedded in cartesian mesh.

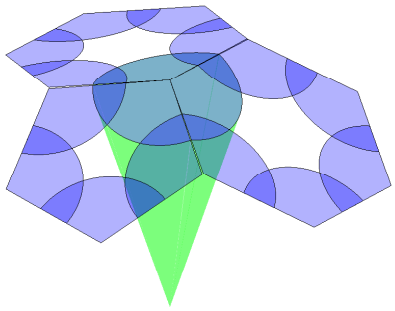

Figure III.4: Surface area of truncated icosahedron over- and under- represented by axii-symmetric region of 1/60 solid angle

power required to run the vacuum system be shown to make a significant impact on overall system efficiency.

III.A.3 Spherical Chamber Temperature Evolution

Figures III.5 and III.6 show the evolution of the chamber temperature from the BUCKY input through $t = 100ms$ for the high and low density xenon cases. Included in these figures is also the energy loss mechanism resulting in the corresponding temperature drop. The red regions show the temperature drop due to radiative cooling while the blue region shows the energy conducted to the walls of the chamber. A green region that represents the temperature in the kinetic energy of the gas is also included but not visible because the kinetic energy for these xenon cases are much smaller than the thermal energy in the system. The importance of this region will be seen in Chapter III.B when deuterium and helium chamber gas is also studied because much more of the fast ions from the burn couple their momentum to these gases.

Both high and low density xenon gases cool approximately $3500K$ through radiative processes though the low density case is initially approximately $1100K$ warmer. The majority of this radiative cooling occurs within the first few milliseconds of the simulations. This stalling of radiative cooling happens because the average charge state, $\bar{Z}$, approaches zero as the gas approaches these temper-

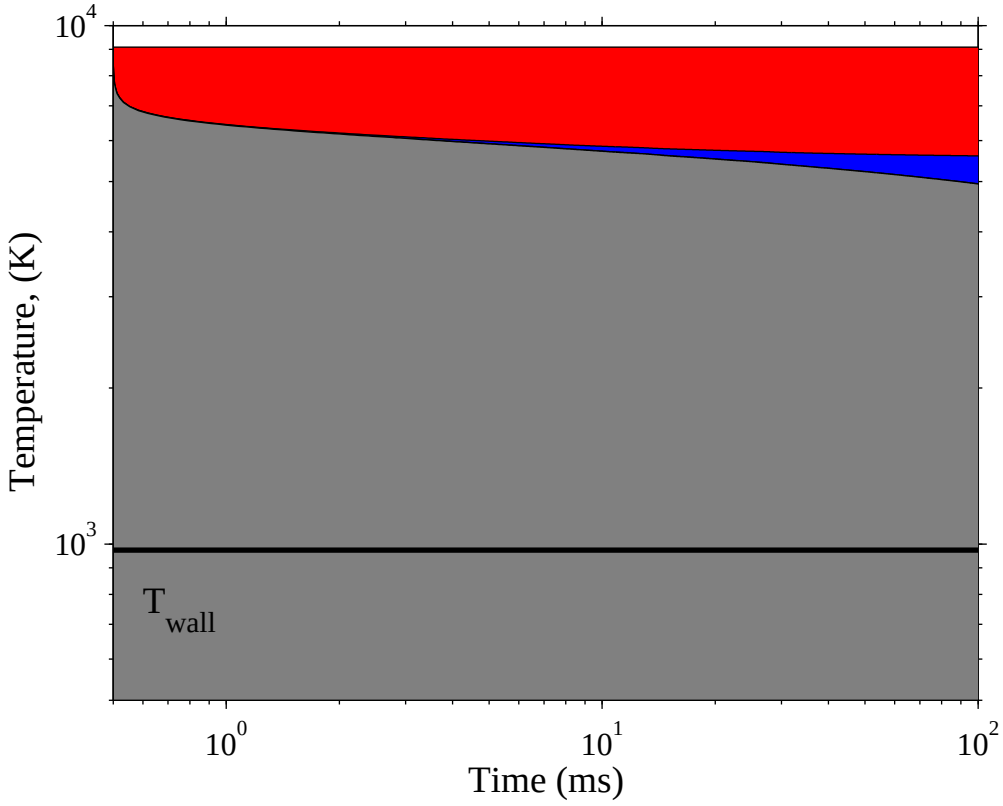

Figure III.5: Temperature evolution by energy loss mechanism for the high density ($n = 1.65e21/m^3$) xenon case. The red region corresponds to energy lost through radiative cooling, blue through conduction to the chamber walls, and gray the remaining thermal energy in the chamber. Though included as a green region which is not visible, the kinetic energy within the chamber is negligible compared to the thermal energy.

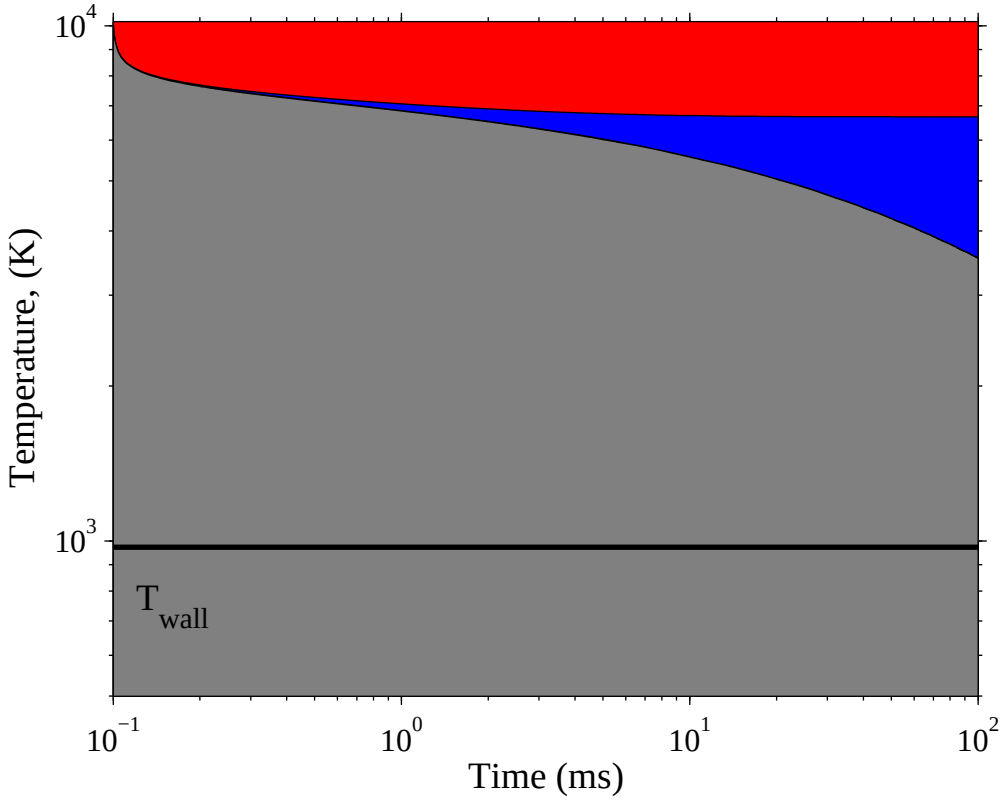

Figure III.6: Temperature evolution by energy loss mechanism for the low density ($n = 1e20/m^3$) xenon case. The red region corresponds to energy lost through radiative cooling, blue through conduction to the chamber walls, and gray the remaining thermal energy in the chamber. Though included as a green region which is not visible, the kinetic energy within the chamber is negligible compared to the thermal energy.

atures. This can be seen as the rapid drop in cooling rate with decreased temperature in Figure II.6. This also implies that this process is completely dependent on the model for the cooling as $\bar{Z}$ approaches zero. Experimental verification of the behavior for the transition from cold plasma to neutral gas would significantly improve confidence in IFE chamber gas temperature estimates.

It is also interesting to note that the low density case cools through conduction to the walls much more rapidly than the high density case. The low density case drops by $3120K$ from the stalled radiation temperature whereas the high density case drops by $656K$. To understand this difference, we refer to the simplified phenomenological description of transport processes given in the beginning of Reference [84]. Through simple arguments relating to the energy transported across a region of one mean free path thickness, the relation for the conductivity, $K = \beta_k \rho \bar{C} \lambda c_v$ is derived. With this combined with a similar analysis that the mean free path is approximately proportional to inverse number density, n^{-1}, it becomes obvious that the conductivity is approximately independent of number density via $\rho\lambda \approx nm/n$. The heat flux, $q = -KdT/dx$, is then also independent of density. However, the total energy in a volume of gas is proportional to the density which means that the lower density gas conductively cools much more rapidly for the same temperature gradient. The longer mean free paths allow each particle to travel further between collisions increasing the rate at which each gas particle collides with the wall and causing the temperature gradients to decrease more rapidly.

III.A.4 Convergence of Heat Fluxes with Grid Refinement

One of the motivations for re-examining the boundary conditions in Section II.B.2 was the strange behavior of the integrated heat flux to the walls demonstrated in Reference [23]. One would expect the highest heat flux at the start of the simulation because the initial conditions are originally much hotter than the wall temperature. As the gas near the walls cool, this flux would decrease. The

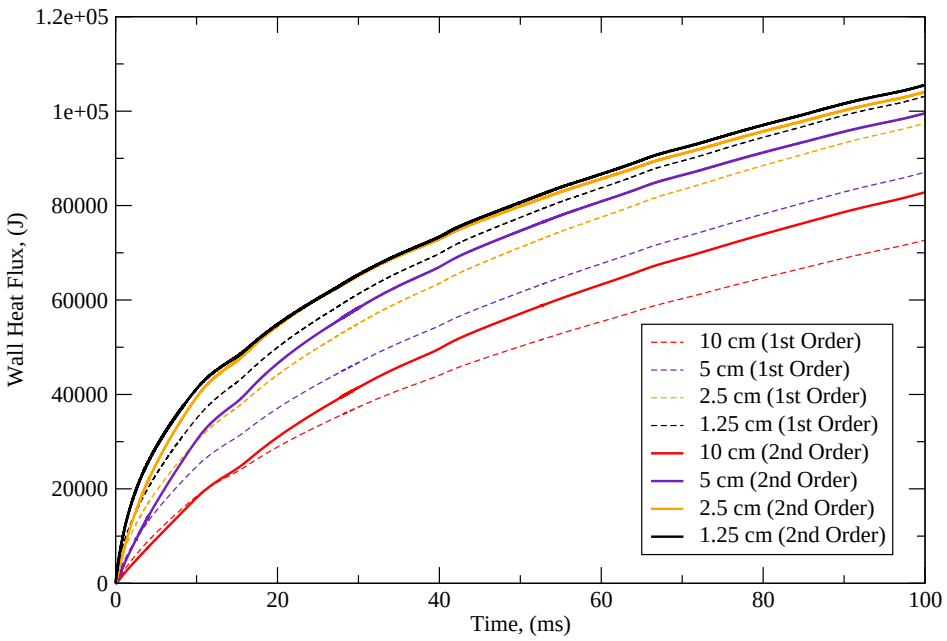

Figure III.7: Convergence of wall total heat flux to the chamber walls with grid refinement for first and second order boundary conditions for the high density xenon simulations.

results for the original version of SPARTAN shown in Reference [23] initially have the opposite behavior. This also results in a decrease of integrated heat flux with grid refinement rather than the opposite.

Figure III.7 shows the convergence of the new integrated wall boundary heat fluxes for the high density xenon case. Included is the model described in Section II.B.2 as well as the first order version which simply only uses the 'near' and 'wall' points of the stencil. The two approaches appear to converge towards a similar limit, but the 2^{nd} order method clearly converges more rapidly. Table III.1 shows the convergence rates at $100ms$ using Equation III.1 from in Reference [23].

With four grid resolutions available, a better approximation of the $10cm \rightarrow 5cm$ grid convergence results from comparing the magnitude of the error relative

Table III.1: Heat flux convergence rates for first and second order boundary conditions at $t = 100ms$ for high density xenon simulations

Grid	1^{st} Order $p_*(100ms)$	2^{nd} Order $p_*(100ms)$
10 cm $\rightarrow$ 5 cm	1.26	2.23
5 cm $\rightarrow$ 2.5 cm	1.49	2.02

to the best available solution on the $1.25cm$ grid instead of the $2.5cm$ grid solution. These results can't be compared directly from those of Reference [23] but are likely closer to the true convergence rates relative to the exact solution. Applying this modified formula yields convergence rates of 0.92 and 1.92 for the first and second order solutions respectively.

$$p_*(t) \approx log_2 \left(\frac{|S_*^{\Delta/4}(t) - S_*^{\Delta}(t)|}{|S_*^{\Delta/4}(t) - S_*^{\Delta/2}(t)|} \right) \tag{III.1}$$

Though the integrated heat flux requires $2.5cm$ cells for 95%+ converged heat fluxes, it is important to note that at $7e5J$ total energy, even the difference between the $10cm$ and $1.25cm$ solution only makes an approximately 3% difference in the final chamber temperature. However, in other chamber configurations where the wall heat flux makes a larger contribution to the final temperature, knowledge of the convergence behavior will be more critical.

III.A.5 Kinetic Spectrum Convergence

One way to ensure that the grid resolution is sufficient to resolve the kinetic energy within the chamber is to examine the kinetic energy spectrum of the solution. To do this, the 2D-FFT of the velocity field of the upper hemi-sphere of the spherical domain solutions is performed. The energy for each wavenumber vector is then calculated using Equation III.2.

$$E = \frac{1}{2} \left[\langle \tilde{u}^2 \rangle + \langle \tilde{v}^2 \rangle \right] \tag{III.2}$$

This 2D-FFT is then converted into a 1D spectrum by summing the

magnitudes at each vector wavenumber, (k_x, k_y), into bins of wavenumber width 1 based on the magnitude of the vector wavenumber. Wavenumber magnitudes larger than the maximum of the individual wavenumber vectors are dropped because the averaging process would only apply for part of the angle in wavenumber space. This summed magnitude is then divided by the number of wavenumber vectors that fall into each bin to calculate the average kinetic energy magnitude versus wavenumber vector magnitude.

Figure III.8 shows one such spectrum for the high density xenon case in a 10m spherical chamber. The line colors represent the spectrum with grid refinement from $10x10cm$ cells down to $2.5x2.5cm$ cells. The plots show only up to 2/3 the maximum wavenumber allowed on the grid because aliasing adds the remainder of the kinetic energy into these modes. We define this maximum dealiased wavenumber as k_{max}^{DA}. The 'Fit' curve is calculated from the slope of the spectrum from the point at $\frac{1}{2}k_{max}^{DA}$ to k_{max}^{DA}.

From this plot, we can see that the fraction of unrepresented kinetic energy falls under the dashed line from k_{max}^{DA} to infinite wavenumber. This allows an estimate of the represented kinetic energy to be performed of the form shown in Equation III.3 where $-s$ is the slope of the fit to the end of the spectrum. Using the finite representation of the spectrum, this equation is approximated by Equation III.4. Table III.2 gives the slopes and corresponding fractions of represented kinetic energy for the grid resolutions shown in Figure III.8.

$$f^{KE} = \frac{\int_0^{k_{max}^{DA}} E(k)dk}{\int_0^{k_{max}^{DA}} E(k)dk + \int_{k_{max}^{DA}}^{\infty} E(k_{max}^{DA})\left[k/k_{max}^{DA}\right]^{-s} dk} \tag{III.3}$$

$$f^{KE} \approx \frac{\sum_{i=0}^{k_{max}^{DA}} E(k_i)\Delta k}{\sum_{i=0}^{k_{max}^{DA}} E(k_i)\Delta k + \frac{E(k_{max}^{DA})}{(s-1)}k_{max}^{DA}} \tag{III.4}$$

It is also important to note that the slope of the energy spectra is supported by the work of Clercx and van Heijst in Reference [20]. This work describes the decay of 2D turbulence in a bounded domain and shows that the spectrum

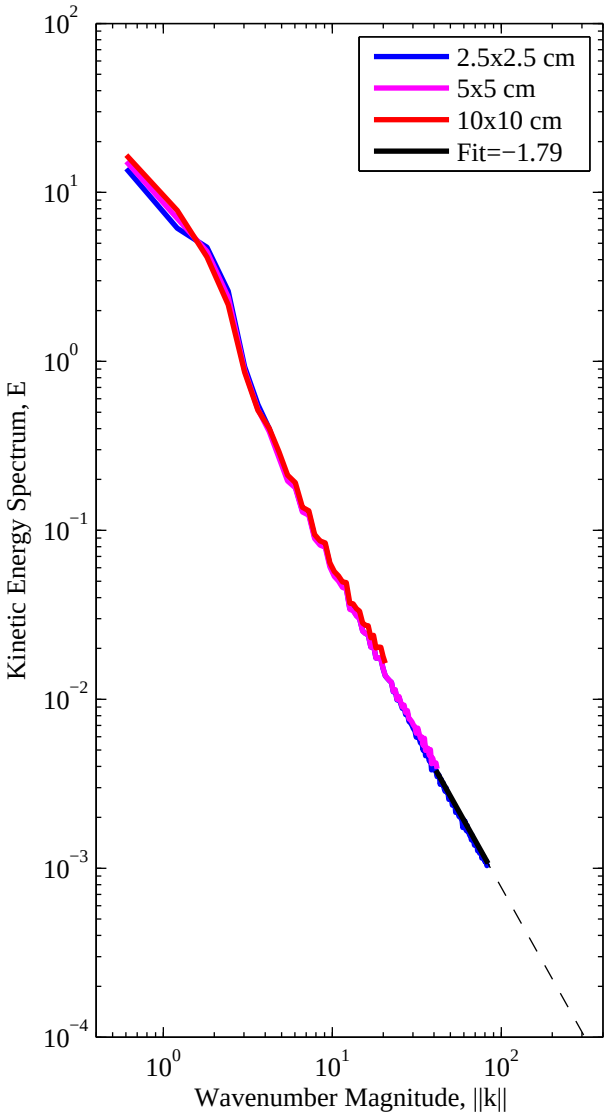

Figure III.8: Kinetic energy spectrum magnitude versus wavenumber magnitude for high density Xe ($n = 1.65e21/m^3$) at 100 ms.

Table III.2: Fraction of represented kinetic energy with grid refinement for high density xenon case at $t = 100ms$.

Grid	Slope, -s	f^{KE}
10x10 cm	-1.81	0.9887
5x5 cm	-1.86	0.9947
2.5x2.5 cm	-1.79	0.9967

generally follows a power law between the $k^{-5/3}$ inertial range scaling and the k^{-3} direct enstrophy cascade scaling. On lines near the walls, they find slopes between -2.5 and -1.8 with at long times with Reynolds number increasing from 5000 to 20000. At the center of their domain, the values ranged from -2.5 to -2.2. However, it is unclear what characteristic velocity was used to calculated the Reynolds number, but the selection was likely related to the initially injected vortex strength. In the case of the IFE chamber, there is no initial vorticity and the wall tangent velocities are initially zero making direct comparison not applicable.

The fractions of kinetic energy represented in the simulations is quite high, but this is due in part because the grid resolutions were selected primarily to resolve the wall heat fluxes. If the energy was not resolved within these cells, the situation would also likely be worse than simply under-resolved turbulence. In these simulations, the cell size is on the order of the mean free path of the gas. If significant sub-grid scale turbulence existed, it would represent a non-equilibrium velocity field rather than just turbulence. Sub-mean free path velocity fluctuations would cast doubt on the definition of velocity and therefore even the continuum approximation.

III.A.6 Comparison of Cylindrical and Spherical Chambers

The average cooling of cylindrical chambers is very similar to that of the spherical chambers. In fact, as seen in Figures III.9 and III.10, the temperature evolution is nearly indistinguishable. The cylindrical chamber results are $18.5K$ cooler for the high density case and $0.1K$ warmer for the low density case. These

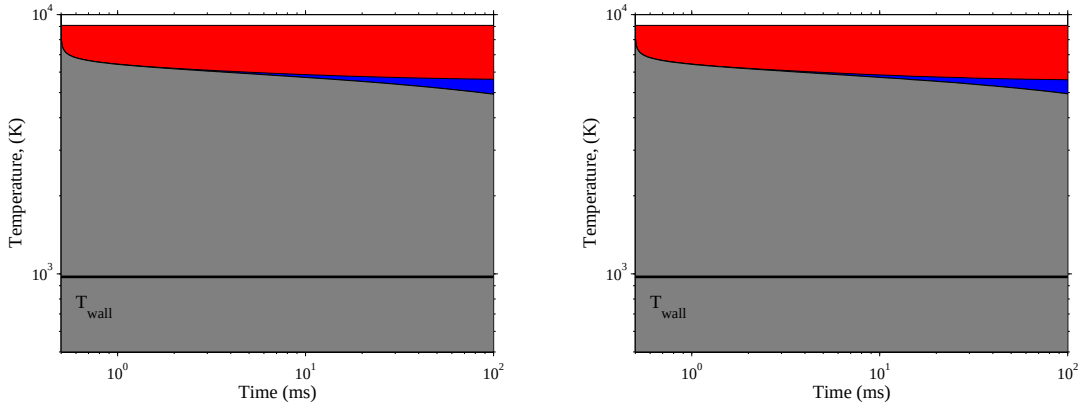

(a) Cylindrical Chamber

(b) Spherical Chamber

Figure III.9: Comparison of temperature evolution by energy loss mechanism for the high density ($n = 1.65e21/m^3$) xenon case for cylindrical and spherical chambers. The red region corresponds to energy lost through radiative cooling, blue through conduction to the chamber walls, and gray the remaining thermal energy in the chamber. Though included as a green region which is not visible, the kinetic energy within the chamber is negligible compared to the thermal energy.

results match as the result of the cylindrical and spherical chamber geometries having identical surface area to volume ratios of $3/r$. These ratios are the same only when the diameter and height of the cylinder are equal to the sphere's diameter. Though the two flows have significantly different velocity fields resulting from the geometry change, the temperature of the kinetic energy as well as the mixing of the thermal boundary layer due to the velocity field is negligible for both cases.

It is also interesting to compare the temperature of the gas near the midplane of the cylindrical solution to the analytical solution of the transient heat equation in an infinite cylindrical domain. Reference [63], gives a thorough description of the analytical problem. The solution is of the form of Equation III.5. In this equation k is the thermal diffusivity, J_n are the Bessel functions of the first kind, and α_n is the n^{th} zero of J_0. The value α_n is related to the eigenvalues and radius such that $\alpha_n = \lambda_n R$. To compare the results of the SPARTAN simulation of a cylindrical chamber, MATLAB was used to evaluate this Equation III.5 for

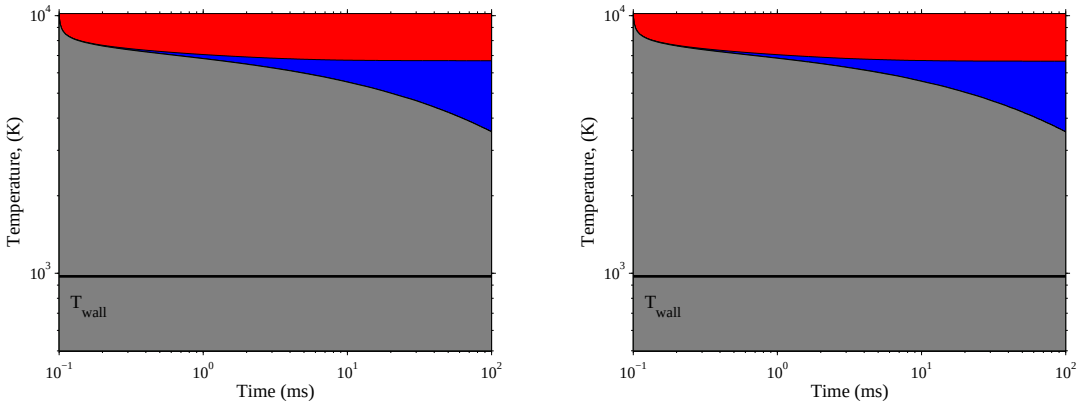

(a) Cylindrical Chamber

(b) Spherical Chamber

Figure III.10: Comparison of temperature evolution by energy loss mechanism for the low density ($n = 1e20/m^3$) xenon case for cylindrical and spherical chambers. The red region corresponds to energy lost through radiative cooling, blue through conduction to the chamber walls, and gray the remaining thermal energy in the chamber. Though included as a green region which is not visible, the kinetic energy within the chamber is negligible compared to the thermal energy.

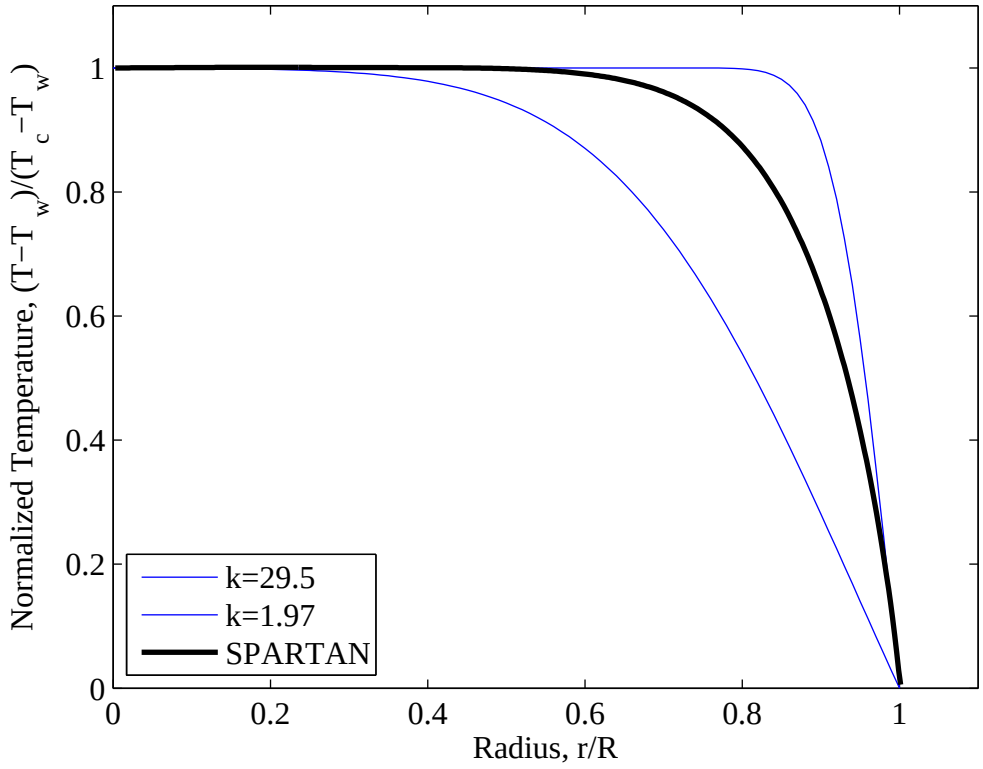

Figure III.11: SPARTAN cylindrical temperature profile relative to the analytical solution to the transient heat equation for the equivalent maximum and minimum thermal diffusivities within the SPARTAN solution

the first 1000 modes.

For the SPARTAN results, the temperature was averaged vertically from $2.8m$ to $4m$ from the center of the chamber to remove the influence of local variations but remain far from the boundaries. To compare the spartan results, we relate the thermal diffusivity to thermal conductivity using the equation $k = K/(\rho C_v)$.

$$T(r,t) = T_0 \sum_{n=1}^{\infty} \frac{2}{\alpha_n J_1(\alpha_n)} J_0(\lambda_n) e^{-\lambda_n^2 kt} \tag{III.5}$$

Figure III.11 compares the SPARTAN simulation temperature profile to exact analytical solutions with the thermal diffusivity of the gas at the average state in the center of the chamber and the diffusivity of the gas at the wall state.

The wall state curve is tangent to the SPARTAN solution at the wall, but the SPARTAN solution falls off more rapidly as the diffusivity increases. The curve of the temperature plot for the high chamber center diffusivity curve compares well to that of SPARTAN near the normalized maximum temperature. However, the curve is displaced inward from the SPARTAN solution because the near wall thermal diffusivity is much lower. These two analytical curves show that the temperature profile from SPARTAN using variable density and conductivity is a reasonable solution within the boundaries of analytical solutions for constant thermal diffusivity.

III.A.7 Validity of Wedge Domain Approximation

As mentioned in Section III.A.2, the purpose of the wedge domain simulations was to ensure that the wedge geometry produced the same results as the spherical chamber results. This ensures that differences in the wedge+beamline domain results from the effect of the beamline rather than the wedge approximation.

The wedge simulations were performed on a rectangular $1.25x2.5cm$ grid instead of the $2.5x2.5cm$ grid on which the spherical and cylindrical simulations were performed. This grid was selected to ensure a maximum of a $2.5cm$ grid size in the wall normal direction while better resolving the tip of the wedge which cannot be fully represented by the embedded boundary method due to the steep slope. The $2.5cm$ choice relates back to the agreement between the $2.5cm$ and 1.25 wall heat fluxes for second order boundaries in Section III.A.4. The limitation of the embedded boundary method in thin domains is discussed in detail in Reference [60].

Figures III.12 and III.13 compare the temperature evolution for the 1/60 wedge and spherical chamber simulations. Again the results are nearly indistinguishable. This confirms the validity of using the wedge approximation allowing the beamline effects to be investigates with the axii-symmetric simulations.

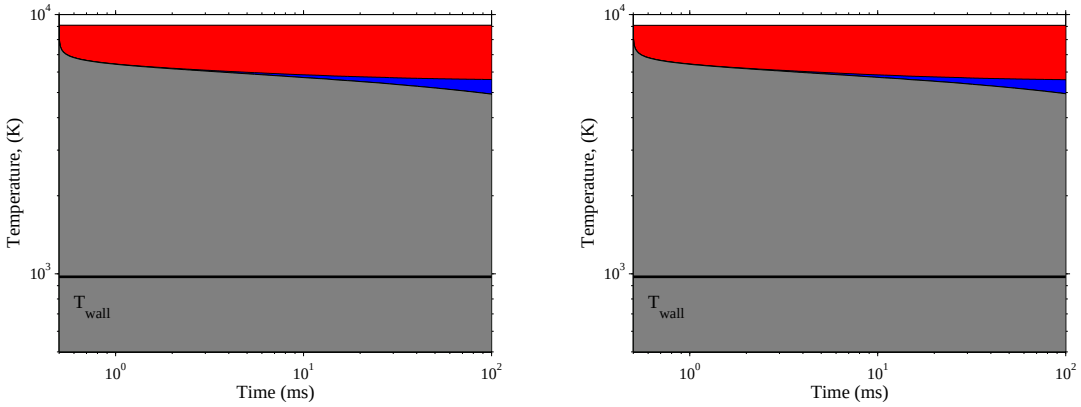

(a) 1/60 Wedge Chamber

(b) Spherical Chamber

Figure III.12: Comparison of temperature evolution by energy loss mechanism for the high density ($n = 1.65e21/m^3$) xenon case for 1/60 wedge and spherical chambers. The red region corresponds to energy lost through radiative cooling, blue through conduction to the chamber walls, and gray the remaining thermal energy in the chamber. Though included as a green region which is not visible, the kinetic energy within the chamber is negligible compared to the thermal energy.

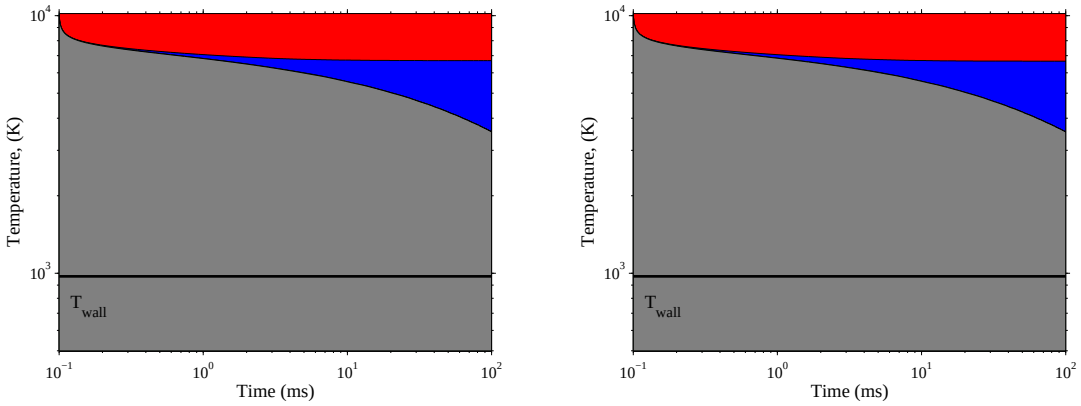

(a) 1/60 Wedge Chamber

(b) Spherical Chamber

Figure III.13: Comparison of temperature evolution by energy loss mechanism for the low density ($n = 1e20/m^3$) xenon case for 1/60 wedge and spherical chambers. The red region corresponds to energy lost through radiative cooling, blue through conduction to the chamber walls, and gray the remaining thermal energy in the chamber. Though included as a green region which is not visible, the kinetic energy within the chamber is negligible compared to the thermal energy.

The agreement of final temperatures between the spherical and wedge solutions was again quite good. The high density xenon case was $18.8K$ cooler and the low density xenon case was $4.3K$ warmer than the spherical results.

III.A.8 Influence of Beamlines

With the confirmation of the wedge domain approximation, the effect of beamlines on chamber state evolution can be determined. Comparing final chamber temperatures, the high density chamber was on average $833K$ cooler and the low density chamber was $1155K$ cooler. Figures III.14 and III.15 compare the temperature evolution for the 1/60 wedge+beamline and spherical chambers.

From Figures III.14 and III.15, it is clear that the conductive cooling is dramatically increased with the addition of beamlines. For the low density case, the conductive cooling went from $3120K$ to $4499K$, and the high density case went from only $656K$ to $1710K$. This change was the direct result of the increased wall surface area to volume ratio due to the beamline. A $1m$ wide beamline at the edge of a $10m$ radius chamber has a solid angle of approximately 1/400. With a length of an additional R outside the chamber this adds only an additional 5% to the volume of the chamber. However, the surface area along the length of the beamline adds 450% to the surface area of the chamber. This results in dramatically more heat conducted through the walls.

Figures III.16 and III.17 show the chamber states for the high an low density xenon cases at $t = 100ms$. Each of the figures is composed of plots of normalized temperature, normalized density, and Mach number. The temperature is normalized by the wall temperature such that zero on the log scale is a temperature equal to the wall temperature. For the density normalization, the average chamber densities of $1.65e21m_{xe}kg/m^3$ and $1e20m_{xe}kg/m^3$ for the high and low density cases. The Mach number plots also include vectors of length proportional to the Mach number in the direction of the velocity field to indicate the flow directions.

Both the high and low density chambers have strong flows into the beam-

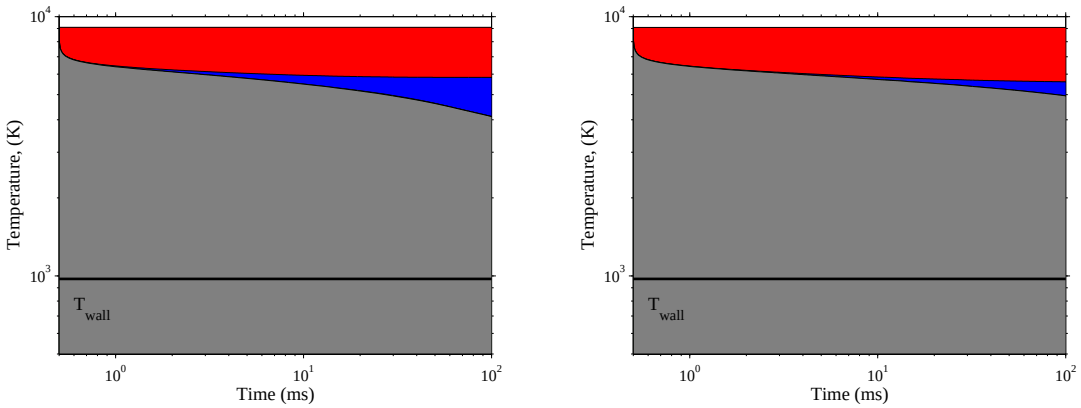

(a) 1/60 Wedge+Beamline Chamber

(b) Spherical Chamber

Figure III.14: Comparison of temperature evolution by energy loss mechanism for the high density ($n = 1.65e21/m^3$) xenon case for 1/60 wedge+beamline and spherical chambers. The red region corresponds to energy lost through radiative cooling, blue through conduction to the chamber walls, and gray the remaining thermal energy in the chamber. Though included as a green region which is not visible, the kinetic energy within the chamber is negligible compared to the thermal energy.

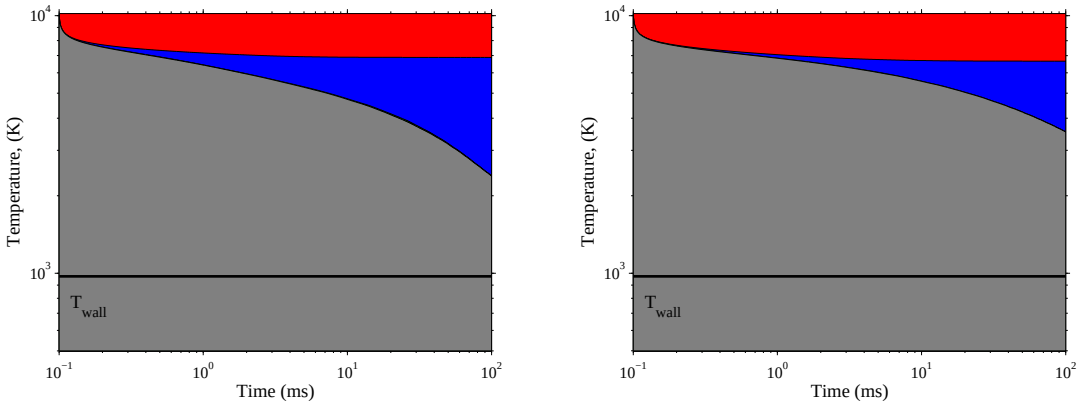

(a) 1/60 Wedge+Beamline Chamber

(b) Spherical Chamber

Figure III.15: Comparison of temperature evolution by energy loss mechanism for the low density ($n = 1e20/m^3$) xenon case for 1/60 wedge+beamline and spherical chambers. The red region corresponds to energy lost through radiative cooling, blue through conduction to the chamber walls, and gray the remaining thermal energy in the chamber. Though included as a green region which is not visible, the kinetic energy within the chamber is negligible compared to the thermal energy.

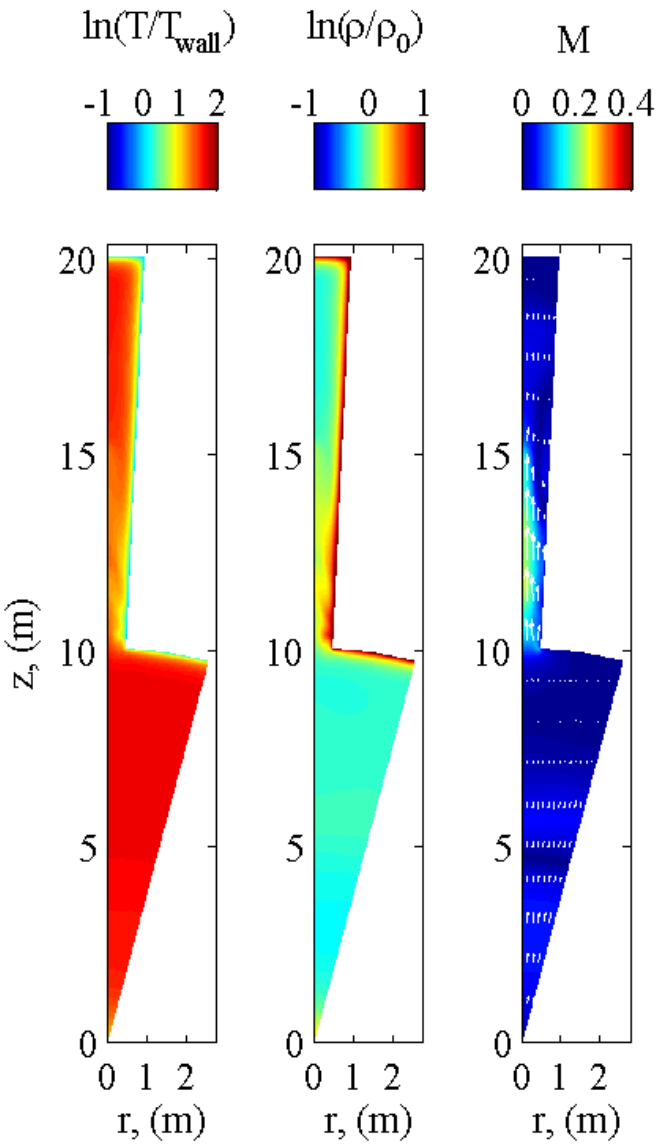

Figure III.16: High density xenon chamber states at $t = 100ms$. Temperature field is normalized to the wall temperature and density field is normalized to the average chamber gas density. The third plot is the Mach number with vectors of Mach number magnitude in direction of the velocity field.

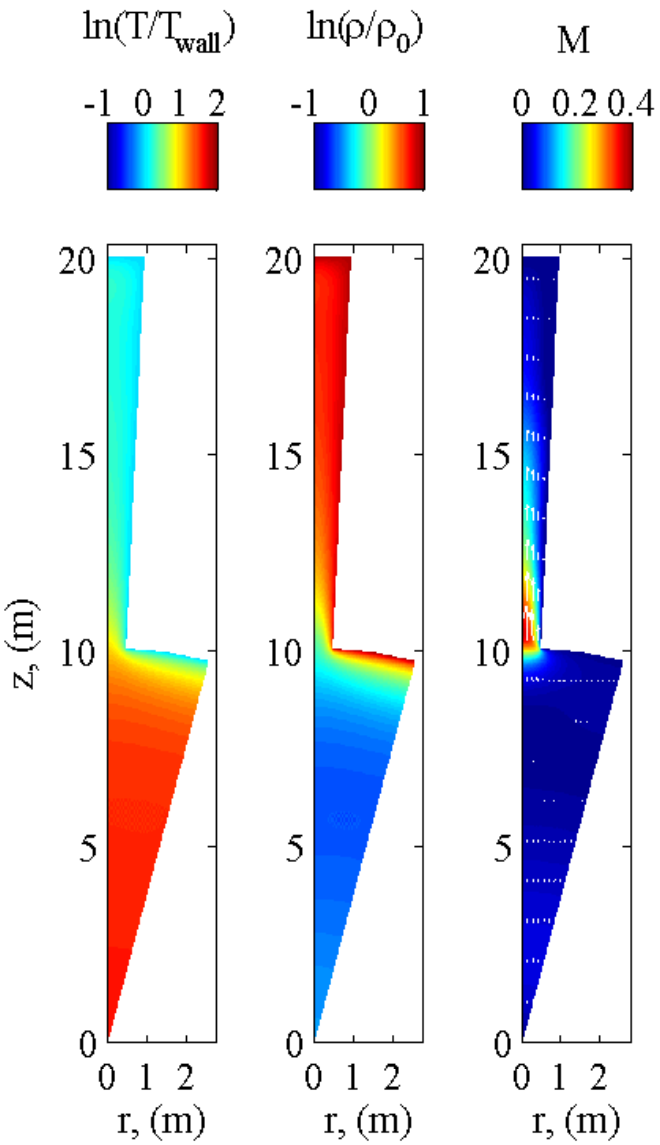

Figure III.17: Low density xenon chamber states at $t = 100ms$. Temperature field is normalized to the wall temperature and density field is normalized to the average chamber gas density. The third plot is the Mach number with vectors of Mach number magnitude in direction of the velocity field.

lines. Initially, all of the gas in the chamber jumps to high temperature due to x-ray deposition. After the first few ms, radiative cooling has completed. The gas in the beamline then cools much faster because the surface area to volume ratio is 90x larger than that of the chamber. Chamber gas flows into the beamline equalizing this pressure gradient resulting from the temperature difference. Relatively high Mach numbers at the throat of the beamline are produced. These Mach number are the result of initializing the gas with a BUCKY solution that does not include the increased density within the beamline. In subsequent target burns, an equilibrium state of higher density within the beamline would occur, and velocity at the throat would depend only on the relative cooling rates near this equilibrium. The decreased chamber gas density relative to the average state impacts wall shielding requiring additional gas to maintain the intended density. This extra gas would have the benefit of providing more protection for the final optic while providing no detriment for a target injected at the chamber radius.

III.B Helium and Deuterium Chamber Gas Evolution

III.B.1 Motivation for Study of other Gases

Xenon was selected as a first choice of chamber gases in part because its relatively high atomic number is beneficial for x-ray capture. With the stalling of the radiative cooling of xenon, it is important to know if this behavior is unique to xenon or common among other candidate chamber gases. These other gases have lower masses and therefore much higher conductivities than xenon which potentially enables much more conduction to the chamber walls as well. However, this same increase in conductivity poses a threat to target survival and is addressed in Chapter IV.

III.B.2 BUCKY Results for Deuterium, Helium

As with the xenon simulations, the deuterium and helium initial conditions come from BUCKY simulation of the 154 MJ NRL reference target design. For both deuterium and helium, the gas number densities were $1.65e21/m^3$ (high density) and $1e21/m^3$ (low density). Again, the high density case corresponds to 50 *mtorr* pressure at standard temperature, but the low density cases are now equivalent to 30 *mtorr* instead of 3 *mtorr* as a result of the data available.

All of the helium and deuterium cases start at $0.01ms$ because the shock arrives at the wall radius well before the $0.1ms$ data. This starts SPARTAN much earlier than the xenon $0.1ms$ and $0.5ms$ starting times. Figures III.18 through III.21 show the high and low density deuterium and helium BUCKY initial conditions used in the SPARTAN simulations.

The much higher velocities in the helium and deuterium cases relative to the xenon cases can be explained considering the behavior of hot low mass ions from the target interacting with the chamber gas. In each collision with a chamber gas particle, momentum and energy are conserved. In two body collisions between particles with equal mass, the particles leave the center of mass frame with similar energy and momentum in the center of mass frame depending on the scattering angle. In the case of a much lighter particle colliding with a massive particle, the light particle transfers much less of its momentum to the heavy particle but scatters in a primarily heavy particle centric center of mass coordinate system. The effect of this behavior is for the target ions to deposit much more of their momentum in a light chamber gas before being thermalized.

The BUCKY solutions for helium and deuterium are much more erratic than the xenon results. This is particularly true of the helium cases, but even the low density deuterium exhibits significant oscillatory behavior near the peak velocity. The strong negative velocity in the low density helium case is particularly strange. Though the source of this behavior is unknown, the SPARTAN results are most meaningful in the sense that some hot chamber gas with significant kinetic

energy rapidly cools radiatively and then dissipates the kinetic energy and conducts heat to the walls. The shape of the initial BUCKY profiles do affect the shape of shocks and the radiative cooling within them, but due to the erratic profiles can also simply be considered as an initial perturbation with appropriate thermal and kinetic energy of a target burn to provide a qualitative understanding of the behavior of the chamber gas.

The xenon cases have a smaller fraction of kinetic energy than the others initially according to the BUCKY inputs. This is likely due to better momentum transfer between fast ions from the burn for low mass chamber gases before burn ions are thermalized.

III.B.3 Helium and Deuterium Radiation Source

The radiation source term for helium and xenon gas was again evaluated using the IONMIX code. The results, shown in Figures III.22 and III.23 indicate that both gases exhibit similar behavior but behavior significantly different than that of xenon from Figure II.6. In particular, for both gases the radiative power remains quite large down to approximately $2000K$ and then falls off rapidly in the next cooler grid and then disappears completely in the next cooler grid point. This results from the gas rapidly approaching $\bar{Z} \rightarrow 0$. The cooling rate in IONMIX is ill-defined when the number of free electrons is zero.

It is likely that when the electron density falls low enough that the neutral-neutral collisions are more frequent than the electron-neutral collisions, collisional de-excitation would become dominated by that process. This is not the regime for which IONMIX was designed but this cutoff radiation temperature is of key importance to the quantitative final temperature. However assuming the behavior from the IONMIX table is correct until this cutoff, these results indicate that both helium and deuterium continue to cool rapidly even in the $3000K - 4000K$ range where xenon's cooling rate has completely stalled.

These results should be verified in the future for the relevant temperature

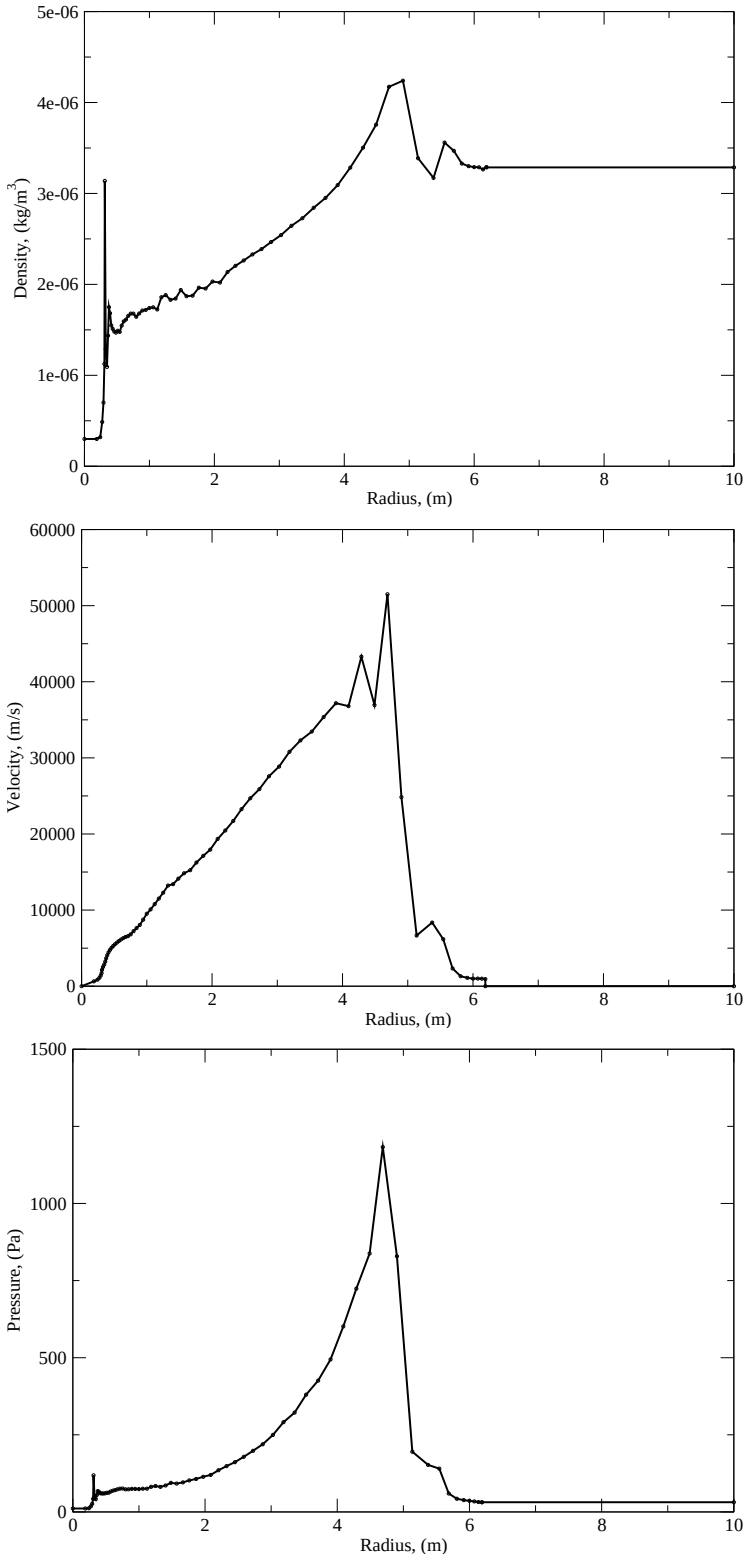

Figure III.18: BUCKY 154 MJ NRL target burn solution for SPARTAN deuterium initial conditions at low density ($n = 1e21/m^3$) and $t = 0.1ms$.

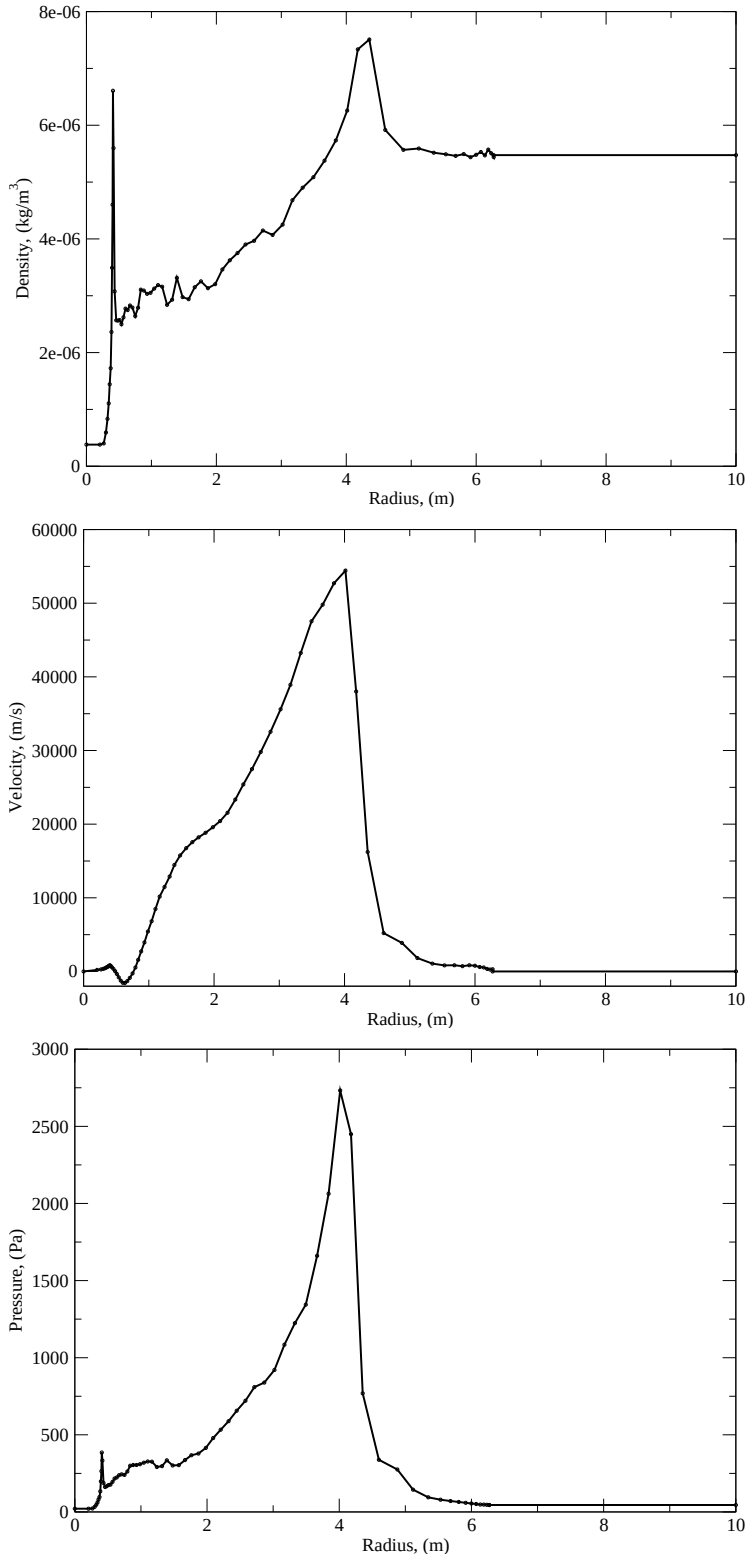

Figure III.19: BUCKY 154 MJ NRL target burn solution for SPARTAN deuterium initial conditions at high density of ($n = 1.65e21/m^3$) and $t = 0.5ms$.

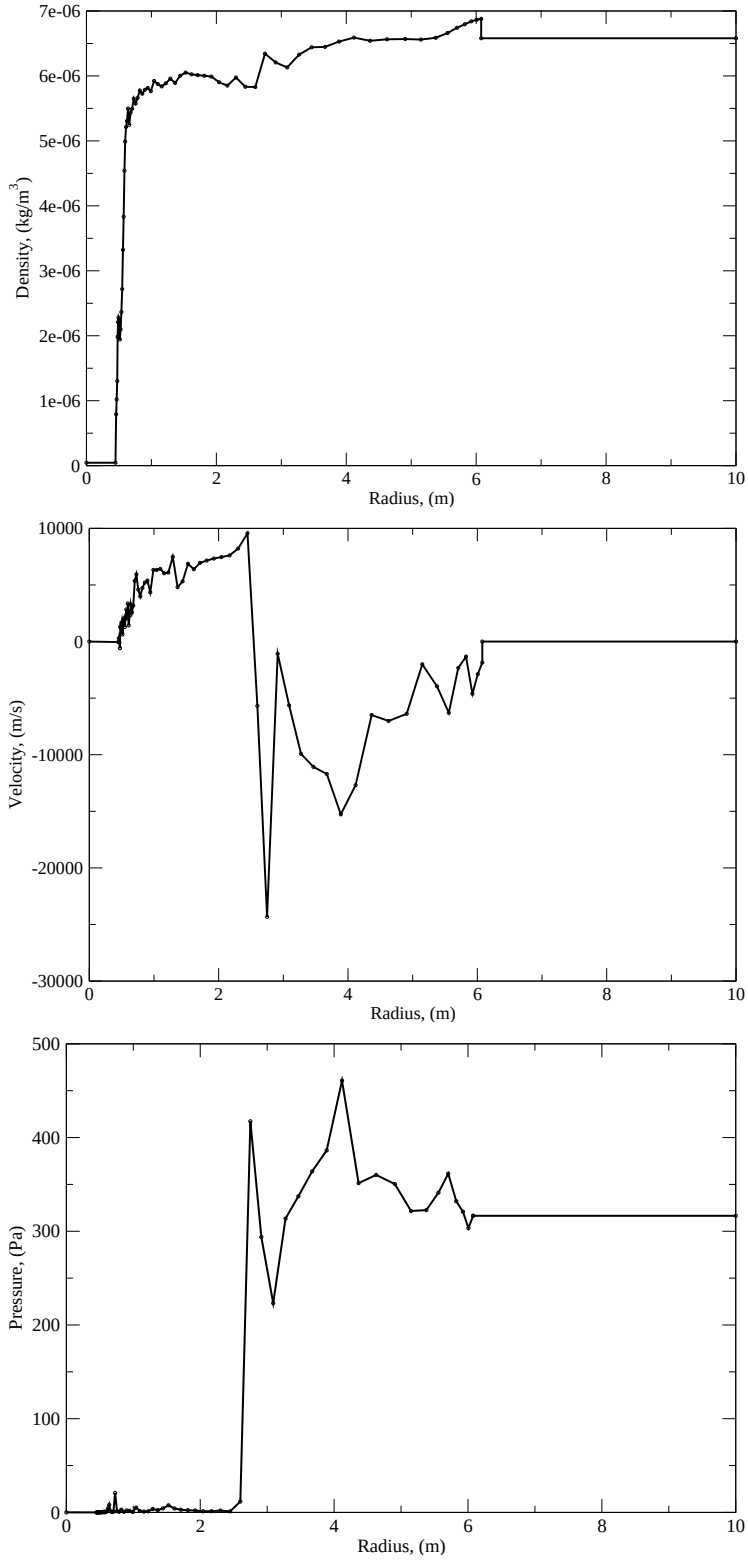

Figure III.20: BUCKY 154 MJ NRL target burn solution for SPARTAN helium initial conditions at low density ($n = 1e21/m^3$) and $t = 0.1ms$.

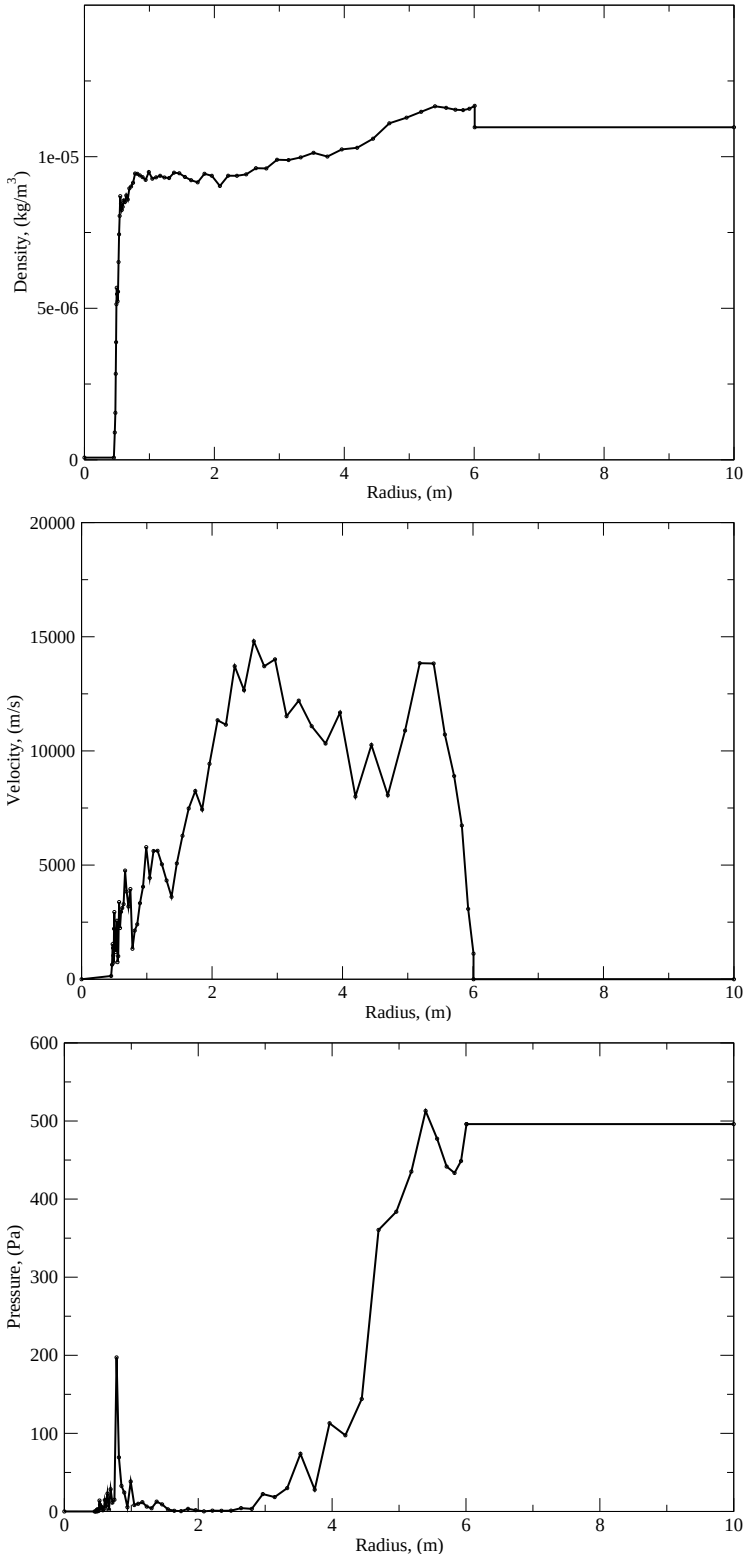

Figure III.21: BUCKY 154 MJ NRL target burn solution for SPARTAN helium initial conditions at high density of ($n = 1.65e21/m^3$) and $t = 0.5ms$.

range either experimentally or though the use of other validated radiation codes to ensure that the are not artifacts resulting from a misapplication of IONMIX.

A potential explanation for why the xenon gas stops radiating at higher temperatures might be the existence of metastable states such as $Xe^*(^3P_2)$. In Reference [5], this metastable xenon states are excited using a probe lamp. The decay frequency, $1/\tau$ of the metastable xenon was found to follow the relationship shown in Equation III.6 where the pressure, P, is in $torr$. In this equation, the second and third term are the result of two- and three-body collisions whereas the first term is the result of excited atoms diffusing to the test-cell wall.

$$\frac{1}{\tau} = \frac{16}{P\Lambda^2} + 75P + 80P^2 \tag{III.6}$$

The first term was investigated by varying the diameter from $2.1cm$ to $7cm$ which resulted in diffusion lengths, Λ of $0.44cm$ to $1.83cm$. This increase in diffusion length scale decreased the pressure of maximum lifetime from about $0.7torr$ to about $0.3torr$. If the diffusion scale for the several meter radius IFE chamber was two orders of magnitude larger than the test-cells, the diffusive term can be neglected for the majority of the chamber gas.

The pressure of the IFE chamber high and low density cases at $100ms$ are $846mtorr$ and $37mtorr$ respectively due to the high temperature. Ignoring the first and last terms gives a decay frequency for the chamber metastable xenon at only between about $63Hz$ and $3Hz$ for the high and low density cases. Though this may be an extension of these result in an incorrect temperature range, it demonstrates that at least some of the excited xenon may persist for 10s or even 100s of milliseconds.

Because the experiments data for every possible atomic transition is not tractable, IONMIX calculates the collisional and radiative de-excitation using oscillator strengths and Gaunt factors from models in References [62, 82, 89]. The validity of these models at low plasma temperatures plays a key role in expected IFE chamber gas states. Verifying the validity of these models deserves careful

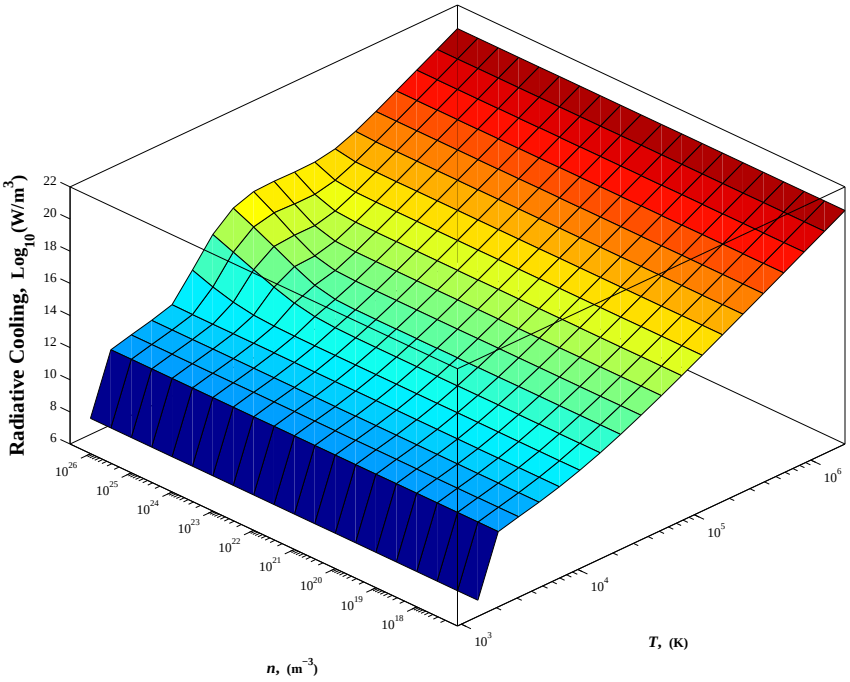

Figure III.22: Tabulated plasma cooling rates for monatomic deuterium gas from IONMIX code

consideration in IFE chamber gas work.

III.B.4 Temporal Gas Evolution by Element

Figure III.24 depicts the chamber temperature evolution across the simulation times. In Figure III.24, the gray region is the temperature of the thermal energy of the system at a given time after the burn. The other colored regions represent the temperature change due to energy lost through different means. The red region is temperature change do to radiative cooling. The green region is the temperature of the kinetic energy in the system which can be exchanged with the thermal energy and dissipated through viscous effects. Finally, the blue region is the temperature change due to energy conducted to the wall.

In the deuterium and higher density helium cases, the estimated radiative

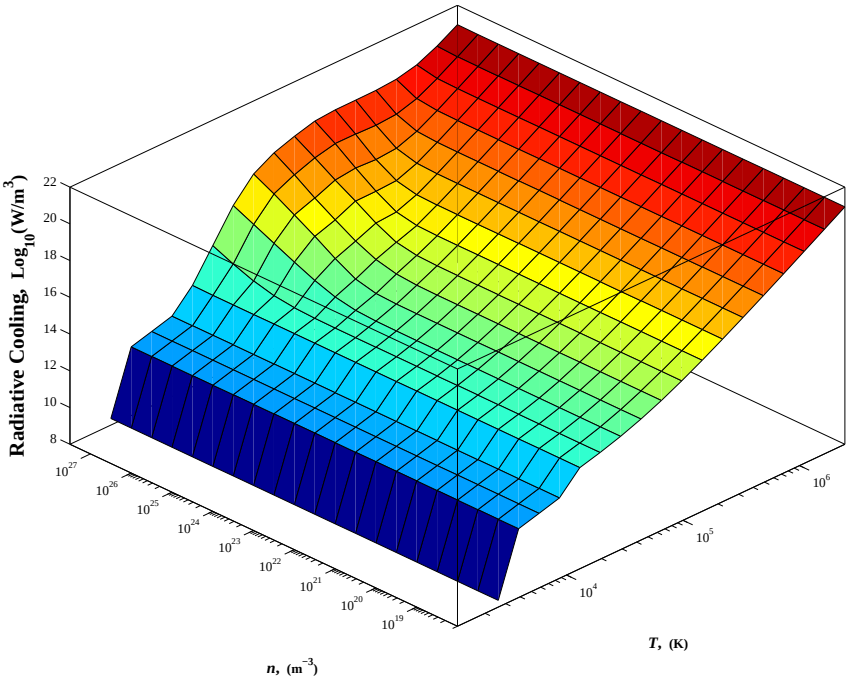

Figure III.23: Tabulated plasma cooling rates for helium gas from IONMIX code

cooling drops the gas temperature below the wall temperature fixed at 973 K. This is possible even though the wall temperature is lower than the radiation source cutoff temperature because, as the shock propagates through the gas, the temperature spikes into the radiative cooling regime. The gas then rapidly radiates to a cooler temperature resulting in a colder gas once the shock has passed and the gas re-expands.

Because the gas drops below the wall temperature, the heat conducted to the walls switches sign and the walls re-heats the gas. In the low density helium case, this re-heating can be seen as the width of the blue region decreasing with time. In the deuterium case however, the gas spends the majority of the time under the wall temperature and the net effect of the wall is heating. A red line that cuts the gray region is included to show what the temperature would be due to radiative cooling without the heat added from the wall.

III.B.5 Change in Beamline Effect in Helium and Xenon

Figures III.25 and III.26 show the chamber states at 100 ms for the Xe and He cases at $1e20/m^3$ and $1.65e21/m^3$ density respectively. These cases were selected because they are representative of the processes involved in the high mass (Xe) and low mass (D, He) results. The temperature is normalized to the wall temperature and the density is normalized to the average density. The third plot is Mach number as a measure of the kinetic energy relative to the thermal energy in the system. The arrows on the Mach number plot are proportional to the Mach number in the direction of the velocity field.

A striking differences between Figures III.25 and III.26 is the ratio of beamline to chamber density. As mentioned in Section III.A.8, the increased density within the xenon beamline is the result of xenons failure to cool to wall temperatures combined with dramatically higher surface area in the beamline. Because the helium case cools to approximately the wall temperature this effect as well as the high density layer covering the entire chamber surface is absent.

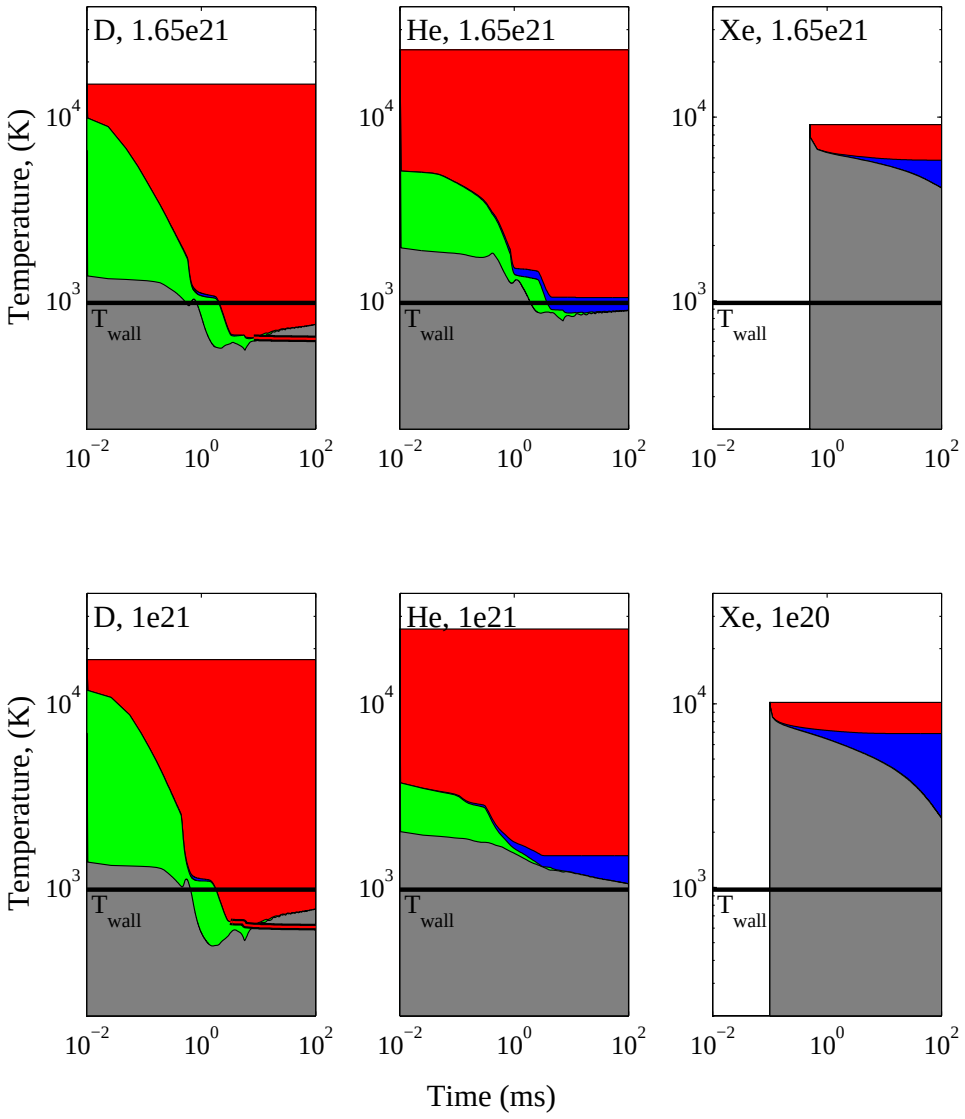

Figure III.24: Average chamber temperatures and energy loss mechanisms. The (gray) regions represent the thermal temperature. The others are the temperature change due to the energy lost through radiation (red), kinetic (green), and conductive (blue) processes. The red cut in D cases show temperature due to radiation without wall conductive re-heating.

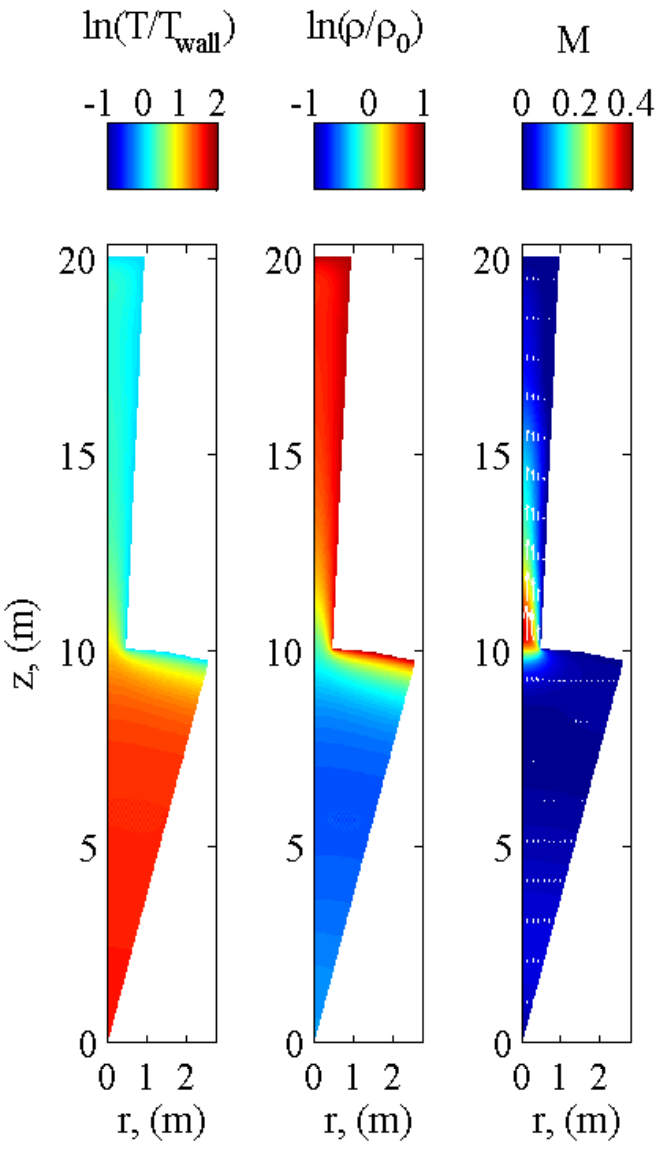

Figure III.25: Non-dimensional chamber temperature, density, and Mach number for $1e20/m^3$ density Xe at t=100 ms.

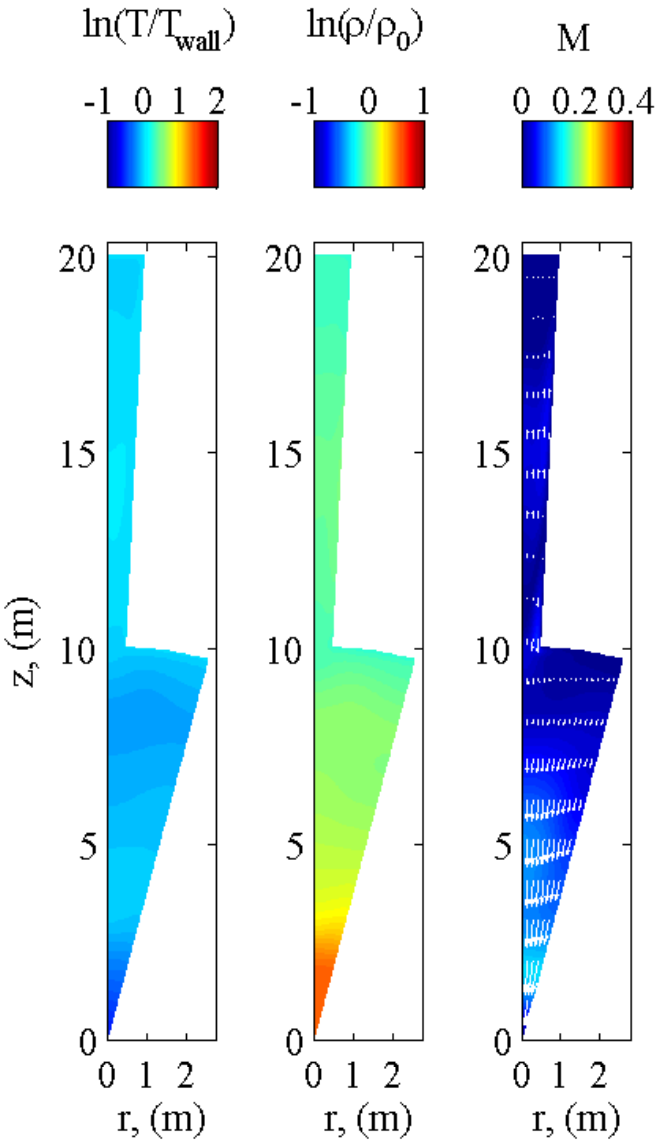

Figure III.26: Non-dimensional chamber temperature, density, and Mach number for $1e20/m^3$ density He at t=100 ms.

III.B.6 Oscillatory Compression of Re-heating Helium

Another difference between Figures III.25 and III.26 is the increased density at the center of the chamber. This is partially due to an oscillation between kinetic and thermal energy in the chamber best demonstrated by a closeup of the last 15 ms of the case of helium at $1.65e21/m^3$ as seen in Figure III.27. The flow is clearly in the deceleration phase towards compressed at the center.

Along with this compression, there is some additional residual density at the center of all spherical runs due to the first wave reflected from the wall converging on the center. When this happens, the density and temperature spike at the center which in turn emits radiation strongly. The radiation drops the pressure at the center, but not the density. When the pressure equalizes with the surrounding fluid the center drops back to a lower temperature and higher density than the surrounding gas. The densities cannot equalize until thermal conduction equalizes the temperatures, and this process is slow compared the simulation duration.

Though this effect may be an artifact of artificially perfect wall boundary conditions, the magnitude is similar in the spherical and wedge+beamline simulations. Though the beamline should significantly break the symmetry of the boundary conditions, more work must be done to ascertain if the asymmetry caused by the beamline is offset by the wedge slip boundary enforcing artificial symmetry on low order angular modes.

III.C Xenon:Target Gas Mixture Chamber Gas Evolution

III.C.1 Motivation for Gas Mixture Simulations

The behavior of mixtures of these candidate chamber gases is of even greater importance than any of them individually. Maintaining a pure chamber gas in steady operation is impossible because target burn products constantly accumulate within the chamber. Each NRL target contains $1e21$ particles. In a $10m$ radius chamber operating at $10Hz$, the chamber gas density would be

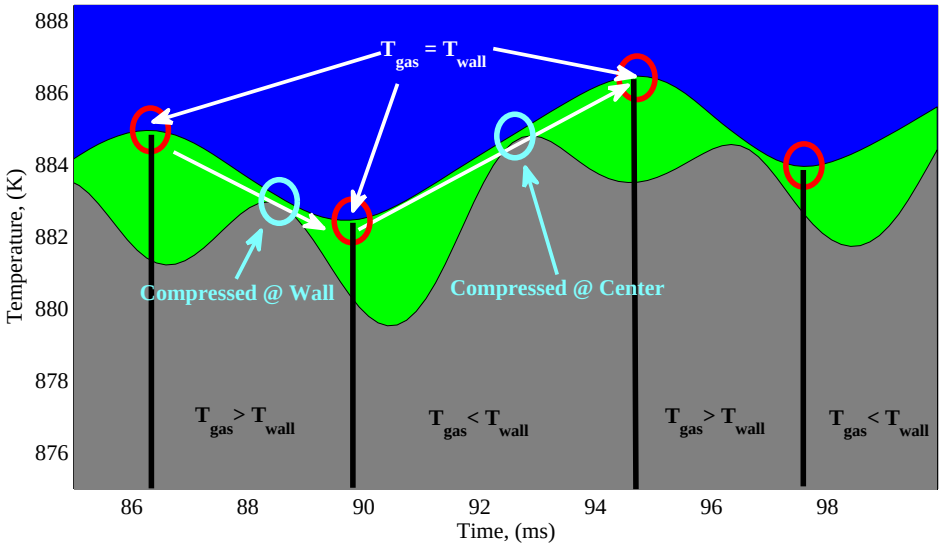

Figure III.27: Close-up of average chamber temperature and energy loss mechanisms for He at $1.65e21/m^3$ density showing radiation (red), oscillatory wall heat fluxes (blue), and oscillatory conversion between kinetic (green) and thermal energy (gray)

Table III.3: HAPL and NRL reference target burn product composition

Gas	T	D	He	H	C
NRL Fraction	46.29 %	45.58 %	6.48 %	0.91%	0.74%
HAPL Fraction	42.27%	40.90 %	10.45%	3.27%	3.11%

increased by $1e21/m^3$ every 7 minutes without the vacuum system.

If that chamber started at a density of $1e21/m^3$, the vacuum system sufficient to prevent density increase due to target particles alone would cause the chamber to drift towards a composition resembling the target emissions with a half-life of 7 minutes. The effects of this drift can be mitigated through additional pure chamber gas, but this is only done at the expense of the vacuum system power. For example, 10x as many chamber gas particles could maintain an approximately 90% pure gas in the chamber, but this is done at the expense of 10x the vacuum pumping power. To determine what fraction of pure gas to target byproduct is optimal requires understanding the behavior of the mixtures.

III.C.2 Gas Mixture and Initial Conditions

As mentioned in Section III.B.1, some mixture of chamber gas and target byproducts is a much more realistic composition for steady state operation of an IFE powerplant. In this chapter, we consider the addition of target byproducts in the proportions of the newer 350 MJ High Average Power Laser (HAPL) target reference design [61]. Though similar in design to the NRL target, the HAPL target design has undergone a more thorough analysis including possible fabrication techniques [14] and would be a good choice for future BUCKY simulations. It was therefore selected to consider the effect of mixtures though the results would likely be similar. Table III.3 shows the relative contribution of the target burn products for the NRL and HAPL target designs. The tables doesn't include the $< 0.01\%$ of gold or gold-palladium used as reflective overcoat and for coupling the laser energy to the target.

To create the initial conditions for the mixture simulations, the pure

xenon BUCKY solutions were simply modified to replace 10% of the chamber gas with a mixture of HAPL target byproducts. The velocity and pressure of the resulting mixture used the same values as the BUCKY initial conditions. This resulted in approximately 10% colder initial chamber temperatures because of the change in specific heat with decreased average particle mass.

Though the ions would likely impart more momentum to the gas through light-light collisions, 90% of the collisions would remain in the ion-xenon collisions and the momentum of the light chamber gas particles is small compared to that of the xenon even at the same density. The x-ray capture would also only be decreased by 10% compared to the pure xenon case.

This approach provides only approximate initial conditions, but is intended as an initial qualitative example used to motivate future research into mixture composition chambers as well as the necessary enhancements to BUCKY to incorporate some of these mixture effects for future BUCKY simulations.

III.C.3 Mixture Radiation Source

Again, IONMIX was used to compute the radiation source term for the mixture gas. The results of this calculation are shown in Figure III.28. These results bear considerably more resemblance to the deuterium and helium radiation sources than they do to the xenon source. This is not surprising considering the peak cooling rates are two orders of magnitude larger in the deuterium and helium cases. Unfortunately, the source term is not simply the sum of individual contributions because the charge state depends on the gas composition.

The composition dependence of the radiation source term poses an additional difficulty in mixture simulations of the chamber gas. If the composition is allowed to vary due to various molecular processes such as therm- and barodiffusion, the composition of the gas will not remain constant throughout the chamber. In this analysis, we assume that the radiation term is unaffected by this variation. We then consider two limits to the evolution of the mixture with

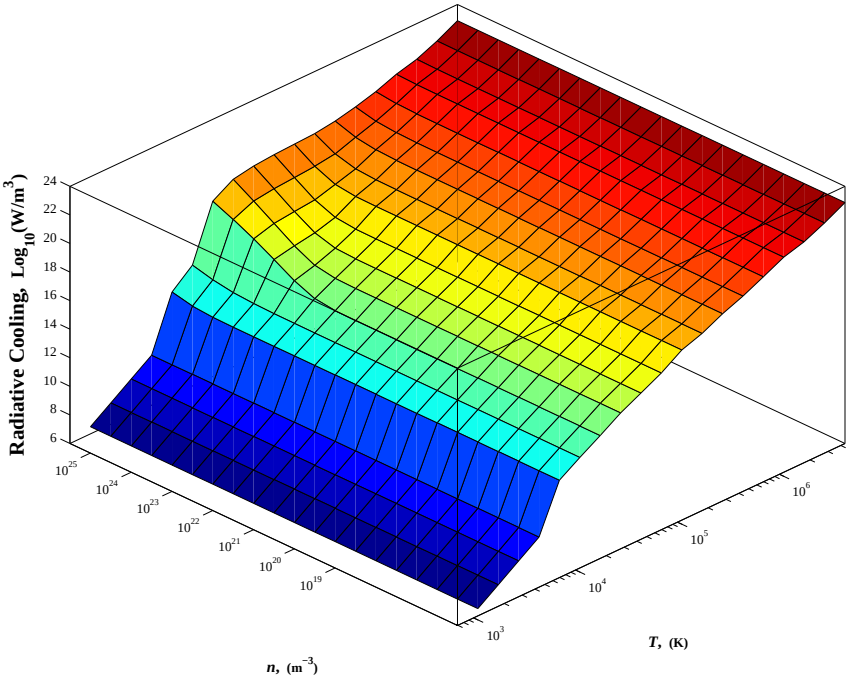

Figure III.28: Tabulated plasma cooling rates for 90:10 xenon to target gas mixture from IONMIX code

regards to the radiation source. In the first case the diffusive processes are turned off such that the mixture remain constant throughout the flow. In the second, we allow the mixture to vary, but assume that the radiation source scales with the mass density is generally dominated by the xenon contribution unless the target fraction becomes much larger than the xenon fraction. Though this is a significant approximation to the radiation source term, it enables an initial look at the contribution of the diffusive fluxes to determine if they are significant enough to warrant a redesign of the calculation of the radiation source term to account for the mixture variation.

III.C.4 Breakdown of the Single Temperature Assumption

Estimation of the breakdown of continuum in an important topic in rarefied gas dynamics. In Reference [10], Bird suggest a breakdown parameter of the form shown in equation III.7 where $\nu =$ is the collision frequency and D/Dt is the Lagrangian material derivative. This quantity compares the the time rate of density change following a fluid element to the collision frequency that re-establishes equilibrium. The collision frequency is simply the average velocity of the gas particles divided by the mean free path, $\nu = \bar{C}/\lambda$. In steady flows, the breakdown parameter can also be viewed as proportional to the Mach Number multiplied by the local Knudsen number defined by the density gradient length scale. Higher values correspond to higher levels of non-equilibrium within the flow, and Bird suggest a value of < 0.02 to apply the continuum formulation. This style of breakdown parameter has also been employed by Wang and Boyd in Reference [85] with the additional consideration of the temperature and velocity gradient length scales for hypersonic flows to enable the development of a Monte Carlo and Navier-Stokes hybrid numerical code. With the inclusion of the pressure and concentration gradient length scales, these limits would effectively limit the maximum diffusion velocity as it depends directly on these scales.

$$P = \frac{1}{\nu}\left|\frac{D(ln\rho)}{Dt}\right| \tag{III.7}$$

The local gradient driven breakdown is analysis is designed to understand the breakdown of gas that is initially in equilibrium. In the case of the IFE chamber, after the first few bounces of the initial burn wave, the Mach number and gradients are generally relatively small. A more relevant question is determining if sufficient thermal relaxation occurs between the initially different temperature gases to allow the use of the single temperature model.

As long as many free electrons are available in the system, the high collision frequency ensures a single temperature. However, once the average charge state approaches zero, the equilibration of the temperature between the gases components depends on the neutral-neutral collision frequency. As shown in the prior sections, xenon cooling stalls at approximately 3-4× higher temperature than helium and deuterium after all of the free electrons are gone. Estimation of the equilibration time provides confidence in the time interval after which the single temperature assumption become valid again.

Bird's development of the mean free path of a gas mixture from Reference [10] provides the framework for analyzing the limit of a small light (p) gas molecule colliding with a heavy large gas (q) molecule. One can assume the collision cross section is at least $\pi d_q^2/4$. Even though xenon remains 3-4× hotter than helium and deuterium after the radiative cooling, its mass is 32-65 times greater. This results in a thermal speeds that are around $\sqrt{10}$ times slower even in hot xenon. Assuming this makes the heavy particle's thermal velocity negligible compared to that of the light gases, the p-q collision frequency can then be estimated as $\nu_{pq} = \pi d_q^2/4 n_p n_q \bar{c_p}$. Comparing this to the heavy-heavy collision frequency results in the ratio shown in Equation III.8. This implies that the ratio is of order n_p/n_q for hot xenon and cold helium or deuterium. We can then obtain a simple estimate of the collision frequency for light cool collisions with hot xenon as approximately $\nu_{light} \approx \nu_{Xe} n_{light}/n_{xe}$. With 10% light gas and pure xenon mean free paths on the

order of $18mm$ based on the low density case of Table I.1 at $4000K$, this results in a collision frequency of approximately $9000Hz$. A thermal equilibration rate is suggested in the NRL formulary [41] as shown in Equation III.9. The frequency of the energy exchange is related to the collision frequency through Equation III.10.

$$\frac{\nu_{pq}}{\nu_{qq}} = \frac{\pi d_q^2/4 n_p n_q \bar{c_p}}{\pi d_q^2 n_q n_q \bar{c_q}} = \frac{n_p \bar{c_p}}{4 n_q \bar{c_q}} \tag{III.8}$$

$$\frac{dT_p}{dt} = \sum_q \nu_\epsilon^{pq} (T_q - T_p) \tag{III.9}$$

$$\nu_\epsilon^{pq} = 2\left[(m_p/m_q)\Psi(x^{pq}) - \Psi'(x^{pq})\right]\nu_0^{pq} \tag{III.10}$$

$$\begin{aligned} x^{pq} &= m_q v_p^2 / 2kT_q \\ \Psi(x) &= \frac{2}{\sqrt{\pi}} \int_0^x t^{1/2} e^{-t} dt \end{aligned} \tag{III.11}$$

In the formulary, the collision frequency, ν_0^{pq} is based on the collision of two charged particles. To make an order of magnitude estimate of the thermal equilibration, the neutral-neutral energy equilibration frequency is assumed to still be related to the collision frequency through Equation III.10. A helium velocity of $v_p = \sqrt{2kT_p/m_p}$ is also assumed such that $x^{pq} = (m_q/m_p)(T_p/T_q)$ rather than using a velocity distribution dependent calculation. This results in an estimated equilibration half-life of approximately 1.9 ms between the xenon and target gases. It is also interesting to note that with $9\times$ more particles, this half-life would move the light temperature up much more than the xenon temperature down. However, as the light gas re-heated, its temperature would be maintained by radiative processes that cooled it originally.

III.C.5 Comparison of Variable and Locked Diffusion Results

The high and low density xenon cases were mixed 90:10 with HAPL target byproducts. They were then evolved in time using either locked diffusion or the full diffusion equations. Figure III.29 shows that the overall mass average temperatures are nearly identical for the high density case diffusion locked and unlocked cases. The average temperatures are within $0.5K$ for the two cases at $100ms$. This is expected using the radiation source term lookup that depends only on xenon density. The low density plots over the full temperature range are also nearly identical. Figure III.30 shows the temperature evolution of the low density cases focused only on the behavior after the initial intense radiative cooling.

The solutions are $3-5x$ colder than the pure xenon runs as a result of the strongly enhanced radiative source. Because the gas spends the majority of the time much closer to the wall temperature, the conductive heat transfer accounts for only approximately $14.5K$ of cooling in the high density case and around $54K$ in the low density case. Considering the gas is between about 150 and $50K$ from the wall temperature for all but the first few microseconds of the simulation, the conductive cooling does represent the removal 27% and 62% for the high and low density cases of the remaining energy relative to the difference between wall and final radiative cooling temperatures. These are larger than the 14% and 55% of the pure xenon because the thermal conductivity of the mixture is much larger than that of the pure xenon despite being much colder.

It is also worth noting that though the cooling curves appear to discontinuously jump down in temperature at the start of the mixture simulations as well as the helium and deuterium simulation, they are smooth continuous curves in the first few 10s of time-steps of the simulations. This large jump is predominately due to the ad-hoc initial conditions. If the stronger radiation source for the mixture was present in the BUCKY simulation, the temperature at the start times would not be as high as the temperature from the xenon initial conditions. This immediate temperature correction also shows that the initial chamber temperature is

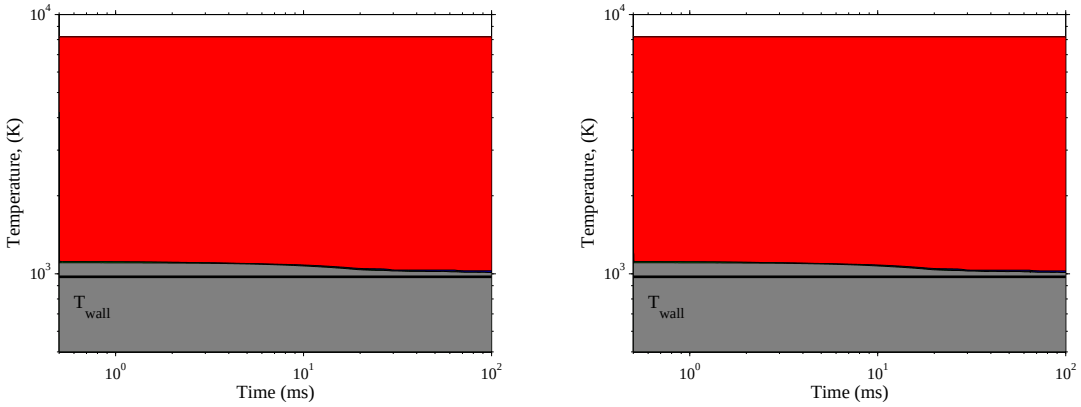

(a) 90:10 Xe-Target with Diffusion

(b) 90:10 Xe-Target without Diffusion

Figure III.29: Comparison of temperature evolution by energy loss mechanism for the high density ($n = 1.65e21/m^3$) 90:10 Xe-Target mixture gas in spherical chambers for locked and unlocked diffusion. The red region corresponds to energy lost through radiative cooling, blue through conduction to the chamber walls, and gray the remaining thermal energy in the chamber. The green region represents the kinetic energy within the chamber.

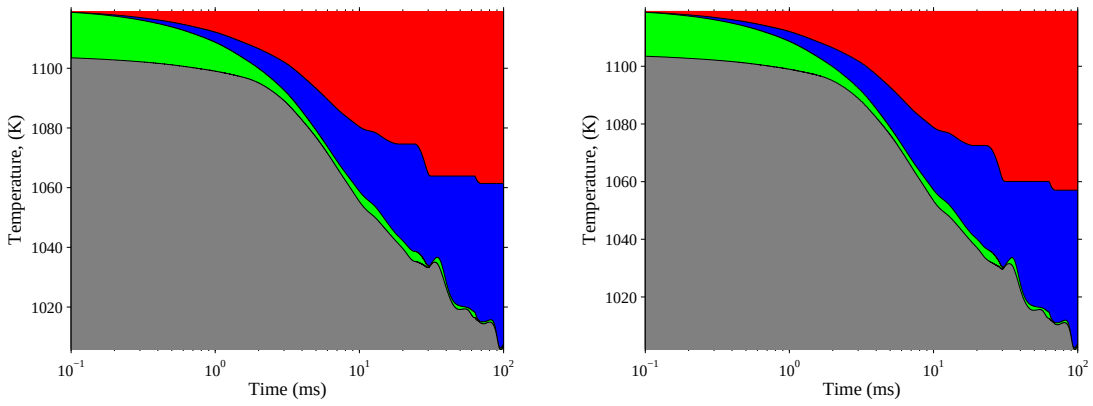

(a) 90:10 Xe-Target with Diffusion

(b) 90:10 Xe-Target without Diffusion

Figure III.30: Comparison of temperature evolution by energy loss mechanism for the low density ($n = 1.00e20/m^3$) 90:10 Xe-Target mixture gas in spherical chambers for locked and unlocked diffusion. The red region corresponds to energy lost through radiative cooling, blue through conduction to the chamber walls, and gray the remaining thermal energy in the chamber. The green region represents the kinetic energy within the chamber.

of less importance than accurate cooling rates and cooling cutoff temperatures for chamber evolution. However, it is interesting to consider how physically realistic such a jump would be if the ad-hoc initial conditions were accurate. This helps to understand some limitations of the radiation source.

Figure III.31 shows these early radiative cooling phases for the high and low density mixture simulations. Though the curves are smooth, the timescale through which this cooling occurs is questionable considering the estimate of $1.9ms$ half-life for thermal equilibration between the xenon and light gas species from Section III.C.4.

While the gas is still weakly ionized, the high electron velocities make electron-neutral collision frequencies much higher than the other possible collisions. To compare the neutral-neutral thermal equilibration to the electron-ion rate, consider the $1e20/m^3$ chamber gas as a plasma with $Z = 1$, T $1ev$, and a coulomb logarithm, λ of order 10. Using Equation III.12 from the NRL Formulary [41] results in a energy relaxation frequency of $24KHz$ or an equilibration half-life of only $28\mu s$. Note that Equation III.12 assumes number densities in $cm^{-}3$, ion mass μ in proton masses, and temperatures in ev.

This equation also shows the strong dependence on the charge state of the plasma to this equilibration rate. Replacing the number of electrons with $n_n\bar{Z}$, the number of neutrals times the average charge state, the thermal relaxation of the remaining electrons and ions falls of as $\bar{Z} \rightarrow 0$ such that at $\bar{Z} = 0.01$, the thermal relaxation half-life jumps to $2.8ms$ and exceeds the relaxation time between the excited neutrals. At some low average charge, the electron-neutral collision rate similarly exceeds the electron-ion collision rate despite a smaller cross section due to the larger number of neutrals.

Though the timescale shown in Figure III.31 is considerably shorter than even the $28\mu s$ for electron equilibration, the radiative cooling is likely completed within the first few milli-seconds after the burn. This makes the exact rates of this early time behavior less relevant than the the total magnitude of cooling. To

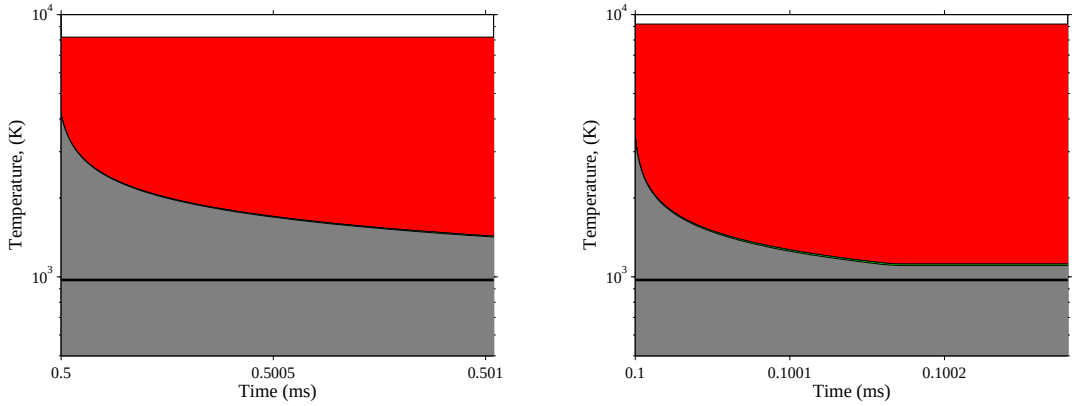

(a) High Density 90:10 Xe-Target Gas

(b) Low Density 90:10 Xe-Target Gas

Figure III.31: Initial rapid radiative cooling in high and low density IFE chamber mixture simulations

understand this behavior better in the future, the target gas should be studied in the context of glow discharge plasma or lighting plasma rather than using a radiation source designed for fully ionized plasma. This will likely also require a new model to allow the ion temperatures to split as the charge state approaches zero and re-equilibrate on the neutral-neutral collision timescale. Assuming the radiative cooling results in temperatures similar to the results presented within the first several milliseconds, the simulations provide useful insight into the conductive cooling and viscous dissipation that can be expected within the chamber.

$$\nu_{\epsilon}^{i|e} = 3.2e - 9n_e Z^2 \lambda / \mu T^{3/2} \tag{III.12}$$

III.C.6 Gas Mixture Separation

The diffusive processes play only a small role in the final temperature of the mixture based on the radiative cooling model that does not account for variations in composition. Examining the evolution of the chamber composition is important to determine the validity of this radiative model.

The pressure and velocity pulse from target ions depositing in the cham-

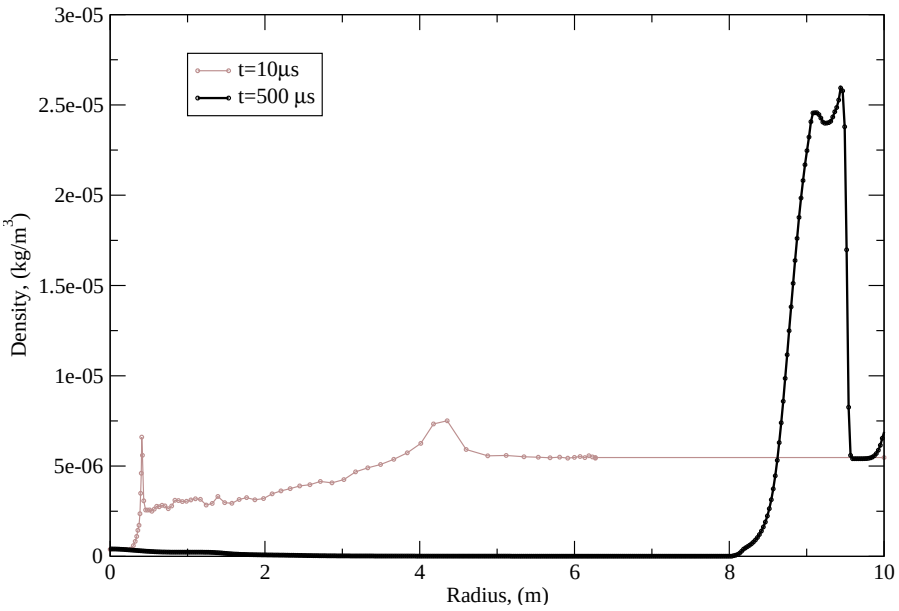

Figure III.32: Comparison of density for high density deuterium BUCKY initial condition at $10\mu s$ and SPARTAN solution at $500\mu s$ showing high density wave approaching the wall and void remaining in the center.

ber gas results in a wave that propagates outward from the burn. Because of the radiative cooling, the Mach number of this wave increases as the temperature drops. The resulting low pressure gas void at the center of the chamber causes a strong pressure gradient that slows the wave. In the helium and deuterium cases, the momentum deposited by the ions is significantly greater than the acceleration due to this pressure gradient and the majority of the chamber gas is driven to the wall leaving an extremely low density core. Figure III.32 compares the original density profile from the BUCKY initial conditions in deuterium. However, this effect does not occur to the same degree in the xenon cases because of the lower velocities. Figure III.33 shows the low density xenon BUCKY initial conditions as well as the SPARTAN solution at three times leading up to a density spike from the pressure driving the xenon back to the blast center.

This initial expanding phase is when baro-diffusion plays the largest role in the composition of the mixture chamber gas. Baro-diffusion forces the light target gases backwards towards the burn center just as the pressure gradient in

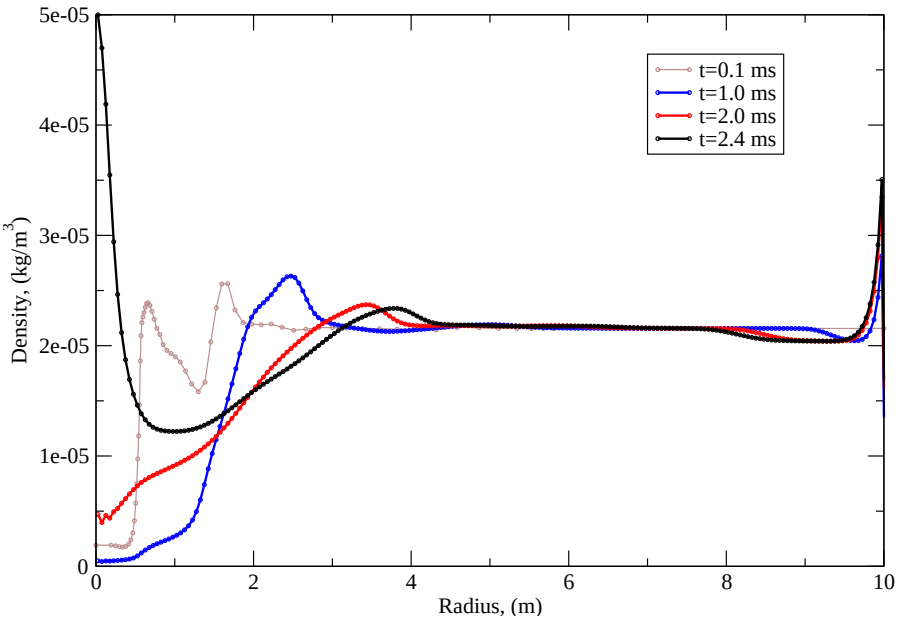

Figure III.33: Comparison of density for low density xenon BUCKY initial condition at 0.1ms and SPARTAN solutions at 1, 2, and 2.4 ms showing blast wave stalling and collapsing with density spike at blast center.

a centrifuge drives lighter particles to the center of the device. The composition in the void left by the expansion wave becomes dominated by target gas atoms. Figure III.34 is similar to the low density plot for the collapse and density spike at the blast center. However, the timescale for this to occur is longer in the mixture case because the radiation has dropped the temperature so much more. The lower temperatures correspond to lower pressures driving gas back towards the chamber center.

With the diffusion unlocked, the overall density results look similar to Figure III.34. To compare the behavior of the constituent gases, the mass density is problematic because the mass of the 90% xenon dominates the other contributions. Figure III.35 shows the number fraction of xenon at three times leading up to the density spike at the center. The density spike in the xenon is delayed slightly compared to the locked diffusion case. These plots show the target byproduct enrichment in the low density core region where the xenon fraction become negligible.

The target particles that cause enrichment of the low density core have

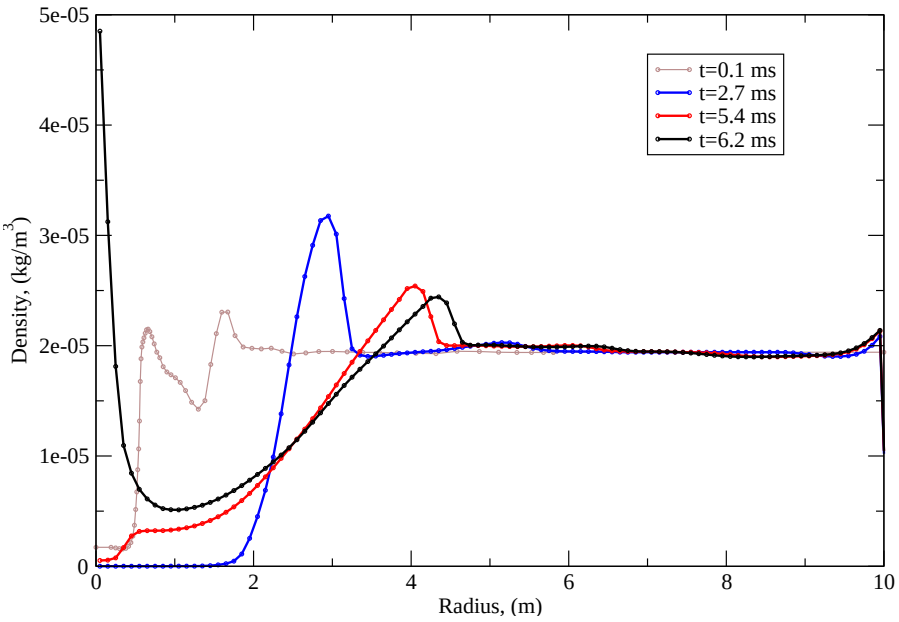

Figure III.34: Comparison of density for locked diffusion low density mixture initial condition at 0.1ms and SPARTAN solutions at 2.7, 5.4, and 6.2 ms showing blast wave stalling and collapsing with density spike at blast center.

diffused out of the high pressure wave region. This causes a slight depletion of target byproducts in the wave. The magnitude of this depletion is important because, after the initial cooling, this is the hottest and densest region of the flow. If variation in composition were to effect the radiative cooling, it would likely occur in this region. Figure III.36 shows the target byproduct enrichment and deficit at the same times as Figure III.35. This shows that the target particles are depleted by as much as 25% in the high pressure wave.

Though this 25% depletion is a significant composition variation, because the radiation source term is changed so dramatically with the addition of only 10% target byproducts, the 7.5% target gas radiation source is expected to resemble the 10% source much more than the pure xenon source. Rerunning IONMIX on this depleted target byproduct gas confirmed this expectation, producing a negligible change in the predicted radiation source. Figure III.37 shows the percent change in the radiation source power between the original mixture and 25% depleted target products mixture. The peak difference is under 5% and at higher densities than the

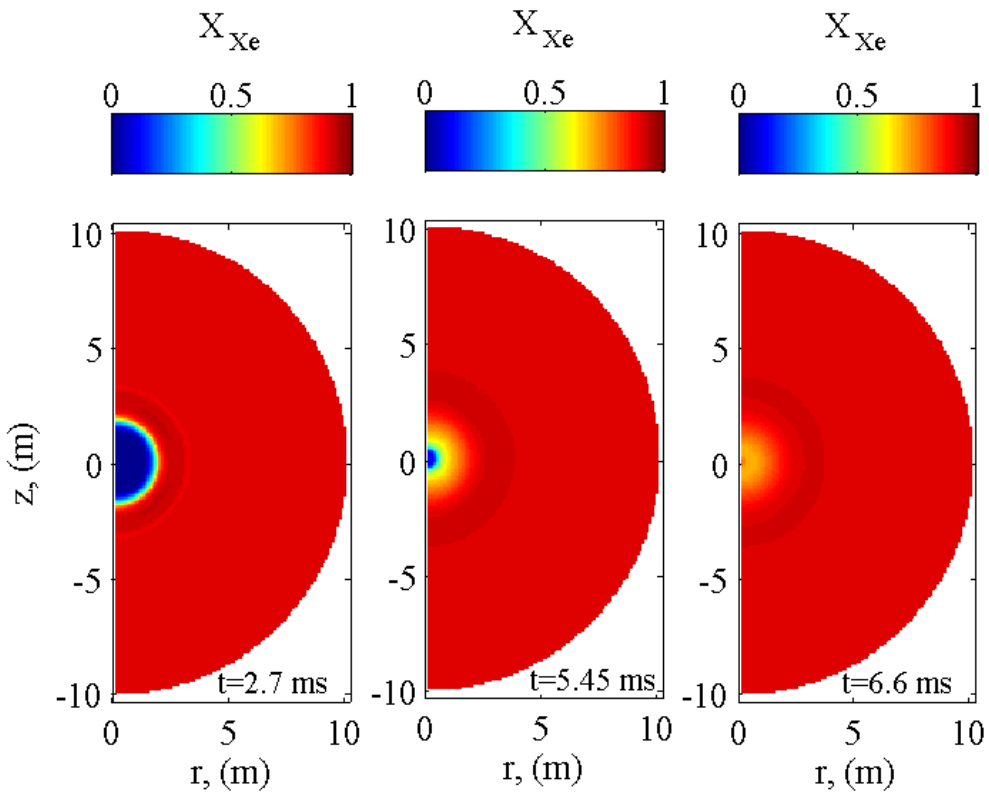

Figure III.35: Xenon number fraction for low density mixture simulation at three times leading up to return density spike at burn center

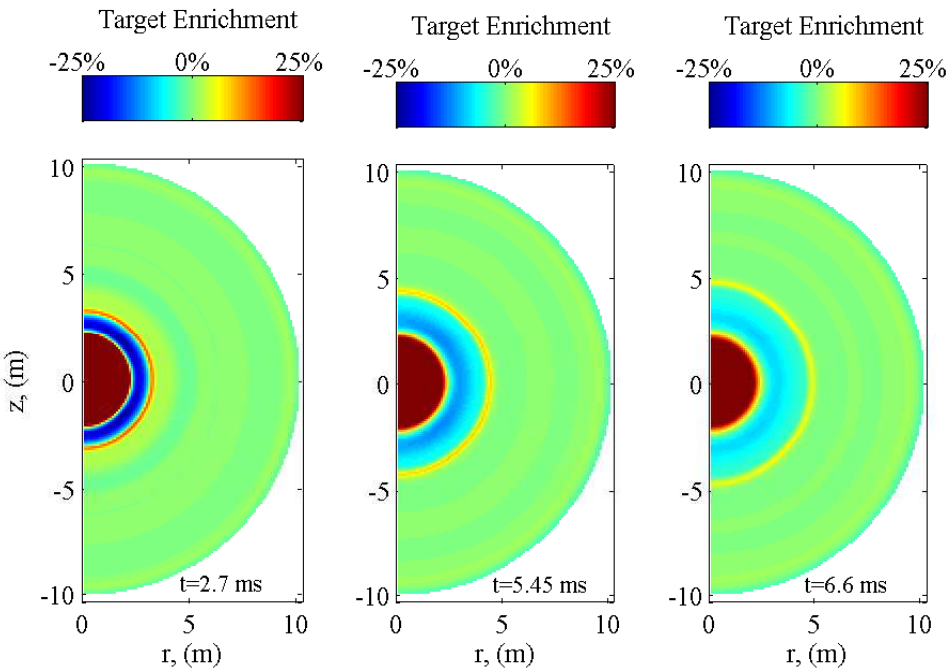

Figure III.36: Percent of target gas fraction enrichment in low density mixture case bounded at ±25% to show deficit in the burn wave

direct drive IFE chamber gas would operate. This implies that the single mixture radiation source is sufficient for initial estimates of chamber conditions in these simulations. In either case the radiative cooling is extremely rapid and the most important factor is the temperature at which the cooling cuts off.

Chapter 3, in part, is a reprint of material submitted to Fusion Science and Technology, November 2010. Martin, R.; Najmabadi, F., 2010. The dissertation author was the primary investigator and author of this paper.

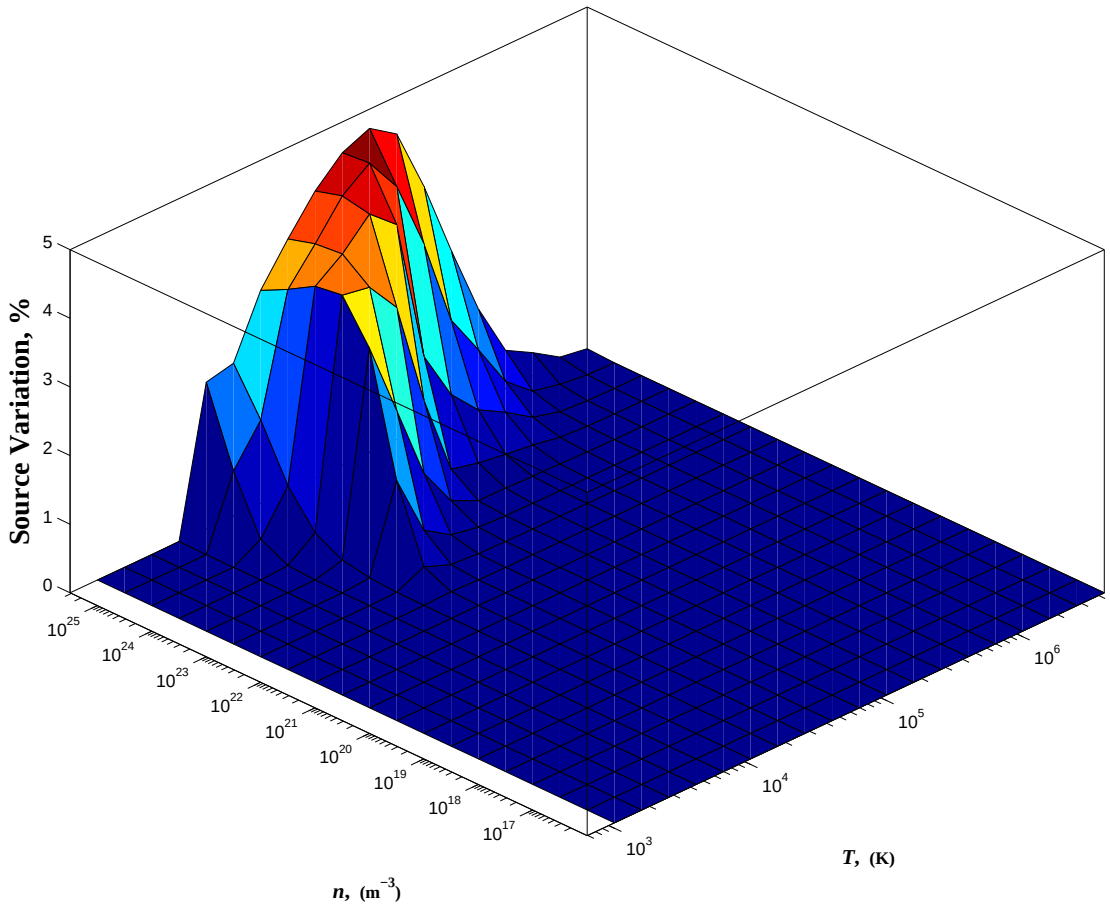

Figure III.37: Radiation source variation in 25% target byproduct depleted mixture gas relative to the original radiation source

Chapter IV

Target Heating

The evolution of the chamber gas state in time alone is insufficient to determine the risk posed to the cryogenic target. In this chapter, the dependence of the target heat flux on chamber conditions is considered to connect the chamber gas simulations to target survival. This information is used to propose an iteration on initial chamber densities to maximize the gas wall protection and minimize required vacuum system power while satisfying the target survival constraints.

IV.A Target Free Molecular Flow Model

The mean free path for chamber gases at 1,000 to 4,000K at pressures considered a few cm. The chamber scale flow features and chamber evolution generally be resolved with a fluid approach. However, the target dimension is typically smaller than the mean free path for the gas and the Knudsen number of the target/gas interaction typically falls within the free molecular regime.

In previous work, the analysis of target heat flux was performed with Birds commercial Monte Carlo code, DS2V [18, 19]. Here we propose an analytical expression for the heat flux based on Bird's analysis of free molecular flow [10] with a modification to incorporate condensation. Bird derives the free molecular heat flux (q) by relating the incoming (q_i) and reflected (q_r) heat fluxes to the corresponding particle fluxes and the associated energy carried by the particles

$(q = q_i - q_r)$.

Bird includes a coefficient for the fraction of specularly reflected molecules, ϵ, such that the equation takes the form of $q = (1-\epsilon)(q_i - q_r)$ because the specularly reflected molecules deposit no net energy. Bird also includes an accommodation coefficient, a_c, such that $a_c = (q_i - q_r)/(q_i - q_w)$ where q_w assumes diffusely reflected particles carry energy equal to the wall temperature. Maintaining this definition of the accommodation coefficient, to account for the possibility of condensation the expression is $q = (1-\epsilon)[(1-\sigma_c)a_c(q_i - q_w) + \sigma_c(q_i + q_{cond})]$ where the sticking coefficient, σ_c, is the fraction of particles that condense on the surface rather than reflect. This analysis ignores the vapor pressure of condensed particle sublimation from the surface because the value is negligibly small for xenon unless the target has heated far beyond the DT triple point temperature.

There is significant uncertainty in the accurate choice of accommodation, sticking, and specular reflection coefficients. Because of this, we focus on the complete and no-sticking limits depending on the chamber gas. For the other coefficient we consider only the highest heat flux case of fully diffuse ($\epsilon = 0$) reflections with full accommodation ($a_c = 1$).

Though these assumptions are typical for most engineering surfaces, Bird lists three scenarios in which these assumptions are called into question [10]. They include smooth out-gassed metal surfaces, low mass gas molecules relative to the surface molecules, and translational energy relative to the surface of several electron volts. The highly uniform high-Z metal overcoat considered for direct drive targets likely satisfies the first criteria. Deuterium and helium chamber gasses relative to this high-Z metal also have a very small mass ratio satisfying the second criteria. Rosner cites several such low energy accommodation coefficients in prior works such as 0.07 for helium on platinum and 0.005 for helium on tungsten [70]. This suggests that experimental measurement of these coefficients for the surface of direct drive IFE targets could potentially demonstrate significantly lower heat fluxes than the estimates in these preliminary design studies. Equation IV.1 shows the expression

for full accommodation fully diffuse free molecular condensing heat flux on an element at temperature T_t with angle α to the flow given the incoming flow number density, n_∞, temperature, T_∞, and velocity, U_∞. The expression also depends on gas particle mass, m, specific heat ratio, γ, and latent heat of deposition, $\Delta_s^g H$, as well as the Boltzmann constant, k_b. Finally, the speed parameter, s, relates the injection speed to most probable thermal speed and is equivalent to $(2/\gamma)^{1/2}$ times the target Mach number.

$$
\begin{aligned}
q &= \frac{n_\infty (k_b T_\infty)^{3/2}}{\sqrt{2\pi m}} \left[\widehat{Q}_0 \, \Gamma(s,\alpha) - \frac{1}{2} e^{-s^2 sin^2 \alpha} \right] \\
\widehat{Q}_0 &= \left(s^2 + \frac{\gamma}{\gamma - 1} - \frac{1}{2} \left(\frac{\gamma + 1}{\gamma - 1} \right) (1 - \sigma_c) \frac{T_t}{T_\infty} + \sigma_c \frac{m \Delta_s^g H}{k_b T_\infty} \right) \\
\Gamma(s,\alpha) &= e^{-s^2 \sin^2 \alpha} + \pi^{1/2} s \sin\alpha \, (1 + \mathrm{erf}(s \sin\alpha)) \\
s &= U_\infty / (2 k_b T_\infty)^{3/2}
\end{aligned}
\tag{IV.1}
$$

IV.A.1 Condensation and Latent Heat of Deposition

The latent heat of deposition is a consequence of the required energy release needed to bring particles of a gas down to a low enough energy that they remain within a crystal lattice. It is useful to consider this in terms of an attractive-repulsive intermolecular potential such as the Lennard-Jones 6-12 potentials used in the transport property calculations. Figure IV.1 shows the Lennard-Jones potential for xenon based on a well depth of $\epsilon/k_b = 229K$ and a spacing of $\sigma = 4.055\mathring{A}$ from Reference [38].

This potential was then used to calculate the potential on an atom at the center of a FCC crystal lattice as one half the sum of all the intermolecular potentials of atoms in the lattice as suggested in Reference [38]. Figure IV.2 shows the arrangement of atoms in the lattice used in the calculation for a $6 \times 6 \times 6$ crystal. The dimensions of this lattice were then scaled to find the lattice size that resulted in a minimum of the combined potentials. The number of lattices was then increased in steps of 2 to $20 \times 20 \times 20$ until a minimum in the limit of

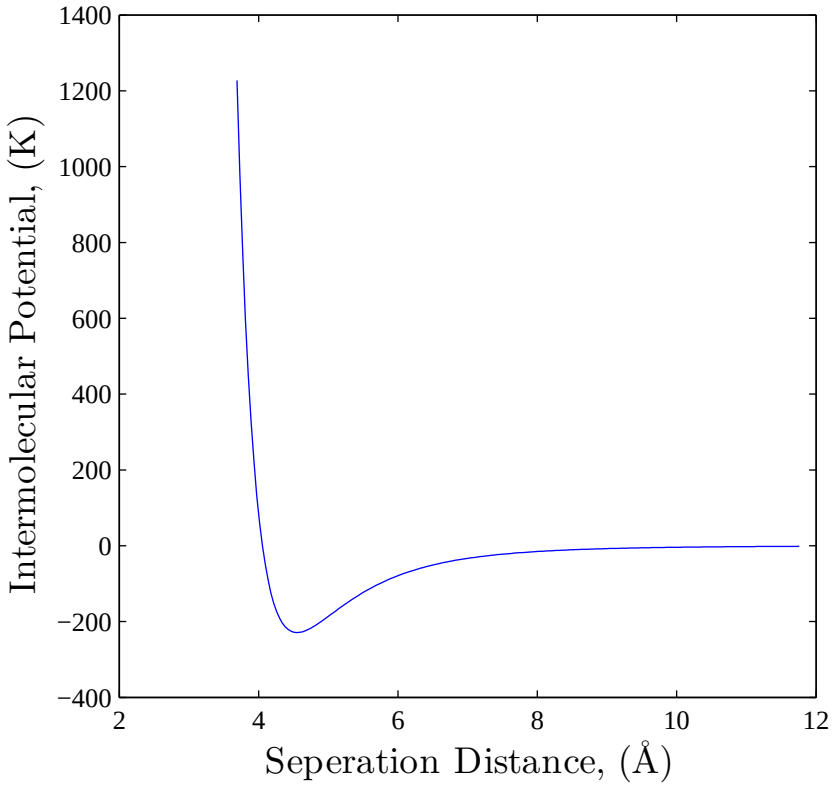

Figure IV.1: Lennard-Jones 6-12 potential for xenon

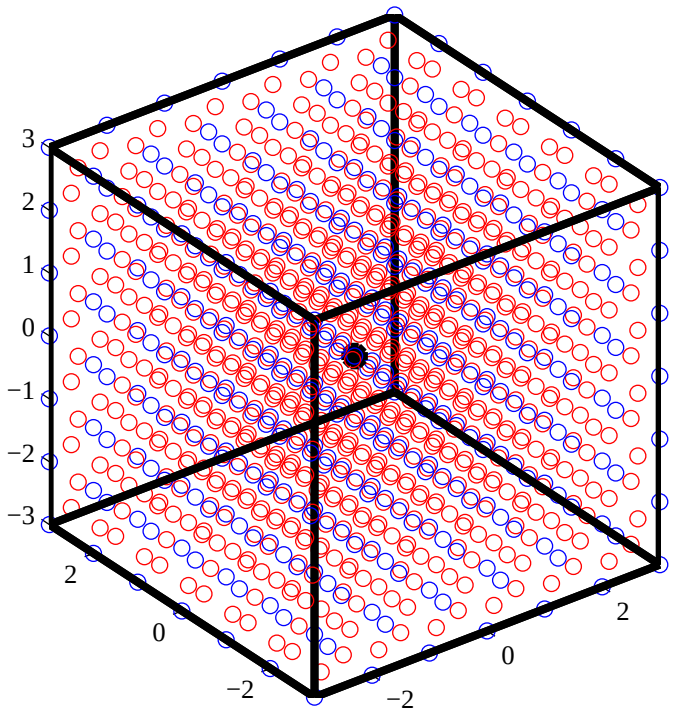

Figure IV.2: FCC crystal structure used to calculate minimum crystal potential. Blue points are lattice corners and red points are face centers.

$1971.5 \pm 0.1K$ was found. Figure IV.3 shows the result of this minimum search for the $20 \times 20 \times 20$ lattice. This plot shows a minimum potential of $-1971.4K$ at $6.25\mathring{A}$ crystal lattice spacing.

The well depth of $-1971.5K$ is the classical minimum of the potential, but doesn't account for the vibrational zero point energy that also must be included [38]. The value of this zero point vibrational energy can be obtained through the development of the debye approximation for the equation of state of a monatomic crystal, and this model is also needed to calculate the energy in xenon ice crystal at the target temperature.

Reference [37] provides a good description of the debye approximation for monatomic crystals which assumes low frequency normal modes of the crystal

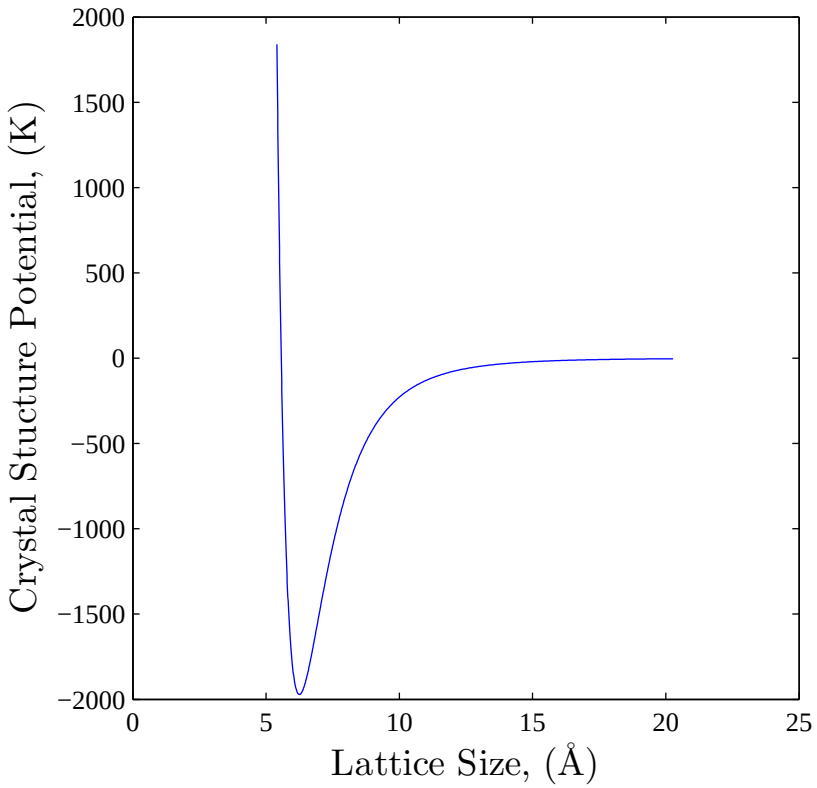

Figure IV.3: Crystal lattice potential versus lattice spacing for xenon

lattice. This results in an expression for the energy in the crystal of the form shown in Equation IV.2. In this equation, the Debye temperature is defined as $\Theta_D = h\nu_m/k_b$ where h is the Planck's constant and ν_m is a maximum cutoff frequency. The quantity $\phi(0)/2k_b$ is minimum potential of $-1971.5K$ for the xenon crystal and the $9/8\Theta_D$ is the crystal lattice zero point vibrational energy.

$$\frac{E}{k_b N} = \frac{\phi(0)}{2k_b} + \frac{9}{8}\Theta_D + 3\left(\frac{T}{\Theta_D}\right)^3 \int_0^{\Theta_D} \frac{x^3}{e^x - 1} dx \tag{IV.2}$$

.

Reference [24] provides experimental measurement the specific heat of solid Xenon between $1.5K$ and $24K$ providing high quality data in the temperature range relevant for xenon ice on a direct drive target. Though they find an equivalent Debye temperature of $64K$ at absolute zero, the value falls near $55K$ from $5-24K$ making it a better choice if a single value is selected for the entire range. This is particularly true because error in the higher temperature range plays a larger role in the error of integrating the specific heat curve for the crystal energy. Figure IV.4 compares the data points for the specific heat, c_v, relative the derivative of Equation IV.2 using a Debye temperature of $55K$.

Adding the vibrational zero point energy from the Debye temperature of $55K$ with the minimization of the Lennard-Jones crystal structure potential yields an energy change of $-1909.6K$. This represents the energy that must be removed from an ideal gas at $0K$ to form a crystal at $0K$. In Reference [26], the same quantity is calculated based on fitting sublimation data along the entire (solid+vapor) equilibrium curve and results in a value of $1916.032K$. These values differ by only 0.34% which is well below the $2-3$ digits of precision from the Lennard-Jones potential well depth and Debye temperature data. The agreement demonstrates the predictive power of the Lennard-Jones potential and Debye approximation. Despite coming from viscosity data and the shape of the specific heat curve at low temperatures, the theories can be used to predict the sublimation energy to within the error of the measurements.

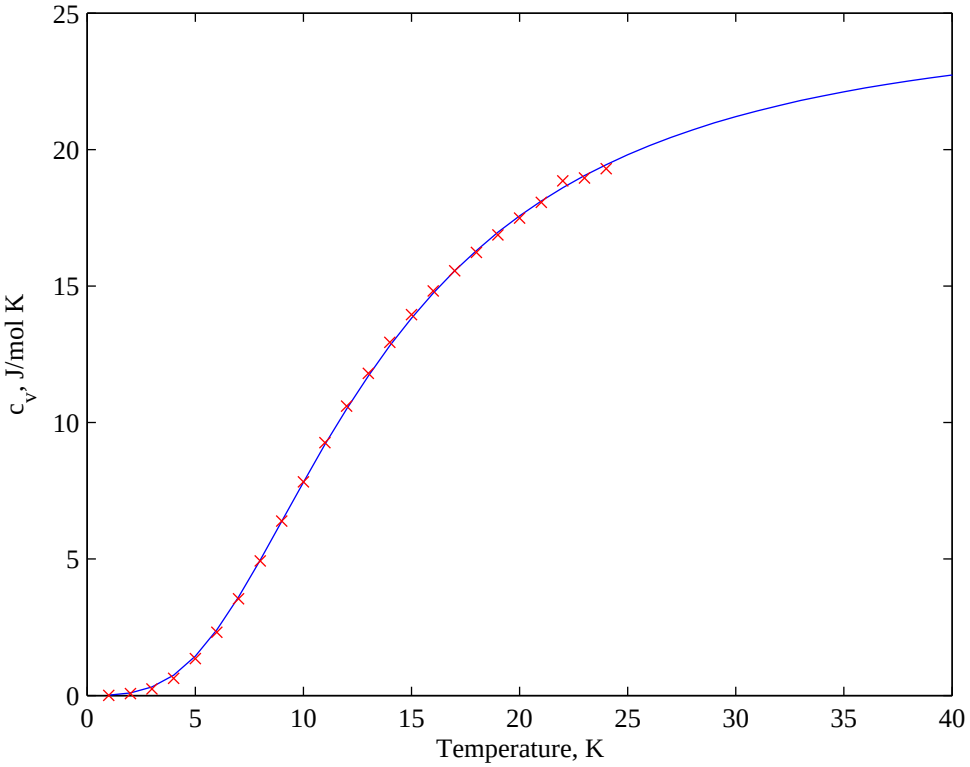

Figure IV.4: Experimentally measured xenon ice specific heat, c_v, and Debye approximation for $\Theta_D = 55K$

Figure IV.5 shows the Debye approximation for the xenon ice energy as well as the ideal gas law translated to $1916.032K$ energy at $0K$ to demonstrate the variation of sublimation energy with temperature. The energy released as a particle of xenon goes from high temperature gas to ice on the target surface can be found by following the ideal gas curve down to the freezing point temperature on a vapor pressure curve, calculating the value of $\Delta_s^g H$ at that point, and then continuing along the energy curve for the solid xenon down to the ice temperature. This process is even more complicated if the chamber pressure is above the triple point temperature and would require an equation of state for the liquid as well to calculate both the latent heats of vaporization and fusion as well as the variation of specific heat across the liquid phase. However, because the Debye approximation and ideal gas law curves are positioned absolutely with respect to each other, these more complicated paths are equivalent to following the ideal gas law down to the target temperature of $20K$ and then summing the contributions of $20K$ ideal gas down to $0K$, dropping the constant $-1916.032K$, and the adding back the $19.02K$ of energy for xenon ice at the target temperature of $20K$. This results in a latent heat of sublimation for $20K$ xenon gas to $20K$ xenon ice of $-1927K$.

The proceeding analysis applies to bulk xenon crystal on the target surface. It is worth noting that the first few layers of xenon ice differ from this configuration and are to some degree material dependent. Reference [53] provides detailed experimental analysis of xenon mono-layers through multi-layers on single crystal palladium. The latent heat of adsorption varies from $5133K$ to $4126K$ as the first monolayer fills. In the second layer, the the heat of adsorption is then $2919K$. Reference [53] then says the the multi-layers proceed with a latent heat of condensation of $1912K$ in good agreement with the results based on the the crystal analysis as well as the results of Reference [26]. Though depositing more energy than the subsequent layers, the first few layers alone pose little threat to the bulk of the target ice.

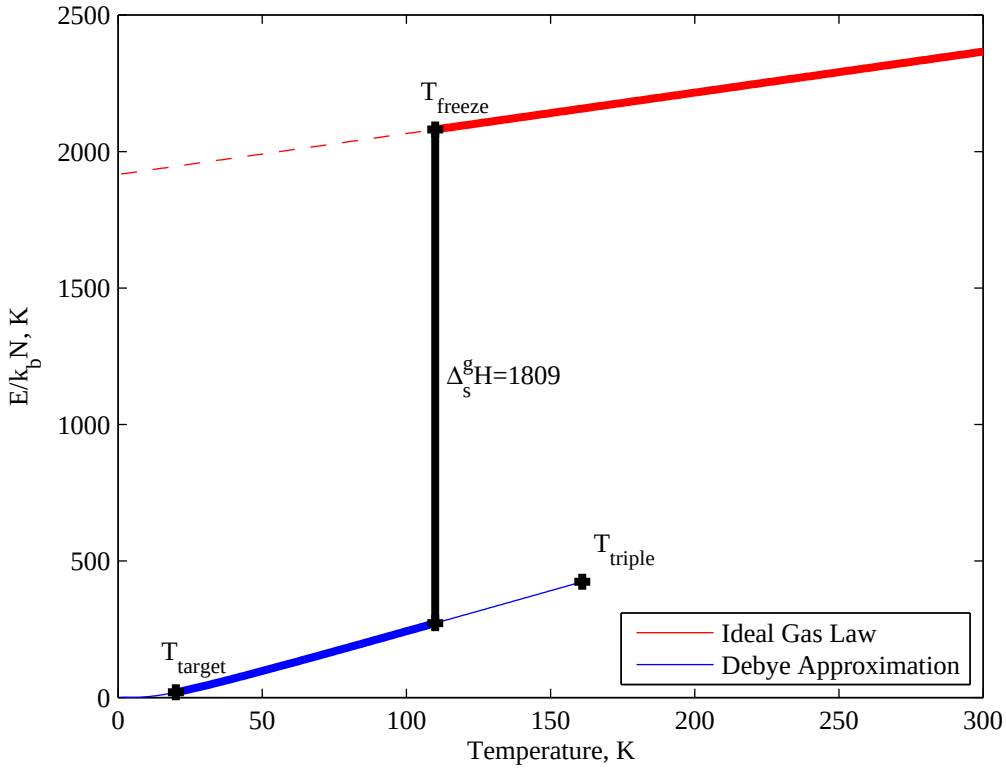

Figure IV.5: Xenon energy versus temperature in solid and gaseous form as a function of temperature from the Debye approximation and ideal gas law

IV.A.2 Target Heating Model Validation

When compared to Christensens Monte Carlo results with condensation at a xenon density of 3.33e19/m3 [19], Equation IV.1 matches the results to within the sampling scatter. To compare these results, the value for the latent heat of deposition is set to the sum of latent heats of fusion and vaporization at $1Atm$ from Christensens work for a total of $-1789K$. This value is smaller than the value calculated in Section IV.A.1 because the slope of the Debye approximation is larger than that of the ideal gas law.

For Knudsen numbers of 10 as in this case the agreement is expected. When Christensens 3.33e21/m3 xenon density results are compared to Equation IV.1, the Monte Carlo heat-fluxes are 2-3 times lower due to the shielding effect of reflected particles when no condensation is included. Breakdown of the free-molecular approximation is expected due to a Knudsen number of 0.1. However, when the sticking coefficient is set to unity for the case of fully condensing flow, the Monte Carlo results are again identical to the free molecular solution to within the sampling scatter. With full sticking, there are no reflected particles to shield the target from the incoming stream.

Because helium and deuterium do not condense at the target temperature, Christensens high density results cast some doubt on the applicability of the Equation IV.1 for the these cases. However, due to the smaller molecular diameters, the Knudsen number of these gases is larger than xenon at the same density and is at least on the order of 1. Figure IV.6 shows that the free molecular equation over-estimates the Monte Carlo peak heat flux for a 400m/s target in 1000 K helium by only 11% at a density of 1.65e21/m3 and 9.5% at a density of 1e21. These errors are much smaller than the uncertainty in the maximum survivable heat flux as well as the accommodation coefficient, and Equation IV.1 is therefore sufficient for a preliminary understanding of the design space.

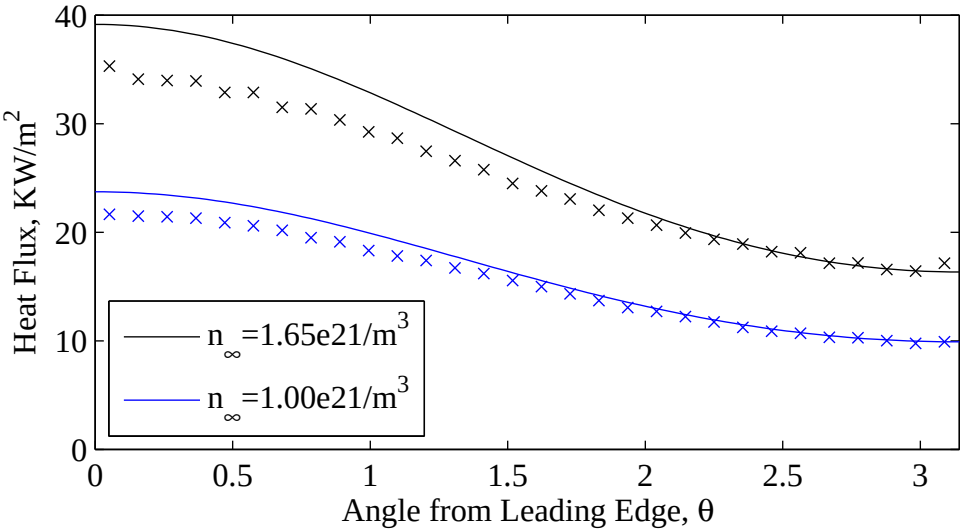

Figure IV.6: Heat flux versus angle from leading edge on a sphere for He gas. Solid lines are the free molecular heat fluxes from Equation IV.1 and x are Monte Carlo sampled values.

IV.B Target Survival in IFE Chamber Gas

As mentioned in the Section I.A.2, Boehm has performed a detailed analysis of the thermo-mechanical behavior of direct drive targets [13, 15]. The triple point limit is the heat flux that increases the target temperature to the melting point from a specified initial temperature. It remains uncertain whether melt alone is sufficient to cause target compression failure due to broken symmetry. In Boehms work, the triple-point limitation was relaxed to allow limited DT-ice melt subject to constraints due to ^{3}He bubble nucleation. Targets with longer shelf-lives have higher ^{3}He concentrations due to tritium decay and are therefore more likely to have larger initial ^{3}He nuclei. A selection of maximum heat flux limits for an initial target temperature of 18 K is listed in Table IV.1. Note that blackbody radiation adds an additional $0.2 KW/m^2$ depending on the wall temperature and target reflectivity, but for the purposes of this work is assumed small and within the error margin of the conductive heating. For 10m radius chambers, these survival times

Table IV.1: Max heat flux by survival time, KW/m^2

Failure Criteria	Survival Time		
	25 ms	50 ms	100 ms
Triple point	5.3	3.6	2.5
Initial 1.8μm ^{3}He Nucleus	14.9	10.0	7.0
Initial 0.4μm ^{3}He Nucleus	19.9	13.5	9.6

Table IV.2: Average chamber gas density, temperature, and 400 m/s injection speed parameter at t=100 ms.

Gas	$n(\times 10^{21} m^{-3})$	$T(K)$	Speed, s_{400}
D	1.0	763	0.16
	1.65	743	0.16
He	1.0	1047	0.19
	1.65	885	0.21
Xe	0.1	2386	0.73
	1.65	4115	0.55

correspond to 400, 200, and 100 m/s target injection speeds respectively. These values result from interpolation on the survival curves of Figure I.1 as shown in Figure IV.7.

Figures IV.8 through IV.10 show the chamber state points from Table IV.2 relative to Equation IV.1 contours of the maximum heat flux for the different failure criteria listed in Table IV.1. In the figures, the 'b' symbol is reference to the state resulting from the 'wedge+beamline' domain. Figure IV.10 also includes points marked with 's' which are the average temperature results for spherical chambers to show the effect of the additional surface area. For the helium and deuterium cases, these points were omitted because they were only slightly further from T_{wall} and overlapped with the sphere+beamline points.

It is also interesting to note that the xenon cases favor lower injection speeds. This is the result of the impact of the both the lower sound speed and condensation which will be discussed in more detail in the following section. The 200 m/s curve being the least restrictive constraint for xenon chamber densities above approximately 2000K implies that an optimal injection speed occurs between

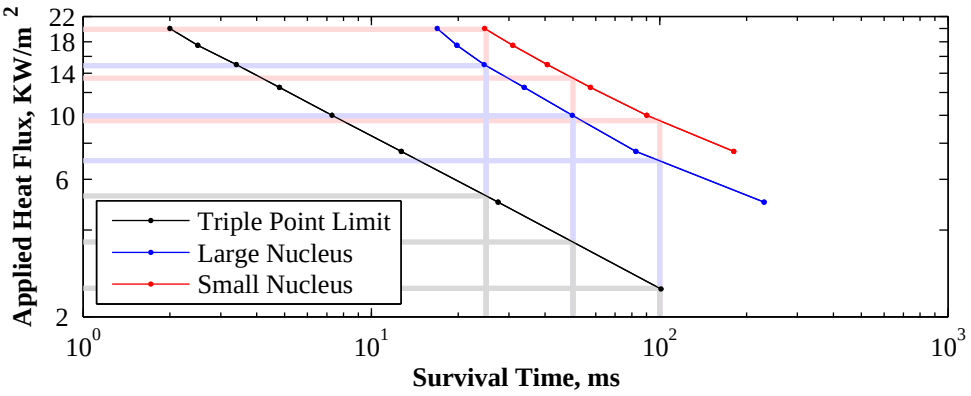

Figure IV.7: Allowable heat fluxes for 25, 50, and 100 ms survival times by target failure mode for initially $18K$ IFE target with $4mm$ diameter

the 100 m/s and 400 m/s limit. In Reference [18], it was also found that 200 m/s injection speed were superior to 100 and 400 m/s in xenon for the conditions they considered. It is also interesting to note that the low density xenon spherical chamber fails to satisfy the triple point constraint whereas the addition of the beamline adds sufficient conductive cooling to meet the constraint.

IV.B.1 Target Heating Scaling Relationships

The asymptotic limits of Equation IV.1 provide insight to the behavior of curves in Figure 3 and provide leading term scaling laws describing the flow regime. The dimensional term in Equation IV.1 scales like $(n_\infty T_\infty^{3/2})/m^{1/2}$. The peak heat-flux occurs when $\alpha = \pi/2$ which corresponds to the leading edge of the target. As s approaches 0, Γ approaches 1 and the inside of the bracket approaches $\hat{Q}_0 - 1/2$. When the target approaches the thermal velocity of the gas, s approaches 1 and the behavior changes completely. As s increases, Γ asymptotes to $2\pi^{1/2}s$. The heat-flux term then scales like $n_\infty T_\infty U_\infty$. In Figure 3, lower temperature corresponds to higher s values for the same injection speed.

The dominant terms of for subsonic injection speeds and target temperatures that are significantly lower than the background gas are the $\gamma/(\gamma-1)$ term

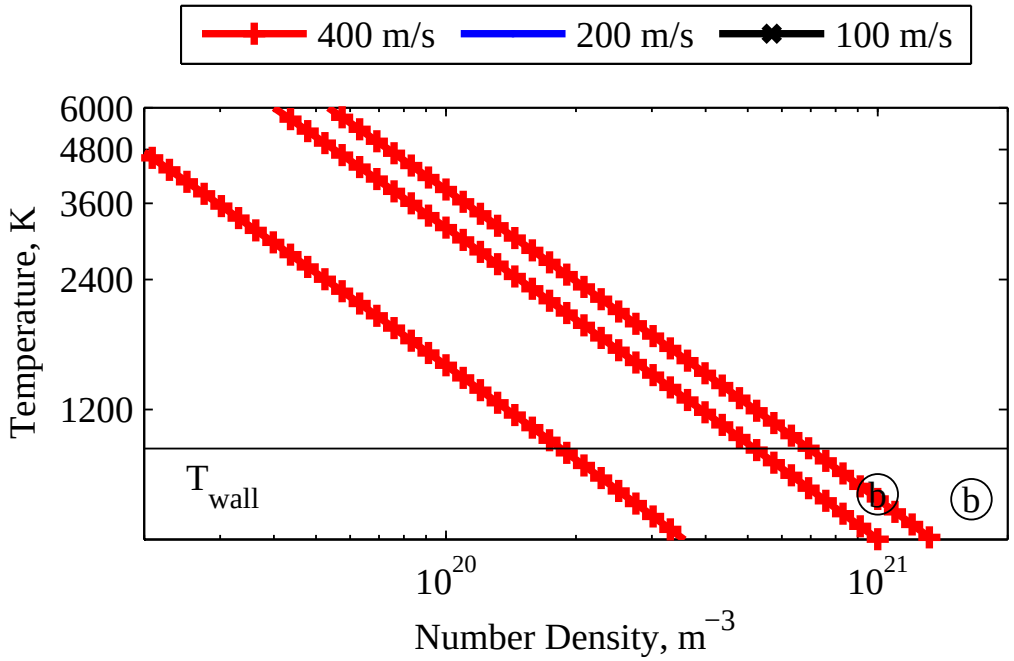

Figure IV.8: Deuterium chamber sphere+beamline (b) states at 100 ms relative to maximum heat-flux contours. Bottom line is restrictive Triple-point criteria and top line is 0.4μm ^{3}He nucleus criteria. Colder and more rarefied states relative to the lines satisfy corresponding constraint. Safest of injection speeds for a given constraint is denoted by line color.

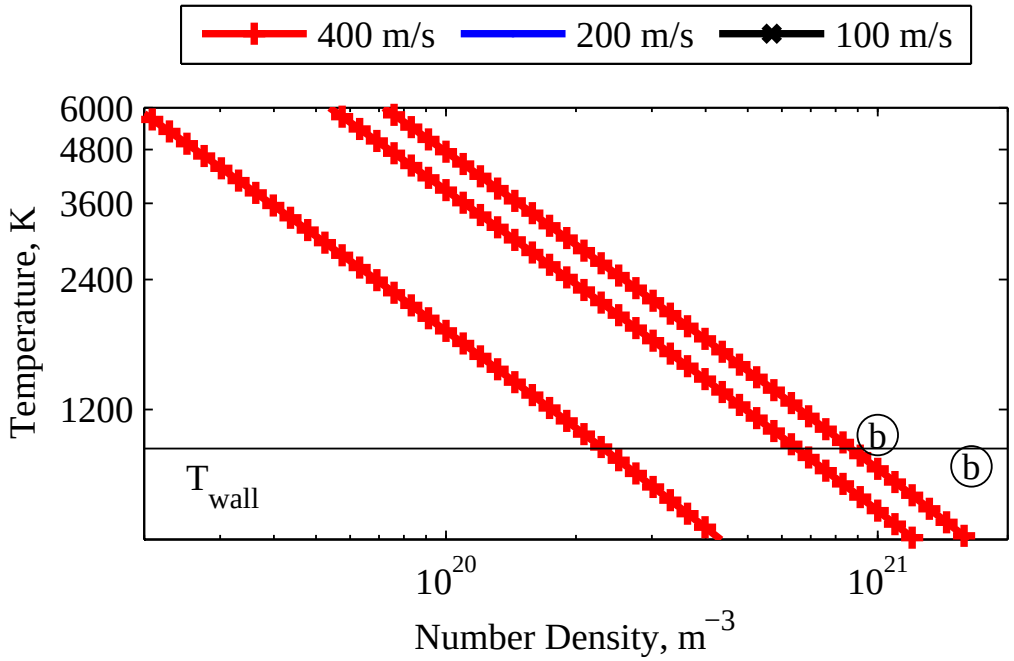

Figure IV.9: Helium chamber sphere+beamline (b) states at 100 ms relative to maximum heat-flux contours. Bottom line is restrictive Triple-point criteria and top line is 0.4μm ^{3}He nucleus criteria. Colder and more rarefied states relative to the lines satisfy corresponding constraint. Safest of injection speeds for a given constraint is denoted by line color.

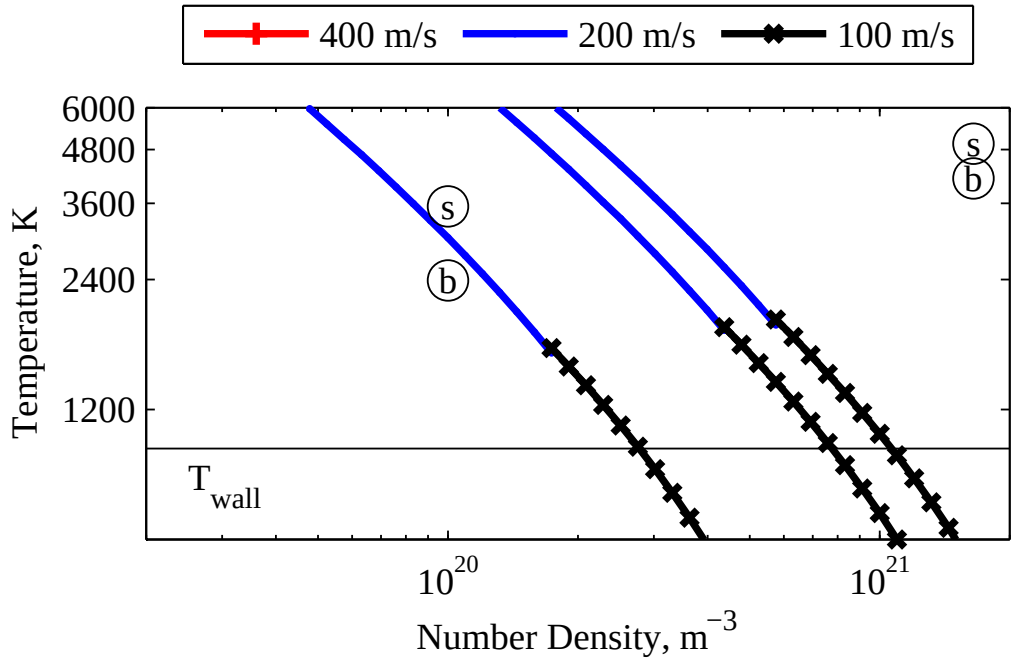

Figure IV.10: Xenon chamber sphere (s) and sphere+beamline (b) states at 100 ms relative to maximum heat-flux contours. Bottom line is restrictive Triple-point criteria and top line is 0.4μm ^{3}He nucleus criteria. Colder and more rarefied states relative to the lines satisfy corresponding constraint. Safest of injection speeds for a given constraint is denoted by line color.

Table IV.3: Target heat-flux scaling powers

Regime	Speed	Heat Scaling
Non-Condensation Dominated	$s \to 0$	$n_\infty m^{-1/2} T_\infty^{3/2}$
	$s \to 1$	$n_\infty U_\infty T_\infty$
Condensation Dominated	$s \to 0$	$n_\infty m^{1/2} T_\infty^{1/2}$
	$s \to 1$	$n_\infty m U_\infty$

and the term involving the latent heat whenever the sticking coefficient approaches unity. When comparing the magnitude of these two terms in the full condensation limit, $\sigma_c = 1$, multiplying through by $k_b T_\infty / m$ shows that the term is dominated by the latent heat term if $C_p T_\infty \ll \Delta_s^g H$. In xenon, these contributions cross at approximately $T_\infty = 771K$. In this condensation dominated regime, heat flux scales like $n_\infty T_\infty^{1/2} m^{1/2}$ instead of $n_\infty T_\infty^{3/2} / m^{1/2}$.

Table IV.3 summarizes these scaling laws for the regimes under consideration. The non-condensation dominated regime corresponds to the cases with either negligible sticking coefficient or those cases such that $C_p T_\infty \gg \Delta_s^g H$. From this table, we see that the heat-flux temperature dependence only exceeds the density dependence with slow injection in the Non-condensation dominated regime. This corresponds to T(n) iso-heatflux contours with a $-2/3^{rds}$ slope in the deuterium and helium plots, Figures IV.8 and IV.9. The slope of these iso-heatflux contours relative to $1:1$ is important because it determines whether the heatflux for a given chamber pressure can be improved by moving towards lower density hotter states or higher density colder states.

IV.C Survival in Mixture Chambers

In the free molecular approximation, the surface heat flux due to a mixture gas is simply the sum of the individual gas contributions. This makes calculation of the heat flux on the target in the chamber composed of 90:10 xenon to target byproducts a simple extension of the previous section with one notable exception. Though the hydrogen isotopes and helium will not freeze on the target

surface, carbon vapor would. This difficulty is compounded because graphite does not behave the same as the bulk monatomic crystal xenon[32] with much of the vibrational energy localized to two dimensions. The carbon is also only a small fraction of the mixture however, so uncertainty in the heat of deposition affects the total heat flux negligibly. Reference [39] determines a value of $85,547K$ at $0K$ for graphite's latent heat of sublimation. This value is much larger than the xenon value, but should be expected for a material with a high melting point. The effect of carbon atoms within the xenon ice lattice is also unknown, but left to future research.

Figure IV.11 shows the mixture chamber states relative to the target survival constraints. The low density gas satisfies all of the constraints whereas the high density case fails all of the criteria. Note that the spherical chamber fails the triple point criteria in the pure xenon case, but satisfies the constraint in the mixture. The low density point does not satisfy the triple point constraint by a wide margin despite being much colder because of the effect of the carbon condensation. Again, in this analysis the carbon is assumed to stick to the target with a sticking coefficient of 1 which may be unrealistically high but prevents underestimation of the contribution. The mixture gas also favors higher injection speeds than the pure xenon case. This is likely due to the interaction of the higher thermal speed of the carbon with the carbon condensation.

IV.D Chamber Density Iteration

Extrapolating the chamber states to the constraint curves provides an estimate for the survivable densities. Though the true chamber states will deviate from the extrapolations when far from calculated points, this process allows for an iterative search of the design space. Once the densities from these extrapolations are provided as initial conditions for new BUCKY simulations, the additional points will allow for better estimates of the optimal chamber conditions. The re-

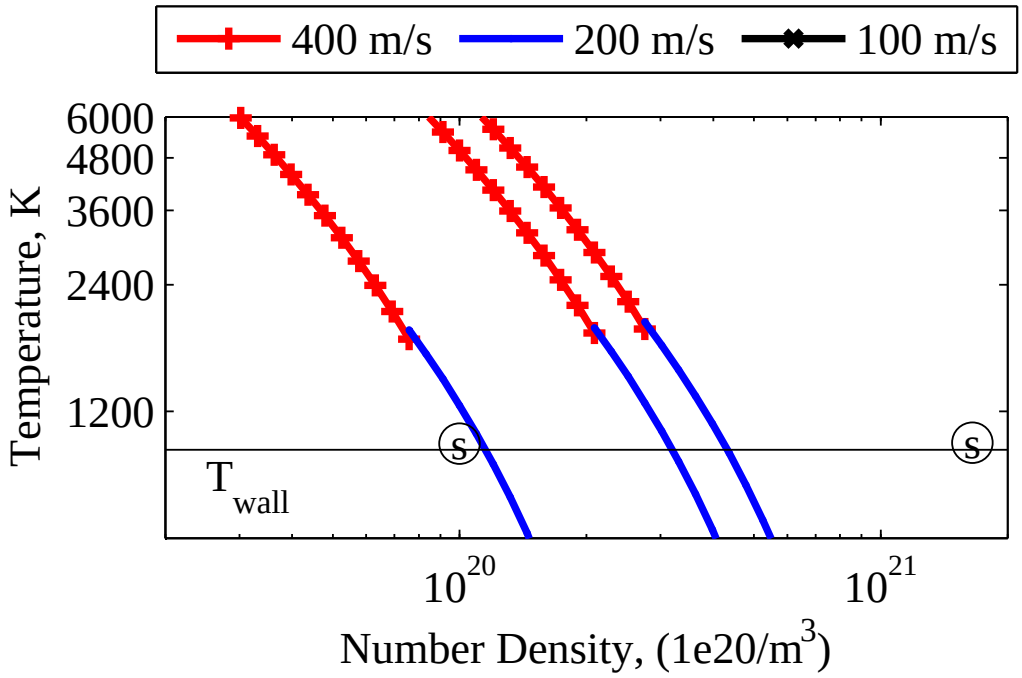

Figure IV.11: Xenon-target gas 90:10 mixture spherical chamber (s) states at 100 ms relative to maximum heat-flux contours. Bottom line is Triple-point criteria and top line is 0.4μm ^{3}He nucleus criteria. Colder and more rarefied states relative to the lines satisfy corresponding constraint. Safest of injection speeds for a given constraint is denoted by line color.

Table IV.4: Estimated survivable chamber densities by gas, geometry, and target heating constraint

Gas (Geometry)	Triple Point n ($\times 10^{20}/m^3$)	$1.8\mu m$ Nucleus n ($\times 10^{20}/m^3$)	$0.4\mu m$ Nucleus n ($\times 10^{20}/m^3$)
Deuterium (Sphere+Beam)	2.47	7.13	9.65
Helium (Sphere+Beam)	1.65	5.11	7.27
Xenon (Sphere)	0.85	2.27	3.01
Xenon (Sphere+Beam)	1.23	3.16	4.11
90:10 Xe-Target (Sphere)	1.13	3.14	4.23

sults of the first step of such an iteration are provided in Table IV.4 for potentially safe chamber densities.

Note that the difference between the geometries for the xenon case assume that the chamber density is the original average density prior to gas flowing into the beamline and average chamber temperature. The points densities listed in the table are defined in a similar manner. The actual chamber gas density would be lower with a higher temperature such that the pressure is approximately matched between the chamber and beam densities.

The estimates in Table IV.4 are for the best injection speed out of 100, 200, and 400 m/s. The helium and deuterium points result from the $400m/s$ injection speed while the xenon and mixture points listed are for the $200m/s$ injection speed. Some additional optimization could be performed allowing any injection speed between 100 and 400 m/s for the xenon and mixture cases, but these estimates are sufficient for a first iteration.

IV.E Hydrogen Isotope Recombination

The dramatic impact of carbon in the mixture chamber gas brought another potential issue for target survival to light. Though the hydrogen isotopes will not freeze on the target surface, if the chamber density is low enough, the hydrogen isotopes will not have a sufficient number three-body collisions to recom-

bine before the subsequent chamber burn dissociates all of the gas again. However, the as the target moves through the dissociated hydrogen, the potential exists for recombination to occur on the surface. Each recombination releases on the order of $52,000K$ of energy [36] though only a fraction is deposited on the surface as the newly formed molecule would carry significant energy off the surface. However, this means hydrogen recombination has the potential to be many times more dangerous than than xenon deposition if the recombination coefficient is significant.

Reference [88] examines the catalytic surface recombination of hydrogen on a wide array of metal materials. In particular, both gold as well as palladium and gold-palladium mixture surfaces were studied. Though the recombination coefficients listed are for temperatures of hundreds of Kelvin, the palladium, gold, and gold-palladium mixtures have values in the range of 0.08-0.3 that increase with decreased temperature. Reference [40] studies the recombination of hydrogen on space dust particles composed of ice or graphite. If the target surface has some impurities or lattice defects, the recombination coefficient may be nearly 1 at temperatures as high as $25 - 50K$.

This suggests that running a very low density chamber composed of only target byproducts may pose a greater risk to the target than estimated in prior work. The energy deposited from the hydrogen recombination could easily be an order of magnitude more than the deposition of xenon on the surface such that the risk resulting from the 9% hydrogen isotopes in the mixture gas might be on the same order as that of the xenon. Furthermore, this would imply that the heat flux would only be approximately doubled going from chamber byproducts at a density of $1e19/m^3$ to the 90:10 xenon-target mixture at $1e20/m^3$. However, the amount of atomic hydrogen needs to be considered in detail. Though the number of three-body collisions becomes vanishingly small with low enough densities, the diffusivity of the gas will increase such that the wall may play a major role in hydrogen recombination. These rough estimates must be refined in future work as they have the potential to dramatically change the target survival characteristics.

IV.F Cold Helium Injection

As another concept to mitigate target damage, injection the target within a mass of cold higher density gas is considered. Because xenon begins condensing on its own at much higher temperatures than the target, helium is a better choice for this gas. In fact, helium has been used in hypersonic wind-tunnel facilities expanded all the way down to $2K$ yielding Mach numbers in the 20s [6].

Consider a closed loop helium wind tunnel mounted on the side of the IFE chamber. With proper selection of the reservoir density and temperature, a steady Mach 2 flow could be created at a temperature of $18K$ at $400m/s$ to match the target temperature. Because the flow is supersonic, it could be diverted with an angled shutter as the diffuser and the flow upstream from the oblique shock would remain undisturbed. The target could then be injected into this stream rather than directly into the chamber. As the target approached the shutters, they would open allowing a mass of Mach 2 helium to enter the chamber. If the density of this gas is selected such that the static pressure matches that of the chamber gas, this mass of air would continue into the chamber with the same cross section. Because the injected gas is on the order of $50\times$ denser than the chamber gas to match the static pressure of the chamber, its momentum could then carry it to the chamber center with the target entrained. Figure IV.12 depicts this concept.

Note that for this concept, the target is still injected into this stream rather than allowing the gas to accelerate the target from rest. The density required to accelerate the target when matched to the chamber pressure would likely result in residual chamber momentum that could significantly impact the target trajectory. However, this assumption may be investigated further in the future.

Not only would this help protect the target from the hot chamber gas, the gas near the target would block target byproduct hydrogen and carbon from interacting with the surface. This also allows a region of higher density gas to be included to absorb the burn ions. Because the ion flux is highest at the target,

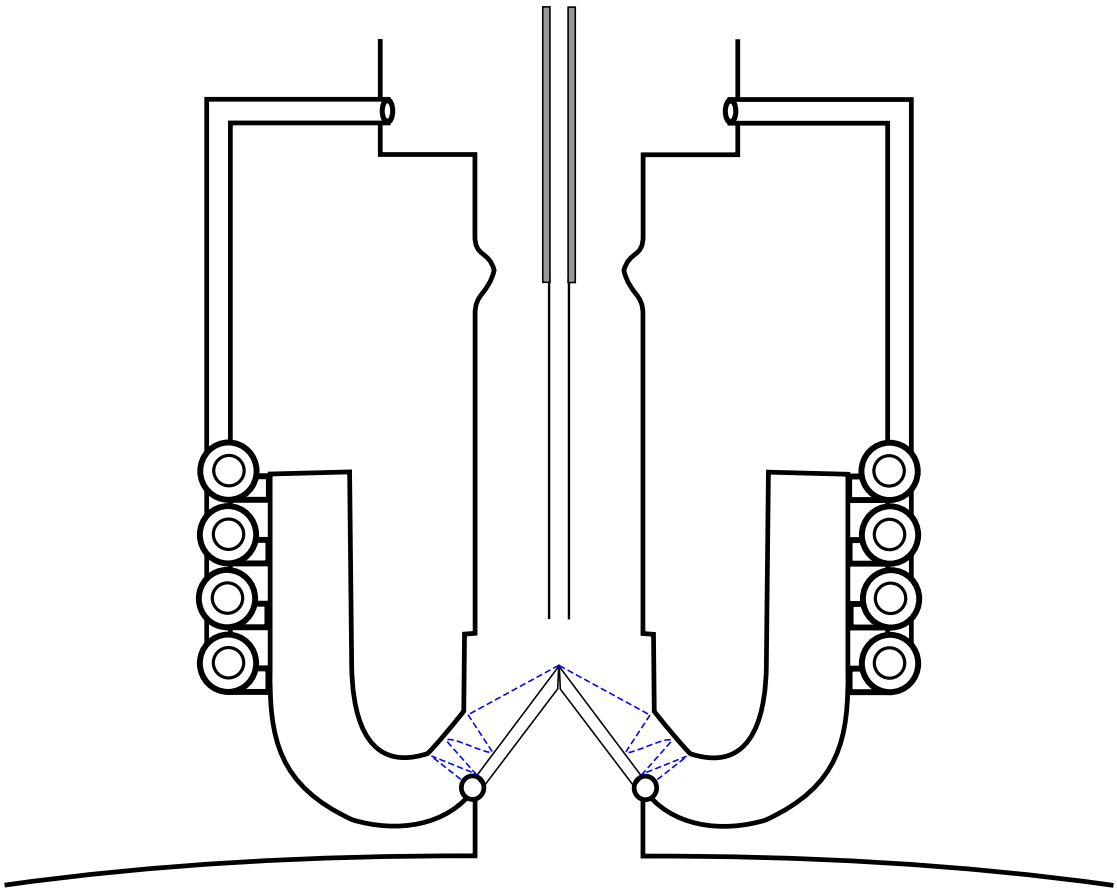

Figure IV.12: Cold helium target injection concept layout. Blue dashed lines are shocks forming the wind tunnel diffuser

higher density gas near the target efficiently blocks more of the ions with the least amount of gas in the chamber overall. At sufficiently high densities, the additional gas could potentially impact laser propagation to the target, but is likely not a problem until the density approaches a significant fraction of atmospheric density as indirect-drive target designs for the LIFE project are filled to 1/3rd atmospheric density helium.

Because the impact of target byproduct hydrogen and carbon on the surface of the target may play an important role on target survival, the high density helium case was rerun with a composition like the 90:10 xenon-target mixture replacing the 90% xenon with helium. The jet was then defined to contain $2.22e22$ particles which is $10\times$ the number of particles as is in the HAPL reference target. This allows simulation of the jet in a background gas of similar composition to a actual chamber in which the jet and target compose the bulk of material injected. This also allows calculation of the diffusion of helium and carbon towards the target surface to estimate if the jet is successful at blocking these gases. Because the jet is cold and at a considerably higher density than allowable in chamber gas alone, the hydrogen would likely recombine in this gas prior to arriving at the surface. The additional heating of the jet gas due to such recombination is beyond the scope of these simulations.

Given a target temperature of $18K$ and background chamber density and temperature of $1.65e21/m^3$ and approximately wall temperature results in a jet density of $8.92e22/m^3$. The $2.2e22$ particles of the jet would then be contained in a volume of approximately $0.25m^3$. This volume along with a geometric aspect ratio is sufficient to fully define an injection jet. Note that the design of the gas injector would be simplest with a square orifice, but because the simulations are axisymmetric a cylindrical geometry is used. An aspect ratio of 2:1 length to diameter for the cylindrical jet geometry is selected as an initial possible shape. This results in a cylindrical jet of radius $27cm$ and length 1.08 meters. With the injection speed of $400m/s$ this results in an open injector shutter of $2.7ms$.

Figure IV.13 shows the propagation of this jet through the hot chamber gas. Though the jet was started at $70ms$ to allow for some extra flight time as the gas slowed, it was found to require an additional $3ms$ to arrive at the chamber center. For reference, the figure includes circles marking the position of a target injected at $70ms$ with constant speed selected to arrive at chamber center at $103ms$ with the jet. Though the gas flowing past the target will result in some acceleration, the target density is such that the net effect is small. However, accurate positioning of the target is important for laser pointing and so the impact of this gas on target deflection whether positive or negative will be an important effect to quantify in future work. Also note that a coarse $10cm$ grid was used to evolve the helium mixture until the jet injection time. Around the jet, 2 levels of adaptive mesh refinement were used to drop the cell size to $2.5cm$ in the jet vicinity. The grid was adapted 1 level in the vicinity of walls and 2 levels wherever injected tracer gas of initially helium density exceed 0.1% of the gas mass fraction. The adaptive grids are shown as gray boxes in the figure. In the future, higher resolution simulations should be performed to better represent the jet evolution.

The times shown in the plot are the starting time of $70ms$, the jet turnoff time at $72.7ms$ and then three more times leading up to the gas and target center time of $103ms$. The resulting temperature and helium fraction on the axis of symmetry for these same times and positions are shown in Table IV.5. Though the figure focuses on the region around the jet injection, the simulations are of the full spherical chamber so that the impact of the chamber gas oscillations are included in the simulation. For reference, the background chamber gas is 91.0% helium as a result of the burn products and jet gas from prior target injections. It is important to note that the initial temperature drop is the result of slight jet expansion due to a slight overestimation of chamber temperature and pressure in selection of jet conditions.

These temperatures on average are an order of magnitude improvement and are likely a significant improvement to the target heat load as well. However,

a full analysis of the resulting heat-flux requires a transient Monte Carlo simulations due to much higher density gas and more variation in gas properties and is left for future work. Though these results have much lower relative speeds than injection directly into chamber gas, it is important to point out that the reduction in survivable heat flux at slower speeds is due to the residence time within the chamber rather than the gas-surface interaction. The allowable heat flux is still based on the transit time, and the heat flux is likely reduced further as reflected target particles shield the target better at low speed.

The highest temperature point and lowest helium purity point in Table IV.5 results from the target falling behind the cold gas before catching up again at the final time. To determine if these results could be improved further, a jet with identical mass but a 10:1 aspect ratio is also considered. The initial density, temperature, velocity, and jet volume remain the same as the prior case. However, the radius is decreased to $15.8cm$ and the length is increased to $3.19m$ before the jet shutter is closed. This results in an $7.969ms$ open time. Note also that due to the smaller radius, three levels of adaptive mesh refinement were used in the vicinity of this jet such that cells around the jet are $1.25cm$ wide. Because the jet input boundary condition only applies to full width cells, on the finest level the jet has a width of only $15.625cm$ and was left open a slightly longer $8.1ms$ but retains an approximately correct mass and intended aspect ratio. Figure IV.14 and Table IV.6 show the results for this jet.

For this higher aspect ratio jet, the target injection was delayed to $3ms$ after the jet and a final time of $99.4ms$ was selected to ensure that the target remained embedded within the jet to avoid chamber gas heat and impurities. This resulted in low temperatures and high helium purity throughout the target flight. Figures IV.15 and IV.16 show line traces of these temperature and purities throughout the injection. Note that the peak impurity remains below $5e-6\%$ throughout the injection significantly diminishing the potential impact of target surface reactions. The target also spends the majority of the flight at temperatures below the

Table IV.5: Target position, temperature, and vicinity gas helium fraction for selected times in 2:1 aspect ratio cold helium jet of 10× target particle number

Time (ms)	Position (m)	Temperature (K)	Helium Fraction
70	10.00	18.00	100.0%
72.7	9.18	17.37	100.0%
81	6.67	15.57	100.0%
92	3.33	110.53	98.0%
103	0.00	55.57	99.3%

DT melt temperature with a peak at only $45K$.

Because the jet and chamber densities scale proportional to the temperature jump, these jet results hold the promise of allowing the chamber density to be increased significantly. This holds the potential of allowing the entire system to be operated in a regime capable of stopping fast ions. It would also facilitate construction of smaller and less expensive chambers and vacuum systems. Though generally less restrictive than direct-drive target injection, a similar sacrificial gas layer could potentially improve indirect-drive target and chamber performance as well. However, increasing the density also increases the Reynolds number of the jet and the growth rate of instability of the shear layer may become a limiting factor.

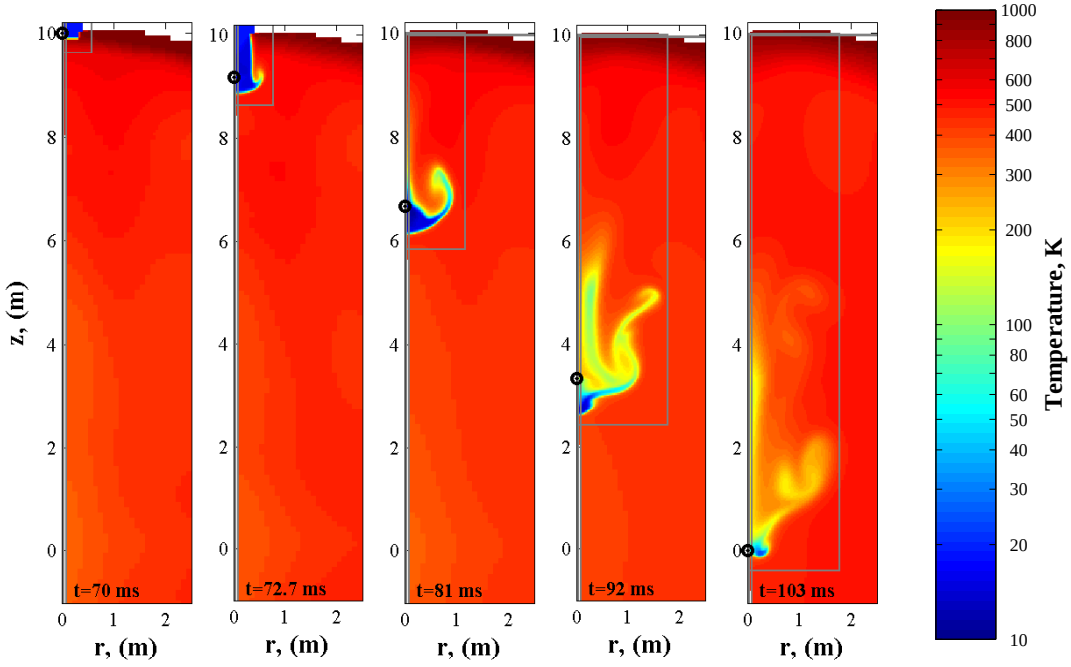

Figure IV.13: Cold helium jet injection of 10× target particle number and 2:1 aspect ratio with target position marked with (○)

Table IV.6: Target position, temperature, and vicinity gas helium fraction for selected times in 10:1 aspect ratio cold helium jet of 10× target particle number

Time (ms)	Position (m)	Temperature (K)	Helium Fraction
72.9	10.00	18.00	100.0%
78.1	8.08	14.92	100.0%
79.7	7.44	19.23	100.0%
89.7	3.66	17.80	100.0%
99.40	0.00	16.56	100.0%

Chapter 4, in part, is a reprint of material submitted to Fusion Science and Technology, November 2010. Martin, R.; Najmabadi, F., 2010. The dissertation author was the primary investigator and author of this paper.

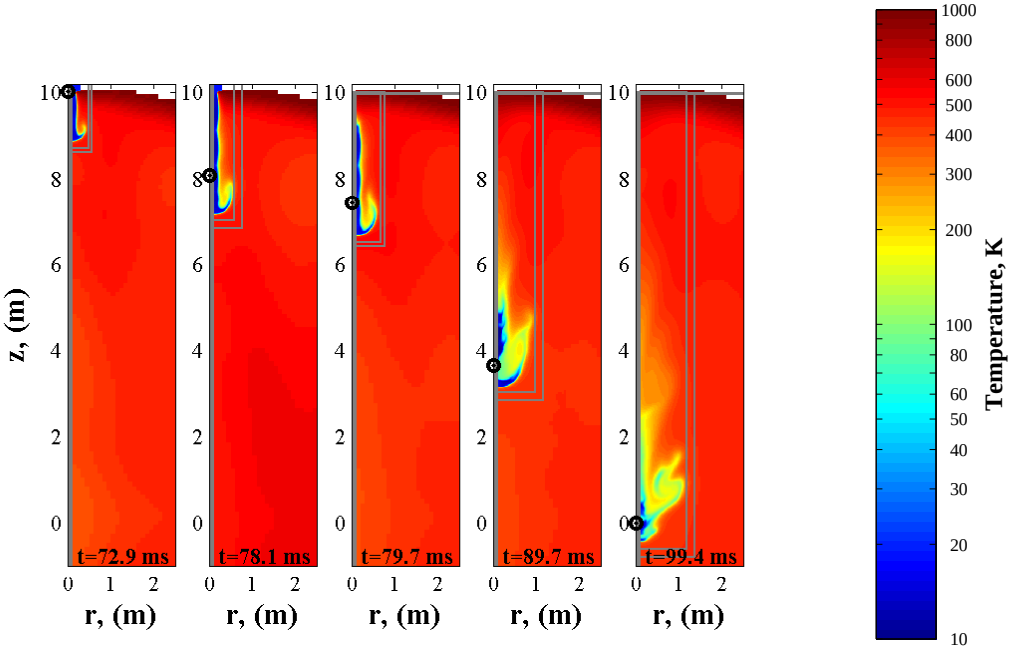

Figure IV.14: Cold helium jet injection of 10× target particle number and 10:1 aspect ratio with target position marked with (○)

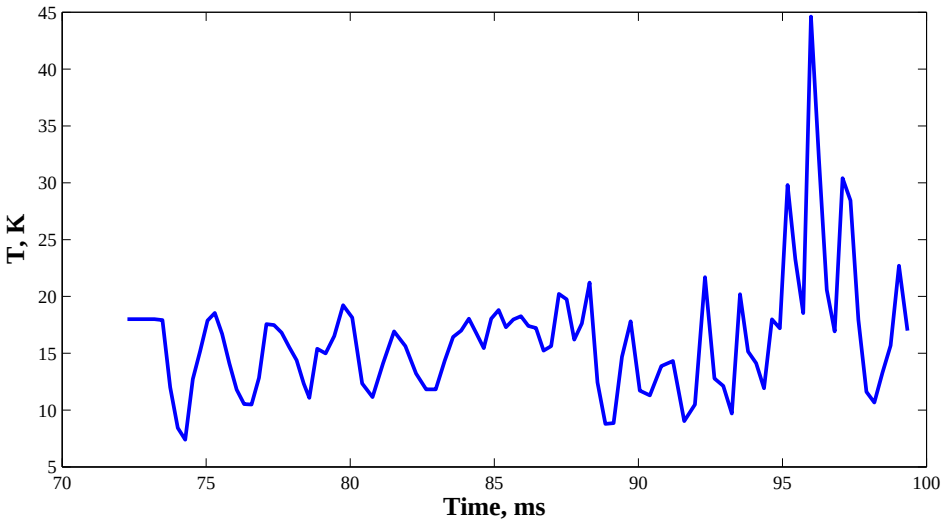

Figure IV.15: Temperature in target vicinity for cold helium jet injection of 10× target particle number and 10:1 aspect ratio

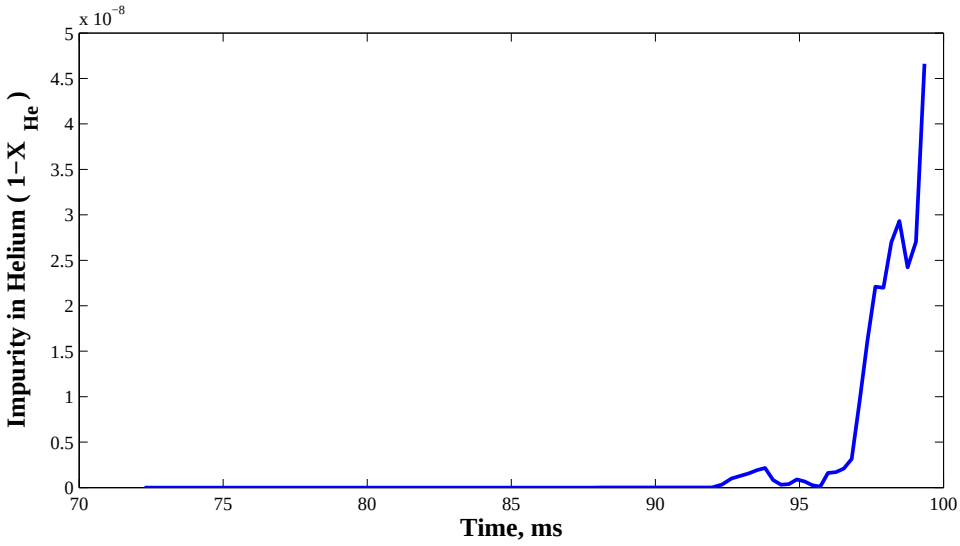

Figure IV.16: Helium impurity in target vicinity for cold helium jet injection of 10× target particle number and 10:1 aspect ratio

Chapter V

Summary and Conclusion

V.A Algorithm Development

A novel algorithm has been created and validated for compressible viscous gas mixtures based on an improved single gas framework for radiating inertial fusion energy chamber gas. Several updates were made to the base single gas code to ensure the correct treatment of viscosity in cylindrical configurations as well as boundary condition convergence. New radiation sources for the simulations were produced using IONMIX and to reduce error caused by the bounds and interpolation within the radiation source table. The calculation of transport properties was also switched to a model derived from kinetic theory based on collision integrals using Lennard-Jones potentials. This change enables calculation of transport properties for any gas over a wide range of temperatures based on two experimentally determined values.

In the extension of the model to multiple mixed gases, the full constitutive expression for diffusion based on the Chapman-Enskog small perturbation solution to the gas mixture Boltzmann equation was employed. In this model, along with the standard Fickian diffusion, gases diffuse relative to each other due to temperature and pressure gradients. These are the same effects that drive thermophoresis and the centrifugal separation of gases and derived in this manner

allow the estimation of needed diffusion and thermal diffusion coefficients from the Lennard-Jones collision model as well. The resulting diffusion velocities were then incorporated into the flux calculations of the Godunov solver to create a new algorithm for a complete multi-dimensional fluid model of the time dependent evolution compressible viscous fluid mixtures.

The performance of this new algorithm was then characterized. First, a modification of the time-step limit to promote stability was proposed to account for the different types of diffusivity. The algorithm was then validated through comparison with experimental results and Monte Carlo simulations of mixture jets and shocks. The performance was quantified in terms of convergence rates as well as the breakdown of the underlying physical formulation for highly non-equilibrium flow. This highly non-equilibrium flow was also studied in more detail in the context of a diffusion flux limit. Monte Carlo simulations of binary gas suggest that such a limit my be physical rather than purely a numerical convenience though more work is necessary to develop this limit for mixtures. However, this limit also enabled estimation of reasonable bounds for the algorithm's applicability.

V.B Chamber Gas Simulation

The new version of the fluid code was then applied to study the evolution of IFE chamber gas in several different configurations. Pure xenon cases were focused on first. Care was taken to the necessary grid refinement to ensure converged wall heat fluxes as well as kinetic energy spectral convergence. The effect of chamber geometry was then considered. Spherical, cylindrical, and wedge+beamline configurations were studied along with a wedge validation case to ensure the error imposed by simulation of a fraction of a spherical domain was not prohibitive.

The cylindrical configuration yielded effectively negligible temperature difference when compared to spherical chambers. This was identified as likely the result of the choice of cylindrical chamber geometries having the same surface area

to volume ratio as the sphere though not necessarily the case for a cylinder of different aspect ratio. Though converging to a similar temperature, the cylinder would require increased vacuum pumping to account for the larger volume.

Simulations of the wedge confirmed that the error introduced by the approximate domain was only slight. This allowed the beamline cases to be considered. The beamline cases demonstrated greatly enhanced conductive cooling as a result of the increased surface area to volume ratio. The temperature of gas within the beamline drops quickly and gas rapidly flows from the chamber into the beamline in xenon simulations. These results also suggest that increased chamber surface area to volume ratios though addition surface area such as a honey comb structured surface with cell sizes proportional to the 20-100x mean paths could potentially increase conductive cooling substantially. However, this concept is left for future work.

Helium and deuterium gas cases were then considered. As a result of strongly enhanced radiation source terms, these gases cooled much more rapidly than xenon. The BUCKY results also suggest significantly more kinetic energy in these gases which is reasonable as the burn ions would couple more momentum to lighter gases before thermalizing. As the gas radiatively cools, the sound speed drops and the initial pressure wave steepens dramatically. The resulting density and temperature spike allows the gas to radiate strongly resulting in average chamber temperatures that drop as low as the wall temperature. In helium and deuterium, this pressure wave propagates to the wall evacuating the chamber center. This gas then bounces from the walls to the chamber center for the remainder of the inter-injection time with diminishing amplitude. Because the radiative cooling can drop the temperature of the gas near or below the wall temperature, the effect of heat conduction to the walls is considerably smaller in these cases though a similar fraction of the remaining difference of the energy content between wall temperature and gas temperature. For the deuterium cases, the low radiation temperatures actually result in negative heat conduction to the wall.

To study the effect of mixture gas in the chamber, an ad-hoc initial condition for the chamber gas was created based on a scenario of 10× the number of particles in a target design of pure xenon gas injected into the chamber using the pure xenon initial conditions. The radiation source for the resulting 90:10 xenon to target byproduct mixture was then calculated using IONMIX. It was found to be significantly stronger than pure xenon and of similar magnitude to the source resulting from the trace impurity gases individually.

Like the helium and deuterium, the mixture gas rapidly cooled to nearly the wall temperature in a short duration. However, it was suggested that these results may be in part due to a misapplication of IONMIX as the different neutral gas temperatures could potentially split due to a drop in collisionality once the electrons have recombined. The formulation of IONMIX depends on the electron-ion collision frequency and is likely erroneous when the number of free electrons drops to zero. The de-excitation of the hot gas may proceed after this drop in collisionality due to spontaneous emissions which would occur at different rates in different gases causing the temperatures to split. These temperatures could only be re-equilibrated on the neutral-neutral collision time scale. However, the half-life of this timescale was estimated to be on the order of a few milliseconds for the low density xenon-target mixture providing some confidence in the late time temperature of the chamber gas.

Finally, the variation of gas composition for the mixture was examined to determine if a single radiation source table could accurately represent the radiative cooling of such a mixture. Though the light gases diffused out of the pressure wave and backfilled the void in the chamber center to become the dominant gas components in this region, this gas is cold and a negligible fraction of the overall chamber gas. Furthermore, the light gas radiation source is of similar magnitude to the mixture source. Within the pressure wave where the radiation is significant, this same diffusion depletes the target byproducts by approximately 25%. However, rerunning IONMIX for a 25% depleted mixture produced less than a 5% variation

of radiation source power in a table that spans many orders of magnitude. This difference is therefore well below the likely error of the physical model and so the single mixture source term is sufficient for the chamber gas simulation.

V.C Target Heating

To relate chamber conditions to the survival of cryogenic direct-drive IFE targets within hot chamber gas requires additional modeling. Unlike the meter scale features of the chamber, the target Knudsen numbers can be relatively large. A new analytical model for condensing free-molecular flow was derived and validated with respect to prior work which used Monte Carlo simulations. Though the Monte Carlo simulations are more accurate at higher densities, the analytical solution allows the chamber state to be plotted in relation to maximum heat flux contours. This provides insight into the scaling behavior of the heat flux absent from individual point states results from the Monte Carlo analysis.

Significant effort was also expended in determining the target heating due to individual xenon particle deposition on the target. To study this problem, the same Lennard-Jones potentials used in the transport property calculations were employed to analyze the properties of a xenon ice crystal. The two parameters that describe the potential were used to calculate a minimal energy lattice spacing. This minimal energy was used along with an estimate of the zero point vibrational energy from the Debye's theory of monatomic crystal thermodynamics in conjunction with the experimental measurement of the variation of specific heat of low temperature xenon crystals. The resulting latent heat of deposition at $0K$ was then calculated using these quantities and found to be identical to the values stated in two other sources to more digits than the significant digits of the input parameters. This provided confidence not only in the choice of deposition energy, but also the Lennard-Jones potentials used in the transport calculations.

Maximum heat fluxes were selected based on prior work by Boehm et al.

[15] on direct drive target survival. In this work not only was the heat flux to reach triple point considered, but the nucleation of ^{3}He bubbles resulting from tritium decay was also suggested as a potential failure mode.

Though the helium and deuterium cases cool considerably more than the pure xenon case, the densities of the initial conditions from BUCKY were too high to meet even the least restrictive target survival criteria from Boehms work assuming full accommodation and sticking. However, the margin by which the helium and low density deuterium cases fail the least restrictive bubble nucleation constraint was likely within the error margin of the methods. Potentially safe lower density points were also produced by extrapolating the chamber state points to the intersection of the survival constraints.

Significant improvement to the model would result from experimental quantification of sticking and accommodation coefficients for these gases on cryogenic targets with high-Z overcoats. This is particularly true for helium chamber gas as the accommodation coefficient may be quite low. The triple point constraints are approximately 1/4th of the small nucleus constraints. If the accommodation coefficients are on the order of 0.25, the constraint contours would shift towards the top right and the triple point constraint would be nearly satisfied by the helium and deuterium cases. Similarly, with a small sticking coefficient the xenon constraints would shift and change slope. Though the sticking coefficient would need to be low to reach the high density xenon state, this would improve the safety-margin for the low density xenon case.

Though the gas mixture temperatures were also much lower than the pure xenon chamber results, the safety margin of the target was not improved as dramatically due to increased heat loads from carbon deposition on the target surface. However, the extent to which the carbon has either reacted with free hydrogen or stuck on the walls before the subsequent target injection is not known. This could potentially remove the additional heating contribution which would change the mixture constraint curves to appear similar to the pure xenon curves

and open the window of target survival.

The impact of carbon on the target survival brought to light the possibility of catalyzed surface recombination of monatomic hydrogen isotopes on the surface. This reaction releases more than 25× the energy of xenon ice deposition, and though some of this energy is carried away by the newly formed hydrogen molecule. If the reaction rate and quantity of monatomic hydrogen isotopes are significant in the chamber, this to could pose a significant risk to target survival. However, a full analysis requires detailed estimation of recombination rates and depletion rate of monatomic hydrogen on the walls. This would require additional chemistry and surface reaction models to be incorporated into the chamber simulations. This topic is therefore simply identified as a potential area of concern and left to future analysis.

Finally, as a potential method to circumvent the impact of uncertainty in chamber gas chemistry and to improve target survival, a novel concept of cold gas jets is investigated as a means to protect direct-drive targets. Because xenon cannot be expanded to target surface temperatures due to condensation, cold helium jets are considered. As helium has been used in hypersonic wind tunnels expanded down to $2K$, designing a gas injector to match the target temperature at around $18K$ should not pose a significant challenge. Because this gas is approximately 50× colder than the chamber gas and wall temperatures, matching the static pressure results in a $50x$ denser gas than the chamber gas. At Mach 2, the momentum of such a gas can be used to penetrate the chamber gas and provide a cool pure helium path in which to inject the target. Though the density is higher within this region, the analysis of heat-flux scaling indicates that colder higher density helium is safer than hotter lower density helium at the same pressure. The exact heat loading within such a gas jet is in a significantly different regime from this analysis and likely requires transient Monte Carlo analysis in the future.

V.D Future Work

The most important area for area of future work in the chamber gas simulations is the careful analysis of the radiative cooling rates in the low charge state transition from cool plasma to hot gas. Modeling this behavior will require a significant investment in determining atomic physics rates. Incorporating more experimental data in the validation of models for this cooling regime will be crucial importance for quantitatively accurate results. These experiments can be of smaller scale and focused only on the final cooling in mixtures below a charge state of $\bar{Z} = 1$. However, care will need to be taken to ensure proper scaling of the experiment to identify the impact of molecular diffusivity on the wall collision rate. Some of this data may already exist in the fields of lighting and glow discharge plasmas and may be a potential starting point for future investigations.

Once the uncertainty in the radiative cooling rates has been diminished, the key area for target survival is the quantification of the sticking and accommodation coefficients on cryogenic target surfaces. If these are even moderate fractions, they would dramatically open the chamber design window. Furthermore, there is some evidence to suggest that the accommodation coefficient could potentially be extremely for the conditions and surfaces involved. With the determination of a quantitatively correct chamber gas temperature after validation of the cool plasma to hot gas transition, a small scale low density blow-down wind tunnel with appropriate gas heating could likely easily reproduce the conditions encountered by a target allowing direct investigation of cryogenic target damage.

The development of this algorithm provides a tool to study many other interesting mixture flows. An example of this can be seen in work already performed on scram-jet fuel injection and diffusion at different points along the body of an x43 aircraft shown in Figures V.1 through V.3. Though hybrid Navier-Stokes Monte-Carlo codes exist for single gases, combining the mixture fluid models with such particle methods could provide an even more powerful research tool for such

transitional flows that span many relevant length scales. The work needed to hybridize the code would also provide a direct route to incorporating collisional chemistry models and more realistic slip boundary conditions. This would also provide another tool for direct modeling of the transient target heating though tight coupling of the target and chamber models is likely unnecessary because of the target dimensions.

Finally, the shock mixture separation and broadening results also suggest that such behavior may be of interest within target implosions if the core gas is composed of different mass gasses such as deuterium and tritium. Though Fickian diffusion is generally not important in short time scales because the concentration of a gas can only vary from zero to one in a mean free path, the pressure diffusion term is only limited by shock strength relative to a mean free path. This could be particularly important if high mass impurities exist within the gas such as the Argon impurity mentioned in References [3, 2]. Additionally, Amendt et al. have recently published work[3] suggesting that such a pressure diffusion occurs in electrons within a target implosion plasma. They also show that this electron baro-diffusion may account for unexplained deviations from expected fusion yields in some fusion experiments including the case with Argon impurity. Hopefully the work contained in this dissertation can contribute to the effort to understand how these effects interact with target implosion behavior in the future work. For example, the impact of pressure and thermal diffusion on the growth rate of Rayleigh-Taylor instabilities may be significant even if the diffusion velocities are small just as thermal diffusion dramatically changes the transition criteria from diffusive to convective cell heat transfer in Rayleigh Bénard flow [1, 33, 34].

Chapter 5, in part, contains material in preparation for submission for publication. Martin, R.; Najmabadi, F., Journal of Computational Physics, 2011. The dissertation author was the primary investigator and author of this material.

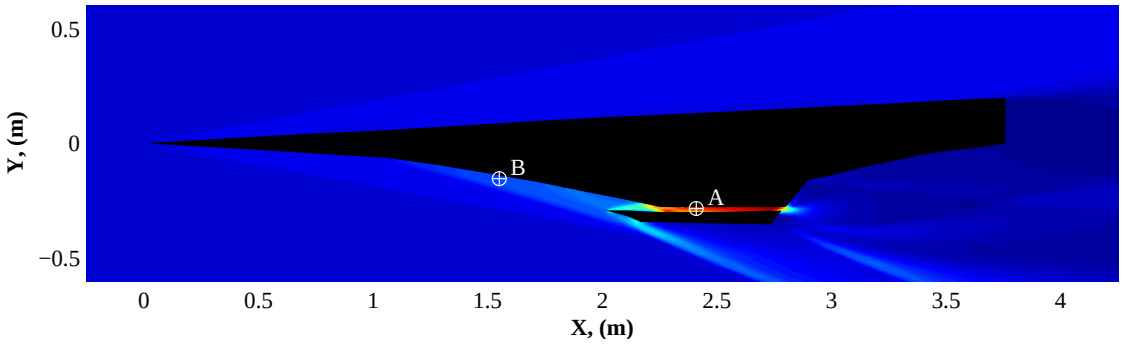

Figure V.1: Exterior flow initial condition positions for scram-jet fuel injector simulations.

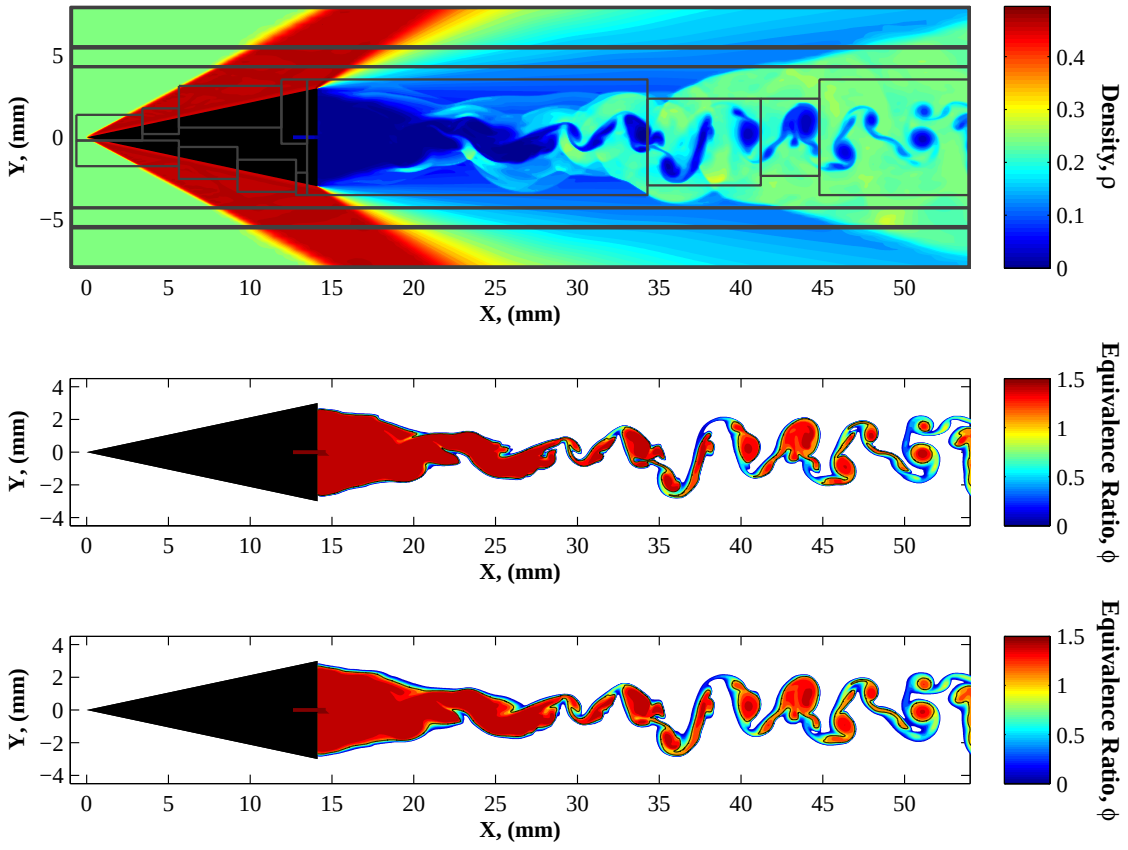

Figure V.2: Scram-jet engine initial condition density (kg/m^3), convected fuel equivalence ratio, and convected diffusing fuel equivalence ratio.

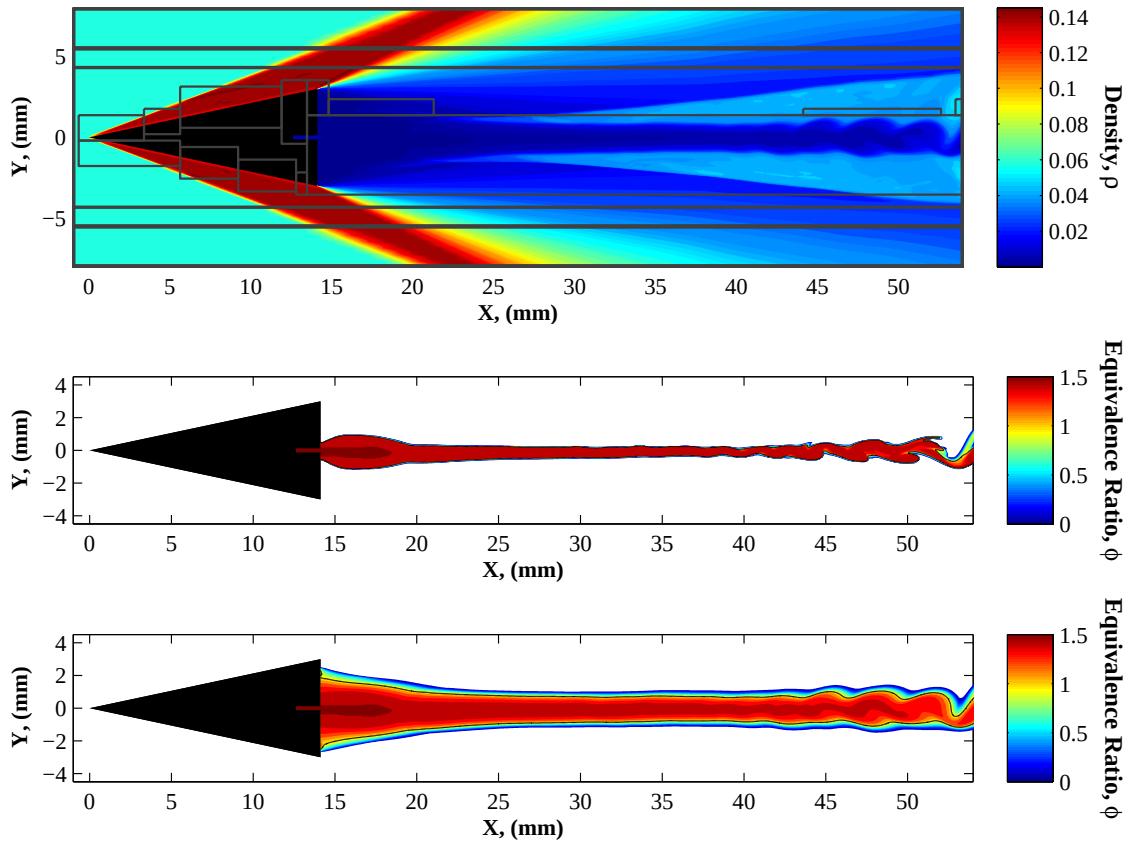

Figure V.3: Compressor initial condition density (kg/m^3), convected fuel equivalence ratio, and convected diffusing fuel equivalence ratio.

Bibliography

[1] J. R. Abernathey and F. Rosenberger. Soret diffusion and convective stability in a closed vertical cylinder. *Physics of Fluids*, 24(3):377–381, 1981.

[2] P. Amendt, C. Bellei, S. Wilks, C. Li, and R. Pertrasso. 52^{nd} APS-DPP Invited Talk Presentation (personal communication), November 2010. The Potential Role of Electric Fields and Plasma Barodiffusion on the Inertial Confinement Fusion Database.

[3] P. Amendt, O. L. Landen, H. F. Robey, C. K. Li, and R. D. Petrasso. Plasma barodiffusion in inertial-confinement-fusion implosions: Application to observed yield anomalies in thermonuclear fuel mixtures. *Phys. Rev. Lett.*, 105(11):115005, Sep 2010.

[4] R. Aris. *Vectors, Tensors, and the Basic Equations of Fluid Mechanics*. Dover, New York, 1962.

[5] A. Barbet, N. Sadeghi, and J. Pebay-Peyroula. Decay of metastable xenon atoms xe*(3 p 2) in a xenon afterglow. *J. Phys. B: At. Mol. Phys.*, 8(10):1776, 1975.

[6] I. E. Beckwith and C. G. Miller. Aerothermodynamics and transition in high-speed wind tunnels at nasa langley. *Annual Review of Fluid Mechanics*, 22(1):419–439, 1990.

[7] J. B. Bell, A. L. Garcia, and S. A. Williams. Computational fluctuating fluid dynamics. *ESAIM: M2AN*, 44(5):1085–1105, 2010.

[8] J. Bertin. *Aerodynamics for Engineers*. Prentice Hall, Upper Saddle River, New Jersey, 4th edition, 2002.

[9] B. Bird, W. Stewart, and E. Lightfoot. *Transport Phenomena*. Prentice Hall, Upper Saddle River, New Jersey, 2nd edition, 1960.

[10] G. Bird. *Molecular Gas Dynamics and the Direct Simulation of Gas Flows*. Oxford University Press, Oxford, UK, 1994.

[11] G. A. Bird. The structure of normal shock waves in a binary gas mixture. *Journal of Fluid Mechanics*, 31(04):657–668, 1968.

[12] A. Bochkarev, V. Kosinov, V. Prikhod'ko, and A. Rebrov. Structure of a supersonic jet of an argon-helium mixture in a vacuum. *J. App. Mech. and Tech. Phys.*, 11(5):857–861, 1970.

[13] K. Boehm. Time dependant thermo-mechanical modeling including phase changes in direct drive inertial fusion energy targets. Report 06-02, University of California San Deigo, Center for Energy Research, San Diego, CA, Feb. 2006.

[14] K. Boehm. Numercial and experimental studies of IFE target layering in a cryogenic fluidized bed. Report 09-03, University of California San Deigo, Center for Energy Research, San Diego, CA, May 2009.

[15] K.-J. Boehm and A. R. Raffray. Transient thermo-mechanical behavior of a direct-drive target during injection in an inertial fusion energy chamber. *Fusion Engineering and Design*, 82(3):265 – 290, 2007.

[16] R. E. Center. Measurement of shock-wave structure in helium-argon mixtures. *Physics of Fluids*, 10(8):1777–1784, 1967.

[17] I. Chern and P. Colella. A conservative front tracking method for hyperbolic conservation laws. UCRL JC-97200, Lawrence Livermore National Laboratories, Livermore, CA, July 1987.

[18] B. Christensen. Thermal and mechanical analysis of IFE direct drive targets. UCSD-ENG- 112, University of California San Deigo, Center for Energy Research, San Diego, CA, July 2004.

[19] B. Christensen, A. Raffray, and M. Tillack. Thermal loading of a direct drive target rarefied gas. *Fusion Science and Technology*, 47(4):1175–1179, May 2005.

[20] H. J. H. Clercx and G. J. F. van Heijst. Energy spectra for decaying 2d turbulence in a bounded domain. *Phys. Rev. Lett.*, 85(2):306–309, Jul 2000.

[21] P. Colella. Glimm's method for gas dynamics. *SIAM J. SCI. STAT. COMPUT.*, 3(1):76–110, 1982.

[22] P. Colella. A direct eulerian muscl scheme for gas dynamics. *SIAM J. SCI. STAT. COMPUT.*, 6(1):104–117, 1985.

[23] Z. Dragojlovic, F. Najmabadi, and M. Day. An embedded boundary method for viscous, conducting compressible flow. *Journal of Computational Physics*, 216(1):37 – 51, 2006.

[24] H. Fenichel and B. Serin. Low-temperature specific heats of solid neon and solid xenon. *Phys. Rev.*, 142(2):490–495, Feb 1966.

[25] R. Fernández-Feria and J. F. D. L. Mora. Shock wave structure in gas mixtures with large mass disparity. *Journal of Fluid Mechanics*, 179(-1):21–40, 1987.

[26] A. Ferreira and L. Lobo. The sublimation of argon, krypton, and xenon. *The Journal of Chemical Thermodynamics*, 40(12):1621 – 1626, 2008.

[27] A. L. Garcia, J. B. Bell, W. Y. Crutchfield, and B. J. Alder. Adaptive mesh and algorithm refinement using direct simulation monte carlo. *Journal of Computational Physics*, 154(1):134 – 155, 1999.

[28] C. Gentile, C. Priniski, J. Sethian, R. Parsells, S. Langish, L. Ciebiera, W. Blanchard, R. Yager, and C. Jun. IFE target chamber vacuum pumping

system 11m radius case. Lawrence Livermore National Laboratory, Livermore CA., USA, June 2005. 12th High Average Power Laser Program Workshop.

[29] E. Goldman and L. Sirovich. Equations for gas mixtures. *Physics of Fluids*, 10(9):1928–1940, 1967.

[30] E. Goldman and L. Sirovich. Equations for gas mixtures. ii. *Physics of Fluids*, 12(1):245–247, 1969.

[31] E. Goldman and L. Sirovich. The structure of shock-waves in gas mixtures. *Journal of Fluid Mechanics*, 35(03):575–597, 1969.

[32] R. W. Gurney. Lattice vibrations in graphite. *Phys. Rev.*, 88(3):465–466, Nov 1952.

[33] D. Gutkowicz-Krusin, M. A. Collins, and J. Ross. Rayleigh–b[e-acute]nard instability in nonreactive binary fluids. i. theory. *Physics of Fluids*, 22(8):1443–1450, 1979.

[34] D. Gutkowicz-Krusin, M. A. Collins, and J. Ross. Rayleigh–b[e-acute]nard instability in nonreactive binary fluids. ii. results. *Physics of Fluids*, 22(8):1451–1460, 1979.

[35] R. Herczynski, M. Tarczynski, and Z. Walenta. Shock waves in binary gas mixtures. In D. Bershader and R. Hanson, editors, *Proceedings of 15th International Symposium on Shock Waves and Shock Tubes*, pages 713–719, Stanford CA, 1986. Stanford University Press.

[36] G. Herzberg. The dissociation energy of the hydrogen molecule. *Journal of Molecular Spectroscopy*, 33(1):147 – 168, 1970.

[37] T. L. Hill. *An Introduction to Statistical Thermodynamics*. Dover, New York, 1986.

[38] J. Hirschfelder, C. Curtiss, and R. Bird. *Molecular Theory of Gases and Liquids*. John Wiley & Sons, New York, 1954.

[39] M. Hoch, P. E. Blackburn, D. P. Dingledy, and H. L. Johnston. The heat of sublimation of carbon. *The Journal of Physical Chemistry*, 59(2):97–99, 1955.

[40] D. Hollenbach and E. E. Salpeter. Surface recombination of hydrogen molecules. *Astrophysical Journal*, pages 155–164, Jan. 1971.

[41] J. Huba. NRL plasma formulary. Naval research laboratory, Plasma Physics Division, Washington, DC 20375, 2007.

[42] J. Hurly and M. Moldover. Ab initio values of the thermophysical properties of helium as standards. *J. Res. Natl. Inst. Stand. Technol.*, (105):667–688, 2000.

[43] H. Johansen and P. Colella. A cartesian grid embedded boundary method for poisson's equation on irregular domains. *Journal of Computational Physics*, 147(1):60 – 85, 1998.

[44] R. Kamali, H. Emdad, and M. Alishahi.

[45] R. Kee, G. Dixon-Lewis, J. Warnatz, M. Coltrin, and J. Miller. A fortran computer code package for the evaluation of gas-phase, multicomponent transport properties. Sandia National Laboratories Report SAND86-8246, Albuquerque, NM and Livermore, CA, Dec. 1986.

[46] R. LeVeque. *Numerical Methods for Conservation Laws*. Birkhäuser Verlag, Basel, 1990.

[47] J. MacFarlane, G. Moses, and R. Peterson. Bucky-1 - a 1-d radiation hydrodynamics code for simulating inertial confinement fusion high energy density plasmas. UWFDM 984, Fusion Technology Institute, University of Wisconsin Madison, Madison, WI, Aug. 1995.

[48] J. J. Macfarlane. Ionmix - a code for computing the equation of state and radiative properties of lte and non-lte plasmas. *Computer Physics Communications*, 56(2):259 – 278, 1989.

[49] A. Marquina and P. Mulet. A flux-split algorithm applied to conservative models for multicomponent compressible flows. *Journal of Computational Physics*, 185(1):120 – 138, 2003.

[50] R. Martin and F. Najmabadi. Breakdown and limit of continuum diffusion velocity for binary gas micutres from direct simulation. July 2010. 27th Int. Symp. on Rarefied Gas Dyn.

[51] R. Martin and F. Najmabadi. Conservative flux limited algorithm for multi-component compressible flow with thermal mass diffusion. J. Comput. Phys (To Be Submitted), April 2010.

[52] S. Matsuo, M. Tanaka, Y. Otobe, H. Kashimura, H. Kim, and T. Setoguchi. Effect of axisymmetric sonic nozzle geometry on characteristics of supersonic air jet. *J. Therm. Sci.*, 13(2):121–126, 2004.

[53] R. Miranda, S. Daiser, K. Wandelt, and G. Ertl. Thermodynamics of xenon adsorption on pd(s)[8(100) (110)]: From steps to multilayers. *Surface Science*, 131(1):61 – 91, 1983.

[54] L. Monchick and E. A. Mason. Transport properties of polar gases. *The Journal of Chemical Physics*, 35(5):1676–1697, 1961.

[55] H. Murphy and D. Miller. Effects of nozzle geometry on kinetics in free-jet expansions. *J. Phys. Chem.*, 88(20):4474–4478, 1984.

[56] M. Oberai. Kinetic-theory approach to the problem of shock-wave structure in a binary mixture. *Phys. Fluids*, 8:5:826–833, 1965.

[57] H. O'Hara and F. J. Smith. Transport collision integrals for a dilute gas. *Computer Physics Communications*, 2(1):47 – 54, 1971.

[58] E. Oran and J. Boris. *Numerical Simulation of Reactive Flow*. Cambridge University Press, Cambridge, UK, 2001.

[59] R. Panton. *Incompressible Flow*. John Wiley & Sons, New York, 2nd edition, 1996.

[60] R. B. Pember, J. B. Bell, P. Colella, W. Y. Curtchfield, and M. L. Welcome. An adaptive cartesian grid method for unsteady compressible flow in irregular regions. *Journal of Computational Physics*, 120(2):278 – 304, 1995.

[61] J. Perkins. Hapl - reference target specification. Photon spectrum and ion specta, High Average Power Laser Program, http://aries.ucsd.edu/HAPL/DOCS/reftarget.html, Oct. 2005.

[62] D. E. Post, R. V. Jensen, C. B. Tarter, W. H. Grasberger, and W. A. Lokke. Steady-state radiative cooling rates for low-density, high-temperature plasmas. *Atomic Data and Nuclear Data Tables*, 20(5):397 – 439, 1977.

[63] D. Powers. *Boundary Value Problems*. Academic Press, San Diego, 4th edition, 1999.

[64] C. Pozrikidis. *Numerical Computation in Science and Engineering*. Oxford University Press, New York, 1998.

[65] A. Raffray. Target survival during injectionthe advantages of getting rid of the buffer gas. Naval Research Laboratory, Washington DC, USA, March 2005. 11th High Average Power Laser Program Workshop.

[66] A. Raffray, D. Haynes, and F. Najmabadi. IFE chamber walls: requirements, design options, and synergy with mfe plasma facing components. *Journal of Nuclear Materials*, 313-316:23 – 31, 2003. Plasma-Surface Interactions in Controlled Fusion Devices 15.

[67] A. R. Raffray. Threats, design limits and design windows for laser IFE dry wall chambers. *Journal of Nuclear Materials*, 347(3):178 – 191, 2005. Laser Fusion Materials.

[68] Reaction Design. *ChemKin® Software Theory Manual*, 4.0.2 edition.

[69] V. Reis and J. Fenn. Separation of gas mixtures in supersonic jets. *J. Chem. Phys.*, 8(12):3240–3250, 1963.

[70] D. E. Rosner and D. H. Papadopoulos. Jump, slip, and creep boundary conditions at nonequilibrium gas/solid interfaces. *Industrial & Engineering Chemistry Research*, 35(9):3210–3222, 1996.

[71] D. Rothe. Electron beam studies of the diffusive separation of helium-argon mixtures in free jets and shock waves. University of Toronto Institute for Aerospace Studies Report 114, Toronto, Canada, July 1966.

[72] D. Rothe. personal communication, April 2010.

[73] D. E. Rothe. Electron beam studies of the diffusive separation of helium-argon mixtures. *Physics of Fluids*, 9(9):1643–1658, 1966.

[74] E. Saloman. Energy levels and observed spectral lines of xenon, xei through xeliv. *J. Phys. Chem. Ref. Data*, 33(3):765–921, 2004.

[75] J. Sethian, D. Colombant, J. Giuliani, R. Lehmberg, M. Myers, S. Obenschain, A. Schmitt, J. Weaver, M. Wolford, F. Hegeler, M. Friedman, A. Robson, A. Bayramian, J. Caird, C. Ebbers, J. Latkowski, W. Hogan, W. Meier, L. Perkins, K. Schaffers, S. Abdel Kahlik, K. Schoonover, D. Sadowski, K. Boehm, L. Carlson, J. Pulsifer, F. Najmabadi, A. Raffray, M. Tillack, G. Kulcinski, J. Blanchard, T. Heltemes, A. Ibrahim, E. Marriott, G. Moses, R. Radell, M. Sawan, J. Santarius, G. Sviatoslavsky, S. Zenobia, N. Ghoniem, S. Sharafat, J. El-Awady, Q. Hu, C. Duty, K. Leonard, G. Romanoski, L. Snead, S. Zinkle, C. Gentile, W. Parsells, C. Prinksi, T. Kozub, T. Dodson, D. Rose, T. Renk, C. Olson, N. Alexander, A. Bozek, G. Flint, D. Goodin, J. Hund, R. Paguio, R. Petzoldt, D. Schroen, J. Sheliak, T. Bernat, D. Bittner, J. Karnes, N. Petta, J. Streit, D. Geller, J. Hoffer, M. McGeoch, S. Glidden, H. Sanders, D. Weidenheimer, D. Morton, I. Smith, M. Bobecia, D. Harding, T. Lehecka, S. Gilliam, S. Gidcumb, D. Forsythe, N. Parikh, S. O'Dell, and

M. Gorensek. The science and technologies for fusion energy with lasers and direct-drive targets. *Plasma Science, IEEE Transactions on*, 38(4):690 –703, 2010.

[76] F. Sherman. Hydrodynamical theory of diffusive separationof mixtures in a free jet. *Phys. Fluids*, 8(5):773–775, 1965.

[77] F. S. Sherman. Shock-wave structure in binary mixtures of chemically inert perfect gases. *Journal of Fluid Mechanics*, 8(03):465–480, 1960.

[78] T.-M. Shih. *Numerical Heat Transfer*. Hemisphere Publishing Corporation, New York, 1984.

[79] K. Srivastava. Mutual diffusion of binary mixtures of helium, argon and xenon at different temperatures. *Physica*, 25(1-6):571 – 578, 1959.

[80] J. Tannehill, D. Anderson, and R. Pletcher. *Computational Fluid Mechanics and Heat Transfer*. Taylor & Francis, Philadelphia, 2nd edition, 1997.

[81] Y. Touloukian, editor. *Thermophysical Properties of Matter*. Plenum, New York, 1970.

[82] H. van Regemorter. Rate of Collisional Excitation in Stellar Atmospheres. *Astrophysics Journal*, 136:906–+, Nov. 1962.

[83] Varian, Inc. Vacuum Technologies, http://www.varianinc.com/image/vimage/docs/products/vacuum/pumps/turbo/shared/turbo-catalog.pdf. *Turbo-V Pumps*.

[84] W. G. Vincenti and C. H. K. Jr, editors. *Introduction to Physical Gas Dynamics*. Krieger Publishing Company, Malabar, FL, 2002.

[85] W.-L. Wang and I. D. Boyd. Predicting continuum breakdown in hypersonic viscous flows. *Physics of Fluids*, 15(1):91–100, 2003.

[86] P. Waterman and S. A. Stern. Separation of gas mixtures in a supersonic jet. *J. Chem. Phys.*, 31(2):405–419, 1959.

[87] H. Wijeshinghe, R. Hornung, A. Garcia, and N. Hadjiconstantinou. Three-dimensional hybrid continuum-atomistic simulations for multiscale hydrodynamics. *J. Fluids Eng.*, 126:768–777, 2004.

[88] B. J. Wood and H. Wise. Kinetics of hydrogen atom recombination on surfaces1. *The Journal of Physical Chemistry*, 65(11):1976–1983, 1961.

[89] Y. Zeldovich and Y. Razier, editors. *Physics of Shock Waves and High-Temperature Hydrodynamic Phenomena*. Academic Press, New York, 1966.

[90] V. Zigan. Gasdynamische berechnung der trenndüsenentmischung. *Z. Naturforsch.*, (17a):772–778, 1962.